October 2021

Computational approaches for the multimodal imaging of nanomaterials and their biochemical effects

Laura J. Castellanos
University of Massachusetts Amherst

COMPUTATIONAL APPROACHES FOR THE MULTIMODAL IMAGING OF NANOMATERIALS AND THEIR BIOCHEMICAL EFFECTS

A Dissertation Presented

by

LAURA JULIANA CASTELLANOS GARCIA

Submitted to the Graduate School of the
University of Massachusetts Amherst in partial fulfillment
of the requirements for the degree of

DOCTOR OF PHILOSOPHY

September 2021

Chemistry

COMPUTATIONAL APPROACHES FOR THE MULTIMODAL IMAGING OF NANOMATERIALS AND THEIR BIOCHEMICAL EFFECTS

A Dissertation Presented

by

LAURA JULIANA CASTELLANOS GARCIA

Approved as to style and content by:

_____

Richard W. Vachet, Chair

_____

Vincent M. Rotello, Member

_____

Ricardo Metz, Member

_____

Stephen J. Eyles, Member

_____

Ricardo Metz, Department Head

Department of Chemistry

DEDICATION

To my family and friends

ACKNOWLEDGMENTS

I want to start by thanking my advisor, Richard, for his support throughout my entire PhD and for encouraging the exploration of the ideas that culminated in this thesis. Some of these ideas seemed very risky bets at the moment when I first proposed them, but he supported me in pursuing them. I always had admired his leadership and compassion to help us navigate graduate school. Many thanks to the members of my committee: professors Vincent Rotello, Steve Eyles and Ricardo Metz. They have been a continuous source of guidance, helping me advance my scientific perspectives through the feedback they have provided to my work. Having scientists with such experience and diverse perspectives in my committee has been a privilege. I also want to thank my mentor, Marianny Combariza, for motivating me to pursue my doctoral studies in first place, and for always being the amazing role model she is to young scientists.

I will be always indebted to many of my fellow PhD students, who collaborated with me on many projects and from who I have learned tremendously. Thanks to Gokhan Elci, and Alyssa Marsico who trained me and introduce me to my first projects during my early years of my Ph.D and to Kristen Sikora, with whom I collaborated in some of the experiments that made up part of the dissertation. Several parts of this work could not had been possible without their help. Thanks to my collaborators in the Rotello lab: Yi-Wei “Bill” Lee, Xianzhi Zhang, Yuanchang Liu, David Luther, for their constant help. Their commitment to their projects secured the success of the work we did together.

I want to thank the continuous help and encouragement from my colleagues at the Vachet lab who shared with me this journey, specially Dheeraj Agrohia, Jeerapat ‘Ping’ Doungchawee, Teerapong ‘Max’ Jantarat and Akaansha Rampal, for the times we spend doing experiments together, sharing ideas, and fixing instruments. Special thanks to Mac Serrano for being such an incredible friend and for many nights spent working at the lab, taking breaks to have fun.

During my time as a Ph.D student I was a member of the association of professional development (APDC) for several years, this gave me the opportunity to know and work with great people from the chemistry department, I want to thank all of them, especially Catherine Tremblay, for her commitment for being the best leader for APDC. Thanks to all my friends in the chemistry department, especially Roberto Cao and Michael Lu, who had been great friends and made my time as a graduate student very enjoyable.

This Ph.D. also gave me the opportunity to grow in other aspects of my life, assuming other roles that extended my vision of the world and made me reflect on my social obligations as a scientist. Part of it has been my work in Science Clubs, which have given me the opportunity to keep in contact with my country by helping students all over Colombia to fall in love with science. Thanks to the people who offered me the opportunity to be part of this project, Antonio Copete, and Maier Avendaño, and to the great people that I had encounter during this journey, as Bernardo Rey and its students, and the incredible team of volunteers at Science Clubs Colombia and its recently created spin-off, ScienteLab.

Finally, I would like to thank who have been through all these struggles and successes my unconditional husband, Jonathan Romero. His love has been a permanent source of comfort and motivation. For him, I have no words to express my gratitude. I thank my unconditional and loving family, whose effort has put me where I am today. Thanks to my parents, Adolfo Castellanos and Luz Holanda Garcia and my sister Angelica Castellanos and all my family in Colombia. This has been an amazing learning experience both professionally and personally and I could not be more grateful with the universe for offering me this incredible opportunity.

ABSTRACT

COMPUTATIONAL APPROACHES FOR THE MULTIMODAL IMAGING OF NANOMATERIALS AND THEIR BIOCHEMICAL EFFECTS

SEPTEMBER 2021

LAURA JULIANA CASTELLANOS GARCIA

B.S., UNIVERSIDAD INDUSTRIAL DE SANTANDER

Ph.D., UNIVERSITY OF MASSACHUSETTS AMHERST

Directed by: Professor Richard W. Vachet

Nanomaterial delivery systems constitute a group of drug delivery vehicles that have been used extensively in biodelivery. The proper characterization of the therapeutic function of these nanomaterials requires analytical methods to track the presence of the cargo and its biochemical effects. In some cases, the detection of the cargo and biochemical changes are not attainable in the same experiment, and more than one technique might be needed for the proper analysis of the drug delivery system. In this case, separate analysis of adjacent tissue sections is performed by techniques that offer complementary information such as MALDI-MS and LA-ICP-MS. However, the approaches to combine the information from these techniques to obtain insights into the mechanism of action of the nanomaterials have been limited to visual inspection and image overlay, which can only provide qualitative information. To advance towards a more quantitative analysis, in this dissertation we have developed computational techniques for image reconstruction, segmentation, and registration of MALDI-MS and LA-ICP-MS images to monitor the biodistribution, excretion and biochemical effects of nanomaterial delivery systems. First, we developed an open-source computational approach for LA-ICP-MS image reconstruction and

segmentation using Python, which revealed that nanomaterials distribute in different sub-organ regions based on their chemical and physical properties. For instance, in the analysis of gold nanoparticles and bismuth nanorods, we find that the nanomaterials distribute in different regions of the spleen, suggesting differences in their biochemical interactions within the same organ. Next, we developed a computational workflow in Python to register LA-ICP-MS and MALDI-MS images using image registration approaches, obtaining a method with errors below 50 µm. Finally, we used the developed approaches for registration of LA-ICP-MS and MALDI-MS images to evaluate the delivery vehicles and cargo, obtaining quantitative information about the correlation of the signals obtained in the two image modalities. The use of image registration for the analysis of siRNA delivery via nanoparticle stabilized capsules (NPSC) reveals that expected changes in lipid levels occur at different locations than the NPSC accumulate, thus providing deeper insight into how siRNA delivery by NPSCs influences lipid biochemistry in vivo.

TABLE OF CONTENTS

LIST OF TABLES

Table **Page**

LIST OF FIGURES

Figure **Page**

CHAPTER 1

INTRODUCTION

1.1 Nanomaterials in biological applications

The development of nanomaterials is revolutionizing many areas of medicine, including imaging,[1–3] sensing[4,5] and therapeutics.[6–8] In particular, functionalized nanoparticles can serve as controlled drug delivery systems, which can improve the effectiveness and selectivity of therapeutics by transporting the drugs directly to the place of action.[9–11] The use of nanomaterials helps to overcome limitations of conventional delivery, such as non-specific distribution,[12] inadequate accumulation,[9] and intracellular trafficking.[13] In addition, nanomaterials provide protection and improve stability of biologicals cargo.[14,15] Although there are several type on nanomaterials used for drug delivery, they are classified in three main categories: inorganic, polymer and lipid-based nanomaterials.[16]

Inorganic nanomaterials, such as gold nanoparticles (NPs),[17] iron NPs,[18] silica NPs[19] and quantum dots,[20] have distinctive electrical and magnetic properties, which make them useful for drug delivery and theranostics applications.[21,22] Due to the extensive methods available for synthesis and functionalization, many types of inorganic nanomaterials with variability in size, structure and geometry had been reported.[23–25]. AuNPs, in particular, have been of great interest in the past decades because of its high intracellular accumulation[17] and low toxicity.[26]

In recent years, we had seen a surge in the development of biological therapies, such as proteins, RNA, CRISPR, among others.[27] Due to this increasing interest, nanoparticle-based vehicles had been designed for the delivery of proteins,[28] enzymes,[14] and genome editing biologics.[15,29] Nanoparticle-based delivery vehicles are synthesized by promoting the self-assembly of the biologics (proteins, enzymes, RNA) with inorganic nanoparticles.[30] The resulting

nanoparticle-based vehicle is very versatile, provides protection to the cargo and have minimal toxicity.[28] More importantly, its mechanism of action through membrane fusion allows efficient cellular transport of the vehicles to the cytosol, avoiding endosomal entrapment.[28]

1.2 Characterization of nanomaterials in biological samples and tissues

Several approaches involving optical, electrical, radioactive or magnetic measurements have been applied to monitor NPs in biological samples.[31,32] Common methods including: scanning and transmission electron microscopy (SEM and TEM), atomic force microscopy (AFM) and X-ray diffraction (XRD) focuses in the characterization of NPs size, shape and surface properties.[33,34] Although these techniques are fundamental for the quality control and reproducibility, the investigation of the NPs modes of action requires the development of methods that allows the characterization of the NPs in biological samples.

Fluorescent imaging had been used successfully for nanomaterial imaging in biological samples using fluorescent probes with high brightness and photostability.[35] Although the resolution of these approaches is noteworthy, the method is limited by the large variety of labels needed, limiting the multiplexed characterization of different NPs.[36] In addition, other spectroscopy techniques as Surface-Enhanced Raman Spectroscopy (SERS) has been applied for metallic NPs imaging,[34] but the lack of reproducibility caused by the variation in size and NPs aggregation prevents a quantitative analysis of *in-vivo* samples.[34] More advanced imaging methods such as scanning electron microscopy with energy-dispersive X-ray analysis (SEM-EDX) and particle-induced X-ray emission (PIXE) offer excellent spatial resolution, whereas, laborious sample preparation is required, and the sensitivity is low.[37] Synchrotron radiation X-ray fluorescence (SR-XRF) also offers good resolution for nanomaterials imaging, but it requires access to a synchrotron facility, making it much less broadly applicable.[38]

1.3 Characterization of nanomaterials using mass spectrometry

Mass spectrometry (MS) can overcome some of the limitations of the analytical techniques described above to characterize NPs in biological samples.[39,40] MS offers multiplexing detection of thousands of chemical species in the same experiment, making this method very useful in the study of NPs mechanism of action in complex samples. Some of the most used methods for NPs detection in mass spectrometry are matrix assisted laser desorption ionization (MALDI-MS),[41,42] laser ablation inductively coupled plasma (LA-ICP-MS),[43,44] electrospray ionization (ESI-MS),[45] and secondary ion mass spectrometry (SIMS).[46,47] Each of the described methods have different sample ionization mechanisms, providing different types of ions and complementary information about the sample. In this dissertation, we use extensively MALDI-MS and LA-ICP-MS, and thus we will provide more details about these two techniques.

In MALDI-MS, laser radiation (355nm) ionizes and desorbs molecules deposited on a thin layer using an organic matrix to protect the sample from fragmentation. The molecules and fragments obtained in this process are sorted by its mass to charge ratio, using a mass analyzer, as shown in Figure 1.1. Generally, MALDI-MS equipment's are coupled to time-of-flight analyzers (TOF), which provide the same kinetic energy to the ions in order to spatially separate them according to their mass to charge value, as shown in Figure 1.1. When applied to biological samples containing NPs, MALDI-MS enables the quantification of NPs, it's cellular uptake and stability in cells and tissues.[48–50]

In LA-ICP-MS, a more energetic laser (213nm) is used for the complete ablation of the sample, generating ion fragments in gas phase. The ions are then transferred to a plasma, creating atoms, which are analyzed using a quadrupole, as shown in Figure 1.1. During the ablation and ionization process the nanomaterials are atomized, leaving only metals for detection. Since LA-ICP-MS is very efficient at performing ablation, the technique is very quantitative and sensitive, allowing proper quantitation of metals in very complex samples.

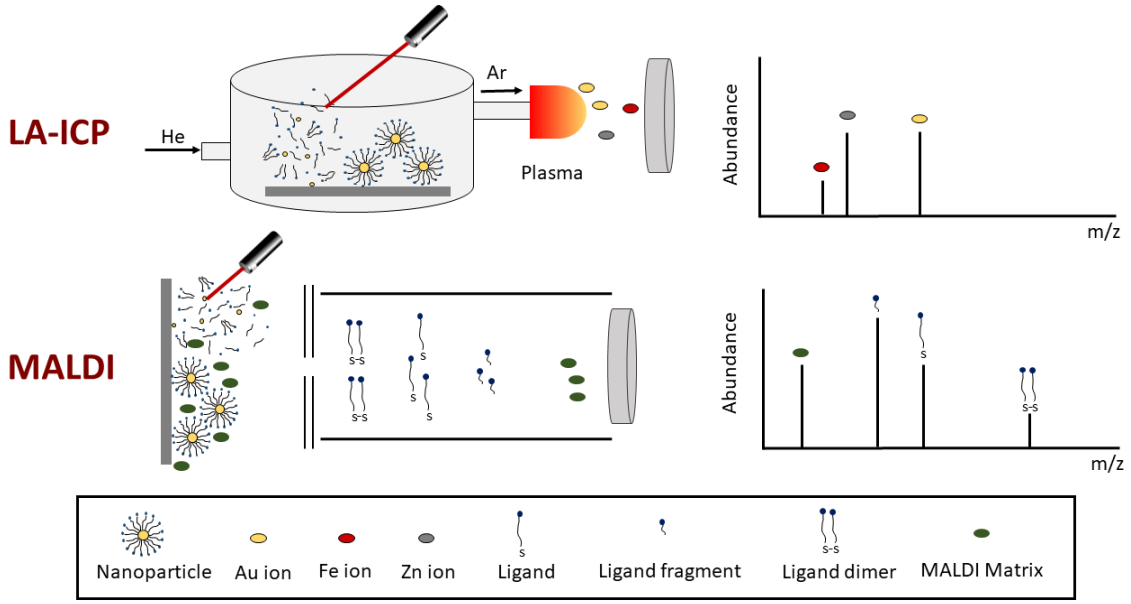

Figure 1.1. MALDI-MS and LA-ICP-MS techniques used in the characterization of NPs.

1.4 Mass Spectrometry Imaging

Mass spectrometry imaging (MSI) comprises several techniques that allow the two-dimensional analysis of several analytes in a solid sample.[51,52] Figure 1.2. explains how MSI operates in MALDI-MS to provide images of a tissue section. Among MSI techniques, matrix-assisted laser desorption/ionization (MALDI-MS)[53–56] have been extensively used for the spatial analysis of metabolites,[57,58] lipids,[59,60] peptides,[61,62] proteins,[63,64] and exogenous analytes, like drugs.[65–67] Alternatively, laser ablation inductively coupled plasma mass spectrometry (LA-ICP-MS) imaging is increasingly used for imaging metal distributions in biological tissues. Among metal imaging techniques, LA-ICP-MS is perhaps the most sensitive technique for elemental imaging with detection limits in the sub µg/g level, while providing multiplexed metal analysis with spatial resolutions in the 10 to 200 µm range.[68–70] Given its combination of sensitivity, multi-metal detection capability, and accessibility, LA-ICP-MS has been used broadly in applications that include analysis of metals in neurogenerative diseases like Alzheimer's, Parkinson's, and

Wilson's disease,[71–73] detection of anti-cancer metallodrugs,[74,75] studies of metalloproteins,[76,77] and analysis of nanomaterials in biological tissues.[49,78] Several reviews have detailed the development and use of LA-ICP-MS imaging for analyzing biological tissues.[37,44,68–70,79,80]

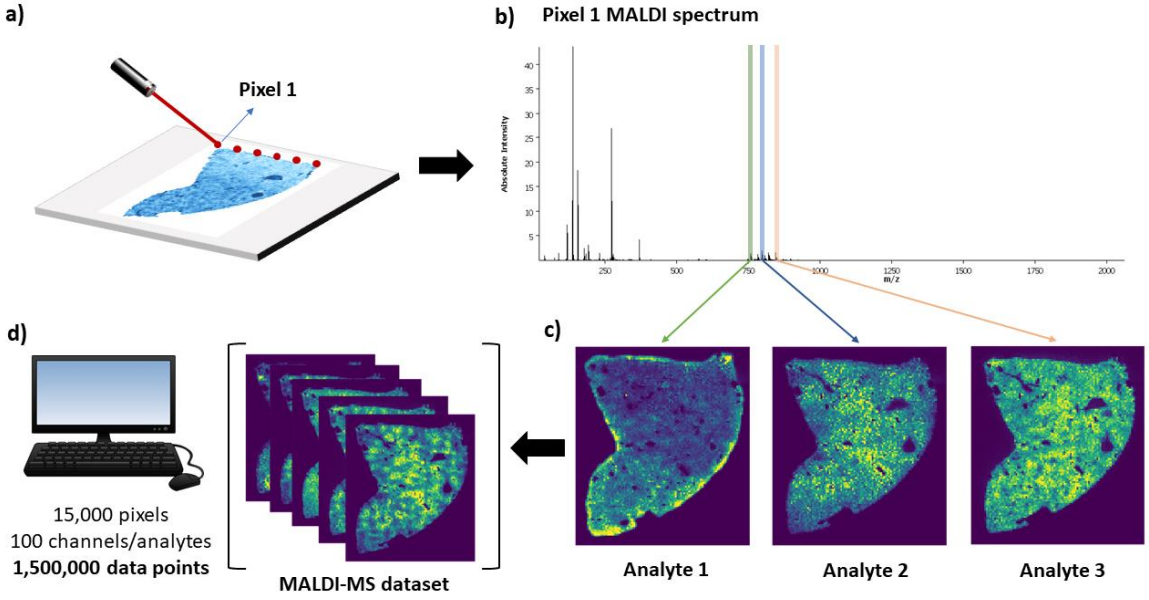

Figure 1.2. MALDI-MS imaging process: pixels in a tissue section are ablated (a), generating a spectra per pixel, containing all the detected analytes (b). Then, images of each analyte are rendered by plotting the signal intensity of the analyte in each pixel (c). Images of the analytes detected are overlaid to create a dataset that is collected and used for computational data analysis (d).

1.5 Multimodal imaging in mass spectrometry imaging MSI

Despite the near universal detection capabilities of MSI, it is difficult to detect all compounds of interest in a given MSI experiment.[81,82] Furthermore, the right combination of MSI modalities can provide complementary data, allowing optimal information to be obtained from a given sample.[76,83,84] Properly combining the data from different imaging modalities can allow the strengths of each modality to be leveraged and provide more in-depth information about a sample.[85–88] For example, MALDI-MSI is very good at providing biomolecule information but can

suffer more significant pixel-to-pixel signal variability.[89] On the other hand, LA-ICP-MSI is less subject to signal suppression and signal variability because samples are completely ablated, allowing it to provide excellent quantitative information about metal distributions.[44] However, LA-ICP-MSI provides less chemical information due to its destructive nature.[68]

Although multimodal imaging implementation dates back two decades, mass spectrometry multimodal imaging is a novel concept, implemented just a few years ago, and considered to be the next generation approach in mass spectrometry molecular mapping.[82,86] Very recently, several registration techniques had been applied to mass spectrometry for multimodal imaging: (i) MALDI-MS and fluorescent microscopy registration to identify malaria infection in liver hepatocytes.[90] (ii) MALDI-MS and confocal microscopy registration to identify stem cell colonies.[91] (ii) Single probe MSI and microscopy registration to track amyloid plaques in Alzheimer's disease.[92] (iv) MALDI-MS in reflectron and MALDI-MS in linear mode registration, for simultaneous lipid and protein analysis to study the mechanism of acute myocardial infarction.[84]

1.6 Image registration

Image registration is the process of transforming two images in the same coordinate system. When images are acquired by different instruments, they have different orientations and spatial coordinates. To correlate information among two image modalities, we can employ several strategies as described in Figure 1.3. First, we can compare the two images by eye and find visual correlation among the images. Second, we can optically overlay the images using image rendering tools. Third, we can use image registration approaches to transform the images to the same coordinate system, obtaining pixel-to-pixel correspondence. When data analysis is performed using only the first two strategies, the trends and correlation among the images are only qualitative. To go beyond a qualitative analysis, image registration becomes necessary as it enables the

combination of information obtained using different modalities as well as the use of statistical methods to quantify correlations and discover trends in the data that escape human inspection. This is particularly relevant for the analysis of multiplexing imaging, such as mass spectrometry imaging, where the richness of the data contains more information than what can be extracted by simply visualizing the images of individual channels. Furthermore, these approaches for image registration and analysis must be computerized in order to process the sheer amount of data generated by multiplexing techniques in an efficient manner, thus requiring the creation of computational workflows that implement these image analysis techniques. The application of such workflows to MALDI imaging opens many avenues for obtaining quantitative insights about the biochemical processes underlying the target *in-vivo* experiments.

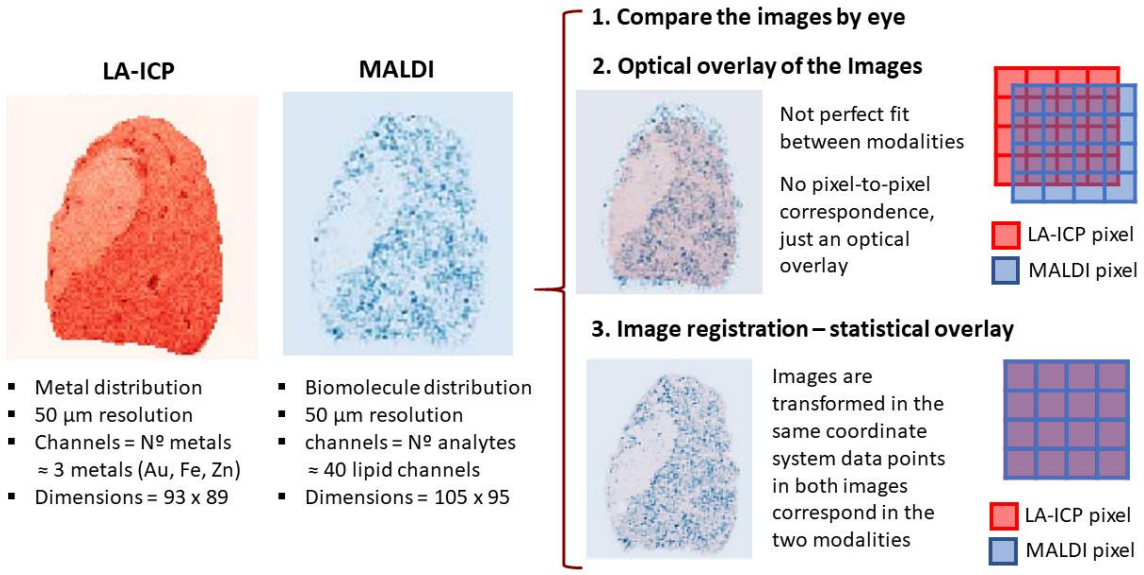

Figure 1.3. Strategies used for the analysis of two images providing complementary information.

For performing image registration, one of the images is set as the fixed image and the other as the moving image, the moving image is then transformed to match the coordinates of the fixed image.[93] This process happens using optimization algorithms, for instance, stochastic gradient descent (SGD), using a cost function to maximize the mutual information among the modalitites.[93]

Several iterations (>500) are needed to reach optimization, and the degree of mutual information is calculated during each iteration, until an optimal is reached. Several parameters determining the quality of the registration process need to be tuned to obtain a good registration. Among them, the parameter map is perhaps the most important factor. The parameter map defines the degrees of freedom that is conferred to the image in the optimization process, for example, a rigid parameter map only allows the translation and rotation of the moving image, while an affine parameter map allows translation, rotation, scaling and shearing.

Table 1.1. Parameter maps for image registration.

Type	Transformation	Degrees of freedom
linear	translation	translation
	rigid	translation, rotation
	affine	translation, rotation, scaling and shearing
non-linear	no-linear	affine + non-linear deformations

1.7 Statistical models applied to mass spectrometry imaging

As new instrumentation becomes available in MS providing better spatial resolution and more sensitivity, the increased number of pixels and molecular species detected considerably increase the amount of data generated in a single experiment. For example, an MSI dataset may contain hundreds or millions of individual data points, making the data very complex.[94] Several approaches in data reduction, segmentation, correlation, and statistical analysis have been developed recently for hyperspectral datasets to help in the data analysis of mass spectrometry large datasets.

Traditional linear correlation methods for MSI imaging analysis as principal component analysis (PCA)[95] and non-negative matrix factorization (NNMF)[96] are useful in MS. However, the linear nature of the statistical model makes them limited in finding subtle relationship between images.[97] New no-linear approaches such as t-distributed stochastic neighbor embedding (t-SNE),[98–100] and uniform manifold approximation and projection (UMP)[101] uses non-linear machine

learning to model local and global structures in high-dimensional data.[100] Providing tools for data dimensionality reduction and finding subtle changes among MS hyperspectral images.

Another very useful method in MS data analysis is segmentation, which comprises a set of methods to divide MS images into segments that possess similar spectral characteristics. One of the most used methods for segmentation is k-means clustering,[102] which divides the image in k chosen segments. The segmentation done by k-means is agnostic of the spatial structure of the data, which does not consider pixel neighbors for the interpretation of each individual pixel. To include spatial awareness into the data analysis Alexandrov and co-workers introduced spatial aware (SA)[103] clustering and spatially aware structure-adaptive (SASA)[104] clustering, which introduce a factor that consider neighbors in the segmentation, while preserving the edges of the segments. To improve segmentation, Vitek and co-workers introduced spatial shrunken centroids segmentation,[105] improving the quality of the SA and SASA segmentation and calculating the probability of segment membership for each pixel and assessing the uncertainty of the segmentation. Although segmentation algorithms for MALDI-MS imaging analysis are well developed, they highly depend on the data quality, making the segmentation process challenging for noisy datasets.[105]

1.8 Dissertation overview

Nanomaterial delivery systems constitute a group of drug delivery vehicles that had been used extensively in biodelivery. Since some of the nanomaterials are designed to perform a therapeutic function, analytical methods to determine the cargo and biochemical changes are needed. In some cases, the detection of the cargo and biochemical changes are not attainable in the same experiment, and more than one technique might be needed for the proper analysis of the drug delivery system. Laser ablation inductively coupled plasma (LA-ICP-MS) and matrix assisted laser desorption

ionization (MALDI-MS) imaging have been used for detecting metals and biomolecules in tissue sections. When both techniques are used on adjacent tissue slices, they provide complementary information about the correlation of the detected species in the two modalities. In this dissertation, we developed computational techniques for image reconstruction, segmentation, and registration of MALDI-MS and LA-ICP-MS images to monitor the biodistribution, excretion and biochemical effects of nanomaterial delivery systems.

In chapter 1, we described a software written in Python that automatically reconstructs, analyses, and segments images from LA-ICP-MS imaging data. Image segmentation is achieved using LA-ICP-MS signals from the biological metals Fe and Zn together with k-means clustering, followed by a spatial awareness strategy to automatically identify sub-organ regions in different tissues that are at the limit of the LA-ICP-MS imaging resolution. The value of the described algorithms is demonstrated for LA-ICP-MS images of nanomaterial biodistributions. The developed image reconstruction and processing approach reveals that nanomaterials distribute in different sub-organ regions based on their chemical and physical properties, opening new possibilities for understanding the impact of such nanomaterials in vivo.

In chapter 2, we developed a computational image registration approach to register LA-ICP-MS and MALDI-MS images of adjacent tissue slices to generate a dataset in the same coordinates. The computational workflow is open source and implemented in Python, with a Jupyter notebook interface for easy distribution and use. Evaluation of the computational method was performed by calculating the overlap of regions of interest (ROIs) in the two imaging modalities, showing more than 80% overlap and registration accuracies below 50 μm. Our computational approach shows that properly combining the data from LA-ICP-MS and MALDI-MS imaging can allow the strengths of the modalities to be leveraged and provide deep quantitative information about a tissue sample.

In chapter 3, we used the developed computational image registration approach to register LA-ICP-MS and MALDI-MS images of adjacent tissue slices of tissue injected with nanoparticle stabilized capsules (NPSC). The method is used to correlate images of gold metal NPSC (detected in LA-ICP-MSI) loaded with siRNA injected into mice, with images of the lipid profile (detected in MALDI-MSI). The correlation coefficients of the nanomaterial vehicles with the lipid biochemical changes provide a deeper insight into how nanomaterial delivery agents influence lipid biochemistry in tissues. Additionally, image registration allows us to leverage the higher quality images associated with LA-ICP-MS to better segment MALDI-MSI images and identify the lipids with a larger correlation to the three different suborgan regions of the spleen.

1.9 References

(1) Han, X.; Xu, K.; Taratula, O.; Farsad, K. Applications of Nanoparticles in Biomedical Imaging. *Nanoscale* **2019**, *11* (3), 799–819.

(2) Wu, Y.; Ali, M. R. K.; Chen, K.; Fang, N.; El-Sayed, M. A. Gold Nanoparticles in Biological Optical Imaging. *Nano Today* **2019**, *24*, 120–140.

(3) Wang, Y.; Feng, L.; Wang, S. Conjugated Polymer Nanoparticles for Imaging, Cell Activity Regulation, and Therapy. *Adv. Funct. Mater.* **2019**, *29* (5), 1–20.

(4) Lee, J. H.; Cho, H. Y.; Choi, H. K.; Lee, J. Y.; Choi, J. W. Application of Gold Nanoparticle to Plasmonic Biosensors. *Int. J. Mol. Sci.* **2018**, *19* (7).

(5) Qing, Z.; Bai, A.; Xing, S.; Zou, Z.; He, X.; Wang, K.; Yang, R. Progress in Biosensor Based on DNA-Templated Copper Nanoparticles. *Biosens. Bioelectron.* **2019**, *137* (April), 96–109.

(6) Grodzinski, P.; Kircher, M.; Goldberg, M.; Gabizon, A. Integrating Nanotechnology into Cancer Care. *ACS Nano* **2019**, *13* (7), 7370–7376.

(7) Parchur, A. K.; Sharma, G.; Jagtap, J. M.; Gogineni, V. R.; Laviolette, P. S.; Flister, M. J.; White, S. B.; Joshi, A. Vascular Interventional Radiology-Guided Photothermal Therapy of Colorectal Cancer Liver Metastasis with Theranostic Gold Nanorods. *ACS Nano* **2018**, *12* (7), 6597–6611.

(8) Dukhinova, M. S.; Prilepskii, A. Y.; Vinogradov, V. V.; Shtil, A. A. Metal Oxide Nanoparticles in Therapeutic Regulation of Macrophage Functions. *Nanomaterials* **2019**, *9* (11), 1–20.

(9) Blanco, E.; Shen, H.; Ferrari, M. Principles of Nanoparticle Design for Overcoming Biological Barriers to Drug Delivery. *Nat. Biotechnol.* **2015**, *33* (9), 941–951.

(10) Han, G.; Ghosh, P.; Rotello, V. M. Functionalized Gold Nanoparticles for Drug Delivery. *Nanomedicine* **2007**, *2*, 113–123.

(11) Tonga, G. Y.; Moyano, D. F.; Kim, C. S.; Rotello, V. M. Inorganic Nanoparticles for Therapeutic Delivery: Trials, Tribulations and Promise. *Curr. Opin. Colloid Interface Sci.* **2014**, *19* (2), 49–55.

(12) García, K. P.; Zarschler, K.; Barbaro, L.; Barreto, J. A.; O'Malley, W.; Spiccia, L.; Stephan, H.; Graham, B. Zwitterionic-Coated "Stealth" Nanoparticles for Biomedical Applications: Recent Advances in Countering Biomolecular Corona Formation and Uptake by the Mononuclear Phagocyte System. *Small* **2014**, *10* (13), 2516–2529.

(13) Wang, Y.; Huang, L. A Window onto SiRNA Delivery. *Nat. Biotechnol.* **2013**, *31* (7), 611–612.

(14) Tang, R.; Kim, C. S.; Solfiell, D. J.; Rana, S.; Mout, R.; Velázquez-Delgado, E. M.; Chompoosor, A.; Jeong, Y.; Yan, B.; Zhu, Z. J.; Kim, C.; Hardy, J. A.; Rotello, V. M. Direct Delivery of Functional Proteins and Enzymes to the Cytosol Using Nanoparticle-Stabilized Nanocapsules. *ACS Nano* **2013**, *7* (8), 6667–6673.

(15) Mout, R.; Ray, M.; Lee, Y.; Tay, T.; Sasaki, K.; Rotello, V. M. Direct Cytosolic Delivery of CRISPR/Cas9- Ribonucleoprotein for Efficient Gene Editing. *ACS Nano* **2017**.

(16) Mitchell, M. J.; Billingsley, M. M.; Haley, R. M.; Wechsler, M. E.; Peppas, N. A.; Langer, R. Engineering Precision Nanoparticles for Drug Delivery. *Nat. Rev. Drug Discov.* **2021**, *20* (2), 101–124.

(17) Liu, X. Y.; Wang, J. Q.; Ashby, C. R.; Zeng, L.; Fan, Y. F.; Chen, Z. S. Gold Nanoparticles: Synthesis, Physiochemical Properties and Therapeutic Applications in Cancer. *Drug Discov. Today* **2021**, *26* (5), 1284–1292.

(18) Alphandéry, E. Iron Oxide Nanoparticles for Therapeutic Applications. *Drug Discov. Today* **2020**, *25* (1), 141–149.

(19) Li, T.; Shi, S.; Goel, S.; Shen, X.; Xie, X.; Chen, Z.; Zhang, H.; Li, S.; Qin, X.; Yang, H.; Wu, C.; Liu, Y. Recent Advancements in Mesoporous Silica Nanoparticles towards Therapeutic Applications for Cancer. *Acta Biomater.* **2019**, *89*, 1–13.

(20) Probst, C. E.; Zrazhevskiy, P.; Bagalkot, V.; Gao, X. Quantum Dots as a Platform for Nanoparticle Drug Delivery Vehicle Design. *Adv. Drug Deliv. Rev.* **2013**, *65* (5), 703–718.

(21) Kevadiya, B. D.; Ottemann, B.; Mukadam, I. Z.; Castellanos, L.; Sikora, K.; Hilaire, J. R.; Machhi, J.; Herskovitz, J.; Soni, D.; Hasan, M.; Anandakumar, S.; Garrison, J.; Mcmillan, J.; Edagwa, B.; Mosley, R. L.; Vachet, R. W.; Gendelman, H. E. Rod-Shape Theranostic Nanoparticles Facilitate Antiretroviral Drug Biodistribution and Activity in Human Immunodeficiency Virus Susceptible Cells and Tissues. *Theranostics* **2020**, *10* (2), 630–656.

(22) Lim, E. K.; Kim, T.; Paik, S.; Haam, S.; Huh, Y. M.; Lee, K. Nanomaterials for Theranostics: Recent Advances and Future Challenges. *Chem. Rev.* **2015**, *115* (1), 327–394.

(23) Rao, C. N. R.; Vivekchand, S. R. C.; Biswas, K.; Govindaraj, A. Synthesis of Inorganic Nanomaterials. *J. Chem. Soc. Dalt. Trans.* **2006**, No. 34, 3728–3749.

(24) Wu, Z.; Yang, S.; Wu, W. Shape Control of Inorganic Nanoparticles from Solution. *Nanoscale* **2016**, *8* (3), 1237–1259.

(25) Heuer-Jungemann, A.; Feliu, N.; Bakaimi, I.; Hamaly, M.; Alkilany, A.; Chakraborty, I.; Masood, A.; Casula, M. F.; Kostopoulou, A.; Oh, E.; Susumu, K.; Stewart, M. H.; Medintz, I. L.; Stratakis, E.; Parak, W. J.; Kanaras, A. G. The Role of Ligands in the Chemical Synthesis and Applications of Inorganic Nanoparticles. *Chem. Rev.* **2019**, *119* (8), 4819–4880.

(26) Dreaden, E. C.; Alkilany, A. M.; Huang, X.; Murphy, C. J.; El-Sayed, M. a. The Golden Age: Gold Nanoparticles for Biomedicine. *Chem. Soc. Rev.* **2012**, *41* (7), 2740.

(27) Anselmo, A. C.; Gokarn, Y.; Mitragotri, S. Non-Invasive Delivery Strategies for Biologics. *Nat. Rev. Drug Discov.* **2018**, *18* (1), 19–40.

(28) Scaletti, F.; Hardie, J.; Lee, Y. W.; Luther, D. C.; Ray, M.; Rotello, V. M. Protein Delivery into Cells Using Inorganic Nanoparticle-Protein Supramolecular Assemblies. *Chem. Soc. Rev.* **2018**, *47* (10), 3421–3432.

(29) Lee, Y. W.; Mout, R.; Luther, D. C.; Liu, Y.; Castellanos-García, L.; Burnside, A. S.; Ray, M.; Tonga, G. Y.; Hardie, J.; Nagaraj, H.; Das, R.; Phillips, E. L.; Tay, T.; Vachet, R. W.; Rotello, V. M. In Vivo Editing of Macrophages through Systemic Delivery of CRISPR-Cas9-Ribonucleoprotein-Nanoparticle Nanoassemblies. *Adv. Ther.* **2019**, *2* (10), 1–7.

(30) Zhang, Y.; Fang, F.; Li, L.; Zhang, J. Self-Assembled Organic Nanomaterials for Drug Delivery, Bioimaging, and Cancer Therapy. *ACS Biomater. Sci. Eng.* **2020**, *6* (9), 4816–4833.

(31) Diamond, A.; Abad, S.; Mench, C.; Rojas, S.; Gispert, J. D.; Martı, R. Biodistribution of Nanoparticles . In Vivo Studies Based on 18 F Radionuclide Emission. **2011**, No. 7, 5552–5559.

(32) Liu, Q.; Sun, Y.; Yang, T.; Feng, W.; Li, C.; Li, F. Sub-10 Nm Hexagonal Lanthanide-Doped NaLuF 4 Upconversion Nanocrystals for Sensitive Bioimaging in Vivo. **2011**, 17122–17125.

(33) Modena, M. M.; Rühle, B.; Burg, T. P.; Wuttke, S. Nanoparticle Characterization: What to Measure? *Adv. Mater.* **2019**, *31* (32), 1–26.

(34) Lin, P.; Lin, S.; Wang, P. C.; Sridhar, R. Techniques for Physicochemical Characterization of Nanomaterials. *Biotechnol. Adv.* **2014**, *32* (4), 711–726.

(35) Zhang, K.; Gao, Y. J.; Yang, P. P.; Qi, G. Bin; Zhang, J. P.; Wang, L.; Wang, H. Self-Assembled Fluorescent Organic Nanomaterials for Biomedical Imaging. *Adv. Healthc. Mater.* **2018**, *7* (20), 1–16.

(36) Peng, H. S.; Chiu, D. T. Soft Fluorescent Nanomaterials for Biological and Biomedical Imaging. *Chem. Soc. Rev.* **2015**, *44* (14), 4699–4722.

(37) Becker, J. S.; Salber, D. New Mass Spectrometric Tools in Brain Research. *TrAC - Trends Anal. Chem.* **2010**, *29* (9), 966–979.

(38) Robison, G.; Zakharova, T.; Fu, S.; Jiang, W.; Fulper, R.; Barrea, R.; Marcus, M. A.; Zheng, W.; Pushkar, Y. X-Ray Fluorescence Imaging: A New Tool for Studying Manganese Neurotoxicity. *PLoS one.* **2012**, *7* (11), e48899.

(39) Nicolardi, S.; Van Der Burgt, Y. E. M.; Codée, J. D. C.; Wuhrer, M.; Hokke, C. H.; Chiodo, F. Structural Characterization of Biofunctionalized Gold Nanoparticles by Ultrahigh-Resolution Mass Spectrometry. *ACS Nano* **2017**, *11* (8), 8257–8264.

(40) Harkness, K. M.; Cliffel, D. E.; McLean, J. A. Characterization of Thiolate-Protected Gold Nanoparticles by Mass Spectrometry. *Analyst* **2010**, *135* (5), 868–874.

(41) Zenobi, R.; Knochenmuss, R. Ion Formation in MALDI Mass Spectrometry. *Mass Spectrom. Rev.* **1998**, *17* (337), 337–366.

(42) Dreisewerd, K. Recent Methodological Advances in MALDI Mass Spectrometry. *Anal. Bioanal. Chem.* **2014**, *406* (9–10), 2261–2278.

(43) Scheffer, A.; Engelhard, C.; Sperling, M.; Buscher, W. ICP-MS as a New Tool for the Determination of Gold Nanoparticles in Bioanalytical Applications. *Anal. Bioanal. Chem.* **2008**, *390* (1), 249–252.

(44) Pozebon, D.; Scheffler, G. L.; Dressler, V. L. Recent Applications of Laser Ablation Inductively Coupled Plasma Mass Spectrometry (LA-ICP-MS) for Biological Sample Analysis: A Follow-up Review. *J. Anal. At. Spectrom.* **2017**, *32* (5), 890–919.

(45) Gaumet, J. J.; Strouse, G. F. Electrospray Mass Spectrometry of Semiconductor Nanoclusters: Comparative Analysis of Positive and Negative Ion Mode. *J. Am. Soc. Mass Spectrom.* **2000**, *11* (4), 338–344.

(46) Yang, L.; Seah, M. P.; Gilmore, I. S.; Morris, R. J. H.; Dowsett, M. G.; Boarino, L.; Sparnacci, K.; Laus, M. Depth Profiling and Melting of Nanoparticles in Secondary Ion Mass Spectrometry (SIMS). *J. Phys. Chem. C* **2013**, *117* (31), 16042–16052.

(47) Kim, Y. P.; Shon, H. K.; Shin, S. K.; Lee, T. G. Probing Nanoparticles and Nanoparticle-Conjugated Biomolecules Using Time-of-Flight Secondary Ion Mass Spectrometry. *Mass Spectrom. Rev.* **2015**, *34* (2), 237–247.

(48) Elci, S. G.; Jiang, Y.; Yan, B.; Kim, S. T.; Saha, K.; Moyano, D. F.; Yesilbag Tonga, G.; Jackson, L. C.; Rotello, V. M.; Vachet, R. W. Surface Charge Controls the Suborgan Biodistributions of Gold Nanoparticles. *ACS Nano* **2016**, *10* (5), 5536–5542.

(49) Elci, S. G.; Yan, B.; Kim, S. T.; Saha, K.; Jiang, Y.; Klemmer, G. A.; Moyano, D. F.; Tonga, G. Y.; Rotello, V. M.; Vachet, R. W. Quantitative Imaging of 2 Nm Monolayer-Protected Gold Nanoparticle Distributions in Tissues Using Laser Ablation Inductively-Coupled Plasma Mass Spectrometry (LA-ICP-MS). *Analyst* **2016**, *141* (8), 2418–2425.

(50) Kim, C.; Tonga, G. Y.; Yan, B.; Kim, C. S.; Kim, S. T.; Park, M.-H.; Zhu, Z.; Duncan, B.; Creran, B.; Rotello, V. M. Regulating Exocytosis of Nanoparticles via Host–Guest Chemistry. *Org. Biomol. Chem.* **2015**, *13* (8), 2474–2479.

(51) Buchberger, A. R.; DeLaney, K.; Johnson, J.; Li, L. Mass Spectrometry Imaging: A Review of Emerging Advancements and Future Insights. *Anal. Chem.* **2018**, *90* (1), 240–265.

(52) Heeren, R. M. A. Getting the Picture: The Coming of Age of Imaging MS. *Int. J. Mass Spectrom.* **2015**, *377* (1), 672–680.

(53) Caprioli, R. M.; Farmer, T. B.; Gile, J. Molecular Imaging of Biological Samples: Localization of Peptides and Proteins Using MALDI-TOF MS. *Anal. Chem.* **1997**, *69* (23), 4751–4760.

(54) Norris, J. L.; Caprioli, R. M. Analysis of Tissue Specimens by Matrix-Assisted Laser Desorption/Ionization Imaging Mass Spectrometry in Biological and Clinical Research. *Chem. Rev.* **2013**, *113* (4), 2309–2342.

(55) Gessel, M. M.; Norris, J. L.; Caprioli, R. M. MALDI Imaging Mass Spectrometry: Spatial Molecular Analysis to Enable a New Age of Discovery. *J. Proteomics* **2014**, *107*, 71–82.

(56) Cornett, D. S.; Reyzer, M. L.; Chaurand, P.; Caprioli, R. M. MALDI Imaging Mass Spectrometry: Molecular Snapshots of Biochemical Systems. *Nat. Methods*. **2007**, *4* (10), 828–833.

(57) Ho, Y.-N.; Shu, L.-J.; Yang, Y.-L. Imaging Mass Spectrometry for Metabolites: Technical Progress, Multimodal Imaging, and Biological Interactions. *Wiley Interdiscip. Rev. Syst. Biol. Med.* **2017**, *9* (5), e1387.

(58) Kleinridders, A.; Ferris, H. A.; Reyzer, M. L.; Rath, M.; Soto, M.; Manier, M. L.; Spraggins, J.; Yang, Z.; Stanton, R. C.; Caprioli, R. M.; Kahn, C. R. Regional Differences in Brain Glucose Metabolism Determined by Imaging Mass Spectrometry. *Mol. Metab.* **2018**, *12*, 113–121.

(59) Ellis, S. R.; Paine, M. R. L.; Eijkel, G. B.; Pauling, J. K.; Husen, P.; Jervelund, M. W.; Hermansson, M.; Ejsing, C. S.; Heeren, R. M. A. Automated, Parallel Mass Spectrometry Imaging and Structural Identification of Lipids. *Nat. Methods.* **2018**, *15* (7), 515–518.

(60) Touboul, D.; Laprévote, O.; Brunelle, A. Micrometric Molecular Histology of Lipids by Mass Spectrometry Imaging. *Curr. Opin. Chem. Biol.* **2011**, *15* (5), 725–732.

(61) Huber, K.; Khamehgir-Silz, P.; Schramm, T.; Gorshkov, V.; Spengler, B.; Römpp, A. Approaching Cellular Resolution and Reliable Identification in Mass Spectrometry Imaging of Tryptic Peptides. *Anal. Bioanal. Chem.* **2018**, *410* (23), 5825–5837.

(62) Gemperline, E.; Keller, C.; Jayaraman, D.; Maeda, J.; Sussman, M. R.; Ané, J.-M.; Li, L. Examination of Endogenous Peptides in Medicago Truncatula Using Mass Spectrometry Imaging. *J. Proteome Res.* **2016**, *15* (12), 4403–4411.

(63) Ryan, D. J.; Spraggins, J. M.; Caprioli, R. M. Protein Identification Strategies in MALDI Imaging Mass Spectrometry: A Brief Review. *Curr. Opin. Chem. Biol.* **2019**, *48*, 64–72.

(64) Llombart, V.; Trejo, S. A.; Bronsoms, S.; Morancho, A.; Feifei, M.; Faura, J.; García-Berrocoso, T.; Simats, A.; Rosell, A.; Canals, F.; Hernández-Guillamón, M.; Montaner, J. Profiling and Identification of New Proteins Involved in Brain Ischemia Using MALDI-Imaging-Mass-Spectrometry. *J. Proteomics.* **2017**, *152*, 243–253.

(65) Swales, J. G.; Hamm, G.; Clench, M. R.; Goodwin, R. J. A. Mass Spectrometry Imaging and Its Application in Pharmaceutical Research and Development: A Concise Review. *Int. J. Mass Spectrom.* **2019**, *437*, 99–112.

(66) Chumbley, C. W.; Reyzer, M. L.; Allen, J. L.; Marriner, G. A.; Via, L. E.; Barry, C. E.; Caprioli, R. M. Absolute Quantitative MALDI Imaging Mass Spectrometry: A Case of Rifampicin in Liver Tissues. *Anal. Chem.* **2016**, *88* (4), 2392–2398.

(67) Groseclose, M. R.; Castellino, S. A Mimetic Tissue Model for the Quantification of Drug Distributions by MALDI Imaging Mass Spectrometry. *Anal. Chem.* **2013**, *85* (21), 10099–10106.

(68) Sussulini, A.; Becker, J. S.; Becker, J. S. Laser Ablation ICP-MS: Application in Biomedical Research. *Mass Spectrom. Rev.* **2017**, *36* (1), 47–57.

(69) Sabine Becker, J. Imaging of Metals in Biological Tissue by Laser Ablation Inductively Coupled Plasma Mass Spectrometry (LA-ICP-MS): State of the Art and Future Developments. *J. Mass Spectrom.* **2013**, *48* (2), 255–268.

(70) Becker, J. S.; Zoriy, M.; Matusch, A.; Wu, B.; Salber, D.; Palm, C.; Becker, S. Bioimaging of Metals by Laser Ablation Inductively Coupled Plasma Mass Spectrometry LA-ICP-MS. *Mass Spectrom. Rev.* **2010**, *29* (1), 156–175.

(71) Cruz-Alonso, M.; Fernandez, B.; Navarro, A.; Junceda, S.; Astudillo, A.; Pereiro, R. Laser Ablation ICP-MS for Simultaneous Quantitative Imaging of Iron and Ferroportin in Hippocampus of Human Brain Tissues with Alzheimer's Disease. *Talanta.* **2019**, *197*, 413–421.

(72) Matusch, A.; Depboylu, C.; Palm, C.; Wu, B.; Höglinger, G. U.; Schäfer, M. K. H.; Becker, J. S. Cerebral Bioimaging of Cu, Fe, Zn, and Mn in the MPTP Mouse Model of Parkinson's Disease Using Laser Ablation Inductively Coupled Plasma Mass Spectrometry (LA-ICP-MS). *J. Am. Soc. Mass Spectrom.* **2010**, *21* (1), 161–171.

(73) Boaru, S. G.; Merle, U.; Uerlings, R.; Zimmermann, A.; Flechtenmacher, C.; Willheim, C.; Eder, E.; Ferenci, P.; Stremmel, W.; Weiskirchen, R. Laser Ablation Inductively Coupled Plasma Mass Spectrometry Imaging of Metals in Experimental and Clinical Wilson's Disease. *J. Cell. Mol. Med.* **2015**, *19* (4), 806–814.

(74) Theiner, S.; Kornauth, C.; Varbanov, H. P.; Galanski, M.; Van Schoonhoven, S.; Heffeter, P.; Berger, W.; Egger, A. E.; Keppler, B. K. Tumor Microenvironment in Focus: LA-ICP-MS Bioimaging of a Preclinical Tumor Model upon Treatment with Platinum(IV)-Based Anticancer Agents. *Metallomics.* **2015**, *7* (8), 1256–1264.

(75) Egger, A. E.; Theiner, S.; Kornauth, C.; Heffeter, P.; Berger, W.; Keppler, B. K.; Hartinger, C. G. Quantitative Bioimaging by LA-ICP-MS: A Methodological Study on the Distribution of Pt and Ru in Viscera Originating from Cisplatin- and KP1339-Treated Mice. *Metallomics* **2014**, *6* (9), 1616–1625.

(76) Perry, W. J.; Spraggins, J. M.; Sheldon, J. R.; Grunenwald, C. M.; Heinrichs, D. E.; Cassat, J. E.; Skaar, E. P.; Caprioli, R. M. Staphylococcus Aureus Exhibits Heterogeneous Siderophore Production within the Vertebrate Host. *Proc. Natl. Acad. Sci.* **2019**, *116* (44), 21980–21982.

(77) González de Vega, R.; Fernández Sanchez, M. L.; Eiro, N.; Vizoso, F. J.; Sperling, M.; Karst, U.; Sanz Medel, A. Multimodal Laser Ablation/Desorption Imaging Analysis of Zn and MMP-11 in Breast Tissues. *Anal. Bioanal. Chem.* **2018**, *410* (3), 913–922.

(78) Böhme, S.; Stärk, H. J.; Kühnel, D.; Reemtsma, T. Exploring LA-ICP-MS as a Quantitative Imaging Technique to Study Nanoparticle Uptake in Daphnia Magna and Zebrafish (Danio Rerio) Embryos. *Anal. Bioanal. Chem.* **2015**, *407* (18), 5477–5485.

(79) Becker, J. S.; Matusch, A.; Wu, B. Bioimaging Mass Spectrometry of Trace Elements - Recent Advance and Applications of LA-ICP-MS: A Review. *Anal. Chim. Acta* **2014**, *835*, 1–18.

(80) Doble, P. A.; de Vega, R. G.; Bishop, D. P.; Hare, D. J.; Clases, D. Laser Ablation–Inductively Coupled Plasma–Mass Spectrometry Imaging in Biology. *Chem. Rev.* **2021**, acs.chemrev.0c01219.

(81) Patterson, N. H.; Yang, E.; Kranjec, E.; Chaurand, P. Co-Registration and Analysis of Multiple Imaging Mass Spectrometry Datasets Targeting Different Analytes. *Bioinformatics.* **2019**, *35* (7), 1261–1262.

(82) Neumann, E. K.; Djambazova, K. V.; Caprioli, R. M.; Spraggins, J. M. Multimodal Imaging Mass Spectrometry: Next Generation Molecular Mapping in Biology and Medicine. *J. Am. Soc. Mass Spectrom.* **2020**, *31* (12), 2401–2415.

(83) Cassat, J. E.; Moore, J. L.; Wilson, K. J.; Stark, Z.; Prentice, B. M.; Van de Plas, R.; Perry, W. J.; Zhang, Y.; Virostko, J.; Colvin, D. C.; Rose, K. L.; Judd, A. M.; Reyzer, M. L.; Spraggins, J. M.; Grunenwald, C. M.; Gore, J. C.; Caprioli, R. M.; Skaar, E. P. Integrated Molecular Imaging Reveals Tissue Heterogeneity Driving Host-Pathogen Interactions. *Sci. Transl. Med.* **2018**, *10* (432), eaan6361.

(84) Kaya, I.; Sämfors, S.; Levin, M.; Borén, J.; Fletcher, J. S. Multimodal MALDI Imaging Mass Spectrometry Reveals Spatially Correlated Lipid and Protein Changes in Mouse Heart with Acute Myocardial Infarction. *J. Am. Soc. Mass Spectrom.* **2020**, *31* (10), 2133–2142.

(85) Porta Siegel, T.; Hamm, G.; Bunch, J.; Cappell, J.; Fletcher, J. S.; Schwamborn, K. Mass Spectrometry Imaging and Integration with Other Imaging Modalities for Greater Molecular Understanding of Biological Tissues. *Mol. Imaging Biol.* **2018**, *20* (6), 888–901.

(86) Iakab, S. A.; Ràfols, P.; Correig-Blanchar, X.; García-Altares, M. Perspective on Multimodal Imaging Techniques Coupling Mass Spectrometry and Vibrational Spectroscopy: Picturing the Best of Both Worlds. *Anal. Chem.* **2021**, *93* (16), 6301–6310.

(87) Neumann, E. K.; Comi, T. J.; Spegazzini, N.; Mitchell, J. W.; Rubakhin, S. S.; Gillette, M. U.; Bhargava, R.; Sweedler, J. V. Multimodal Chemical Analysis of the Brain by High Mass Resolution Mass Spectrometry and Infrared Spectroscopic Imaging. *Anal. Chem.* **2018**, *90* (19), 11572–11580.

(88) Bocklitz, T. W.; Crecelius, A. C.; Matthäus, C.; Tarcea, N.; Von Eggeling, F.; Schmitt, M.; Schubert, U. S.; Popp, J. Deeper Understanding of Biological Tissue: Quantitative Correlation of MALDI-TOF and Raman Imaging. *Anal. Chem.* **2013**, *85* (22), 10829–10834.

(89) Tobias, F.; Hummon, A. B. Considerations for MALDI-Based Quantitative Mass Spectrometry Imaging Studies. *J. Proteome Res.* **2020**, *19* (9), 3620–3630.

(90) Patterson, N. H.; Tuck, M.; Lewis, A.; Kaushansky, A.; Norris, J. L.; Van de Plas, R.; Caprioli, R. M. Next Generation Histology-Directed Imaging Mass Spectrometry Driven by Autofluorescence Microscopy. *Anal. Chem.* **2018**, *90* (21), 12404–12413.

(91) Nikitina, A.; Huang, D.; Li, L.; Peterman, N.; Cleavenger, S. E.; Fernández, F. M.; Kemp, M. L. A Co-Registration Pipeline for Multimodal MALDI and Confocal Imaging Analysis of Stem Cell Colonies. *J. Am. Soc. Mass Spectrom.* **2020**, *31* (4), 986–989.

(92) Tian, X.; Xie, B.; Zou, Z.; Jiao, Y.; Lin, L. E.; Chen, C. L.; Hsu, C. C.; Peng, J.; Yang, Z. Multimodal Imaging of Amyloid Plaques: Fusion of the Single-Probe Mass Spectrometry Image and Fluorescence Microscopy Image. *Anal. Chem.* **2019**, *91* (20), 12882–12889.

(93) Klein, S.; Staring, M. Elastix 4.9.0 - Manual. **2018**, 60.

(94) Zhang, Y.; Liu, X. Machine Learning Techniques for Mass Spectrometry Imaging Data Analysis and Applications. *Bioanalysis* **2018**, *10*, 519–522.

(95) McCombie, G.; Staab, D.; Stoeckli, M.; Knochenmuss, R. Spatial and Spectral Correlations in MALDI Mass Spectrometry Images by Clustering and Multivariate Analysis. *Anal. Chem.* **2005**, *77* (19), 6118–6124.

(96) Jones, E. A.; Deininger, S. O.; Hogendoorn, P. C. W.; Deelder, A. M.; McDonnell, L. A. Imaging Mass Spectrometry Statistical Analysis. *J. Proteomics* **2012**, *75* (16), 4962–4989.

(97) Fonville, J. M.; Carter, C. L.; Pizarro, L.; Steven, R. T.; Palmer, A. D.; Griffiths, R. L.; Lalor, P. F.; Lindon, J. C.; Nicholson, J. K.; Holmes, E.; Bunch, J. Hyperspectral Visualization of Mass Spectrometry Imaging Data. *Anal. Chem.* **2013**, *85* (3), 1415–1423.

(98) Abdelmoula, W. M.; Škrášková, K.; Balluff, B.; Carreira, R. J.; Tolner, E. A.; Lelieveldt, B. P. F.; van der Maaten, L.; Morreau, H.; van den Maagdenberg, A. M. J. M.; Heeren, R. M. A.; McDonnell, L. A.; Dijkstra, J. Automatic Generic Registration of Mass Spectrometry Imaging Data to Histology Using Nonlinear Stochastic Embedding. *Anal. Chem.* **2014**, *86* (18), 9204–9211.

(99) Abdelmoula, W. M.; Balluff, B.; Englert, S.; Dijkstra, J.; Reinders, M. J. T.; Walch, A.; McDonnell, L. A.; Lelieveldt, B. P. F. Data-Driven Identification of Prognostic Tumor Subpopulations Using Spatially Mapped t-SNE of Mass Spectrometry Imaging Data. *Proc. Natl. Acad. Sci. U. S. A.* **2016**, *113* (43), 12244–12249.

(100) Gardner, W.; Cutts, S. M.; Phillips, D. R.; Pigram, P. J. Understanding Mass Spectrometry Images: Complexity to Clarity with Machine Learning. *Biopolymers.* **2021**, *112* (4), e23400.

(101) Smets, T.; Waelkens, E.; De Moor, B. Prioritization of m/ z-Values in Mass Spectrometry Imaging Profiles Obtained Using Uniform Manifold Approximation and Projection for Dimensionality Reduction. *Anal. Chem.* **2020**, *92* (7), 5240–5248.

(102) Oros-Peusquens, A. M.; Matusch, A.; Becker, J. S.; Shah, N. J. Automatic Segmentation of Tissue Sections Using the Multielement Information Provided by LA-ICP-MS Imaging and k-Means Cluster Analysis. *Int. J. Mass Spectrom.* **2011**, *307*, 245–252.

(103) Alexandrov, T.; Kobarg, J. H. Efficient Spatial Segmentation of Large Imaging Mass Spectrometry Datasets with Spatially Aware Clustering. *Bioinformatics.* **2011**, *27* (13), i230–i238.

(104) Alexandrov, T.; Becker, M.; Deininger, S.-O.; Ernst, G.; Wehder, L.; Grasmair, M.; von Eggeling, F.; Thiele, H.; Maass, P. Spatial Segmentation of Imaging Mass Spectrometry Data with Edge-Preserving Image Denoising and Clustering. *J. Proteome Res.* **2010**, *9* (12), 6535–6546.

(105) Bemis, K. D.; Harry, A.; Eberlin, L. S.; Ferreira, C. R.; van de Ven, S. M.; Mallick, P.; Stolowitz, M.; Vitek, O. Probabilistic Segmentation of Mass Spectrometry (MS) Images Helps Select Important Ions and Characterize Confidence in the Resulting Segments. *Mol. Cell. Proteomics.* **2016**, *15* (5), 1761–1772.

CHAPTER 2

AUTOMATIC IDENTIFICATION OF SUB-ORGAN REGIONS IN TISSUES VIA MULTI-METAL ANALYSIS IN LA-ICP-MS IMAGING

Majority of this chapter is published: Castellanos-García, L. J.; Elci, S. G.; Vachet, R. W. *Analyst* **2020**, *145*, 3705-3712.

2.1 Introduction

Obtaining site-specific information about metal distributions in LA-ICP-MS imaging requires images to be reconstructed from the metal ion signals. In contrast to more widely used matrix assisted laser desorption\ionization (MALDI) MS imaging, relatively few approaches have been described for image reconstruction and statistical analysis. The program IMAGENA, which was developed by Osterholt et al.,[1] was one of the first software developed for visualizing LA-ICP-MS data. A similar program called HDIP[2] was recently developed by Teledyne for image reconstruction of LA-ICP-MS images. While IMAGENA, HDIP, Iolite[3] and its associated interphases: monocle[4] and biolite[5] are versatile tools for reconstructing images, they are not open source and offer minimal tools for the statistical analysis of the resulting images.

In contrast, software such as LA-iMageS,[6] MapIT![7] and iQuant2[8] are open-source programs that enable image reconstruction from LA-ICP-MS data via user-friendly graphical user interfaces, but they also have limited built-in statistical analysis tools. Other image reconstruction approaches, including those based on readily available software such as Microsoft Excel[9] have also been described, although most have limited capability for the statistical analysis of the imaging data sets. For most existing software, image reconstruction is the principal aim.

As the applicability of LA-ICP-MS grows, though, especially for applications such as nanomaterial-based drug delivery systems,[10–12] more sophisticated image processing methods such as image segmentation for region of interest (ROI) analysis or other statistical analysis methods are needed to extract more information from reconstructed images.[13] Image segmentation, in particular, is valuable for characterizing analyte signals in histologically relevant regions of a tissue, so that the underlying biochemistry and biology can be better understood. Deeper biological insight into MALDI-MS imaging data has been achieved with image segmentation algorithms,[14,15] but to our knowledge analogous approaches have not been readily adopted in LA-ICP-MS imaging methods.

Here, we present an open-source software written in Python for LA-ICP-MS imaging reconstruction that implements more advanced segmentation algorithms for classification of ROIs in LA-ICP-MS images. The use of Python for image analysis offers tremendous flexibility because of the numerous libraries accessible via the software for image visualization,[16] matrix operations,[17] statistical analysis,[18] and even more complex tasks like multimodal imaging.[19] Using code written in Python, we demonstrate that distinct sub-organ features can be automatically identified using different metal distributions to perform spatially aware segmentation analysis. As an application of these image segmentation approaches, we show that nanomaterials distribute in different sub-organ regions based on their chemical and physical properties. We believe the described software will benefit current and potential users of LA-ICP-MS imaging as it will make accessible more sophisticated image processing tools for more deeply understanding the biological ramifications of metal distributions in tissues.

2.2 Results and discussion

2.2.1 Image reconstruction

Generating a LA-ICP-MS image after data acquisition involves several data handling steps (Figure 2.1). Because the metal signals are generated by scanning the laser in a line across the tissue, the continuously ablated and detected stream of material must be summed to generate an image pixel. To do this, the file that is generated for each ablation line, which contains all the metal intensity data, is subjected to a data reduction step (Step 2, Figure 2.1). This step uses the laser spot size and scan rate to define the number of ion intensity measurements that are summed to create a pixel. For example, if the laser spot size is 50 µm and the laser scan rate is 15 µm/s, data acquired over a 3.3 s period is summed to create a single pixel. The resulting collection of pixels that contains ion intensity information is then separated into a set of different data matrices that correspond to the number of different metals measured (Step 3, Figure 2.1). Separate images for each metal can then be reconstructed using plotting tools such as Matplotlib to generate a 2D image for each of the studied metals (Step 4, Figure 2.1).[16] Our approach, generates images with few user inputs that can be subsequently analyzed by the many Python statistical libraries that exist, such as SciPy[20] and scikit-learn[18] enabling us to automatically identify different tissue regions in LA-ICP-MS images.

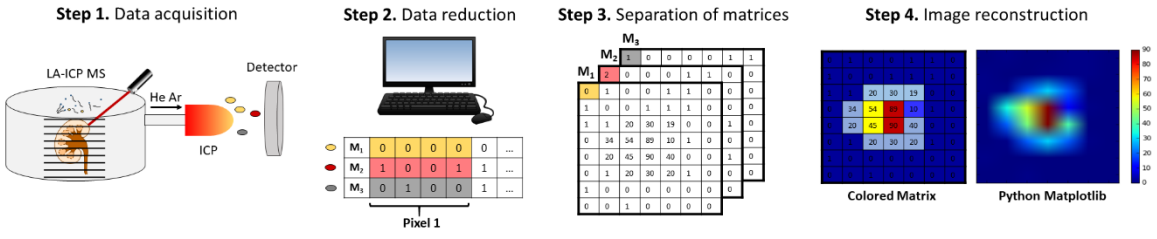

Figure 2.1. Process of image generation in LA-ICP-MS. Data is acquired, and then processed by data reduction and separation into data matrices for each metal (e.g. M1, M2, M3, etc.).

2.2.2 Tissue boundary identification

The distribution of Zn signals from an imaging experiment can be used to delineate the edge of the tissue by differentiating the pixels that correspond to the tissue and those that correspond to the background. The procedure, illustrated in Figure 2.2, requires measurements of background regions outside the tissue. In the first step of the procedure, the background Zn signal is calculated from any row or column of the imaging dataset. The row and column data are saved as two independent vectors, and the signal average and standard deviations in each case are calculated. The resulting average signals and standard deviations calculated are used to set the background value B. Each pixel in the entire image is then compared against the background and classified as tissue or background depending on whether its intensity is significantly different from the background signal, according to the equation in Figure 2.2. From the classified image a background mask is generated in which tissue pixels are given a value of 1 and background pixels are 0. Any element can be used in the program to perform background subtraction by this thresholding approach.[21] Defining the tissue boundary is necessary for performing various statistical analyses on the images, that will be described in subsequent chapters.

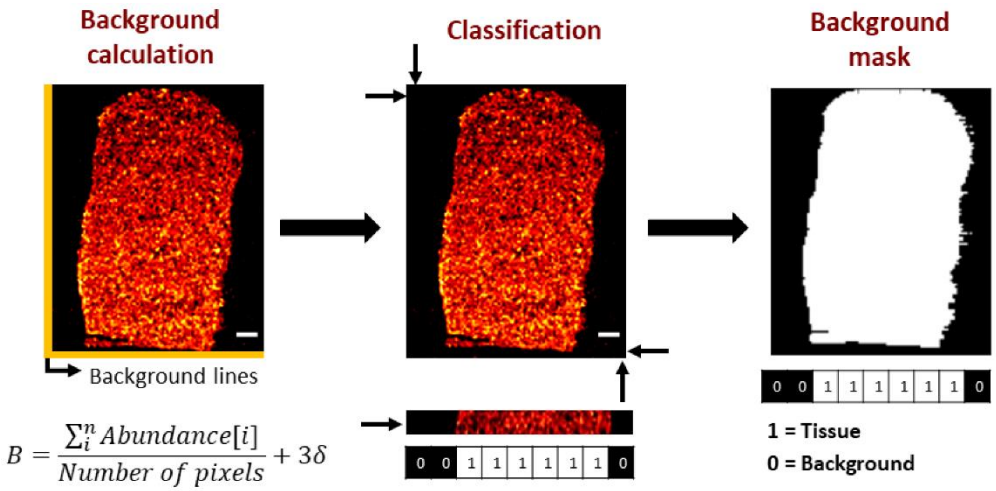

Figure 2.2. Tissue boundary detection is determined from a background signal calculation, statistical classification of pixels as background or tissue, and creation of a background mask. Scale bars correspond to 500 µm.

2.2.3 Image optimization

In addition to helping define tissue boundaries, Zn signals can also help improve image quality in regions that are degraded by tissue inhomogeneities arising during sample preparation or from fluctuations in laser fluence or mass ablation rates. Zn is homogeneously distributed in many healthy tissues, such as liver, kidney and spleen, and in the tissues imaged in this work, Zn signals are homogeneously distributed as compared to other elements as seen in Figure 2.3.[22] This relative

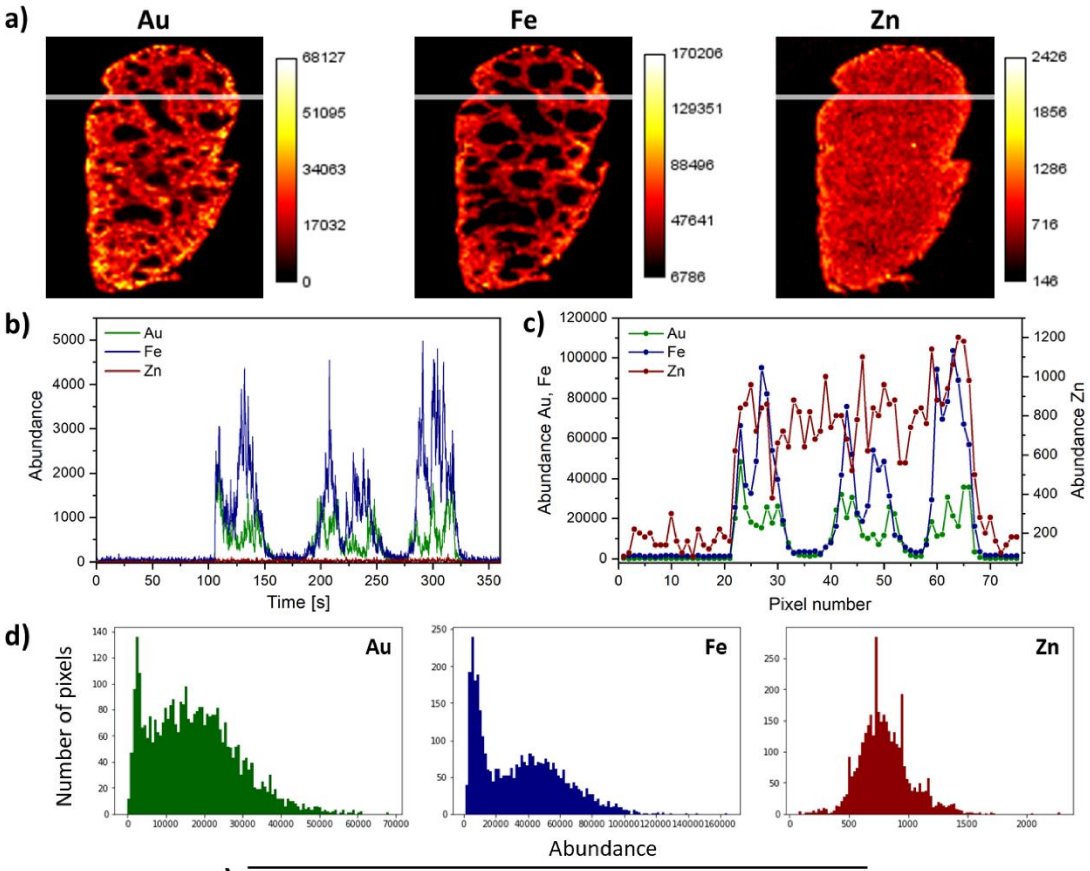

e)

Tissue signal average			
Metal	**Average**	**Std**	**% Deviation**
Au	17595	11248	64
Fe	35136	25868	74
Zn	807	219	27

Figure 2.3. Elemental distribution of Au, Fe and Zn in a spleen tissue from a mouse injected with Au nanoparticles. The figure show: a) Spleen images of Au, Fe and Zn. b) Raw signal data for the ablation of one of the tissue lines analyzed in LA-ICP-MS. The line is shown in gray over the LA-ICP-MS image. c) Data binning every 33 points is performed on the raw signal to obtain a pixel size of 50 µm x 50 µm. d) Histograms for the distribution of Au, Fe and Zn signals found in the tissue. e) Average Au, Fe and Zn signals, standard deviations, and % deviations across the tissue. One key conclusion from these data is that the Zn signal is relatively constant across the tissue.

homogeneity allows Zn to be used for normalization. Any element, like carbon[23] or phosphorous[24,25] could be used for normalization in the developed program. Figure 2.4 shows two examples of the advantage of using Zn signals for improving image quality. In Figure 2.4a, wrinkling of the edges of a mouse spleen section causes the Au image to be poor throughout most of the tissue. When the Au intensity matrix is divided by the Zn matrix on a pixel-by-pixel basis, this normalization process improves the image by eliminating the zones with anomalously high overall Au signal that are caused by folding of the tissue edges. Similar improvements can be obtained for Fe images where the laser energy deviated during the experiment (Figure 2.4b).

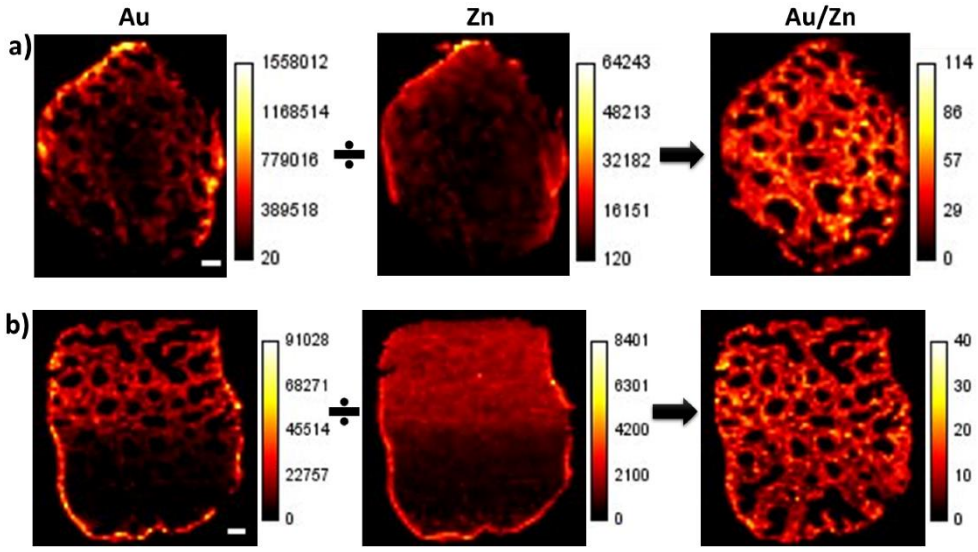

Figure 2.4. Zn-based normalization improves LA-ICP-MS image quality. a) Image of a spleen tissue section from a mouse injected with gold nanocapsules that shows wrinkling of the edges of the tissue. b) Image of a spleen tissue section from a mouse injected with TTMA nanozymes that shows laser energy deviations. White scale bars in Au images correspond to 500 µm.

2.2.4 Image segmentation for automatic sub-organ differentiation

The distribution of Fe levels in a tissue depends on the blood flow to a specific sub-organ region and can be used to differentiate regions in various tissues, as shown in Figure 2.5.[26–28] To distinguish sub-organ regions, image segmentation was performed using *k*-means clustering[29] to partition areas of differential Fe composition. Figure 2.6 shows H&E stained, optical and LA-ICP-

MS images of liver and kidney sections from a mouse injected with TTMA and TEG-COOH NPs. While the areas of high blood flow (i.e. veins) are readily apparent from the H&E stained, optical, and Fe LA-ICP-MS images, image segmentation can be used to automatically identify these and other regions that are not as readily apparent. Using the Fe matrix as input, we performed *k*-means clustering with the number of clusters assigned as 3, based on the 'elbow method' (as describe in the materials and methods section).

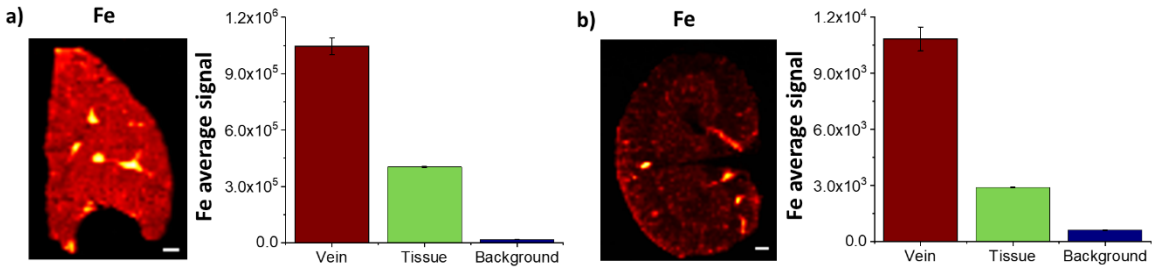

Figure 2.5. Distribution of Fe signal in different suborgan areas for: a) liver section from a mouse injected with TTMA Au nanoparticles and b) kidney section from a mouse injected with TEG-COOH Au nanoparticles. White scale bars in both images correspond to 500 µm

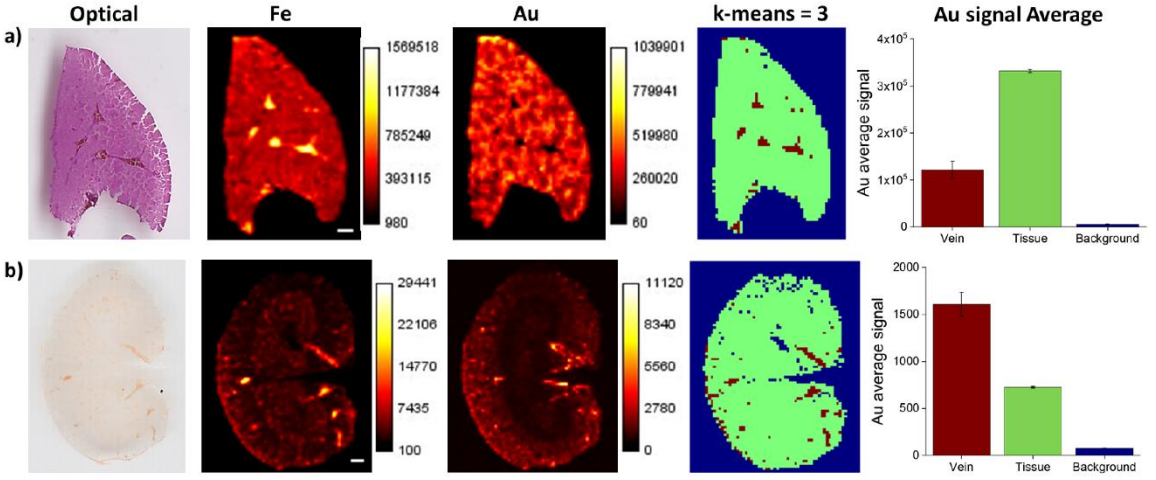

Figure 2.6. H&E stained, optical, Fe LA-ICP-MS, and Au LA-ICP-MS images illustrating how *k*-means clustering can be used to automatically segment images into biologically relevant regions. a) Images and segmentation of images from a liver section from a mouse injected with TTMA Au nanoparticles. b) Images and segmentation of images from a kidney section from a mouse injected with TEG-COOH Au nanoparticles. Bar graphs show the average Au signal with standard deviations in each of the segmented areas. White scale bars in both Fe images correspond to 500 µm. Distribution of Fe signal in different areas of the liver and kidney is found in Figure 2.5.

When using *k*-means clustering, it is possible to effectively segment the image between background, low Fe (tissue), and high Fe (vein). Using image segmentation in this way allows one to determine the average signal of another metal in a given classified area. For example, the average Au signal can be determined in the three classified areas in liver and kidney sections from mice injected with TTMA (Figure 2.6a) or TEG-COOH (Figure 2.6b) Au nanoparticles. From the signal averages we can conclude that the Au nanoparticles accumulate differently in the liver and kidney. In the liver, we find more Au in the tissue than in the veins, and in the kidney, we find higher Au signal in the veins than in the rest of the tissue. Previous work by our group found that positively-charged nanoparticles, like TTMA are readily cleared from circulation while negatively-charged nanoparticles like TEG-COOH circulate longer in the bloodstream[28] which explains the differences in the nanoparticle concentrations in the veins of the two organs. This image segmentation approach allows this information to be automatically determined for any LA-ICP-MS image that is imported into the developed Python program.

The image segmentation method was also used to distinguish sub-organ regions of the spleen. The spleen tissue has a marked difference between the red pulp and white pulp in that each region fulfils a different biological role in this vital organ.[26] The spleen red and white pulp can be differentiated by their Fe concentrations, as the red pulp has higher blood flow than the white pulp. An example Fe LA-ICP-MS image from a spleen section is shown in Figure 2.7a, showing areas of high and low Fe concentrations. To differentiate the sub-organ areas, we performed *k*-means clustering in the same manner as before. Using the elbow method, three clusters are again identified, but using a *k*-means clustering of three does not allow an effective differentiation between the white pulp and the background primarily because of the spread of Fe signals in the red pulp exceeds the difference between the white pulp and background Fe signals (Figure 2.7a, *k*-means = 3 image). To solve this issue and effectively differentiate the background and white pulp regions, we used a multi-metal segmentation strategy that is illustrated within the brackets of Figure 2.7a. For this

strategy, we choose a *k*-means cluster value of 2 for the Fe image to differentiate two clusters, one exclusively for the red pulp and another for the white pulp and background. The white pulp and background are then differentiated in the *k*-means = 2 clustered images using the Zn signal and the background mask procedure illustrated in Figure 2.2. By conjugating the *k*-means = 2 clustered image and the background mask (Figure 2.7a), we can generate a multi-metal segmented image with three distinctive areas: background, red pulp, and white pulp.

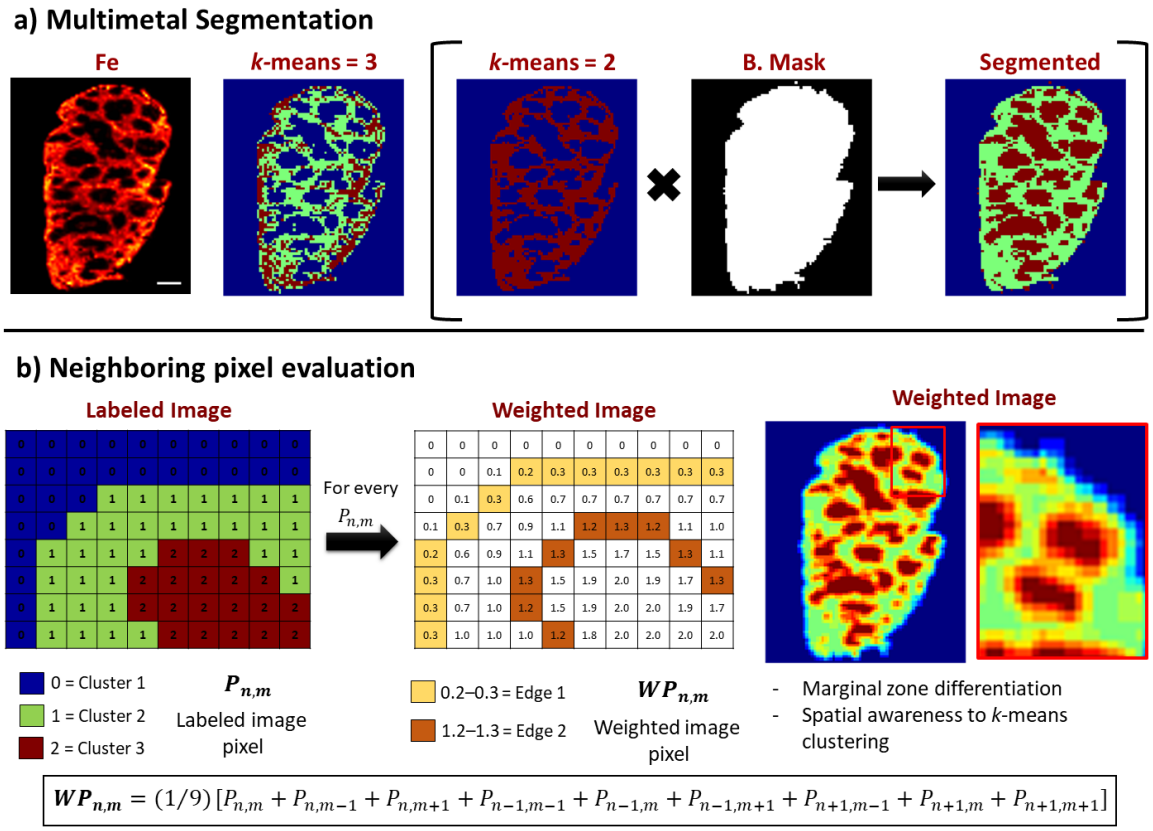

Figure 2.7. Multimetal image segmentation and pixel evaluation for the differentiation of red pulp, white pulp, and marginal zones of spleen sections using LA-ICP-MS imaging. a) An Fe LA-ICP-MS image that is segmented using k-means = 3 does not allow the white pulp and background to be distinguished, but a k-means = 2 clustering and Zn-based background mask (B. Mask) determination (in brackets) produces a segmented image that accurately defines the red pulp, white pulp, and background. b) Neighboring pixel evaluation adds spatial awareness to the multimetal segmented image by redefining each labeled image pixel ($P_{n,m}$) to a weighted image pixel ($WP_{n,m}$) using the indicated equation. The result is a weighted image that clearly defines the boundary between the red and white pulp, allowing differentiation of the marginal zone that separates the two regions. White scale bars in Fe image correspond to 500 µm.

In addition to the distinct red and white pulp regions of the spleen, there is boundary region known as the marginal zone where the first steps of an immune response occur in this organ.[28] Image segmentation alone makes it difficult to effectively differentiate the marginal zone because it does not have a distinct metal composition. Because the marginal zone surrounds each white pulp region and is approximately 50 μm in size,[26] this region can be distinguished if spatial awareness is added to the segmented image. The *k*-means approach, however, is performed on a vectorized dataset and thus does not have spatial awareness.[14,29] Spatial awareness can be added by considering the neighboring pixels around any particular pixel in the image by arbitrarily assigning values of 0, 1, and 2 to the background, red pulp, and white pulp pixels, respectively, that were identified via the multi-metal segmentation approach (see label image in Figure 2.7b).

To further classify distinct areas in the spleen, including the marginal zone, each pixel value or label ($P_{n,m}$) can be redefined as a weighted pixel ($WP_{n,m}$) that is equal to the weighted average of its eight immediately neighbor pixels (see equation in Figure 2.7b). In short, we apply an image filtering strategy with a linear filter to classify the boundary regions of the labeled image. After redefining the value of each pixel, we can then generate a weighted image that effectively distinguishes the marginal zone (in yellow) from the red and white pulp (see weighted image in Figure 2.7b). Newly weighted values of 1.2-1.3 correspond to the marginal zone, while lower and higher values correspond to the red and white pulp, respectively. This approach for distinguishing the red pulp, white pulp, and marginal zone can be validated by comparing the Fe image and an H&E stain of the spleen tissue with the multi-metal segmented image (Figures 2.8 and 2.9).

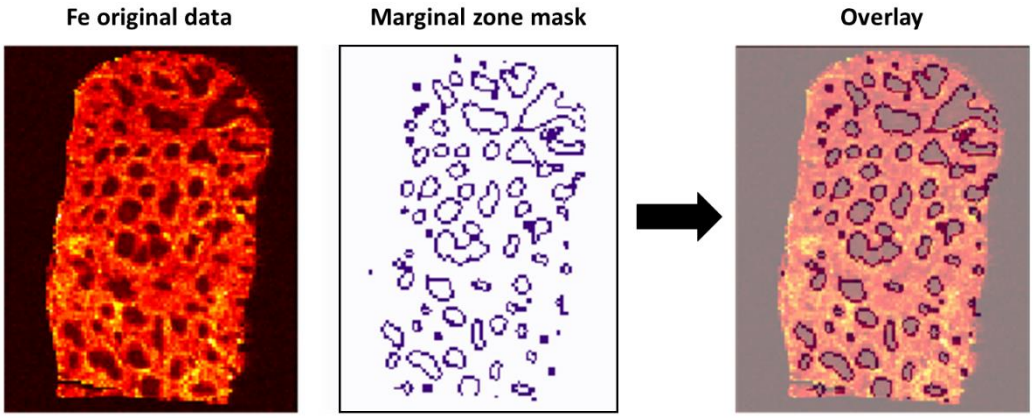

Figure 2.8. Overlay of the Fe distributions in the LA-ICP-MS data from a spleen tissue with the marginal zone mask calculated through multi-metal segmentation and neighboring pixel evaluation

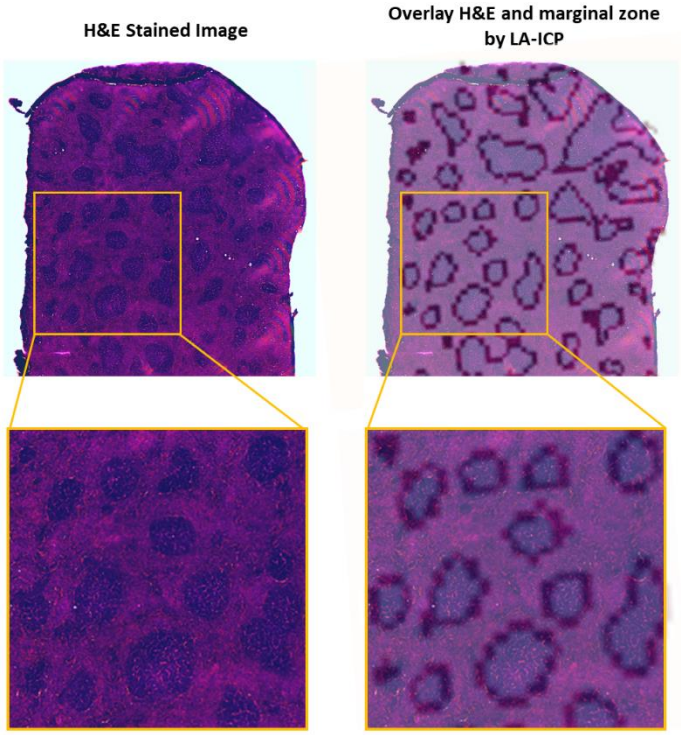

Figure 2.9. H&E stained image (left), and an overlay of the H&E stained and segmented images (right), demonstrating the success of the multi-metal image segmentation and pixel evaluation for the differentiation of the different regions of the spleen.

2.2.5 Gold nanoparticles and bismuth nanorods distributions in spleen tissues

The value of distinguishing the three different regions in the spleen using multi-metal segmentation and the neighboring pixel evaluation can be illustrated by considering LA-ICP-MS images of tissue slices from mice injected with Au nanoparticles or bismuth sulfide nanorods. The Fe and Zn images from LA-ICP-MS imaging analysis of separate spleen tissues were used to segment the images into red pulp, white pulp, and background regions, and a neighboring pixel evaluation was used to further classify the marginal zone. By averaging the Au (Figure 2.10a) and Bi (Figure 2.10b) signals in each of the identified regions, which can be facilitated by a series of spatial mask images created by the proposed computational method (Figure 2.11), we find that Au and Bi accumulate in distinctive patterns in the spleen. Au tends to accumulate more extensively in the red pulp, whereas Bi tends to accumulate to a greater extent in the marginal zone. This observation is particularly important because these Bi nanorods were designed specially to target the marginal zone of the spleen.[30]

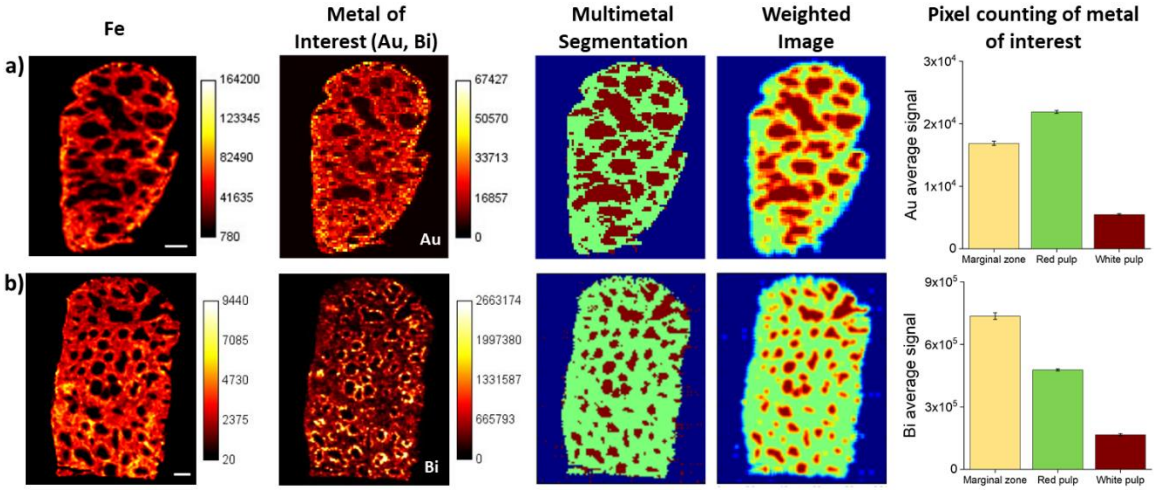

Figure 2.10. Use of multi-metal segmentation and neighboring pixel evaluation to evaluate the distributions of a) Au nanoparticles and b) Bi sulfide nanorods in spleen tissues. Fe and Zn LA-ICP-MS images are used to perform multi-metal segmentation combined with a neighboring pixel evaluation approach to obtain a weighted image like that shown in Figure 2.7. The weighted images allow a determination of the relative amount of each metal in the marginal zone, red pulp, and white pulp, as show in each bar graph. White scale bars in Fe image correspond to 500 µm.

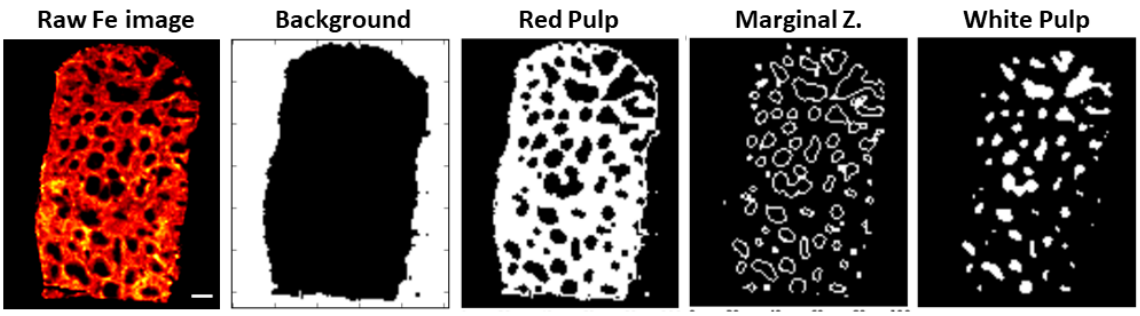

Figure 2.11. Spatial mask images of a spleen from a mouse injected with bismuth sulfide nanorods. Fe-based classification through k-means clustering and neighboring pixel evaluation allows the creation of different spatial masks that facilitate determination of the amount of the metal of interest in each sub-organ region. Scale bar correspond to 500 μm.

2.3 Conclusions

We have developed software written in Python that can automatically reconstruct and segment images from LA-ICP-MS imaging data. This new software identifies sub-organ regions of interest with minimal user input and can find regions that might be missed by manual analysis. The image reconstruction program takes advantage of the capability of open-source scientific libraries such as: NumPy, Matplotlib, Scikit-learn for various numerical and statistical analyses. Our image reconstruction and analysis method represent the first software, to our knowledge, that can perform sophisticated manipulations automatically and directly on LA-ICP-MS imaging data. Using this software, we demonstrate that segmentation of LA-ICP-MS images can be performed using a combination of Fe and Zn images, *k*-means clustering analysis, and neighboring-pixel evaluation to automatically classify sub-organ regions in kidney, liver, and spleen tissues. The neighboring-pixel evaluation procedure introduces spatial awareness to the segmentation process that can correct for misclassified pixels and can classify boundary regions that are at the limit of the measurement resolution (e.g. marginal zone in the spleen). Using tissues from mice injected with different nanomaterials as examples, classification of different sub-organ regions reveals the value of our described approach. For example, we find that Bi sulfide nanorods accumulate more

extensively than Au nanoparticles in the marginal zone as compared to other regions of the spleen. We believe that the described data reconstruction and image segmentation strategy that we have developed in Python will be beneficial to LA-ICP-MS imaging experts and non-experts alike. Moreover, the use of Python allows a wide array of other statistical methods to be applied to the data taken during an LA-ICP-MS imaging experiment. We envision future development of the code by the incorporation of standards into the workflow, Pearson's coefficient calculation for calculating co-localization between the data channels and outlier detection in ROIs.

2.4 Materials and methods

2.4.1 Nanomaterial synthesis

Different nanomaterials, including gold nanoparticles, nanozymes, nanocapsule and bismuth sulfide nanorods (Figure 2.12), were provided by collaborators who synthesized them according to published protocols. Gold nanoparticles were synthesized according to the Brust-Schiffrin two phase method.[31] Different ligand coatings, including ones with positively-charged (TTMA) and negatively-charged (TEG-COOH) functional groups were used.[32] Nanozymes were synthesized using the method described by Rotello and co-workers.[33,34] Nanocapsule synthesis was performed according to the protocol described by Rotello and co-workers,[35–37] and the bismuth sulfide nanorods were synthesized according to the method developed by Gendelman and co-workers.[38]

2.4.2 Tissue sections

To obtain tissues for the imaging experiments involving gold nanoparticles, nanozymes and nanocapsules, female Balb/c mice (8-week-old) were injected with the nanomaterial of interest.

After 24 h (nanoparticles, nanozymes) or 48 h (nanocapsules), the mouse tissues of interest were extracted, and flash frozen in liquid nitrogen and then kept at -80 °C until used for MS imaging. All animal protocols involving the gold nanomaterials were approved by the UMass Institutional Animal Care and Use Committee (IACUC), which is guided by the U.S. Animal Welfare Act and U.S. Public Health Service Policy. For the imaging experiments involving bismuth sulfide nanorods, six mice were injected, and the mouse tissues were extracted after 48 h, flash frozen, and sent to the University of Massachusetts Amherst for sectioning. The animal protocols in this case were conducted under the Animal Care protocols of the University of Nebraska Medical Center. In all cases, tissues were sliced at 20 µm using a LEICA CM1850 at -20˚C, and then deposited on regular glass slides. Hematoxylin and Eosin (H&E) staining on adjacent slices was performed using the Rapid Chrome frozen section staining kit (Thermo Fisher Scientific).

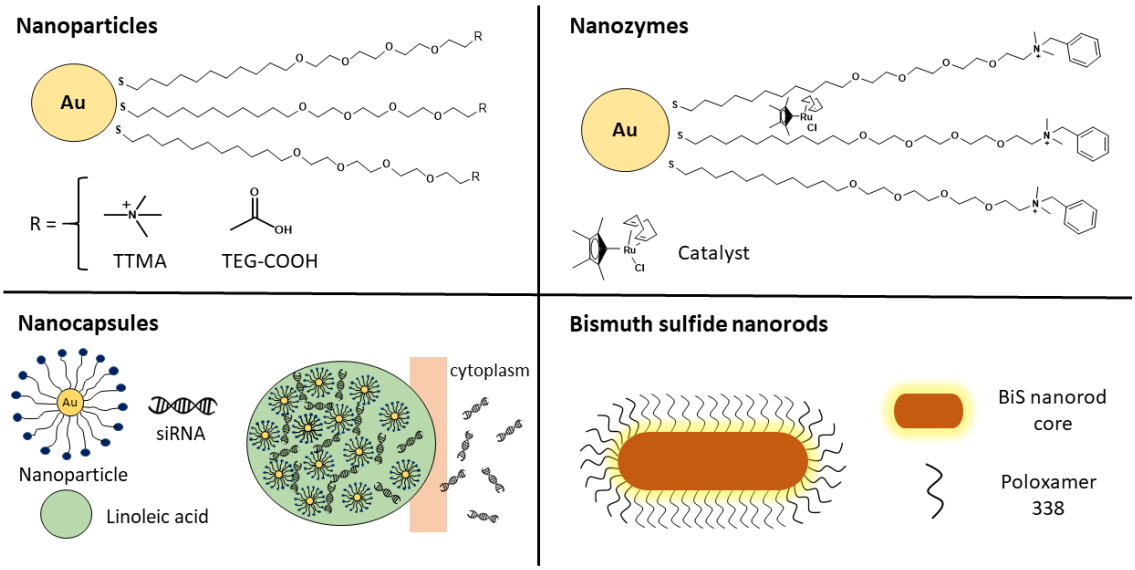

Figure 2.12. Description of the nanomaterials used in this work. Nanoparticles, nanozymes, nanocapsules and bismuth sulfide nanorods.

2.4.3 LA-ICP-MS data acquisition

LA-ICP-MS images were obtained on a CETAC LSX-213 G2 laser ablation system coupled with a Perkin Elmer NexION 300x ICP-MS. Unless otherwise specified, the following laser parameters were used: 50 μm spot size, 15 μm/s scan rate, 3.65 J laser energy, 10 Hz laser frequency, and a 10 s of shutter delay. The He carrier gas from laser ablation system was set to 0.6 L/min. The ICP-MS parameters were the following: 0.7 L/min nebulizer argon flow rate, 16.5 L/min plasma argon flow rate, 1.4 L/min auxiliary argon flow rate, -1650 V analog stage voltage, and 1000 V pulse stage voltage. These parameters were optimized for nanoparticle analysis in tissue sections, based on previous work.[27,28,39] Different elements, including ^{197}Au, ^{209}Bi, ^{102}Ru ^{57}Fe, and ^{66}Zn, were detected with 50 ms dwell times.

2.4.4 Code structure and repository

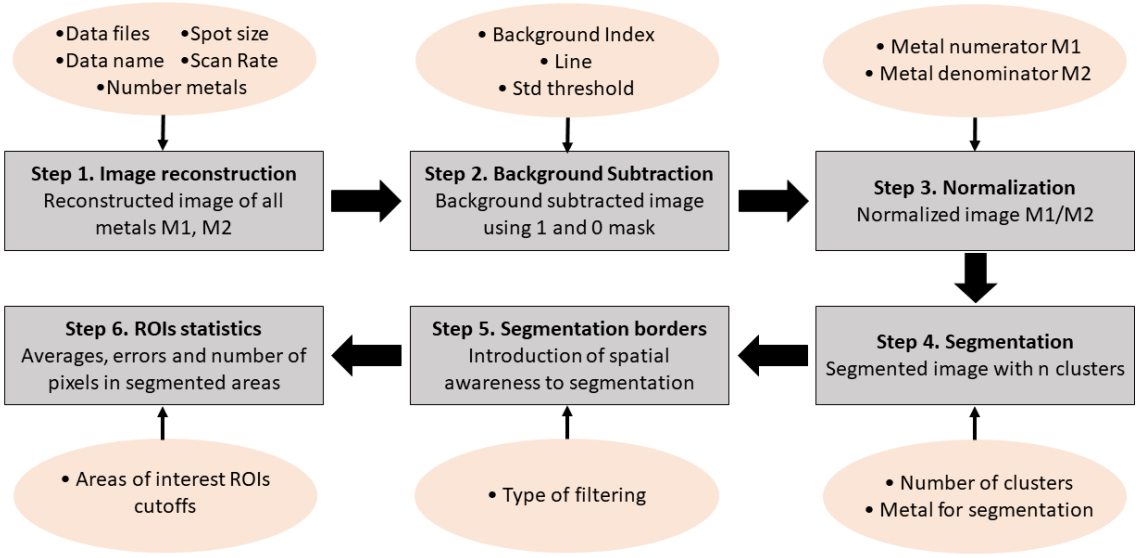

Figure 2.13. Code workflow explained step by step. Gray boxes correspond to transformations performed to the imaging data; orange circles contain the inputs required by the program to run the workflow. The inputs are added to the program using a Jupyter notebook interphase as shown in Figure 2.14.

Image reconstruction and analysis was performed using a program written in Python, their key functions are described in Figure 2.13. The computational workflow consists of a series of steps (gray boxes in Figure 2.13) which perform a particular computational transformation to the data. The inputs needed for a particular step are highlighted in orange. For example, for step 1, that consists of image reconstruction, the program takes: the data files, data name, number of metals, spot size and scan rate, to perform step 1. This information is provided by the user into the code

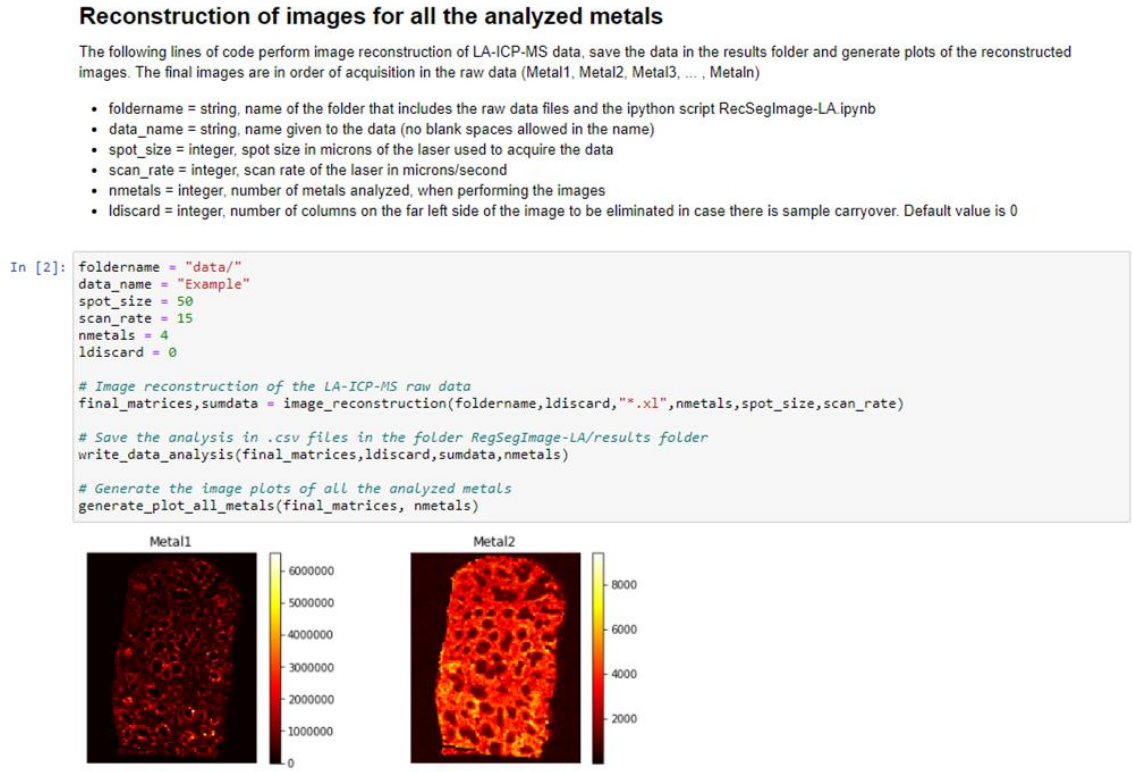

Figure 2.14. Jupyter notebook interphase for interacting with the source code. The image shows a grey box in which the inputs are added by the user, the images at the bottom correspond to the outputs generated when the code is compiled.

using a graphical Jupyter notebook[40] interphase as shown in Figure 2.14, the outputs or results of the particular step are displayed in the Jupyter notebook, after the code is compiled. The code consists of the Jupyter notebook and a source code. The Jupyter notebook contains only the inputs and outputs of each of the steps (Appendix A), while the source code contains all the functions

required to perform each step (Appendix B). The user only interacts with the Jupyter graphical interphase, making the processing of the data easier. Access to the scripts, examples and documentation can be found in Appendix A and B and in Github: https://github.com/Vachet-Lab/RecSegImage-LA,

2.4.5 Normalization

Normalization of the data allows the correction of tissue inhomogeneities during sample preparation and due to differences in mass ablation rates during laser ablation. Normalization of the tissues were performed using the Zn signals as an internal standard, because we have empirically found that this element is constant over the tissue section at the spatial resolutions studied (see Figure 2.3). However, the user can perform normalization in the code using other metals, like Phosphorous or Carbon, they just need to specify the type of metal in the input of the analysis workflow. Each of the studied metals (Au, Fe, and Bi) were divided by the Zn matrix in the Python script, on a pixel-by-pixel basis.[17] Matrix division is possible because the metal ion abundance matrices are co-registered as the multiple metals are detected at the same time during data acquisition.

2.4.6 Image segmentation and *k*-means clustering

A *k*-means clustering protocol was performed in Python, using the scikit-learn machine learning library.[18] To do this, the image of interest was vectorized, and the clustering was performed over the flattened image, as shown in Figure 2.15. The number of clusters was specified as a parameter in the program. If the number of clusters were unknown, the 'elbow method' was used to estimate the number of clusters into which the data should be divided, as shown in Figure 2.16.[41] For the elbow method calculation, the segmentation is done with different *k* values, until the inertia values reach the inflection point. After *k*-means clustering was performed, the centroids of the

clusters were calculated, the data was reshaped, and the labelled image was generated, as shown in Figure 2.15. The labelled image corresponds to an arbitrary mathematical label that marks a specific area of the tissue as part of a cluster.

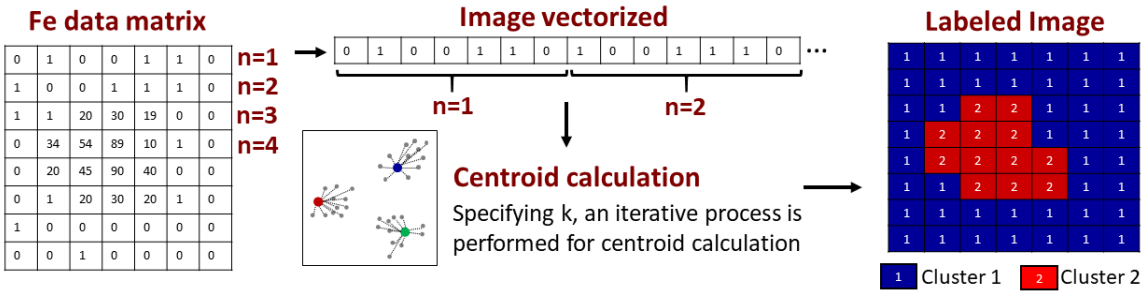

Figure 2.15. k-means clustering process. The data matrix is vectorized, *k* centroids are calculated in an iterative process until the overall error remains constant, and finally the labeled image is reshaped

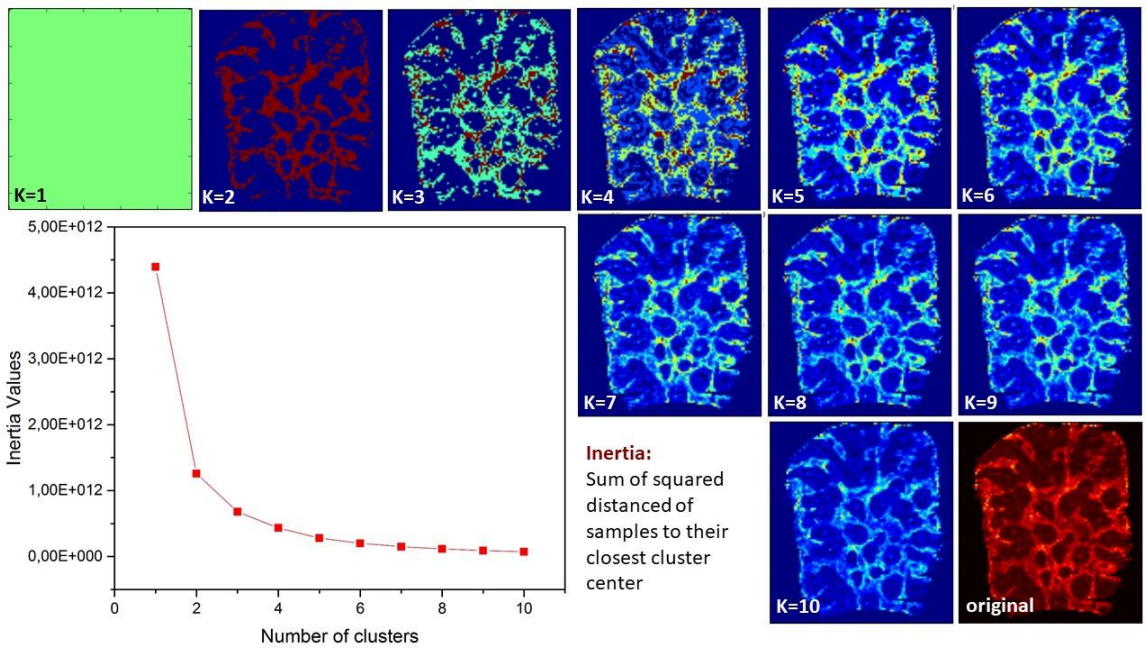

Figure 2.16. Example of the use of the elbow method for clustering of an image. Inertia values were calculated for each number of clusters for the same image. The ideal value in these data corresponds to k=2 or k=3. The elbow method is an empirical approach that allows the data analyst to select the optimal number of clusters from a given data set or image. For this purpose, k-means clustering is performed on the same data set, for different k values, and inertia values are calculated. The inertia values for each dataset correspond to the sum of squared distances of every sample to their closest cluster center. Once inertia values are calculated, they are plotted against the number of clusters to find the "elbow" or inflection point of the curve

2.5 References

(1) Osterholt, T.; Salber, D.; Matusch, A.; Becker, J. S.; Palm, C. IMAGENA : Image Generation and Analysis – An Interactive Software Tool Handling LA-ICP-MS Data. *Int. J. Mass Spectrom.* **2011**, *307* (1–3), 232–239.

(2) Tededyne CETAC Technologies. HDIP LA-ICP-MS Image Processing Software http://www.teledynecetac.com/products/laser-ablation/hdip-imaging-software.

(3) Paton, C.; Hellstrom, J.; Paul, B.; Woodhead, J.; Hergt, J. Iolite: Freeware for the Visualisation and Processing of Mass Spectrometric Data. *J. Anal. At. Spectrom.* **2011**, *26* (12), 2508–2518.

(4) Petrus, J. A.; Chew, D. M.; Leybourne, M. I.; Kamber, B. S. A New Approach to LA-ICP-MS Using the Flexible Map Interrogation Tool Monocle. *Chem. Geol.* **2017**, *463*, 76–93.

(5) Paul, B.; Hare, D. J.; Bishop, D. P.; Paton, C.; Nguyen, V. T.; Cole, N.; Niedwiecki, M. M.; Andreozzi, E.; Vais, A.; Billings, J. L.; Bray, L.; Bush, A.; McColl, G.; Roberts, B. R.; Adlard, P. A.; Finkelstein, D. I.; Hellstrom, J.; Hergt, J. M.; Woodhead, J. D.; Doble, P. A. Visualising Mouse Neuroanatomy and Function by Metal Distribution Using Laser Ablation-Inductively Coupled Plasma-Mass Spectrometry Imaging. *Chem. Sci.* **2015**, *6* (10), 5383–5393.

(6) López-Fernández, H.; Pessôa, G. D. S.; Arruda, M. A. Z.; Capelo-Martínez, J. L.; Fdez-Riverola, F.; Glez-Peña, D.; Reboiro-Jato, M. LA - IMageS : A Software for Elemental Distribution Bioimaging Using LA – ICP – MS Data. *J. Cheminform.* **2016**, *8* (1), 65.

(7) Sforna, M. C.; Lugli, F. MapIT! A Simple and User-Friendly MATLAB Script to Elaborate Elemental Distribution Images from LA-ICP-MS Data. *J. Anal. At. Spectrom.* **2017**, *32* (5), 1035–1043.

(8) Suzuki, T.; Sakata, S.; Makino, Y.; Obayashi, H.; Ohara, S.; Hattori, K.; Hirata, T. IQuant2: Software for Rapid and Quantitative Imaging Using Laser Ablation-ICP Mass Spectrometry. *Mass Spectrom.* **2018**, *7* (1), A0065.

(9) Uerlings, R.; Matusch, A.; Weiskirchen, R. Reconstruction of Laser Ablation Inductively Coupled Plasma Mass Spectrometry (LA-ICP-MS) Spatial Distribution Images in Microsoft Excel 2007. *Int. J. Mass Spectrom.* **2016**, *395*, 27–35.

(10) Böhme, S.; Stärk, H. J.; Kühnel, D.; Reemtsma, T. Exploring LA-ICP-MS as a Quantitative Imaging Technique to Study Nanoparticle Uptake in Daphnia Magna and Zebrafish (Danio Rerio) Embryos. *Anal. Bioanal. Chem.* **2015**, *407* (18), 5477–5485.

(11) Drescher, D.; Giesen, C.; Traub, H.; Panne, U.; Kneipp, J.; Jakubowski, N. Quantitative Imaging of Gold and Silver Nanoparticles in Single Eukaryotic Cells by Laser Ablation ICP-MS. *Anal. Chem.* **2012**, *84* (22), 9684–9688.

(12) Büchner, T.; Drescher, D.; Traub, H.; Schrade, P.; Bachmann, S.; Jakubowski, N.; Kneipp, J. Relating Surface-Enhanced Raman Scattering Signals of Cells to Gold Nanoparticle Aggregation as Determined by LA-ICP-MS Micromapping. *Anal. Bioanal. Chem.* **2014**, *406* (27), 7003–7014.

(13) Oros-Peusquens, A. M.; Matusch, A.; Becker, J. S.; Shah, N. J. Automatic Segmentation of Tissue Sections Using the Multielement Information Provided by LA-ICP-MS Imaging and k-Means Cluster Analysis. *Int. J. Mass Spectrom.* **2011**, *307*, 245–252.

(14) Alexandrov, T.; Becker, M.; Deininger, S.-O.; Ernst, G.; Wehder, L.; Grasmair, M.; von Eggeling, F.; Thiele, H.; Maass, P. Spatial Segmentation of Imaging Mass Spectrometry Data with Edge-Preserving Image Denoising and Clustering. *J. Proteome Res.* **2010**, *9* (12), 6535–6546.

(15) Alexandrov, T.; Kobarg, J. H. Efficient Spatial Segmentation of Large Imaging Mass Spectrometry Datasets with Spatially Aware Clustering. *Bioinformatics.* **2011**, *27* (13), i230–i238.

(16) Hunter, J. D. Matplotlib: A 2D Graphics Environment. *Comput. Sci. Eng.* **2007**, *9* (3), 90–95.

(17) Van Der Walt, S.; Colbert, S. C.; Varoquaux, G. The NumPy Array: A Structure for Efficient Numerical Computation. *Comput. Sci. Eng.* **2011**, *13* (2), 22–30.

(18) Pedregosa, F.; Varoquaux, G.; Gramfort, A.; Michael, V.; Thirion, B.; Grisel, O.; Blondel, M.; Prettenhofer, P.; Weiss, R.; Dubourg, V.; Vanderplas, J.; Passos, A.; Cournapeau, D.; Brucher, M.; Perrot, M.; Duchesnay, E. Scikit-Learn: Machine Learning in Python. *J. Mach. Learn. Res.* **2011**, *12*, 2825–2830.

(19) Klein, S.; Staring, M.; Murphy, K.; Viergever, M. A.; Pluim, J. P. W. Elastix: A Toolbox for Intensity-Based Medical Image Registration. *IEEE Trans. Med. Imaging.* **2010**, *29* (1), 196–205.

(20) Virtanen, P.; Gommers, R.; Oliphant, T. E.; Haberland, M.; Reddy, T.; Cournapeau, D.; Burovski, E.; Peterson, P.; Weckesser, W.; Bright, J.; Walt, S. J. Van Der; Brett, M.; Wilson, J.; Millman, K. J.; Mayorov, N.; Nelson, A. R. J.; Jones, E.; Kern, R.; Larson, E.; Carey, C. J.; Polat, I.; Feng, Y.; Moore, E. W.; VanderPlas, J.; Laxalde, D.; Perktold, J.; Cimrman, R.; Henriksen, I.; Quintero, E. A.; Harris, C. R.; Archibald, A. M.; Ribeiro, A. H.; Pedregosa, F.; Mulbregt, P. van. SciPy 1.0: Fundamental Algorithms for Scientific Computing in Python. *Nat. Methods.* **2020**, *17* (3), 261–272.

(21) Kaur, D.; Kaur, Y. Various Image Segmentation Techniques: A Review. *Int. J. Comput. Sci. Mob. Comput.* **2014**, *3* (5), 809–814.

(22) Boaru, S. G.; Merle, U.; Uerlings, R.; Zimmermann, A.; Flechtenmacher, C.; Willheim, C.; Eder, E.; Ferenci, P.; Stremmel, W.; Weiskirchen, R. Laser Ablation Inductively Coupled Plasma Mass Spectrometry Imaging of Metals in Experimental and Clinical Wilson's Disease. *J. Cell. Mol. Med.* **2015**, *19* (4), 806–814.

(23) Austin, C.; Fryer, F.; Lear, J.; Bishop, D.; Hare, D.; Rawling, T.; Kirkup, L.; McDonagh, A.; Doble, P. Factors Affecting Internal Standard Selection for Quantitative Elemental Bio-Imaging of Soft Tissues by LA-ICP-MS. *J. Anal. At. Spectrom.* **2011**, *26* (7), 1494–1501.

(24) Hare, D.; Burger, F.; Austin, C.; Fryer, F.; Grimm, R.; Reedy, B.; Scolyer, R. A.; Thompson, J. F.; Doble, P. Elemental Bio-Imaging of Melanoma in Lymph Node Biopsies. *Analyst* **2009**, *134* (3), 450–453.

(25) Becker, J. S.; Matusch, A.; Wu, B. Bioimaging Mass Spectrometry of Trace Elements - Recent Advance and Applications of LA-ICP-MS: A Review. *Anal. Chim. Acta* **2014**, *835*, 1–18.

(26) Mebius, R. E.; Kraal, G. Structure and Function of the Spleen. *Nat. Rev. Immunol.* **2005**, *5* (8), 606–616.

(27) Elci, S. G.; Yan, B.; Kim, S. T.; Saha, K.; Jiang, Y.; Klemmer, G. A.; Moyano, D. F.; Tonga, G. Y.; Rotello, V. M.; Vachet, R. W. Quantitative Imaging of 2 Nm Monolayer-Protected Gold Nanoparticle Distributions in Tissues Using Laser Ablation Inductively-Coupled Plasma Mass Spectrometry (LA-ICP-MS). *Analyst* **2016**, *141* (8), 2418–2425.

(28) Elci, S. G.; Jiang, Y.; Yan, B.; Kim, S. T.; Saha, K.; Moyano, D. F.; Yesilbag Tonga, G.; Jackson, L. C.; Rotello, V. M.; Vachet, R. W. Surface Charge Controls the Suborgan Biodistributions of Gold Nanoparticles. *ACS Nano* **2016**, *10* (5), 5536–5542.

(29) Jones, E. A.; Deininger, S. O.; Hogendoorn, P. C. W.; Deelder, A. M.; McDonnell, L. A. Imaging Mass Spectrometry Statistical Analysis. *J. Proteomics* **2012**, *75* (16), 4962–4989.

(30) Kevadiya, B. D.; Ottemann, B.; Mukadam, I. Z.; Castellanos, L.; Sikora, K.; Hilaire, J. R.; Machhi, J.; Herskovitz, J.; Soni, D.; Hasan, M.; Anandakumar, S.; Garrison, J.; Mcmillan, J.; Edagwa, B.; Mosley, R. L.; Vachet, R. W.; Gendelman, H. E. Rod-Shape Theranostic Nanoparticles Facilitate Antiretroviral Drug Biodistribution and Activity in Human Immunodeficiency Virus Susceptible Cells and Tissues. *Theranostics* **2020**, *10* (2), 630–656.

(31) Brust, M.; Walker, M.; Bethell, D.; Schiffrin, D. J.; Whyman, R. Synthesis of Thiol-Derivatised Gold Nanoparticles in a Two-Phase Liquid–Liquid System. *J. Chem. Soc., Chem. Commun.* **1994**, *7* (7), 801–802.

(32) Jiang, Y.; Huo, S.; Mizuhara, T.; Das, R.; Lee, Y. W.; Hou, S.; Moyano, D. F.; Duncan, B.; Liang, X. J.; Rotello, V. M. The Interplay of Size and Surface Functionality on the Cellular Uptake of Sub-10 Nm Gold Nanoparticles. *ACS Nano* **2015**, *9* (10), 9986–9993.

(33) Tonga, G. Y.; Jeong, Y.; Duncan, B.; Mizuhara, T.; Mout, R.; Das, R.; Kim, S. T.; Yeh, Y. C.; Yan, B.; Hou, S.; Rotello, V. M. Supramolecular Regulation of Bioorthogonal Catalysis in Cells Using Nanoparticle-Embedded Transition Metal Catalysts. *Nat. Chem.* **2015**, *7* (7), 597–603.

(34) Cao-Milán, R.; He, L. D.; Shorkey, S.; Tonga, G. Y.; Wang, L.-S.; Zhang, X.; Uddin, I.; Das, R.; Sulak, M.; Rotello, V. M. Modulating the Catalytic Activity of Enzyme-like Nanoparticles through Their Surface Functionalization. *Mol. Syst. Des. Eng.* **2017**, *2* (5), 624–628.

(35) Jiang, Y.; Hardie, J.; Liu, Y.; Ray, M.; Luo, X.; Das, R.; Landis, R. F.; Farkas, M. E.; Rotello, V. M. Nanocapsule-Mediated Cytosolic SiRNA Delivery for Anti-Inflammatory Treatment. *J. Control. Release.* **2018**, *283*, 235–240.

(36) Hardie, J.; Jiang, Y.; Tetrault, E. R.; Ghazi, P. C.; Tonga, G. Y.; Farkas, M. E.; Rotello, V. M. Simultaneous Cytosolic Delivery of a Chemotherapeutic and SiRNA Using Nanoparticle-Stabilized Nanocapsules. *Nanotechnology.* **2016**, *27* (37), 374001.

(37) Jiang, Y.; Tang, R.; Duncan, B.; Jiang, Z.; Yan, B.; Mout, R.; Rotello, V. M. Direct Cytosolic Delivery of SiRNA Using Nanoparticle-Stabilized Nanocapsules. *Angew. Chemie Int. Ed.* **2014**, *54* (2), 506–510.

(38) Ottemann, B. M.; Helmink, A. J.; Zhang, W.; Mukadam, I.; Woldstad, C.; Hilaire, J. R.; Liu, Y.; Mcmillan, J. M.; Edagwa, B. J.; Mosley, R. L.; Garrison, J. C.; Kevadiya, B. D.; Gendelman, H. E. Bioimaging Predictors of Rilpivirine Biodistribution and Antiretroviral Activities. *Biomaterials* **2018**, *185*, 174–193.

(39) Elci, S. G.; Tonga, G. Y.; Yan, B.; Kim, S. T.; Kim, C. S.; Jiang, Y.; Saha, K.; Moyano, D. F.; Marsico, A. L. M.; Rotello, V. M.; Vachet, R. W. Dual-Mode Mass Spectrometric Imaging for Determination of in Vivo Stability of Nanoparticle Monolayers. *ACS Nano.* **2017**, *11* (7), 7424–7430.

(40) Jupyter. https://jupyter.org/ 2014.

(41) Kodinariya, T. M.; Makwana, P. R. Review on Determining Number of Cluster in K-Means Clustering. *Int. J. Adv. Res. Comput. Sci. Manag. Stud.* **2013**, *1* (6), 90–95.

CHAPTER 3

A COMPUTATIONAL WORKFLOW FOR REGISTRATION OF LA-ICP-MS AND MALDI-MS IMAGES

3.1 Introduction

By appropriately leveraging the datasets from MALDI-MS and LA-ICP-MS imaging of a given tissue section, higher quality and more informative images should be accessible. The analysis of tissue sections by LA-ICP-MSI and MALDI-MSI is usually done by optical overlays of the data.[1–3] However, simple image overlays hinder quantitative comparisons because the images have different coordinate systems and orientations.[4] Multimodal image registration is the process of transforming a set of images from different sources, into a common spatial coordinate system.[5] The aim of image registration is to align features to enable pixel-to-pixel comparison of datasets to obtain quantitative correlations among the images.[6] Consequently, more quantitative information emerges from the dataset, enabling a level of analysis of the data that is hard to find by traditional data analysis methods, especially in multidimensional datasets, as in the case of mass spectrometry imaging.[7]

Other groups have explored approaches for multimodal image registration. For instance, mass spectrometry imaging multimodal registration approaches have been implemented by Caprioli and co-workers to register MALDI-MS images (20 µm resolution) with autofluorescence microscopy images (1 µm resolution), in their python software regToolboxMSRC.[8] However, this approach is harder to apply to cases where images have similar resolutions, as in the case of MALDI-MSI and LA-ICP-MSI, because the parameters used for the registration are optimized for images of different resolution. Although the regtools package is open source, it does not provide a

systematic way of optimizing parameters for LA-ICP-MS and MALDI-MS image registration. Holzlechner et al. recently reported an approach to register LA-ICP-MS and MALDI-MS images[9] that was based upon a multisensor image integration method that uses fiducial markers to align images in the same coordinate system.[10] Since the approach is based on fiducial markers, the accuracy of the registration is limited, and only linear transformations of the images are possible, making it unsuitable for registering images from adjacent tissue slices.[8] Moreover, this registration approach is performed in the software package Epina Imagelab[10], which is not open source.

Here, we describe a freely available computational workflow implemented in Python that allows the pre-processing and registration of LA-ICP-MS and MALDI-MS images in the same coordinate system, even for images from adjacent tissue sections. The proposed method was evaluated by calculating the overlap of regions of interest (ROIs), in the two imaging modalities, obtaining over 80% ROIs overlap. Additionally, the spatial accuracy of the registration was calculated to be close to 50 μm in many cases, demonstrating the applicability of the proposed method for the comparison of suborgan ROIs from LA-ICP-MS and MALDI-MS images.

3.2 Results and discussion

The computational workflow for LA-ICP-MS and MALDI-MS image registration and evaluation is summarized in Figure 3.1. First, we perform rendering and pre-processing (cropping, rotation, hotspot removal) of the LA-ICP-MS and MALDI-MS images. Second, a dimensionality reduction strategy is used to obtain a single MALDI-MS image representation for registration. Third, the registration of LA-ICP-MS and MALDI-MS images is implemented using a computational optimization, which maximizes the mutual information among the images, to bring them to the same coordinate system. Finally, the validation of the registration is performed by

calculating the ROI masks overlap and the accuracy of registration of corresponding points in the two images. These steps are described in more detail in the following sections.

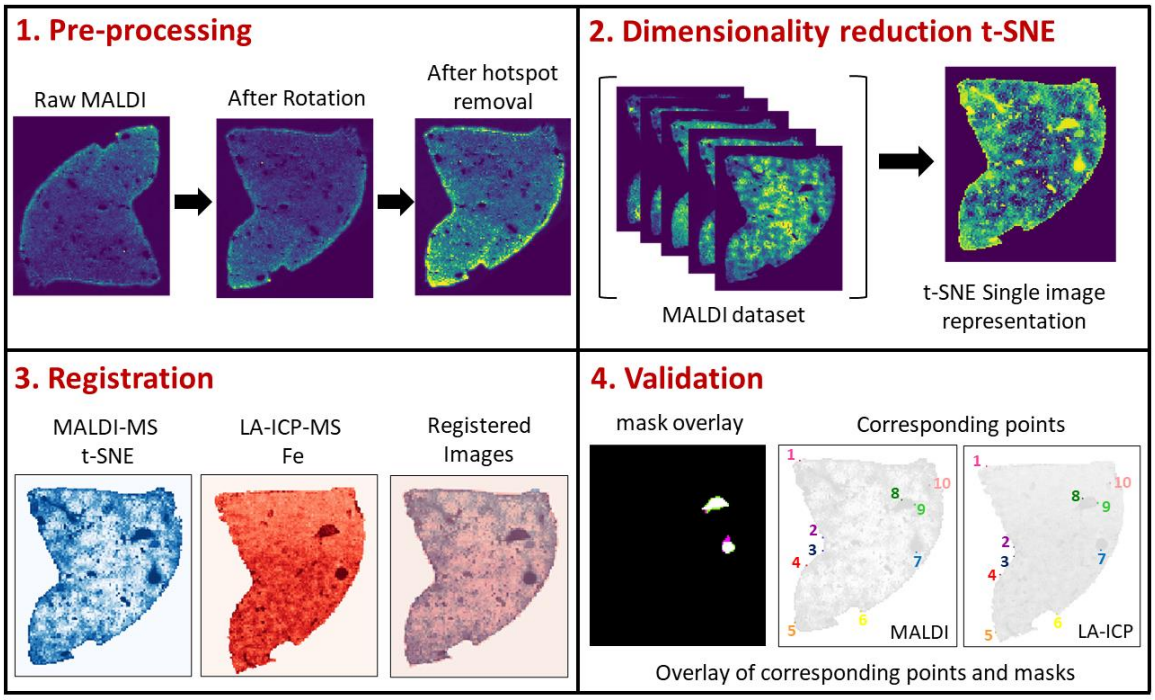

Figure 3.1. Summary of the steps followed to perform image registration and validation of LA-ICP-MS and MALDI-MS images. The process consists of the following steps: 1. Pre-processing of LA-ICP-MS and MALDI-MS data that involves: rendering, cropping, rotation, hotspot removal. 2. Dimensionality reduction to obtain a single image representation of the whole MALDI-MS dataset. 3. Registration of the LA-ICP-MS and MALDI-MS images. 4. Validation of the registration using mask overlay of ROIs and overlap of corresponding data points.

3.2.1 Image pre-processing

MALDI-MS images constitute complex datasets. They are usually composed of thousands of spectra, which results in large datafiles that are difficult to manipulate. For example, Figure 3.2a shows an image of a MALDI-MS experiment composed of three tissues and 30,631 spectra. In order to analyze this dataset, we use the parser pyimzML,[11] to create a function for MALDI-MS data rendering and manipulation in Python. Additionally, we added a function for cropping, hotspot removal rotation of MALDI-MS and LA-ICP-MS images to render them in the proper

configuration as shown in Figure 3.2. Hotspots are pixels with very high intensity values, corresponding to outliers in the intensity scale typically produced by fluctuations in the data acquisition process. Experimental factors such as the presence of large crystals of the matrix and disturbances of the equipment might contribute to hotspots. For that reason, several methods to perform hotspot removal in MALDI-MS image processing had been reported.[12] Preliminary runs for dimensionality reduction, registration, and calculation of correlation coefficients showed that the presence of hotspots decreases the quality of the output of these procedures. The hotspot removal function works by identifying pixels in the >0.99 quantile (1% high abundance pixels) and

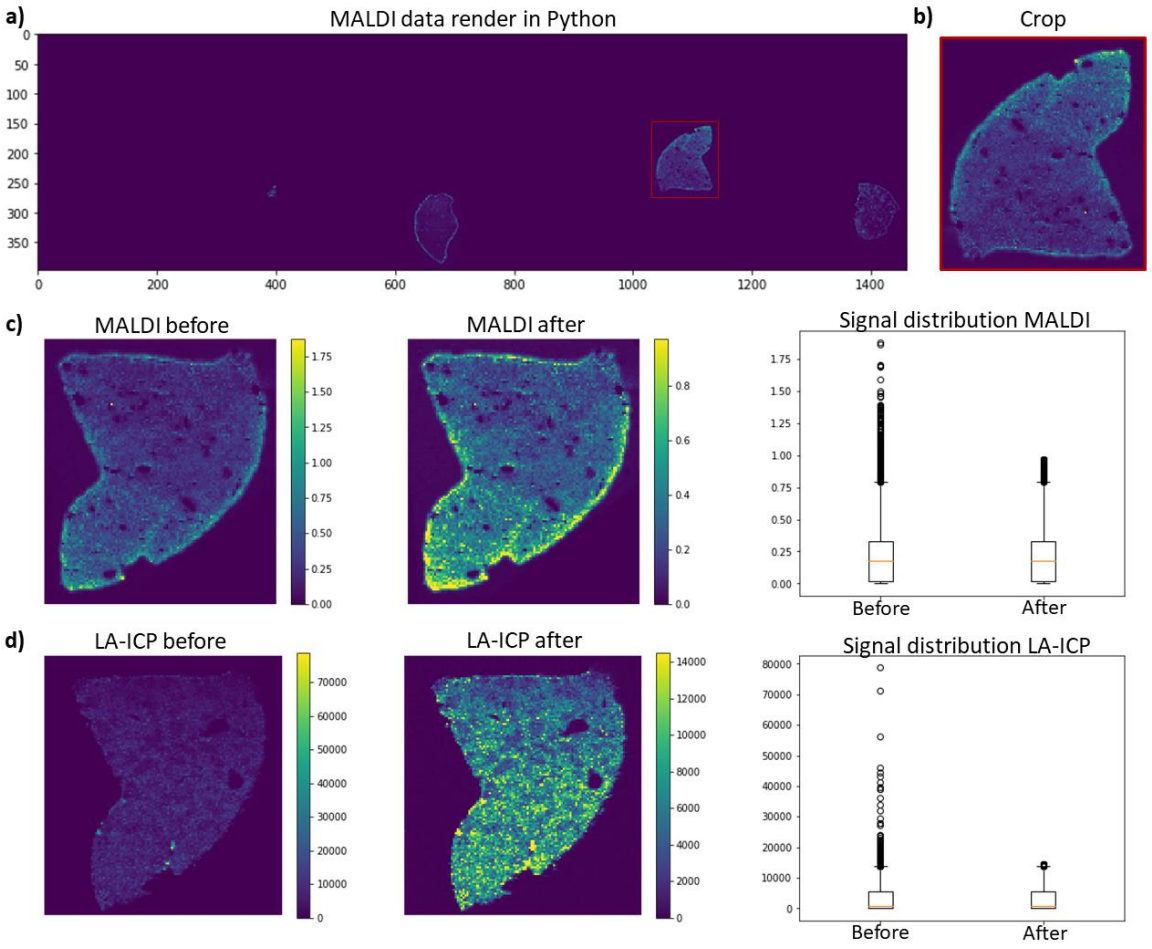

Figure 3.2. Pre-processing of MALDI-MS and LA-ICP-MS data. a) Rendered overview of a tissue slide containing a MALDI-MS experiment in which several tissues were analyzed. b) crop of the tissue section that will be used for registration, c) MALDI-MS image before and after hotspot removal, and box a whisker plots of the signal distribution (*m/z* 399.088). d) Au LA-ICP-MS image before and after hotspot removal, and box and whisker plots of signal distribution.

replacing them by the 0.99 quantile value, as shown in the box and whisker plots. After hotspot removal, the quality of the image processing routines as well as the statistical correlations inferred from the data improve significantly. The included functions for: cropping, rotation, and hotspot removal in the computational workflow are applied automatically to all the channels imported into the workflow for MALDI-MS (40 to 60 channels), and LA-ICP-MS (3 channels).

3.2.2 Dimensionality reduction of MALDI-MSI datasets using t-SNE

To properly implement image registration, one image per modality (LA-ICP-MS and MALDI-MS) is required as input. Generally, the Fe channel for LA-ICP-MS and the heme b channel for the MALDI-MS are used as the informative signal channels that display internal features of the image, such as the red pulp, white pulp, veins, etc.[1] However, some sample preparation approaches, such as the use of sublimation for MALDI-MS matrix deposition, decrease considerably the abundance of the heme b signal in MALDI-MSI. In this case, we employ a dimensionality reduction approach to obtain a single image representation of the MALDI-MS dataset. The image obtained from this procedure is expected to capture most of the salient features from the images of different ion channels. The dimensionality reduction was performed using a t-distributed stochastic neighboring embedding model (t-SNE) that operates by representing the hyperspectral data relationships associated with each pixel in a low-dimension 2D map.[13] We built a function in the Python workflow to perform t-SNE on a set of selected ions in MALDI-MS to generate the t-SNE single image representation. Figure 3.3 illustrates the application of t-SNE for dimensionality reduction of the MALDI-MS dataset to generate a single t-SNE image (Figure 3.3a) by combining 39 different ions measured in MALDI-MS (Figure 3.3b). The resulting t-SNE MALDI-MS image is used as the MALDI-MS input in the registration process.

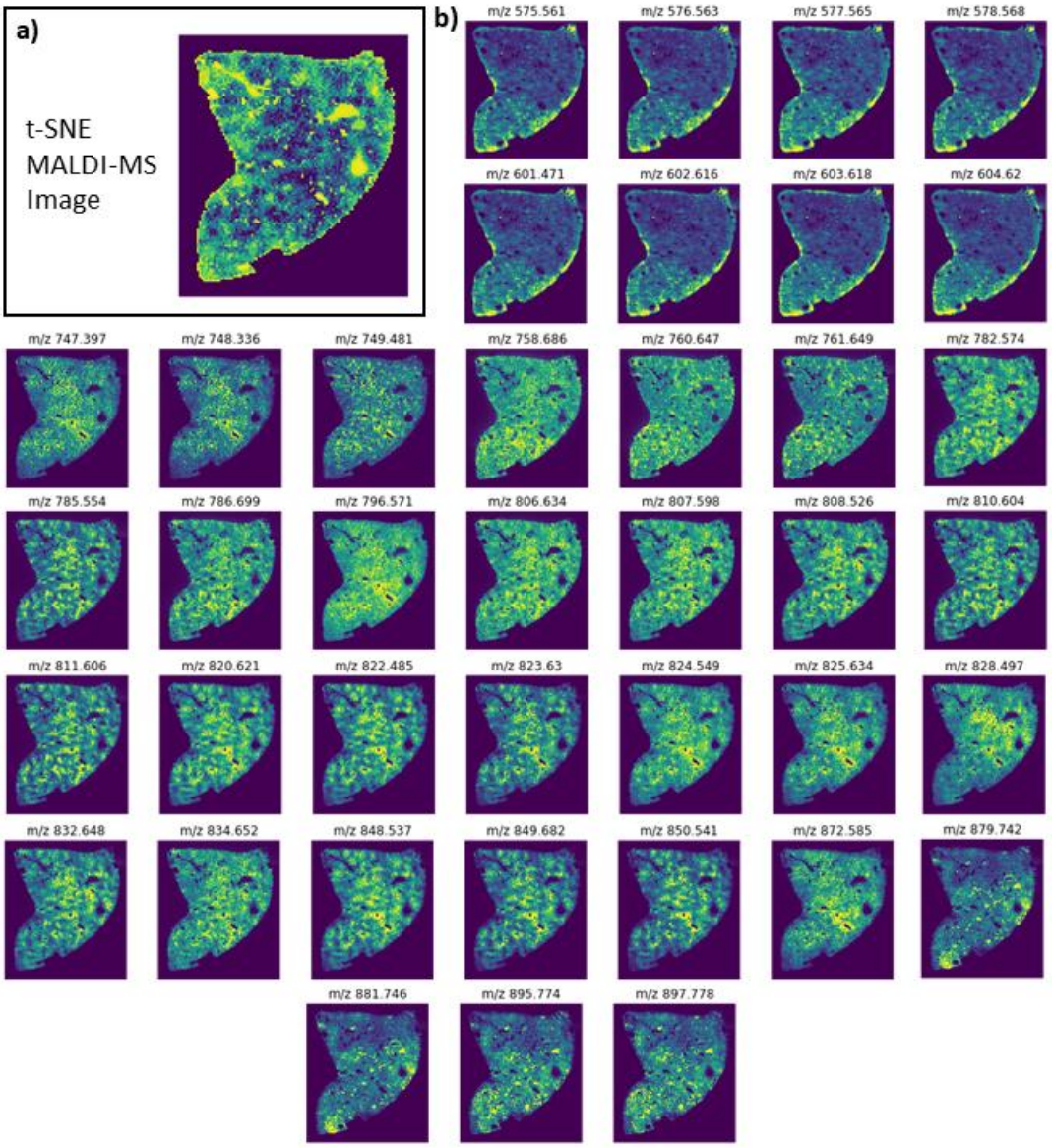

Figure 3.3. a) t-SNE MALDI-MS single image representation of the MALDI-MS dataset. b) 39 MALDI-MS representative images in the mass range m/z 500 – 900 which were used as inputs to calculate the t-SNE MALDI-MS single image representation.

3.2.3 Registration of LA-ICP-MS and MALDI-MS images

Image registration involves transforming two or more images containing different data features into the same coordinate system. Once the images are registered, the combined information from the different imaging modalities allows deeper statistical and quantitative analyses of the

images. In the process of image registration, one of the images is set as the fixed image, and the other one is the moving image (e.g., Figure 3.4). The moving image is transformed to maximize its similarity to the fixed image, resulting in an image that has the same coordinates and pixel number as the fixed image. In this work, LA-ICP-MS and MALDI-MS images were registered using SimpleElastix registration algorithms[14] in a custom Python workflow. Access to the scripts, examples and documentation can be found at Appendix C.

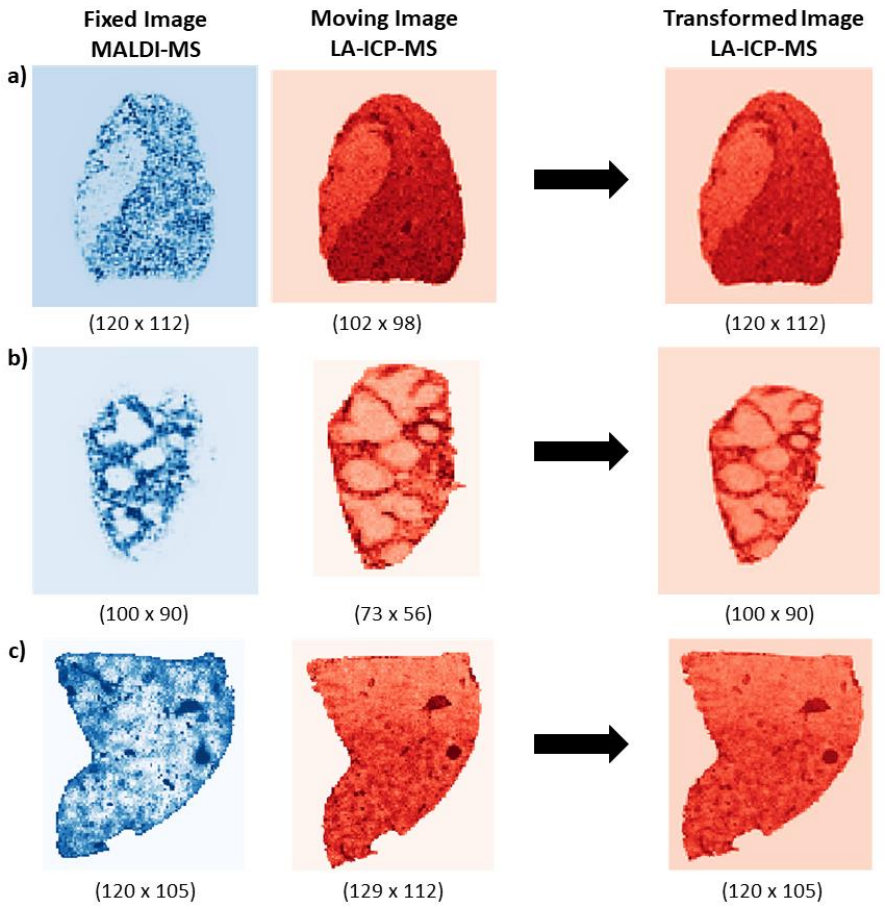

Figure 3.4. Fixed, moving, and transformed images for: a) mouse liver sections analyzed by MALDI-MS, with matrix deposition via the ImagePrep matrix sprayer, and LA-ICP-MS, b) mouse spleen sections analyzed by MALDI-MS, with matrix deposition via the ImagePrep matrix sprayer, and LA-ICP-MS, c) mouse liver sections analyzed by MALDI-MS, with matrix deposition via sublimation, and LA-ICP-MS. The numbers at the bottom represent the pixel dimensions of the given image. The pixel dimensions of the moving image are transformed into the same coordinate system as the fixed image after registration

To carry out the registration we need to pick two images, one from each modality. Since each modality offers several images corresponding to different channels (different ions in the case of MALDI-MS or different elements for LA-ICP-MS), one strategy can be picking a pair of images that share common features. These internal signal features help to drive the optimization process, which seeks to maximize the mutual information present in both images. Ideally, these signal features should reflect the morphologic structure of the image (e.g., distinct sub-organ regions in a tissue) to ensure the best registration possible. Proper choice of the signal channels enables successful registration of LA-ICP-MS and MALDI-MS images when different MALDI-MS matrix deposition approaches are used or even when adjacent tissue sections are imaged. For LA-ICP-MS, we find that the Fe signal channel (i.e., ^{57}Fe) is an effective feature to use as it indicates blood-rich regions that often define different regions in a tissue. For MALDI-MS images, we initially used the heme b signal (*m/z* 616), as analogous indicator of blood flow. Figures 3.5a and 3.5b illustrate the LA-ICP-MS (red) and MALDI-MS (blue) images of liver and spleen tissue sections before and after registration. The MALDI-MS image was used as the fixed image, and the LA-ICP-MS image was used as the moving image. Visual inspection of these images shows that the registration process successfully aligns the tissue boundaries and other internal structure features. For example, in Figure 3.5a, a large piece of connective tissue (CT) that is devoid of heme signal in the MALDI-MS image aligns well with the same low Fe signal in the LA-ICP-MS image. Similarly, the red pulp (RP) and white pulp (WP) regions of the spleen are very well aligned after registration (Figure 3.5b).

When it is difficult to identify a single signal channel that captures the necessary features for registration, one can alternatively use computational techniques to generate a single image from multiple channels. In this case, we used a t-distributed stochastic neighbor embedding (t-SNE) approach to carry out dimensionality reduction for the MALDI-MSI datasets, as described in Section 3.2.2. This method has been used successfully on MALDI-MSI data.[13,15,16] When the t-SNE

generated features from MALDI-MS images are used together with the Fe signal from LA-ICP-MS, registration of the two images can be achieved. Using a liver section as an example (Figure 3.5c), our approach successfully registers the two images, as indicated by the excellent overlap of the tissue boundaries and veins (V) in the images.

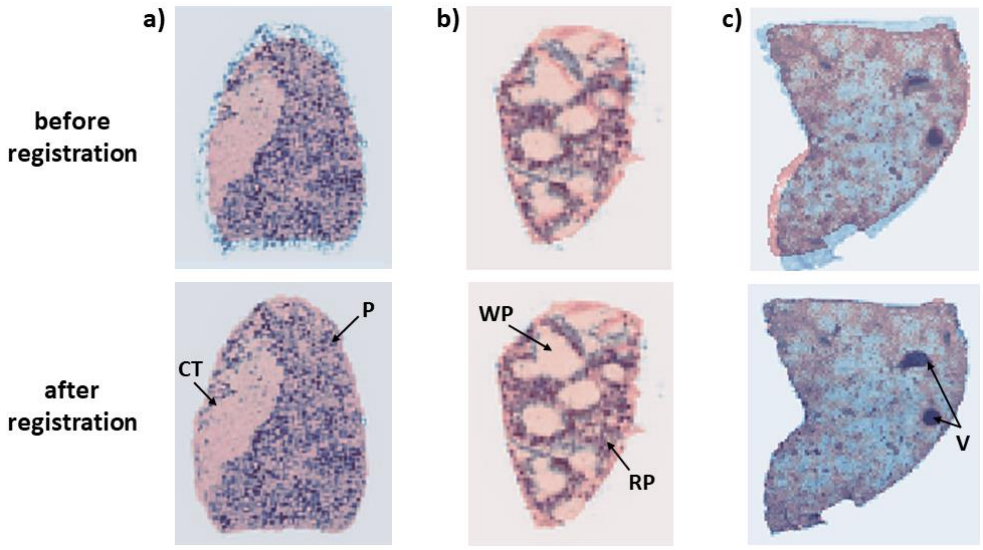

Figure 3.5. Sequential slices of liver and spleen tissues from mice analyzed by LA-ICP-MS (red) and MALDI-MS (blue) using different MALDI-MS matrix deposition strategies and compared before and after registration. a) Liver: The MALDI-MS tissue sample was prepared using a matrix sprayer. Low heme and Fe signals are present in the connective tissue (CT), while higher heme and Fe signals are present in the parenchyma (P). b) Spleen: The MALDI-MS tissue sample was prepared using a matrix sprayer. High Fe and heme signals are present in the red pulp (RP), while low signals are found in the white pulp (WP). c) Liver: The MALDI-MS tissue sample was prepared using a sublimation chamber. High Fe and t-SNE signals are present in the vein (V).

It should be noted that the registered images shown in Figure 3.5 are from adjacent tissue sections. Using adjacent tissue slices allows MALDI-MS and LA-ICP-MS imaging conditions to be separately optimized. Figure 3.6 shows the registration of the tissue sections using different transformations including linear (rigid and affine) and no-linear registration. The different transformations shows that registering adjacent tissue sections is more accurate when using non-linear registration approaches to correct for local deformations in the tissues that can arise from placement of adjacent tissue slices.[8]

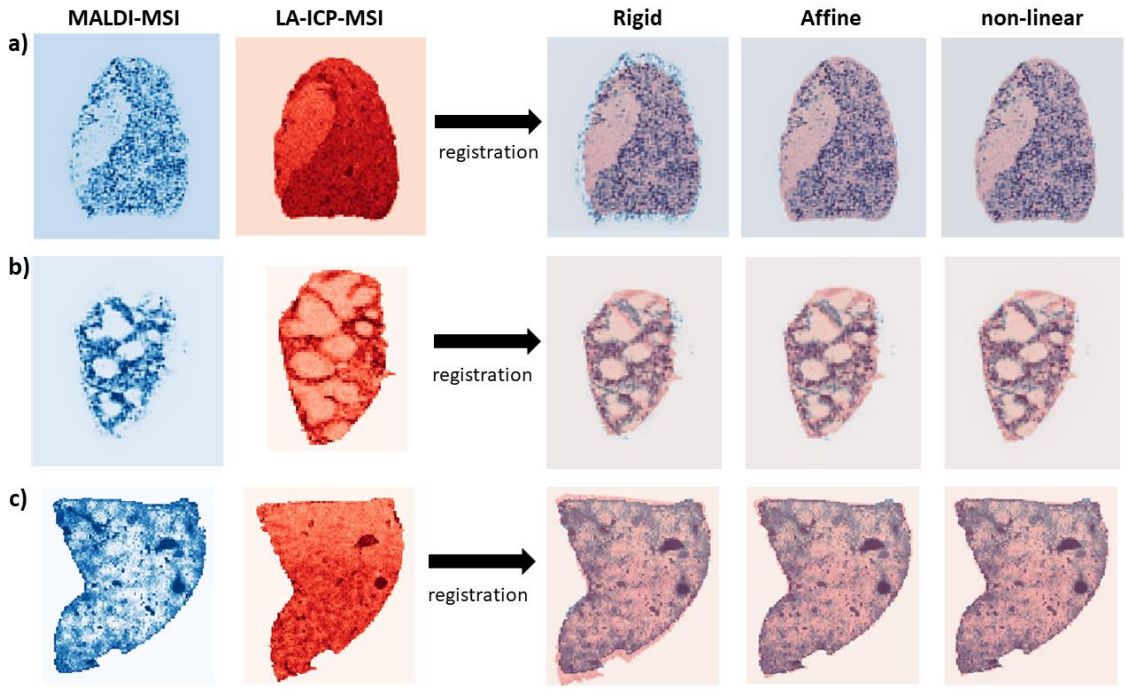

Figure 3.6. Examples of rigid, affine, and non-linear transformation for registering MALDI-MS and LA-ICP-MS images of liver (a and c) and spleen tissues from mice. Rigid transformations involve translating or rotating images for better overlap. Affine transformations add scaling and skewing factors for images that are different sizes. non-linear transformation compensates for localized distortions.

3.2.4 Registration evaluation

The effectiveness of our registration approach was evaluated by two methods: Dice similarity coefficient (DSC) calculations and landmark validation. DSC values were calculated using the approach described by Rohlfin[17] (equation 1 of the materials and methods section). For calculating the DSC values, ROIs were first chosen in both the LA-ICP-MS and MALDI-MS images (Figure 3.7). The chosen ROIs depended on the tissue type. For the liver, we used blood vessels, and for the spleen, we used the white pulp. Figure 3.7 shows the DSC analysis for the chosen ROIs before and after registration. White pixels in the overlay represent pixels that overlap in LA-ICP-MS and MALDI-MS images. The DSC value for the liver images increases from 0.42 after simply overlaying the images before registration to 0.85 after registration, and in the spleen tissue the increase is from 0.64 to 0.77. Perfect overlap of the images would correspond to DSC

values of 1.0. Because these images are from adjacent tissue slices, DSC values below 1.0 are expected, as there are slight differences in the ROIs due to biological variations and imperfect placement of the tissue sections. The improvement in DSC values after registration is comparable to previous work by Caprioli and co-workers[8] in which MALDI-MS and immunostained images of liver and spleen sections were registered.[18] To further test the ability of our registration methods, we also tested tissues sections that were not immediately adjacent but were two sections apart. In one example, the DSC value increased from 0.34 to 0.69 after registration (Figure 3.8), indicating there is reasonable similarity between non-adjacent tissue sections.

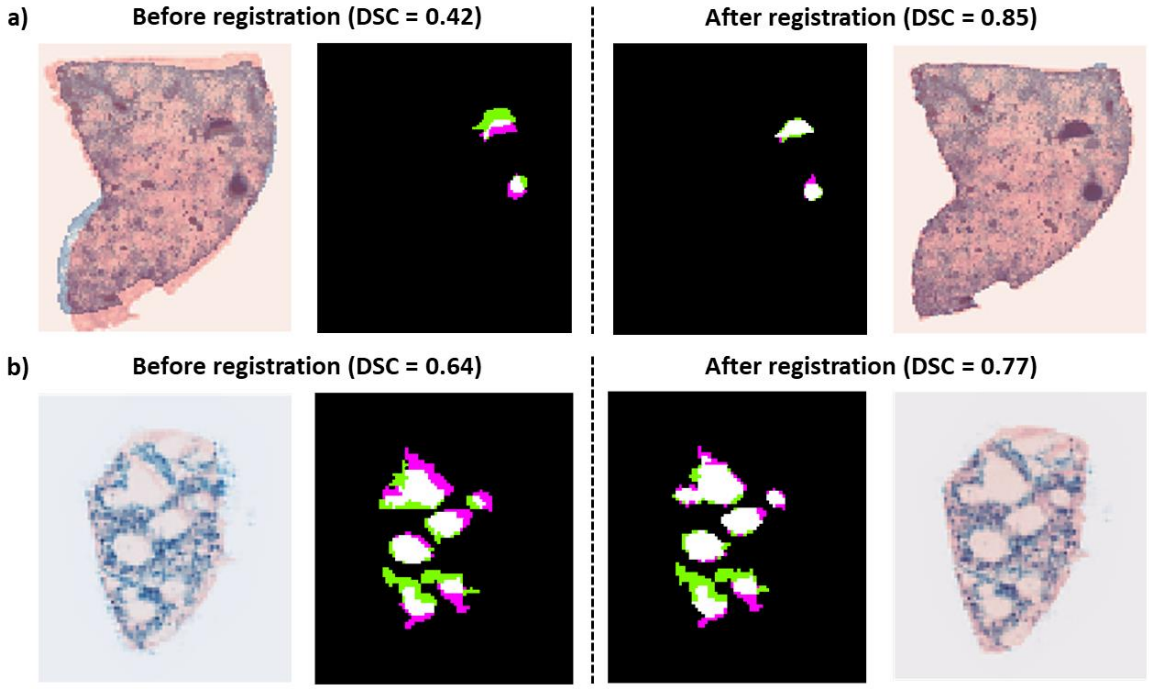

Figure 3.7. Registration validation using DSC calculations for liver and spleen tissue sections after registration of the MALDI-MS and LA-ICP-MS images from Figures 3.4c and b. a) Overlay of blood vessel masks and resulting DSC values before and after registration. b) Overlay of white pulp masks and resulting DSC values before and after registration. Green = LA-ICP-MS only pixels, Magenta = MALDI-MS only pixels, White = Overlayed pixels. Segmentation of the veins and white pulp was performed manually using the Fe image in LA-ICP-MS and the t-SNE image in MALDI-MS to generate computational masks for each of the two images.

Landmark validation[8] was also used to assess registration effectiveness. In the landmark approach, several morphologically distinct points are chosen in both LA-ICP-MS and MALDI-MS images, and the distance between these points is calculated and averaged to provide an effective registration accuracy (Figure 3.9). For the images shown in Figure 3.4, average registration accuracies of 40 ± 30 µm and 70 ± 20 µm are obtained for the liver and spleen, respectively. Since the images were acquired at 50 µm resolution, the landmark distances show that most of the pixels are either perfectly correlated or one pixel off. Given that the diameters of veins in the liver vary between 300 and 600 µm, and the diameters of white pulp areas are typically between 300 and 900 µm, these registration accuracies allow us to make conclusions about the veins and white pulp sub-organ regions.

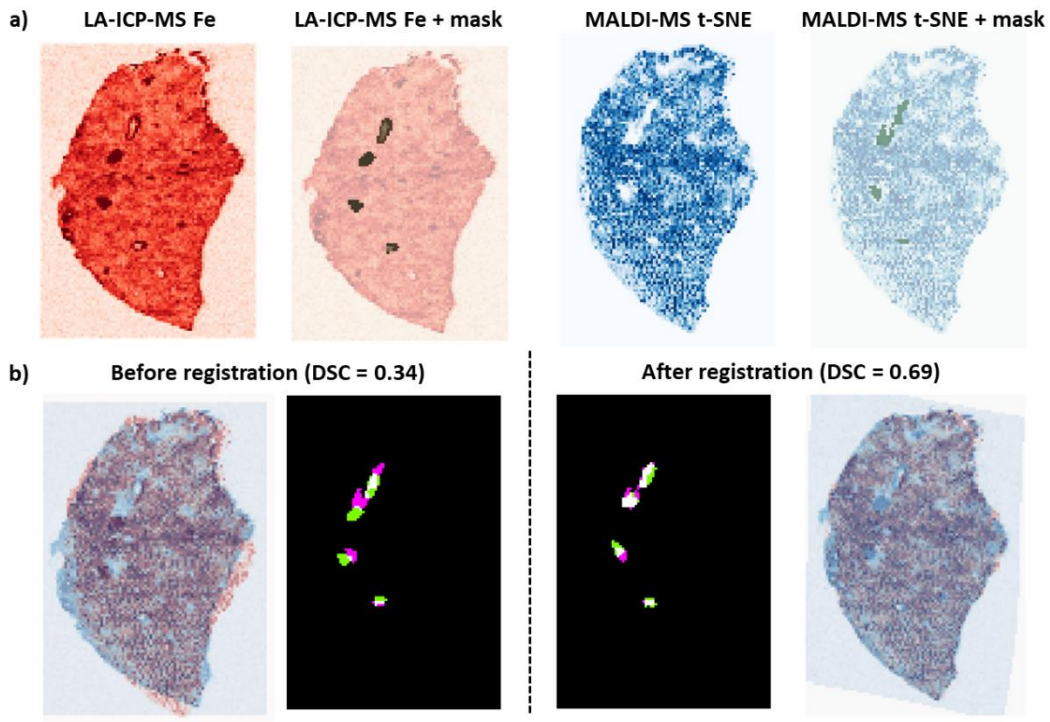

Figure 3.8. Registration validation using DSC calculations for non-adjacent mouse liver tissue sections. a) LA-ICP-MS and MALDI-MS images and masks before registration. b) Overlay of vein masks and DSC values, before and after registration. Green = LA only pixels, Magenta = MALDI only pixels, White = Overlay pixels. Segmentation of the veins was performed manually using the Fe image in LA-ICP-MS and the t-SNE image in MALDI-MS to generate computational masks for each of the two images.

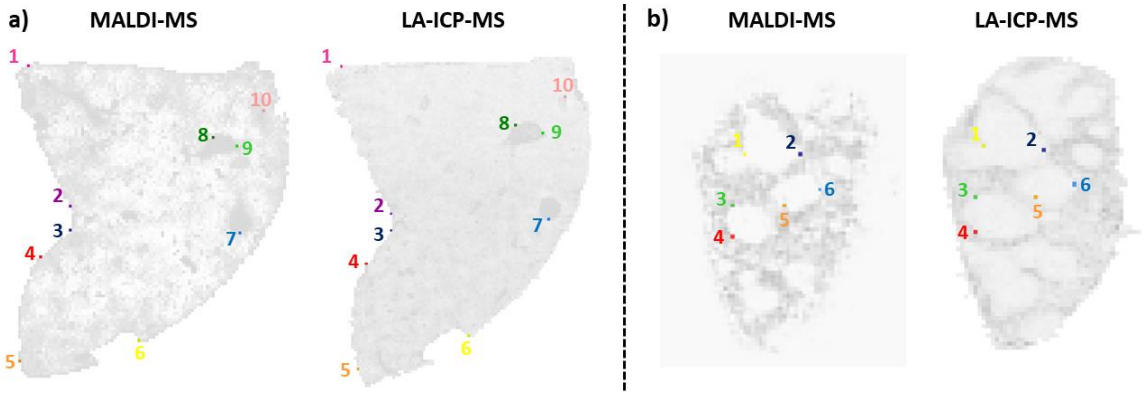

Figure 3.9. Landmark validation of LA-ICP-MS and MALDI-MS registration using selected pixels corresponding to morphologically distinct sites in liver and spleen tissues in mice. a) Mouse liver and b) mouse spleen. The numbers indicate the pixels that were chosen as landmarks in both imaging modalities. In the landmark validation process, the images are overlaid, and the Euclidean distance between corresponding points is measured to determine the registration accuracy

3.3 Conclusions

We have developed and evaluated a freely available computation workflow to register LA-ICP-MS and MALDI-MS images. Our proposed workflow is the first computational approach, to our knowledge, that is developed for registration of adjacent tissue slices of LA-ICP-MS and MALDI-MS images. The workflow is written in Python and contains functions for image pre-processing, dimensionality reduction, registration, and validation. By using the proposed method, we are able to render and pre-process MALDI-MS data using cropping, rotation, and hotspot removal functions. In addition, we have demonstrated the use of dimensionality reduction functions to obtain a single image representation of a MALDI-MS liver dataset. Registration of MALDI-MS and LA-ICP-MS images of several spleen and liver tissues from adjacent tissue slices were performed using the registration workflow functions. After registration, we obtain high correlations among the image modalities for the white and red pulp in the spleen and connective tissue, parenchyma, and veins in the liver tissue. Using different transformations (rigid, affine and non-linear) indicates that non-linear transformations are crucial to ensure a proper registration among

adjacent tissue slices. Finally, the registration method has been evaluated using DSC and landmark registration, obtaining overlapping of ROIs close to 80% and registration accuracies below 50 µm. We point out that the combination of LA-ICP-MS and MALDI-MS images enabled by our workflow constitutes a systematic and statistically accurate approach for integrating the strengths of these two image modalities, providing access to quantitative information about tissue samples that cannot be obtain independently by each modality. In subsequent chapters, we will explore specific applications of these image processing techniques to acquire insight into biochemical processes in these tissue samples.

3.4 Materials and methods:

3.4.1 Nanomaterial synthesis:

Nanoparticle (NP) synthesis was performed using the Brust-Schiffrin reaction,[19] followed by functionalization of the Au NP core with different ligands, as described in previous work.[20–23] Similarly, nanoparticle stabilized capsules (NPSC) were synthesized by mixing arginine nanoparticles with linoleic acid, followed by its functionalization with siRNA.[24–26]

3.4.2 Animal experiments and tissue sectioning:

Balb/c mice were tail vein injected with the nanoparticles (NP) or nanoparticle stabilized capsules (NPSC) and euthanized after 24 and 48 hours, respectively. Mice were sacrificed by carbon dioxide inhalation and cervical dislocation. All animal experiments were approved by the University of Massachusetts Amherst Institutional Animal Care and Use Committee (IACUC), which is guided by the U.S. Animal Welfare Act and U.S. Public Health Service Policy. Tissues were flash frozen and kept at -80 °C, until slicing for imaging. Frozen tissues were sliced using a LEICA CMM1850 cryostat. Adjacent tissue slices of 12 µm thickness were thaw-mounted on

indium tin oxide (ITO)-coated glass and glass slides, for MALDI-MSI and LA-ICP-MSI experiments, respectively.

3.4.3 MALDI-MSI:

MALDI-MSI experiments were performed using 2,5-dihydroxybenzoic acid (2,5-DHB) as a matrix. Two different methods for matrix deposition were used: spraying and sublimation. Spraying was performed using a Bruker ImagePrep device to spray a 25 mg/mL matrix solution in 1:1 methanol:water on the sliced tissue. Sublimation was performed on a home-built sublimation apparatus similar to the setup described by Chaurand and co-workers.[27] For liver tissues, 200 mg of matrix were deposited at 140 °C at 7 mTorr for 9 minutes. For spleen tissue, 170 mg of matrix were deposited at 140 °C at 7 mTorr for 8 minutes. Data acquisition was performed on a Bruker UltrafleXetreme MALDI TOF/TOF at 50 μm resolution over an *m/z* range of 200 to 2000.

3.4.4 LA-ICP-MSI:

LA-ICP-MS images of ^{197}Au, ^{57}Fe, and ^{66}Zn were acquired on a CETAC LSX-213 G2 laser ablation system coupled with a Perkin Elmer NexION 300x ICP-MS instrument. The following laser parameters were used: 50 μm spot size, 20 μm/s scan rate, 3.65 J laser energy, 10 Hz laser frequency, and a 10 s shutter delay. The He carrier gas from laser ablation system was set to 0.6 L/min. The described parameters were used in previous contributions for the analysis of nanomaterials in tissue sections.[28–30]

3.4.5 Image preprocessing:

MALDI-MS images were normalized and exported as imzML files using FlexImaging (Bruker, Daltonics). The imzML files were imported to Python using the pyimzML parser, developed by Alexandrov and co-workers.[31] Peak picking was performed using SCiLS Lab 2015b,

and the list of selected ions and mass tolerances were imported to Python as a text file. Images of the selected ions were rendered with the pyimzML parser using the text file ion list. LA-ICP-MS images were reconstructed, analyzed, and segmented using a custom Python script RecSegImage-LA, which is described in Chapter 2 and is freely available at GitHub (https://github.com/Vachet-Lab/RecSegImage-LA).[32] Hotspot removal was performed on MALDI-MS and LA-ICP-MS images by selecting the intensities in the >0.99 quantile and replacing them with the 0.99 quantile value.[12] In some cases, t-stochastic non-linear embedding (t-SNE) dimensionality reduction module from the scikit-learn Python library[33] was applied to selected ion datasets in MALDI-MSI to obtain a single image representation of the dataset.

3.4.6 Image registration and validation:

Image registration was performed using the SimpleElastix[14] Python wrapper of the Elastix C++ library.[6] The MALDI-MSI image (t-SNE or heme channel) was set as the fixed image, while the LA-ICP-MSI image (Fe channel) was set as the moving image. Registration was performed using the default affine parameter map followed by the default no-linear parameter map in SimpleElastix with certain modifications as follows: 4,000 iterations for the affine parameter map, 8,000 iterations for the non-linear parameter map and 50 final grid spacing in physical units. Validation of the registration was performed by Dice similarity coefficient calculations (DSC). We used the DSC equation described by Klein and co-workers (equation 1), Where X and Y represent the binary label images. Selected regions, such veins (liver) and white pulp (spleen) regions, were manually selected in Fiji,[34] and imported to Python to calculate the DSC value. Landmark distance analysis after registration was calculated by selecting corresponding points in the two images, followed by image overlay and calculation of their distances in Fiji.

$$DSC(X,Y) = \frac{2|X \cap Y|}{|X| + |Y|} \qquad \textbf{Equation (1)}$$

3.5 References

(1) Sikora, K. N.; Hardie, J. M.; Castellanos-García, L. J.; Liu, Y.; Reinhardt, B. M.; Farkas, M. E.; Rotello, V. M.; Vachet, R. W. Dual Mass Spectrometric Tissue Imaging of Nanocarrier Distributions and Their Biochemical Effects. *Anal. Chem.* **2020**, *92* (2), 2011–2018.

(2) Niehoff, A.-C.; Schulz, J.; Soltwisch, J.; Meyer, S.; Kettling, H.; Sperling, M.; Jeibmann, A.; Dreisewerd, K.; Francesconi, K. A.; Schwerdtle, T.; Karst, U. Imaging by Elemental and Molecular Mass Spectrometry Reveals the Uptake of an Arsenolipid in the Brain of Drosophila Melanogaster. *Anal. Chem.* **2016**, *88* (10), 5258–5263.

(3) González de Vega, R.; Fernández Sanchez, M. L.; Eiro, N.; Vizoso, F. J.; Sperling, M.; Karst, U.; Sanz Medel, A. Multimodal Laser Ablation/Desorption Imaging Analysis of Zn and MMP-11 in Breast Tissues. *Anal. Bioanal. Chem.* **2018**, *410* (3), 913–922.

(4) Masyuko, R.; Lanni, E. J.; Sweedler, J. V; Bohn, P. W. Correlated Imaging – a Grand Challenge in Chemical Analysis. *Analyst* **2013**, *138* (7), 1924–1939.

(5) Klein, S.; Staring, M. Elastix 4.9.0 - Manual. **2018**, 60.

(6) Klein, S.; Staring, M.; Murphy, K.; Viergever, M. A.; Pluim, J. P. W. Elastix: A Toolbox for Intensity-Based Medical Image Registration. *IEEE Trans. Med. Imaging.* **2010**, *29* (1), 196–205.

(7) Neumann, E. K.; Djambazova, K. V.; Caprioli, R. M.; Spraggins, J. M. Multimodal Imaging Mass Spectrometry: Next Generation Molecular Mapping in Biology and Medicine. *J. Am. Soc. Mass Spectrom.* **2020**, *31* (12), 2401–2415.

(8) Patterson, N. H.; Tuck, M.; Lewis, A.; Kaushansky, A.; Norris, J. L.; Van De Plas, R.; Caprioli, R. M. Next Generation Histology-Directed Imaging Mass Spectrometry Driven by Autofluorescence Microscopy. *Anal. Chem.* **2018**, *90* (21), 12404–12413.

(9) Holzlechner, M.; Bonta, M.; Lohninger, H.; Limbeck, A.; Marchetti-Deschmann, M. Multisensor Imaging—From Sample Preparation to Integrated Multimodal Interpretation of LA-ICPMS and MALDI MS Imaging Data. *Anal. Chem.* **2018**, *90* (15), 8831–8837.

(10) Lohninger, H.; Ofner, J. Multisensor Hyperspectral Imaging as a Versatile Tool for Image-Based Chemical Structure Determination. *Spectrosc. Eur.* **2014**, *26* (5), 6–10.

(11) Alexandrov, T. PyimzML. https://github.com/alexandrovteam/pyimzML 2021.

(12) Ovchinnikova, K.; Stuart, L.; Rakhlin, A.; Nikolenko, S.; Alexandrov, T. ColocML: Machine Learning Quantifies Co-Localization between Mass Spectrometry Images. *Bioinformatics* **2020**, *36* (10), 3215–3224.

(13) Gardner, W.; Cutts, S. M.; Phillips, D. R.; Pigram, P. J. Understanding Mass Spectrometry Images: Complexity to Clarity with Machine Learning. *Biopolymers.* **2021**, *112* (4), e23400.

(14) Lowekamp, B.; Marstal, K.; Blezek, D.; Chen, D.; Yaniv, Z.; King, B. SimpleElastix. *GitHub*. 2020.

(15) Abdelmoula, W. M.; Škrášková, K.; Balluff, B.; Carreira, R. J.; Tolner, E. A.; Lelieveldt, B. P. F.; van der Maaten, L.; Morreau, H.; van den Maagdenberg, A. M. J. M.; Heeren, R. M. A.; McDonnell, L. A.; Dijkstra, J. Automatic Generic Registration of Mass Spectrometry Imaging Data to Histology Using Nonlinear Stochastic Embedding. *Anal. Chem.* **2014**, *86* (18), 9204–9211.

(16) Abdelmoula, W. M.; Balluff, B.; Englert, S.; Dijkstra, J.; Reinders, M. J. T.; Walch, A.; McDonnell, L. A.; Lelieveldt, B. P. F. Data-Driven Identification of Prognostic Tumor Subpopulations Using Spatially Mapped t-SNE of Mass Spectrometry Imaging Data. *Proc. Natl. Acad. Sci. U. S. A.* **2016**, *113* (43), 12244–12249.

(17) Rohlfing, T. Image Similarity and Tissue Overlaps as Surrogates for Image Registration Accuracy: Widely Used but Unreliable. *IEEE Trans. Med. Imaging.* **2012**, *31* (2), 153–163.

(18) Jones, M. A.; Cho, S. H.; Patterson, N. H.; Van de Plas, R.; Spraggins, J. M.; Boothby, M. R.; Caprioli, R. M. Discovering New Lipidomic Features Using Cell Type Specific Fluorophore Expression to Provide Spatial and Biological Specificity in a Multimodal Workflow with MALDI Imaging Mass Spectrometry. *Anal. Chem.* **2020**, *92* (10), 7079–7086.

(19) Brust, M.; Walker, M.; Bethell, D.; Schiffrin, D. J.; Whyman, R. Synthesis of Thiol-Derivatised Gold Nanoparticles in a Two-Phase Liquid–Liquid System. *J. Chem. Soc., Chem. Commun.* **1994**, *7* (7), 801–802.

(20) Chompoosor, A.; Han, G.; Rotello, V. M. Charge Dependence of Ligand Release and Monolayer Stability of Gold Nanoparticles by Biogenic Thiols. *Bioconjug. Chem.* **2008**, *19* (7), 1342–1345.

(21) Kim, S. T.; Saha, K.; Kim, C.; Rotello, V. M. The Role of Surface Functionality in Determining Nanoparticle Cytotoxicity. *Acc. Chem. Res.* **2013**, *46* (3), 681–691.

(22) Jiang, Y.; Huo, S.; Mizuhara, T.; Das, R.; Lee, Y. W.; Hou, S.; Moyano, D. F.; Duncan, B.; Liang, X. J.; Rotello, V. M. The Interplay of Size and Surface Functionality on the Cellular Uptake of Sub-10 Nm Gold Nanoparticles. *ACS Nano* **2015**, *9* (10), 9986–9993.

(23) Yan, B.; Zhu, Z.-J.; Miranda, O. R.; Chompoosor, A.; Rotello, V. M.; Vachet, R. W. Laser Desorption/Ionization Mass Spectrometry Analysis of Monolayer-Protected Gold Nanoparticles. *Anal. Bioanal. Chem.* **2010**, *396* (3), 1025–1035.

(24) Jiang, Y.; Tang, R.; Duncan, B.; Jiang, Z.; Yan, B.; Mout, R.; Rotello, V. M. Direct Cytosolic Delivery of SiRNA Using Nanoparticle-Stabilized Nanocapsules. *Angew. Chemie Int. Ed.* **2014**, *54* (2), 506–510.

(25) Hardie, J.; Jiang, Y.; Tetrault, E. R.; Ghazi, P. C.; Tonga, G. Y.; Farkas, M. E.; Rotello, V. M. Simultaneous Cytosolic Delivery of a Chemotherapeutic and SiRNA Using Nanoparticle-Stabilized Nanocapsules. *Nanotechnology.* **2016**, *27* (37), 374001.

(26) Jiang, Y.; Hardie, J.; Liu, Y.; Ray, M.; Luo, X.; Das, R.; Landis, R. F.; Farkas, M. E.; Rotello, V. M. Nanocapsule-Mediated Cytosolic SiRNA Delivery for Anti-Inflammatory Treatment. *J. Control. Release.* **2018**, *283*, 235–240.

(27) Chaurand, P.; Cornett, D. S.; Angel, P. M.; Caprioli, R. M. From Whole-Body Sections down to Cellular Level, Multiscale Imaging of Phospholipids by MALDI Mass Spectrometry. *Mol. Cell. Proteomics.* **2011**, *10* (2), S1–S11.

(28) Elci, S. G.; Yan, B.; Kim, S. T.; Saha, K.; Jiang, Y.; Klemmer, G. A.; Moyano, D. F.; Tonga, G. Y.; Rotello, V. M.; Vachet, R. W. Quantitative Imaging of 2 Nm Monolayer-Protected Gold Nanoparticle Distributions in Tissues Using Laser Ablation Inductively-Coupled Plasma Mass Spectrometry (LA-ICP-MS). *Analyst* **2016**, *141* (8), 2418–2425.

(29) Elci, S. G.; Jiang, Y.; Yan, B.; Kim, S. T.; Saha, K.; Moyano, D. F.; Yesilbag Tonga, G.; Jackson, L. C.; Rotello, V. M.; Vachet, R. W. Surface Charge Controls the Suborgan Biodistributions of Gold Nanoparticles. *ACS Nano* **2016**, *10* (5), 5536–5542.

(30) Elci, S. G.; Tonga, G. Y.; Yan, B.; Kim, S. T.; Kim, C. S.; Jiang, Y.; Saha, K.; Moyano, D. F.; Marsico, A. L. M.; Rotello, V. M.; Vachet, R. W. Dual-Mode Mass Spectrometric Imaging for Determination of in Vivo Stability of Nanoparticle Monolayers. *ACS Nano.* **2017**, *11* (7), 7424–7430.

(31) Fay, D.; Palmer, A. D.; Vitaly, K.; Alexandrov, T. pyimzML. https://github.com/alexandrovteam/pyimzML (accessed 2020 -01 -11).

(32) Castellanos-García, L. J.; Gokhan Elci, S.; Vachet, R. W. Reconstruction, Analysis, and Segmentation of LA-ICP-MS Imaging Data Using Python for the Identification of Sub-Organ Regions in Tissues. *Analyst* **2020**, *145* (10), 3705–3712.

(33) Pedregosa, F.; Varoquaux, G.; Gramfort, A.; Michael, V.; Thirion, B.; Grisel, O.; Blondel, M.; Prettenhofer, P.; Weiss, R.; Dubourg, V.; Vanderplas, J.; Passos, A.; Cournapeau, D.; Brucher, M.; Perrot, M.; Duchesnay, E. Scikit-Learn: Machine Learning in Python. *J. Mach. Learn. Res.* **2011**, *12*, 2825–2830.

(34) Schindelin, J.; Arganda-Carreras, I.; Frise, E.; Kaynig, V.; Longair, M.; Pietzsch, T.; Preibisch, S.; Rueden, C.; Saalfeld, S.; Schmid, B.; Tinevez, J. Y.; White, D. J.; Hartenstein, V.; Eliceiri, K.; Tomancak, P.; Cardona, A. Fiji: An Open-Source Platform for Biological-Image Analysis. *Nat. Methods.* **2012**, *9* (7), 676–682.

CHAPTER 4

LA-ICP-MS AND MALDI-MS IMAGING FOR CORRELATING NANOMATERIAL DISTRIBUTIONS AND THEIR BIOCHEMICAL EFFECTS

Some of the analysis of this chapter is published in two papers: (1) Sikora, K. N.; Hardie, J. M.; Castellanos-García, L. J.; Liu, Y.; Reinhardt, B. M.; Farkas, M. E.; Rotello, V. M.; Vachet, R. W. *Anal Chem*. **2020**, 92, 2011-2018. And (2) Sikora, K. N., Castellanos-García, L. J., Hardie, J., Liu, Y., Farkas, M., Rotello, V., & Vachet, R. Nanodelivery Vehicles Induce Remote Biochemical Changes in vivo. *Nanoscale.* **2021**. In press.

4.1 Introduction

Nanoparticle-stabilized capsules (NPSC) (Figure 4.1) have been successfully used for the delivery of siRNA. NPSCs loaded with siRNA that is specific for tumor necrosis factor alpha (TNF-α) have demonstrated the ability to knockdown the production of TNF-α in cell culture and *in-vivo*.[1–3] These particular NPSCs have potential as therapeutics as they can regulate the expression of this important protein To investigate the intracellular trafficking of the NPSC, several methods based on fluorescence imaging have been used to determine the mechanism of NPSC uptake.[4] However, fluorescent methods generally provide information of the NPSC distribution, but do not provide information about their biochemical effects.

Mass spectrometry imaging (MSI) is an analytical technique that enables the untargeted spatial analysis of hundreds of analytes in tissue sections.[5,6] Despite the multiplexing capabilities of MSI, not all analytes are detected in a single MSI experiment, and complementary MSI techniques are often required for the thorough analysis of the variety of elemental and molecular species in tissues.[7] Among the MSI techniques, MALDI-MSI has been extensively used for the

spatial analysis of metabolites,[8,9] lipids,[10,11] peptides,[12,13] and proteins,[14,15] and thus it should be capable of revealing any biochemical changes caused by NPSCs. On the other hand, LA-ICP-MS is a powerful tool for the analysis of metal distributions,[16] and this method would be an excellent means of mapping the distributions of NPSCs that contain gold. Leveraging the information from the two imaging techniques to more fully understand the site-specific biochemical changes caused by the presence of the NPSCs requires the two modalities to be properly combined.

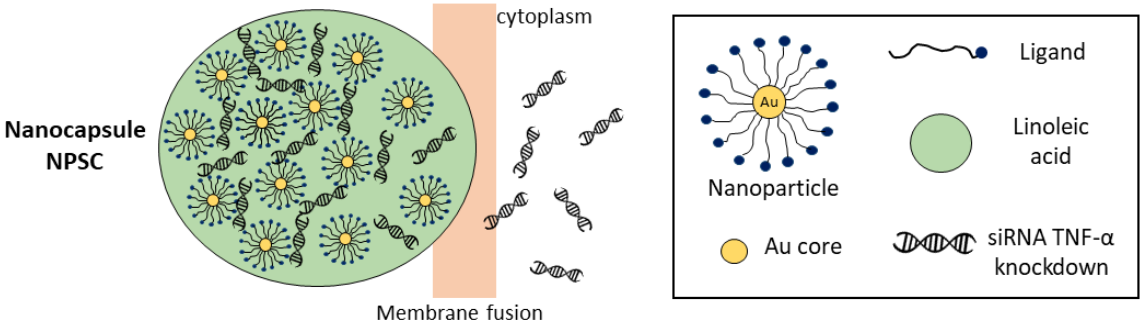

Figure 4.1. Nanoparticle stabilize capsules (NPSC or nanocapsule) structure and its components (nanoparticle, SiRNA, linoleic acid). The NPSC delivers siRNA to the cells through a membrane fusion mechanism.

Several approaches have been developed to combine MALDI-MS and LA-ICP-MS images, most of them named dual[17] or dual-mode[18] mass spectrometry imaging. Although these methods are very informative, the images from the two different modalities (LA-ICP-MS and MALDI-MS) are typically overlaid and not compared quantitatively on a pixel-by-pixel basis, making the analysis of the images heavily reliant on the observer. Recently developed image registration approaches allow the combination of images from different sources into the same coordinates,[19–21] opening an avenue for multimodal statistical analyses in complex datasets. Registration techniques have been applied to mass spectrometry images to register methods such as MALDI-MSI and fluorescence microscopy,[22] MALDI-MSI and confocal microscopy[23], microliquid extraction single probe MSI with microscopy imaging,[24] and two different MALDI-

MSI images.[25] Despite, this work, there have been no examples of registering MALDI-MS and LA-ICP-MS images.

Here, we describe the application of a computational workflow for the registration of LA-ICP-MS and MALDI-MS images to improve the analysis of NPSC drug delivery vehicles and their biochemical effects. Once the images are registered in the same coordinates, we investigate the use of two approaches for quantitative statistical analysis: multimodal calculations of Pearson's correlation coefficients and LA-ICP-MSI assisted segmentation of MALDI-MSI datasets. The benefit of this approach is twofold. First, the use of correlation coefficients provides a means to calculate the co-localization of two analytes. Correlation coefficients are typically used in the exploration of MALDI-MS images of the same tissue;[26] however, we report here a novel approach to perform this calculation among images obtained from different modalities (MALDI-MSI and LA-ICP-MSI) and tissue sections in registered datasets. Second, we leverage the information of the registered MALDI-MSI and LA-ICP-MSI datasets to improve segmentation of MALDI-MS images. Although segmentation algorithms for MALDI-MS imaging analysis are well developed,[27–29] they highly depend on the data quality, making the segmentation process challenging for noisy datasets.[29] LA-ICP-MSI usually produces images of higher quality than MALDI-MSI, primarily because the tissue section is completely ablated during the imaging process. We present a method to improve segmentation in MALDI-MS images using the segmentation obtained from LA-ICP-MS.

To summarize, we have applied a computational workflow previously developed (see Chapter 3) to quantify the correlation between the nanomaterial vehicle and lipid biochemical changes, providing a deeper insight into how nanomaterial delivery agents influence lipid biochemistry in tissues. Additionally, registration allows us to leverage the higher quality images

associated with LA-ICP-MSI to better segment MALDI-MSI images and identify lipids that are correlated with different suborgan regions of the spleen, an organ in which the NPSCs accumulate.

4.2 Results and discussion

The results contained in this chapter uses the computational methods and datasets for image registration developed in chapter 3. Advances in the implementation and application of statistical functions for calculating correlation coefficients are described below, as well as the use of segmentation-based statistical analyses.

4.2.1 Statistical correlations to study analyte co-localization in spleen tissues

Spleen tissues from NPSC-treated and control mice were registered using the computational workflow described in chapter 3 (Figure 4.2). The overlay of the two registered images shows that there is a good image overlap of the red and white pulp features in the spleen. Furthermore, the two images share coordinates, enabling pixel-by-pixel comparisons between the two modalities. Once the images are registered, we can then compare how the signals in one image modality (LA-ICP-MS) correlate with the signals in the other modality (MALDI-MS), which allows us to understand better the underlying biochemistry of the tissues. Using Pearson's correlations, which are one of the more accurate methods for quantifying the degree of co-localization of two images,[26] we can compare the extent to which metal distributions that are detected in LA-ICP-MS images correlate to specific biomolecule distributions that are detected in MALDI-MS images.

As examples, we correlate Fe signals in LA-ICP-MS images of the spleen with a range of lipids that are observed in MALDI-MS images of this same organ (Figure 4.3). For the spleen, we find that the signal levels for two classes of lipids, including ceramides (Cer) and some phosphatidylethanolamines (PE), correlate with the Fe signals (Figure 4.3a and 4.3b). Since high Fe signals in LA-ICP-MS indicate the location of red pulp regions in the spleen, the lipids that positively correlate with the Fe are predominantly located in the red pulp. In contrast, the lipids that anticorrelate with the Fe, including lysophosphatidylcholines (LPC), phosphatidylcholines (PC), sphingomyelins (SM), and carnitines (CAR) (Figure 4.3c and 4.3d), are predominantly located in the white pulp, which has low Fe levels. In fact, we have identified several lipids that can act as biomarkers of the red and white pulp regions of the spleen.

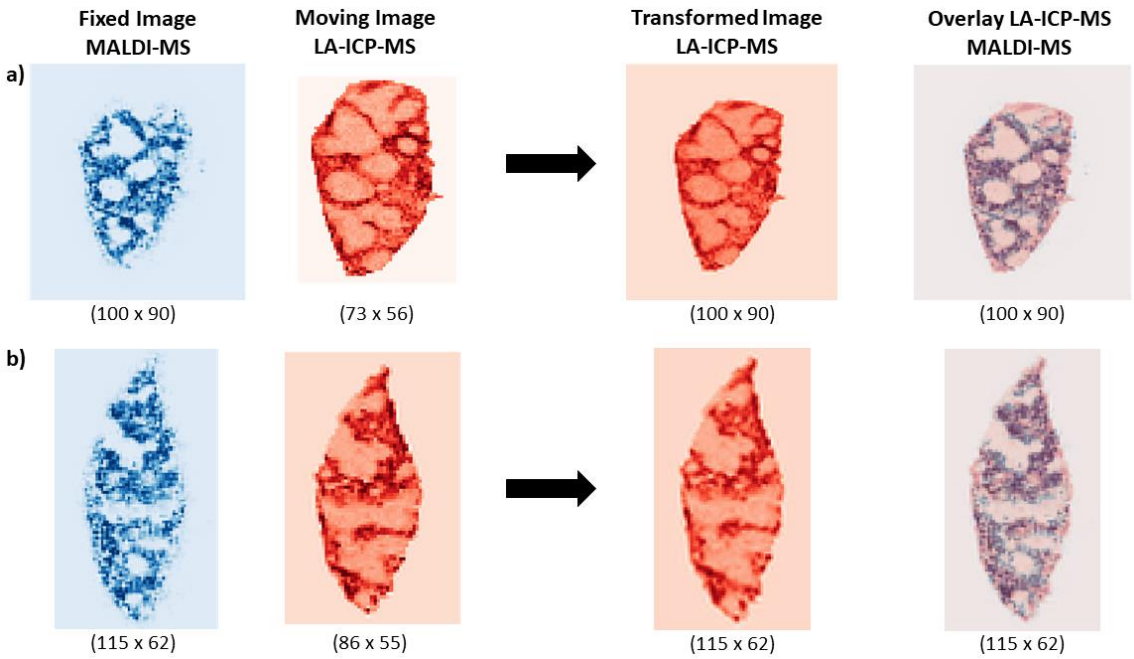

Figure 4.2. Registration of MALDI-MS and LA-ICP-MS spleen adjacent images from: a) NPSC tissue and b) control tissue. Image dimensions are shown below the images.

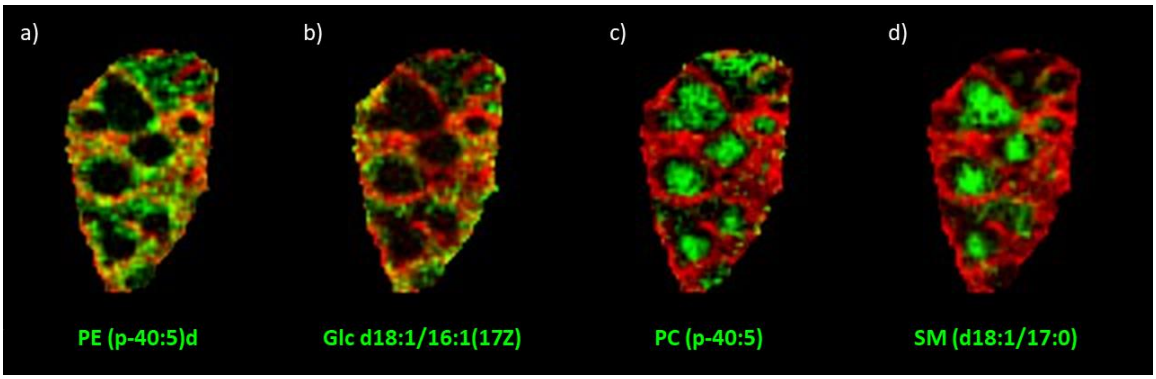

Figure 4.3. Overlay of registered images from the with Fe images detected by LA-ICP-MS shown in red and different lipids detected by MALDI-MS in green. The lipids include a) PE (p-40:5)d and b) Glc d18:1/16:1(17Z) that localize in the red pulp, and lipids c) PC (p-40:5) and d) SM (d18:1/17:0) that localize in the white pulp.

To correlate the Fe signal with the Au signal of NPSC injected tissues, we overlay the Fe and Au images (Figure 4.4). Visual inspection of the overlaid images shows high co-localization of the signals. When the Pearson's correlation coefficient for Au and Fe images is calculated, we obtain a value of 0.69, which quantitatively indicates high co-localization of Au and Fe. Additionally, using the segmentation approach RecSegImage-LA[30] described in chapter 2, we determine that the NPSC tissue shows 80% accumulation of the Au NPSC in the red pulp,[17] demonstrating that most of the NPSC localize in the red pulp of the spleen.

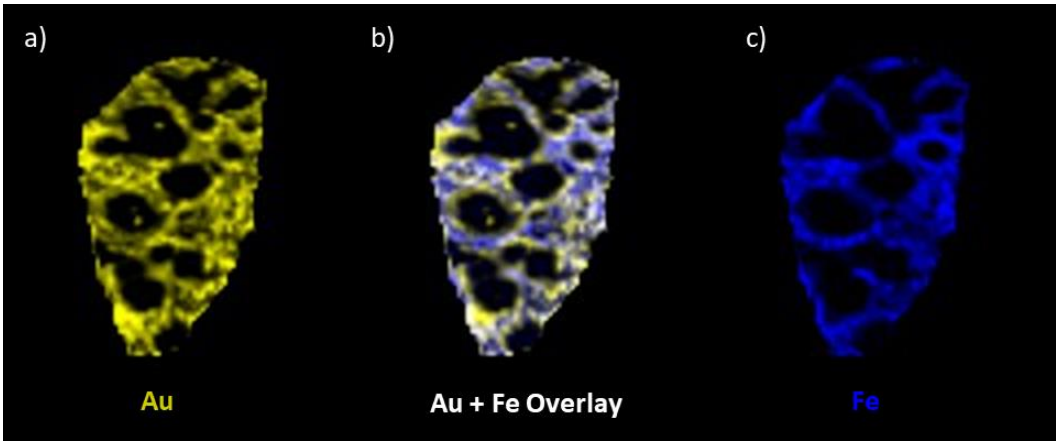

Figure 4.4. Overlay of Au and Fe signals from a spleen tissue from a NPSC-treated mouse. The Au image shows nanomaterial accumulation in the red pulp of the spleen, and the Fe image distinguishes the areas between red and white pulp using blood as marker of the suborgan regions.

The value of these correlations is more informative when we analyze the tissue sections from mice injected with NPSCs that deliver TNF-α-specific siRNA. These NPSCs have shown the ability to knockdown the production of TNF-α in cell culture and in animals,[1–3] and this knockdown causes changes in the levels of various lipids.[31] LA-ICP-MS imaging is capable of indicating the distributions of the Au from the nanomaterials, while MALDI-MS images can indicate how biomolecules change in response to knockdown of TNF-α.

Figure 4.5 indicates the distribution of the Au in a spleen from a NPSC-treated mouse as detected by LA-ICP-MS together with the lipid signals of 4 different lipid species as detected by MALDI-MS. These images indicate the localization of the lipids in the red or white pulp of the spleen. The overlaid images of carrier (Au) and biochemical effect (lipids) can only be rendered properly if the two images share coordinates, stressing the value of the registration approaches developed here. The rendered images in Figure 4.5 provide a quick qualitative method to compare the distribution of the lipids in the suborgan regions of the spleen. However, a qualitative approach alone is too reliant on the observer and is not informative for lipids that have signals in both suborgan regions,.

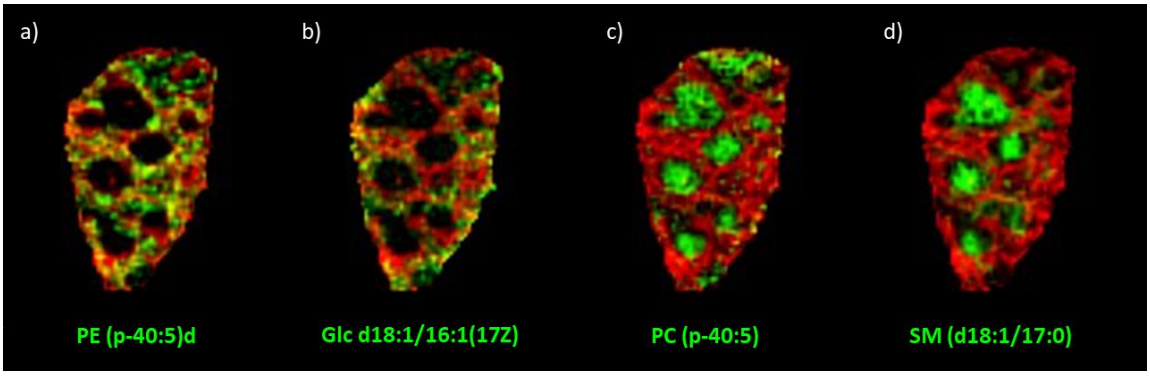

Figure 4.5. Overlay of Au images detected by LA-ICP-MSI (red) with different lipids detected by MALDI-MSI (green) after registration of the LA-ICP-MS and MALDI-MS images. The included lipids are a) PE (p-40:5)d and b) Glc d18:1/16:1(17Z), which localize in the red pulp, and c) PC (p-40:5) and d) SM (d18:1/17:0), which localize in the white pulp.

To quantitatively determine the co-localization of the biochemical changes (MALDI-MSI) in comparison to the vehicle distribution (LA-ICP-MSI), we calculated the correlation map for the NPSC tissue (Figure 4.6) and control tissue (Figure 4.7). The map contains the Pearson's correlation coefficients between each of the lipids detected in the MALDI-MS dataset to the Au and biometals (Fe and Zn) detected in LA-ICP-MS. Additionally, we can also calculate the correlations between images in the same modalities. For example, we can calculate the correlation

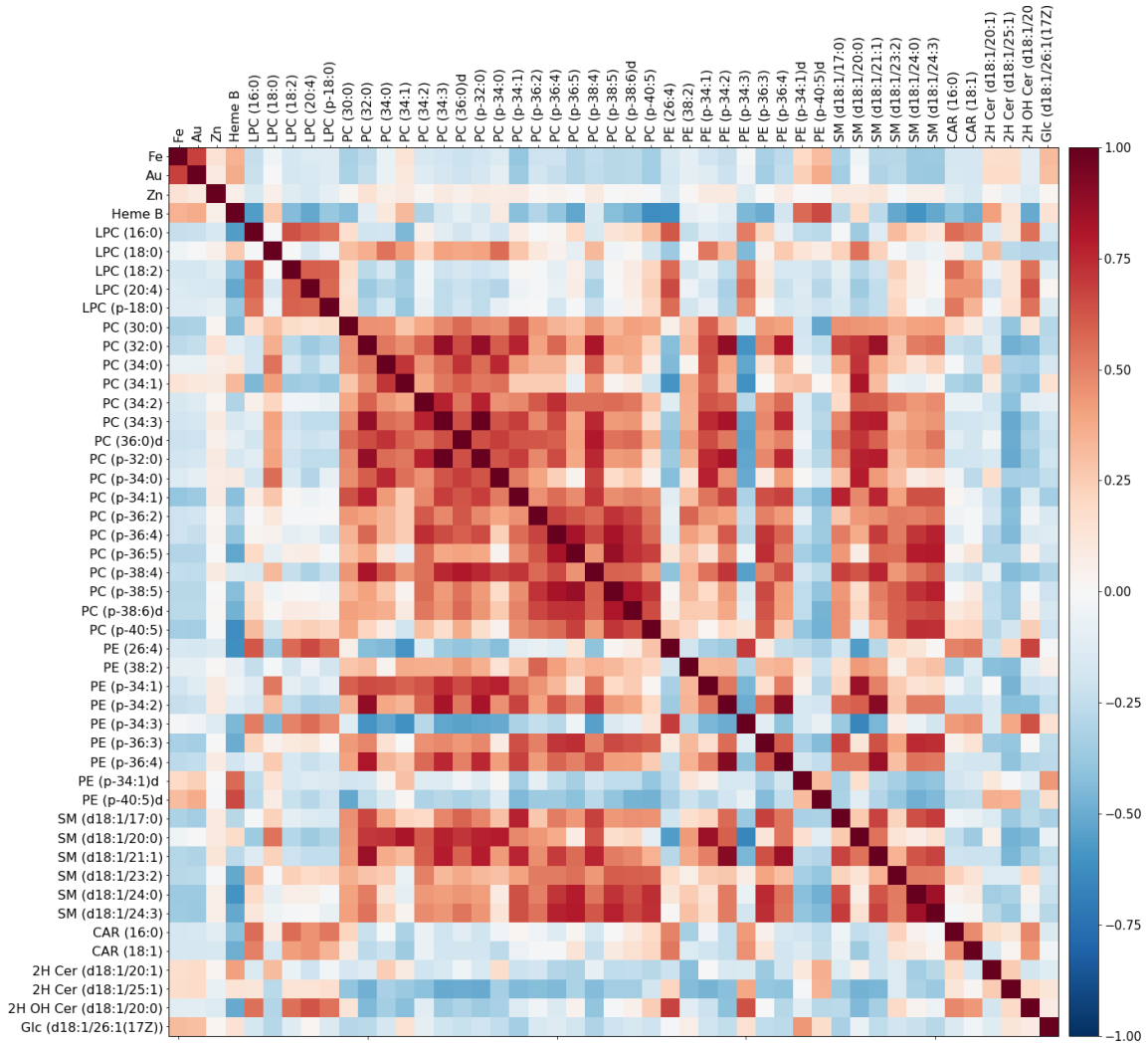

Figure 4.6. Correlation map plot for a spleen from a NPSC-injected mouse, showing correlations among the LA-ICP-MS analytes (Au, Fe, Zn) with the lipids detected by MALDI-MS.

coefficient of Au vs. Fe images, both detected in LA-ICP-MS, and the correlation of PE (p-40:5)d with PC (p-40:5) images, both detected in MALDI-MS. Each of the correlation values correspond to a value between +1 and -1. A positive correlation indicates that two chemical species are co-localized, with a value of +1 being perfect co-localization, while a negative value indicates that two chemical species tend not to co-localize, with a value of -1 being no co-localization.

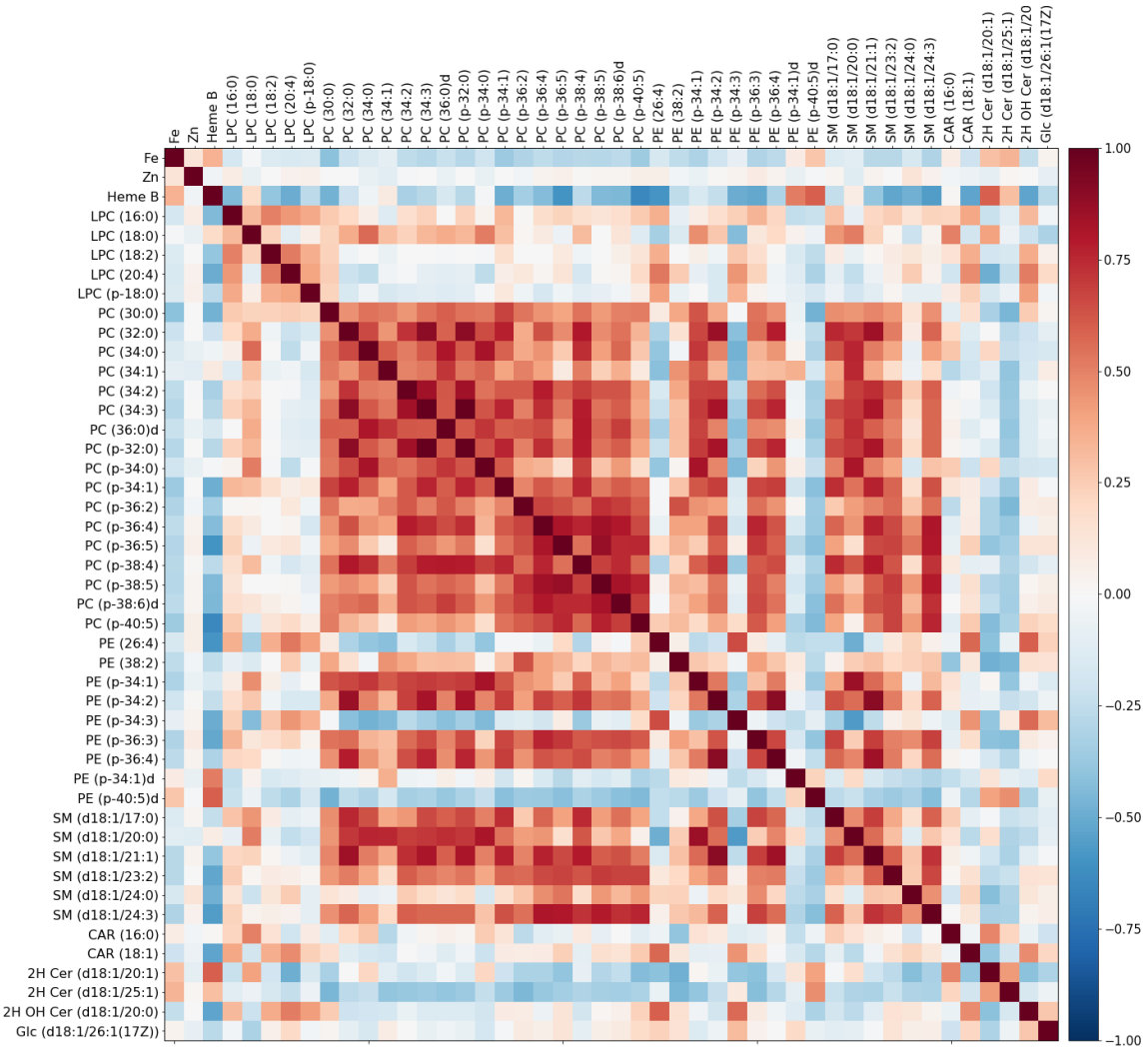

Figure 4.7. Correlation map plot for a spleen control mouse, showing correlations among the LA-ICP-MS analytes (Fe, Zn), with the lipids detected by MALDI-MS.

We extracted the correlations of the Fe and Au signals with the lipids for control and NPSC-treated mice (TNF-α) in spleen tissue sections, and we plot them in Figure 4.8. Several of the lipids exhibit a significant change in their Pearson's correlation values in spleens taken from NPSC-treated mice as compared to control mice (Figure 4.8a). For example, glucoceramide (Glc) d18:1/16:1(17Z) has a low correlation coefficient with Fe (i.e., 0.03) in the control tissue, which indicates the signal is located equally in the Fe-rich red pulp region and the Fe-poor white pulp region. After NPSC treatment, the Glc d18:1/16:1(17Z) correlation with Fe increases to 0.32, indicating higher localization of this lipid in the red pulp. Because the Au signal also highly correlates with this lipid (Figure 4.8b) and the Fe and Au signals have a high positive correlation value of 0.69. We conclude

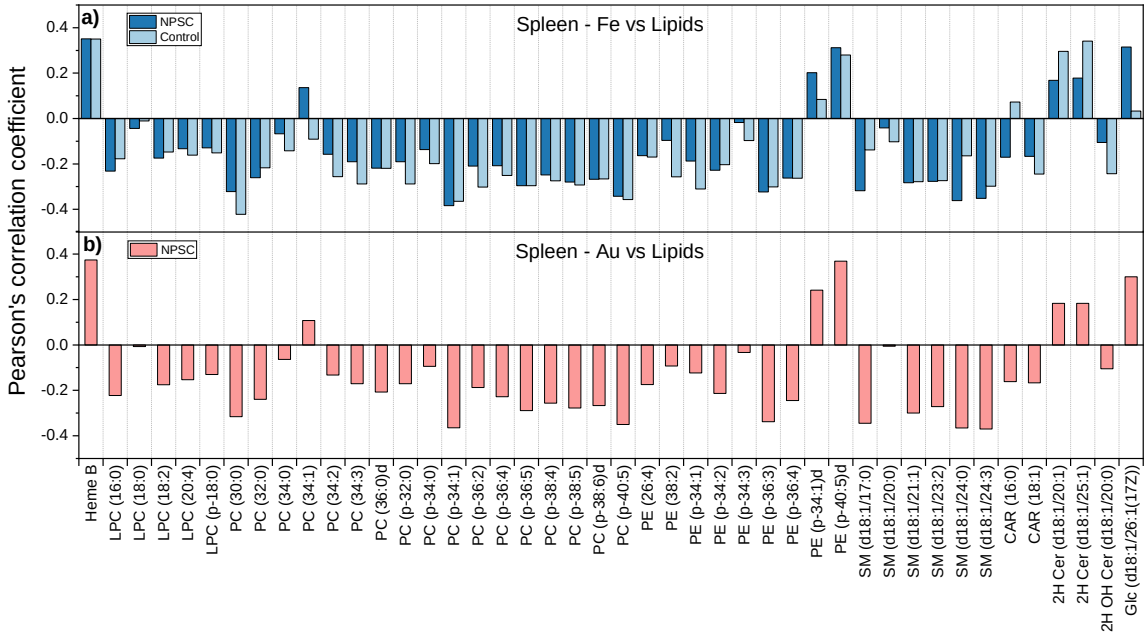

Figure 4.8. Pearson's correlation coefficients obtained after registering LA-ICP-MS and MALDI-MS images of spleen tissue sections from control and NPSC treated mice. a) Correlation coefficients for Fe and select lipids that are measured from control and NPSC-treated mice. b) Correlation coefficients for Au and select lipids that are measured from NPSC-treated mice. LPC = lysophosphatidylcholines; PC = phosphatidylcholines; PE = phosphatidylethanolamines; SM = sphingomyelins; CAR = carnitines; Cer = ceramides; Glc = glucosylceramides.

that the presence of the NPSC promotes changes in the Glc d18:1/16:1(17Z) level. Glucosylceramides are known markers of inflammation,[32] so it is possible that the presence of the NPSCs causes localized inflammation in the red pulp where they accumulate. PC (34:1) exhibits a similar behavior with its Pearson's value changing from -0.09 in the control to 0.14 in the NPSC-treated tissue. This lipid also positively correlates with Au, suggesting an NPSC-induced effect to the level of this lipid as well.

In contrast, many more lipids show the opposite trend, becoming more negatively correlated with Fe and Au. For example, CAR (16:0) and SM (d18:1/17:0) have correlation values that change from 0.07 and -0.14 to -0.17 and -0.32, respectively. These anti-correlated values suggest that the presence of the NPSCs is generating changes to the levels of these lipids in places where the Fe and Au concentrations are low. That means that these lipid changes are occurring primarily in the white pulp where Fe concentrations are low and where Au accumulation is minimal (Figure 4.4 and Figure 4.5). TNF-α knockdown therapies, like these NPSCs, typically target macrophages and lymphocytes, which are highly abundant in the white pulp of the spleen,[33] likely explaining why so many lipid changes occur in the white pulp. CAR (16:0), SM (d18:1/17:0), and several of the PC lipids are signaling lipids known to undergo changes in concentrations upon TNF-α suppression,[31] and the ability to correlate MALDI-MS and LA-ICP-MS images helps identify the specific sub-organ regions in which these changes are happening.

4.2.2 LA-ICP-MS assisted segmentation of MALDI-MS spleen images

The analysis of tissue regions upon MSI often involves the division of the image into segments so that the detected molecular features can be associated with different cell types and regions of the analyzed tissue. A commonly used methods for such image segmentation is k-means clustering, which is a statistical method that divides the image into segments that possess similar

spectral characteristics.[34] In MALDI-MS imaging, several approaches have been used to further improve segmentation, such as the implementation of more sophisticated spatially aware methods[27,28] and spatial shrunken centroids.[29] Although segmentation algorithms for MALDI-MS imaging analysis are well developed, they highly depend on the data quality, making the segmentation process challenging for noisy datasets.[29] LA-ICP-MSI usually produces less noisy images than MALDI-MSI primarily because the tissue section is completely ablated during the imaging process. Consequently, we sought to leverage this quality of LA-ICP-MSI to improve segmentation in MALDI-MS images. To do this, we first segment the LA-ICP-MS image and then apply the resulting segmentation masks to the registered MALDI-MS images to improve the segmentation of the MALDI-MS data.

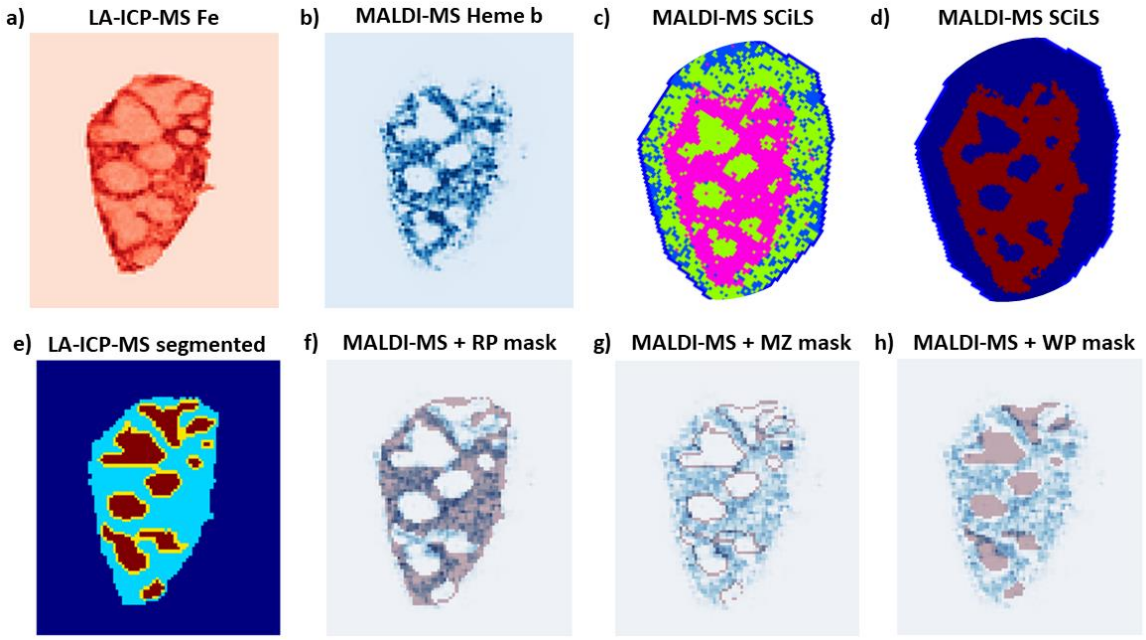

Figure 4.9. LA-ICP-MS assisted segmentation of MALDI-MS images. a) LA-ICP-MS Fe image, b) MALDI heme b image, c) MALDI segmentation in SCiLS using k-means with a cluster number of 4, d) MALDI segmentation in SciLS using bisecting k-means, e) LA-ICP-MS segmentation using RecSegImage-LA,[30] and MALDI heme b images overlaid with the f) red pulp (RP) mask, g) marginal zone (MZ) mask, and h) white pulp (WP) mask.

As an example of LA-ICP-MS-assisted segmentation of MALDI-MS images, imaging data from mouse spleen tissues were acquired by both techniques (Figures 4.9a and 4.9b). First, we segmented the MALDI-MS images using two methods available in SCiLS lab: (i) k-means[35] on the normalized dataset with a cluster number of 4 (Figure 4.9c) and (ii) bisecting k-means[36] (Figure 4.9d). Both segmentation approaches differentiate the red and white pulp regions of the spleen, but neither method identifies a segment associated with the marginal zone, which is the 50 – 100 µm-sized region where initial immune responses occur in this organ.[37] In contrast, segmentation of the Fe image from LA-ICP-MSI using RecSegImage-LA[30] does classify the marginal zone of the spleen as a separate segment in the image in addition to the red and white pulp regions (Figure 4.9e). The segmented areas from the LA-ICP-MS image can then be used as computational masks to classify the lipid signals from the MALDI-MS images that are most associated with each of the three different regions of the spleen (Figure 4.9f, 4.9g, and 4.9h).

The segmented areas in Figure 4.9f, 4.9g, and 4.9h are used as computational masks for extracting the signals of the lipids in each of the areas and performing a comparison of the data using statistical approaches in python. A t test was applied to calculate the probability of statistical significance between the extracted values in the red pulp vs. white pulp, red pulp vs. marginal zone and white pulp vs. marginal zone, as shown in Table 4.1. The obtained values show that out of the 43 analyzed lipids, 39 show statistically significant differences between the red and white pulp, as shown in yellow in Table 4.1. Additionally, the table also shows that there are more significant differences among the lipids in the red pulp and the marginal zone (34 lipids have significant differences) than the lipids in the white pulp and the marginal zone (22 lipids have significant differences).

Considering the data more closely, lipids such as glucoceramide and PC (34:1), we obtain the following average signal in the red pulp vs. white pulp for the two species: Glc (RP=44.2, WP=29.7) and PC (34:1) (RP=51.7, WP=44.7), demonstrating the higher localization of these lipids in the red pulp. CAR (16:0) has average signals of 37.0 and 44.3 in the red pulp and white pulp, respectively, and SM (d18:1/17:0) has values of 27.7 and 49.4 in the red and white pulp, respectively, demonstrating that these two lipids have higher average signals in the white pulp. The data for these lipids s is consistent with the localization of the lipids as determined by the Pearson's correlation coefficients (see Figure 4.8).

Table 4.1. Normalized signal intensities in each of the segmented regions (red pulp, white pulp, and marginal zone) of LA-ICP-MS and MALDI-MS signals. t test probabilities were calculated to obtain if there are statistically significant differences among red pulp and white pulp, red pulp and marginal zone and white pulp and marginal zone. Yes in green indicates significant differences between the compared areas, No in orange indicates no significant difference between the compared areas.

Ion identity	Red Pulp		White Pulp		Marginal Zone		t test probabilities (P)		
	Average	SD	Average	SD	Average	SD	RP vs WP	RP vs MZ	WP vs MZ
Au	60.5	19.1	19.2	6.5	34.3	12.3	Yes	Yes	Yes
Fe	71.9	14.8	44.6	3.2	50.1	7.0	Yes	Yes	Yes
Heme B	53.3	25.9	24.9	21.5	39.3	26.1	Yes	Yes	Yes
LPC (16:0)	52.8	11.2	60.6	13.5	57.1	13.2	Yes	Yes	Yes
LPC (18:0)	37.1	13.9	36.7	11.9	38.9	13.6	No	No	No
LPC (18:2)	72.0	6.6	75.0	6.8	74.1	6.6	Yes	Yes	No
LPC (20:4)	46.2	13.9	52.2	14.4	48.8	13.6	Yes	No	Yes
LPC (p-18:0)	43.9	14.4	50.3	15.9	47.8	16.3	Yes	Yes	No
PC (30:0)	44.8	8.9	54.8	11.9	49.9	10.4	Yes	Yes	Yes
PC (32:0)	49.0	20.6	63.9	23.7	61.5	25.5	Yes	Yes	No
PC (34:0)	46.3	14.1	47.6	13.7	48.5	12.8	No	No	No
PC (34:1)	51.7	16.7	44.7	13.4	49.5	15.4	Yes	No	Yes
PC (34:2)	59.2	15.9	62.8	15.6	66.6	17.9	Yes	Yes	No
PC (34:3)	50.6	14.2	56.0	15.0	58.0	17.9	Yes	Yes	No
PC (36:0)d	54.5	16.6	64.4	19.8	62.7	18.9	Yes	Yes	No
PC (p-32:0)	50.6	14.2	56.0	15.0	58.0	17.9	Yes	Yes	No
PC (p-34:0)	47.9	18.7	51.6	20.5	55.9	20.1	Yes	Yes	No
PC (p-34:1)	55.8	13.8	74.3	18.1	66.5	16.6	Yes	Yes	Yes
PC (p-36:2)	53.4	15.2	61.8	17.2	60.4	16.7	Yes	Yes	No

PC (p-36:4)	53.6	17.7	64.2	18.2	60.0	18.6	Yes	Yes	No
PC (p-36:5)	40.4	15.8	55.2	16.9	47.7	16.9	Yes	Yes	Yes
PC (p-38:4)	47.5	18.6	61.6	22.8	58.5	21.2	Yes	Yes	No
PC (p-38:5)	45.5	14.3	58.8	16.9	52.3	15.4	Yes	Yes	Yes
PC (p-38:6)d	52.0	15.0	65.0	18.0	59.6	16.8	Yes	Yes	Yes
PC (p-40:5)	48.8	14.1	68.2	18.7	58.2	16.6	Yes	Yes	Yes
PE (26:4)	38.2	13.0	45.4	14.9	40.6	14.0	Yes	No	Yes
PE (38:2)	44.0	20.3	48.6	22.5	50.5	22.8	Yes	Yes	No
PE (p-34:1)	47.4	15.8	51.7	17.2	55.2	19.0	Yes	Yes	No
PE (p-34:2)	44.2	20.6	55.9	22.6	54.8	25.1	Yes	Yes	No
PE (p-34:3)	51.5	12.0	52.9	12.1	50.7	12.0	No	No	No
PE (p-36:3)	52.8	12.0	66.7	16.3	58.9	13.9	Yes	Yes	Yes
PE (p-36:4)	56.1	16.2	67.4	17.3	64.7	19.4	Yes	Yes	No
PE (p-34:1)d	45.2	21.6	30.6	17.8	40.5	21.4	Yes	Yes	Yes
PE (p-40:5)d	58.1	18.1	39.5	15.2	48.0	18.9	Yes	Yes	Yes
SM (d18:1/17:0)	27.7	13.0	49.4	29.1	34.4	18.1	Yes	Yes	Yes
SM (d18:1/20:0)	56.5	18.3	54.4	18.4	61.8	20.3	No	Yes	Yes
SM (d18:1/21:1)	49.6	17.5	65.2	20.8	59.5	21.3	Yes	Yes	Yes
SM (d18:1/23:2)	58.9	13.9	69.7	15.0	67.1	16.3	Yes	Yes	No
SM (d18:1/24:0)	52.8	14.4	72.6	18.1	61.7	16.1	Yes	Yes	Yes
SM (d18:1/24:3)	44.9	13.9	66.1	21.8	53.6	16.9	Yes	Yes	Yes
CAR (16:0)	37.0	17.1	44.3	17.2	38.5	15.6	Yes	No	Yes
CAR (18:1)	21.6	4.8	24.0	3.6	22.4	4.2	Yes	No	Yes
2H Cer (d18:1/20:1)	42.1	20.4	33.6	9.6	36.2	14.3	Yes	Yes	No
2H Cer (d18:1/25:1)	57.6	16.0	48.6	14.8	52.3	15.8	Yes	Yes	Yes
2H OH Cer (d18:1/20:0)	46.0	13.7	50.4	14.7	48.2	15.1	Yes	No	No
Glc(d18:1/26:1(17Z))	44.2	19.6	29.7	10.7	36.4	14.9	Yes	Yes	Yes

4.3 Conclusions

We had used a custom computational workflow to register LA-ICP-MS and MALDI-MS images to generate a unified dataset and perform quantitative comparisons of NPSC-treated and

control spleen tissues. Registration of these images allows us to quantitatively compare the chemical information from both image modalities using statistical functions in Python, such as the calculation of Pearson's correlation coefficients. By understanding changes in localization patterns of the lipids in the NPSC-treated tissues vs. control tissues, we obtain deeper insight into how NPSCs influence lipid biochemistry in tissues. Additionally, the registration also allows us to leverage the higher quality images associated with LA-ICP-MS to better segment MALDI-MS images, so that we can identify lipids that are most associated with the three different regions of the spleen and identify statistically significant changes. The development of statistical methods in Python for these compelling datasets (46 images, 414,000 data points), allows the automatic calculation of 1,058 correlation coefficients and 92 probability values for each image (NPSC and control). We believe that the automation of the tissue image data analysis workflows benefits researchers in need of methods to interrogate large datasets. We envision that Pearson's correlations and segmentation t tests are just the initial examples of the statistical possibilities than can be achieved in these multimodal datasets. We expect that in the future, other statistical models, already present as libraries in Python, can be used to advance the interrogation of multimodal datasets and improve our understanding of drug delivery systems as NPSC.

4.4 Materials and methods

4.4.1 Nanomaterial synthesis:

Nanoparticle (NP) synthesis was performed using the Brust-Schiffrin reaction,[38] followed by functionalization of the Au NP core with different ligands, as described in previous work.[39–42] Similarly, nanoparticle stabilized capsules (NPSC) were synthesized by mixing arginine nanoparticles with linoleic acid, followed by its functionalization with siRNA that causes knockdown of tumor necrosis factor α (TNFα), as described in detail in previous reports.[1–3]

4.4.2 Animal experiments and tissue sectioning:

Balb/c mice were tail-vein injected with the nanoparticles (NP) or nanoparticle stabilized capsules (NPSC) and euthanized after 24 and 48 hours, respectively. Mice were sacrificed by carbon dioxide inhalation and cervical dislocation. All animal experiments were approved by the University of Massachusetts Amherst Institutional Animal Care and Use Committee (IACUC), which is guided by the U.S. Animal Welfare Act and U.S. Public Health Service Policy. Tissues were flash frozen and kept at -80 °C, until slicing for imaging. Frozen tissues were sliced using a LEICA CMM1850 cryostat. Adjacent tissue slices of 12 μm thickness were thaw-mounted on indium tin oxide (ITO)-coated glass and glass slides, for MALDI-MSI and LA-ICP-MSI experiments, respectively.

4.4.3 MALDI-MSI:

MALDI-MSI experiments were performed using 2,5-dihydroxybenzoic acid (2,5-DHB) as a matrix. Spraying was performed using a Bruker ImagePrep device to spray a 25 mg/mL matrix solution in 1:1 methanol:water on the sliced tissue. Data acquisition was performed on a Bruker UltrafleXetreme MALDI TOF/TOF at 50 μm resolution over an *m/z* range of 200 to 2000. MS/MS experiments to confirm analyte identities were performed in a collision-induced dissociation (CID) LIFT cell.

4.4.4 LA-ICP-MSI:

LA-ICP-MS images of ^{197}Au, ^{57}Fe, and ^{66}Zn were acquired on a CETAC LSX-213 G2 laser ablation system coupled with a Perkin Elmer NexION 300x ICP-MS instrument. The following laser parameters were used: 50 μm spot size, 20 μm/s scan rate, 3.65 J laser energy, 10 Hz laser frequency, and a 10 s shutter delay. The He carrier gas from laser ablation system was set to 0.6

L/min. The described parameters were used in previous contributions for the analysis of nanomaterials in tissue sections.[18,43,44]

4.4.5 Image preprocessing:

MALDI-MS images were normalized and exported as imzML files using FlexImaging (Bruker, Daltonics). The imzML files were imported to Python using the pyimzML parser, developed by Alexandrov and co-workers.[45] Peak picking was performed using SCiLS Lab 2015b, and the list of selected ions and mass tolerances were imported to Python as a text file. Images of the selected ions were rendered with the pyimzML parser using the text file ion list. LA-ICP-MS images were reconstructed, analyzed, and segmented using a custom Python script RecSegImage-LA, which was described recently and is freely available at GitHub (https://github.com/Vachet-Lab/RecSegImage-LA).[30] Hotspot removal was performed on MALDI-MS and LA-ICP-MS images by selecting the intensities in the >0.99 quantile and replacing them with the 0.99 quantile value.[26]

4.4.6 Image registration:

Image registration was performed using the SimpleElastix[46] Python extension of the Elastix C++ library.[20] The MALDI-MSI image (t-SNE or heme channel) was set as the fixed image, while the LA-ICP-MSI image (Fe channel) was set as the moving image. Registration was performed using the default affine parameter map followed by the default no-linear parameter map in SimpleElastix with certain modifications as follows: 4,000 iterations for the affine parameter map, 8,000 iterations for the non-linear parameter map and 50 final grid spacing in physical units.

4.4.7 Statistical analysis of the registered images:

Correlation coefficients between signals in MALDI-MSI and LA-ICP-MSI data were calculated using the Pearson implementation in the Scipy library (pearsonsr)[47] on the vectorized, background subtracted MALDI-MS and LA-ICP-MS images. Implementation of the t test statistical analysis was performed by segmentation and vectorization of the segments, followed by the application of the stats (stats.ttest_ind) implementation in Scipy.

4.5 References

(1) Jiang, Y.; Tang, R.; Duncan, B.; Jiang, Z.; Yan, B.; Mout, R.; Rotello, V. M. Direct Cytosolic Delivery of SiRNA Using Nanoparticle-Stabilized Nanocapsules. *Angew. Chemie Int. Ed.* **2014**, *54* (2), 506–510.

(2) Hardie, J.; Jiang, Y.; Tetrault, E. R.; Ghazi, P. C.; Tonga, G. Y.; Farkas, M. E.; Rotello, V. M. Simultaneous Cytosolic Delivery of a Chemotherapeutic and SiRNA Using Nanoparticle-Stabilized Nanocapsules. *Nanotechnology.* **2016**, *27* (37), 374001.

(3) Jiang, Y.; Hardie, J.; Liu, Y.; Ray, M.; Luo, X.; Das, R.; Landis, R. F.; Farkas, M. E.; Rotello, V. M. Nanocapsule-Mediated Cytosolic SiRNA Delivery for Anti-Inflammatory Treatment. *J. Control. Release.* **2018**, *283*, 235–240.

(4) Wang, Y.; Huang, L. A Window onto SiRNA Delivery. *Nat. Biotechnol.* **2013**, *31* (7), 611–612.

(5) Buchberger, A. R.; DeLaney, K.; Johnson, J.; Li, L. Mass Spectrometry Imaging: A Review of Emerging Advancements and Future Insights. *Anal. Chem.* **2018**, *90* (1), 240–265.

(6) Heeren, R. M. A. Getting the Picture: The Coming of Age of Imaging MS. *Int. J. Mass Spectrom.* **2015**, *377* (1), 672–680.

(7) Neumann, E. K.; Djambazova, K. V.; Caprioli, R. M.; Spraggins, J. M. Multimodal Imaging Mass Spectrometry: Next Generation Molecular Mapping in Biology and Medicine. *J. Am. Soc. Mass Spectrom.* **2020**, *31* (12), 2401–2415.

(8) Ho, Y.-N.; Shu, L.-J.; Yang, Y.-L. Imaging Mass Spectrometry for Metabolites: Technical Progress, Multimodal Imaging, and Biological Interactions. *Wiley Interdiscip. Rev. Syst. Biol. Med.* **2017**, *9* (5), e1387.

(9) Kleinridders, A.; Ferris, H. A.; Reyzer, M. L.; Rath, M.; Soto, M.; Manier, M. L.; Spraggins, J.; Yang, Z.; Stanton, R. C.; Caprioli, R. M.; Kahn, C. R. Regional Differences in Brain Glucose Metabolism Determined by Imaging Mass Spectrometry. *Mol. Metab.* **2018**, *12*, 113–121.

(10) Ellis, S. R.; Paine, M. R. L.; Eijkel, G. B.; Pauling, J. K.; Husen, P.; Jervelund, M. W.; Hermansson, M.; Ejsing, C. S.; Heeren, R. M. A. Automated, Parallel Mass Spectrometry Imaging and Structural Identification of Lipids. *Nat. Methods.* **2018**, *15* (7), 515–518.

(11) Touboul, D.; Laprévote, O.; Brunelle, A. Micrometric Molecular Histology of Lipids by Mass Spectrometry Imaging. *Curr. Opin. Chem. Biol.* **2011**, *15* (5), 725–732.

(12) Huber, K.; Khamehgir-Silz, P.; Schramm, T.; Gorshkov, V.; Spengler, B.; Römpp, A. Approaching Cellular Resolution and Reliable Identification in Mass Spectrometry Imaging of Tryptic Peptides. *Anal. Bioanal. Chem.* **2018**, *410* (23), 5825–5837.

(13) Gemperline, E.; Keller, C.; Jayaraman, D.; Maeda, J.; Sussman, M. R.; Ané, J.-M.; Li, L. Examination of Endogenous Peptides in Medicago Truncatula Using Mass Spectrometry Imaging. *J. Proteome Res.* **2016**, *15* (12), 4403–4411.

(14) Ryan, D. J.; Spraggins, J. M.; Caprioli, R. M. Protein Identification Strategies in MALDI Imaging Mass Spectrometry: A Brief Review. *Curr. Opin. Chem. Biol.* **2019**, *48*, 64–72.

(15) Llombart, V.; Trejo, S. A.; Bronsoms, S.; Morancho, A.; Feifei, M.; Faura, J.; García-Berrocoso, T.; Simats, A.; Rosell, A.; Canals, F.; Hernández-Guillamón, M.; Montaner, J. Profiling and Identification of New Proteins Involved in Brain Ischemia Using MALDI-Imaging-Mass-Spectrometry. *J. Proteomics.* **2017**, *152*, 243–253.

(16) Pozebon, D.; Scheffler, G. L.; Dressler, V. L. Recent Applications of Laser Ablation Inductively Coupled Plasma Mass Spectrometry (LA-ICP-MS) for Biological Sample Analysis: A Follow-up Review. *J. Anal. At. Spectrom.* **2017**, *32* (5), 890–919.

(17) Sikora, K. N.; Hardie, J. M.; Castellanos-García, L. J.; Liu, Y.; Reinhardt, B. M.; Farkas, M. E.; Rotello, V. M.; Vachet, R. W. Dual Mass Spectrometric Tissue Imaging of Nanocarrier Distributions and Their Biochemical Effects. *Anal. Chem.* **2020**, *92* (2), 2011–2018.

(18) Elci, S. G.; Tonga, G. Y.; Yan, B.; Kim, S. T.; Kim, C. S.; Jiang, Y.; Saha, K.; Moyano, D. F.; Marsico, A. L. M.; Rotello, V. M.; Vachet, R. W. Dual-Mode Mass Spectrometric Imaging for Determination of in Vivo Stability of Nanoparticle Monolayers. *ACS Nano.* **2017**, *11* (7), 7424–7430.

(19) Mccormick, M.; Liu, X.; Jomier, J.; Marion, C.; Ibanez, L. ITK: Enabling Reproducible Research and Open Science. *Front. Neuroinform.* **2014**, *8* (FEB), 1–11.

(20) Klein, S.; Staring, M.; Murphy, K.; Viergever, M. A.; Pluim, J. P. W. Elastix: A Toolbox for Intensity-Based Medical Image Registration. *IEEE Trans. Med. Imaging.* **2010**, *29* (1), 196–205.

(21) Abdelmoula, W. M.; Škrášková, K.; Balluff, B.; Carreira, R. J.; Tolner, E. A.; Lelieveldt, B. P. F.; van der Maaten, L.; Morreau, H.; van den Maagdenberg, A. M. J. M.; Heeren, R. M. A.; McDonnell, L. A.; Dijkstra, J. Automatic Generic Registration of Mass Spectrometry Imaging Data to Histology Using Nonlinear Stochastic Embedding. *Anal. Chem.* **2014**, *86* (18), 9204–9211.

(22) Patterson, N. H.; Tuck, M.; Lewis, A.; Kaushansky, A.; Norris, J. L.; Van de Plas, R.; Caprioli, R. M. Next Generation Histology-Directed Imaging Mass Spectrometry Driven by Autofluorescence Microscopy. *Anal. Chem.* **2018**, *90* (21), 12404–12413.

(23) Nikitina, A.; Huang, D.; Li, L.; Peterman, N.; Cleavenger, S. E.; Fernández, F. M.; Kemp, M. L. A Co-Registration Pipeline for Multimodal MALDI and Confocal Imaging Analysis of Stem Cell Colonies. *J. Am. Soc. Mass Spectrom.* **2020**, *31* (4), 986–989.

(24) Tian, X.; Xie, B.; Zou, Z.; Jiao, Y.; Lin, L. E.; Chen, C. L.; Hsu, C. C.; Peng, J.; Yang, Z. Multimodal Imaging of Amyloid Plaques: Fusion of the Single-Probe Mass Spectrometry Image and Fluorescence Microscopy Image. *Anal. Chem.* **2019**, *91* (20), 12882–12889.

(25) Kaya, I.; Sämfors, S.; Levin, M.; Borén, J.; Fletcher, J. S. Multimodal MALDI Imaging Mass Spectrometry Reveals Spatially Correlated Lipid and Protein Changes in Mouse Heart with Acute Myocardial Infarction. *J. Am. Soc. Mass Spectrom.* **2020**, *31* (10), 2133–2142.

(26) Ovchinnikova, K.; Stuart, L.; Rakhlin, A.; Nikolenko, S.; Alexandrov, T. ColocML: Machine Learning Quantifies Co-Localization between Mass Spectrometry Images. *Bioinformatics* **2020**, *36* (10), 3215–3224.

(27) Alexandrov, T.; Kobarg, J. H. Efficient Spatial Segmentation of Large Imaging Mass Spectrometry Datasets with Spatially Aware Clustering. *Bioinformatics.* **2011**, *27* (13), i230–i238.

(28) Alexandrov, T.; Becker, M.; Deininger, S.-O.; Ernst, G.; Wehder, L.; Grasmair, M.; von Eggeling, F.; Thiele, H.; Maass, P. Spatial Segmentation of Imaging Mass Spectrometry Data with Edge-Preserving Image Denoising and Clustering. *J. Proteome Res.* **2010**, *9* (12), 6535–6546.

(29) Bemis, K. D.; Harry, A.; Eberlin, L. S.; Ferreira, C. R.; van de Ven, S. M.; Mallick, P.; Stolowitz, M.; Vitek, O. Probabilistic Segmentation of Mass Spectrometry (MS) Images Helps Select Important Ions and Characterize Confidence in the Resulting Segments. *Mol. Cell. Proteomics.* **2016**, *15* (5), 1761–1772.

(30) Castellanos-García, L. J.; Gokhan Elci, S.; Vachet, R. W. Reconstruction, Analysis, and Segmentation of LA-ICP-MS Imaging Data Using Python for the Identification of Sub-Organ Regions in Tissues. *Analyst* **2020**, *145* (10), 3705–3712.

(31) Wallace, M.; Morris, C.; O'Grada, C. M.; Ryan, M.; Dillon, E. T.; Coleman, E.; Gibney, E. R.; Gibney, M. J.; Roche, H. M.; Brennan, L. Relationship between the Lipidome, Inflammatory Markers and Insulin Resistance. *Mol. Biosyst.* **2014**, *10* (6), 1586–1595.

(32) Khovidhunkit, W.; Kim, M. S.; Memon, R. A.; Shigenaga, J. K.; Moser, A. H.; Feingold, K. R.; Grunfeld, C. Effects of Infection and Inflammation on Lipid and Lipoprotein Metabolism: Mechanisms and Consequences to the Host. *J. Lipid Res.* **2004**, *45* (7), 1169–1196.

(33) Parameswaran, N.; Patial, S. Tumor Necrosis Factor-α Signaling in Macrophages Narayanan. *Crit Rev Eukaryot Gene Expr.* **2010**, *20* (2), 87–103.

(34) Oros-Peusquens, A. M.; Matusch, A.; Becker, J. S.; Shah, N. J. Automatic Segmentation of Tissue Sections Using the Multielement Information Provided by LA-ICP-MS Imaging and k-Means Cluster Analysis. *Int. J. Mass Spectrom.* **2011**, *307*, 245–252.

(35) Jones, E. A.; Deininger, S. O.; Hogendoorn, P. C. W.; Deelder, A. M.; McDonnell, L. A. Imaging Mass Spectrometry Statistical Analysis. *J. Proteomics* **2012**, *75* (16), 4962–4989.

(36) Johnson, J.; Sharick, J. T.; Skala, M. C.; Li, L. Sample Preparation Strategies for High-Throughput Mass Spectrometry Imaging of Primary Tumor Organoids. *J. Mass Spectrom.* **2020**, *55* (4), e4452.

(37) Mebius, R. E.; Kraal, G. Structure and Function of the Spleen. *Nat. Rev. Immunol.* **2005**, *5* (8), 606–616.

(38) Brust, M.; Walker, M.; Bethell, D.; Schiffrin, D. J.; Whyman, R. Synthesis of Thiol-Derivatised Gold Nanoparticles in a Two-Phase Liquid–Liquid System. *J. Chem. Soc., Chem. Commun.* **1994**, *7* (7), 801–802.

(39) Jiang, Y.; Huo, S.; Mizuhara, T.; Das, R.; Lee, Y. W.; Hou, S.; Moyano, D. F.; Duncan, B.; Liang, X. J.; Rotello, V. M. The Interplay of Size and Surface Functionality on the Cellular Uptake of Sub-10 Nm Gold Nanoparticles. *ACS Nano* **2015**, *9* (10), 9986–9993.

(40) Chompoosor, A.; Han, G.; Rotello, V. M. Charge Dependence of Ligand Release and Monolayer Stability of Gold Nanoparticles by Biogenic Thiols. *Bioconjug. Chem.* **2008**, *19* (7), 1342–1345.

(41) Kim, S. T.; Saha, K.; Kim, C.; Rotello, V. M. The Role of Surface Functionality in Determining Nanoparticle Cytotoxicity. *Acc. Chem. Res.* **2013**, *46* (3), 681–691.

(42) Yan, B.; Zhu, Z.-J.; Miranda, O. R.; Chompoosor, A.; Rotello, V. M.; Vachet, R. W. Laser Desorption/Ionization Mass Spectrometry Analysis of Monolayer-Protected Gold Nanoparticles. *Anal. Bioanal. Chem.* **2010**, *396* (3), 1025–1035.

(43) Elci, S. G.; Jiang, Y.; Yan, B.; Kim, S. T.; Saha, K.; Moyano, D. F.; Yesilbag Tonga, G.; Jackson, L. C.; Rotello, V. M.; Vachet, R. W. Surface Charge Controls the Suborgan Biodistributions of Gold Nanoparticles. *ACS Nano* **2016**, *10* (5), 5536–5542.

(44) Elci, S. G.; Yan, B.; Kim, S. T.; Saha, K.; Jiang, Y.; Klemmer, G. A.; Moyano, D. F.; Tonga, G. Y.; Rotello, V. M.; Vachet, R. W. Quantitative Imaging of 2 Nm Monolayer-Protected Gold Nanoparticle Distributions in Tissues Using Laser Ablation Inductively-Coupled Plasma Mass Spectrometry (LA-ICP-MS). *Analyst* **2016**, *141* (8), 2418–2425.

(45) Fay, D.; Palmer, A. D.; Vitaly, K.; Alexandrov, T. pyimzML. https://github.com/alexandrovteam/pyimzML (accessed 2020 -01 -11).

(46) Lowekamp, B.; Marstal, K.; Blezek, D.; Chen, D.; Yaniv, Z.; King, B. SimpleElastix. *GitHub*. 2020.

(47) Virtanen, P.; Gommers, R.; Oliphant, T. E.; Haberland, M.; Reddy, T.; Cournapeau, D.; Burovski, E.; Peterson, P.; Weckesser, W.; Bright, J.; Walt, S. J. Van Der; Brett, M.; Wilson, J.; Millman, K. J.; Mayorov, N.; Nelson, A. R. J.; Jones, E.; Kern, R.; Larson, E.; Carey, C. J.; Polat, I.; Feng, Y.; Moore, E. W.; VanderPlas, J.; Laxalde, D.; Perktold, J.; Cimrman, R.; Henriksen, I.; Quintero, E. A.; Harris, C. R.; Archibald, A. M.; Ribeiro, A. H.; Pedregosa, F.; Mulbregt, P. van. SciPy 1.0: Fundamental Algorithms for Scientific Computing in Python. *Nat. Methods.* **2020**, *17* (3), 261–272.

CHAPTER 5

SUMMARY AND FUTURE WORK

5.1 Dissertation summary

In this dissertation, we developed computational method to advance the reconstruction, segmentation, and registration of MS data from MALDI-MS and LA-ICP-MS images. The computational and experimental methods introduced here helped us gain a deeper understanding of nanomaterials accumulation, distribution, and biochemical effects on tissue samples. First, we developed an open-source software in Python that automatically reconstructs, analyses, and segments images from LA-ICP-MSI. This approach allowed us to automatically segment ROIs from LA-ICP-MS images to extract information and automatically perform statistical calculations on the segmented areas, such as averages, standard deviation, etc. This software enabled us to automatically determine the difference in the distributions of Au NPs and Bismuth nanorods in spleen tissue, where we see accumulation in different suborgan regions. Before the software, we used to do manual reconstruction of the images, a process that took between 6 to 8 hours per tissue. Our new methodology reduces the processing time to less than 1 minute. Although the software works very well for LA-ICP-MS PerkinElmer data, it is not compatible with other vendor's software, due to the differences in the data structure. We believe that if needed, we can expand the functionality of our program to import data from other vendors. Additionally, the functions we currently have for data analysis can be expanded to calculate other metrics among ROIs, as t-tests, histogram analysis, among others.

After the successful reconstruction and segmentation of LA-ICP-MS data, we decided to conjugate the information obtained with MALDI-MS with LA-ICP-MS. To that purpose, in Chapter 2 we developed a computational workflow in Python to register LA-ICP-MS and MALDI-

MS images of adjacent tissue slices to generate a dataset in the same coordinates. The workflow showed high registration accuracy with errors below 50 µm, making it ideal for finding correlations among suborgan regions. The combination of image modalities provides deeper quantitative information from the tissue sample to gain understanding about the complex biochemical processes happening in the tissues.

We used the developed computational image registration workflow to register LA-ICP-MS and MALDI-MS images of adjacent tissue slices of tissue injected with nanoparticle stabilized capsules (NPSC). We were able to correlate images of the NPSC carriers (detected by LA-ICP-MS) and the biochemical effects of the NPSC functionalized with siRNA (detected by MALDI-MS). For quantifying correlations, we calculated the multimodal Pearson's correlation coefficient between the Au and each of the detected lipids to identify lipids that change localization after NPSC injection. Several lipids (e.g., Glc(d18:1/26:1(17Z)) and PC (34:1)) were identified to correlate with the presence of the NPSC in comparison to the control, showing that these lipids change in locations in which the NPSC is present. In contrast, other lipids (e.g., SM (d18:1/17:0) and CAR (16:0)) were anticorrelated with the presence of the NPSC, suggesting that the NPSC might promote lipid changes in regions proximal to its accumulation sites. Using image registration, we were able to get a deeper insight into how nanomaterial delivery agents influence lipid biochemistry in tissues.

The ability to track nanomaterials in tissues had showed us that some of the lipid changes occurs in suborgan regions in which the NPSC are found (red pulp), and others in regions proximal to where the NPSC are located (white pulp). Although the NPSC do not reach the white pulp, it generates biochemical changes to lipids in both suborgan areas. The obtained information of non-localized biochemical changes is valuable to understand that certain nanomaterials might generate responses in suborgan regions that are distant to its accumulation sites and opens a route to generate indirect means of therapy.

Additionally, since the LA-ICP-MSI and MALDI-MSI datasets are registered, we were able to perform segmentation in LA-ICP-MSI and apply the segmented masks to extract data from MALDI-MS images. Using this process, we performed t-tests over the segmented regions of the spleen for all lipids detected to determine the significant changes of the lipid in each of the regions. Using the automated workflow, we were able to calculate nearly 1,058 correlation coefficients and 92 probability values for each of the analyzed tissues. We expect that in the future, other statistical models, already available as Python libraries, can be used to advance the interrogation of multimodal datasets and improve our understanding of drug delivery systems such as NPSC. The computational methods described in this work are applicable to the study of more types of nanomaterials, other than the gold nanoparticles, nanocapsules and the bismuth nanorods described. We envision that other nanomaterials, such as nanozymes in which the detection of the nanoparticle core is performed by LA-ICP-MS and the detection of the catalyst structure can be performed using MALDI-MS could be analyzed using the described computational methods to evaluate nanozyme stability.

5.2 Future directions

In the following sections, potential new applications of LA-ICP-MSI and MALDI-MSI to the analysis of nanomaterials will be discussed.

5.2.1 Improving LA-ICP-MS image registration and image resolution

The multimodal analysis of tissues by LA-ICP-MS and MALDI-MS allowed us to understand better how nanomaterials distribute in tissue sections, and how to correlate spatial biochemical effects (in MALDI-MSI) with the distribution of the nanomaterial (in LA-ICP-MS).

Our method for registration of LA-ICP-MS and MALDI-MS images work by registering images of 50µm resolution in both modalities, as shown in figure 5.1 as direct registration. When calculating the accuracy of the registration, we obtain that the accuracy of our method is around 50 µm, meaning that the registration in some areas of the tissue might be 1 pixel off the spatial location, which is expected due to the 50 µm resolution of our input images. The approach introduced in this thesis is useful in comparison of tissue areas higher than 50 µm in size, for example white pulp areas of the spleen that varies between 300 µm to 900 µm in size. However, our approach is limited in the comparison of very small areas in the tissue as the hepatocytes in the liver, which usually have sizes around the 100 µm. For comparing hepatocytes, a registration with better resolution should be performed. An example of such type of approach is shown in Figure 5.1 left, labeled as microscopy mediated registration. In microscopy mediated registration, before LA-ICP-MS and MALDI-MS image acquisition, we acquire an autofluorescence (AF) image at high resolution (1 µm).

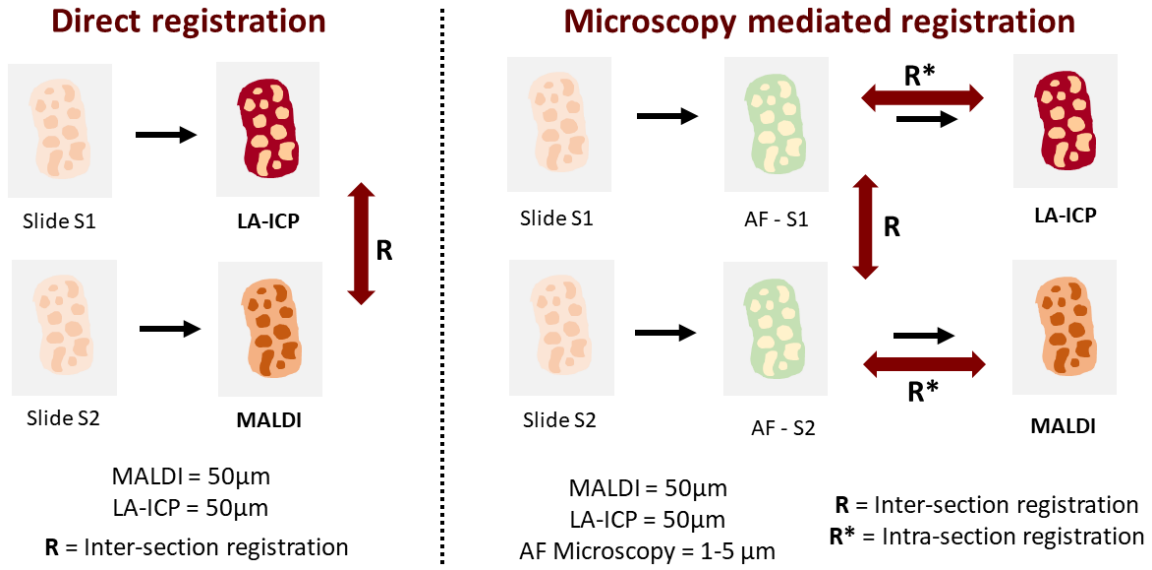

Figure 5.1. Comparison of direct registration (left) with microscopy mediated registration (right).

This AF image can be acquired on the same tissue section because the process is non-destructive. Each of the MS images are registered first to their AF counterparts through an intra-section registration R* process, and then an inter-section registration is performed (R), as shown in Figure 5.1. Since the inter-section registration is performed on tissue sections that has resolutions in the 1 µm range, the final accuracy of the microscopy mediated registration for the two sections falls between 1 µm and 3 µm. Through microscopy mediated registration we can compare small features of the images, such as hepatocyte signal in LA-ICP-MS and MALDI-MS images, and obtain valuable information about NPs distribution. Some previous work in our group have determined that some of the NPs showed high accumulation in the liver hepatocytes,[1,2] which are fundamental in the excretion and clearance of NPs from the liver. A registration method with higher accuracy will be fundamental to advance our understanding of the biochemical processes that occurs in small areas of the tissues.

Microscopy mediated registration was first described for MS images by Caprioli and coworkers for the registration of MALDI-MSI images with H&E microscopy images, using a AF intermediate image to improve the registration.[3] But, the approach has not been used for LA-ICP-MS and MALDI-MS image registration. The Caprioli group developed a code in Python named regToolboxMSRC for performing this registration, but the documentation is very limited. Additionally, since the code is based on SimpleElastix libraries in Python, debugging the code becomes difficult since many of the error messages observed during the registration correspond to errors in SimpleElastix and not regToolboxMSRC perse, making the troubleshooting more complex. For that reason, we developed code using SimpleElastix directly to optimize the registration of AF images with LA-ICP-MS images, and we were successful to certain extend in two areas as shown in Figure 5.2: (a) in designing an experimental method for the combined acquisition of LA-ICP-MS, MALDI-MS, and AF images in adjacent tissue slices and (b) improving the registration of AF sections of 8 µm images. However, optimizing the registration for images of

1 µm resolution was challenging. We believe that by investing time in optimizing the registration parameters, we can achieve registration at 1 µm for AF and 50 µm resolution for LA-ICP-MS and be close in the implementation of microscopy mediated registration.

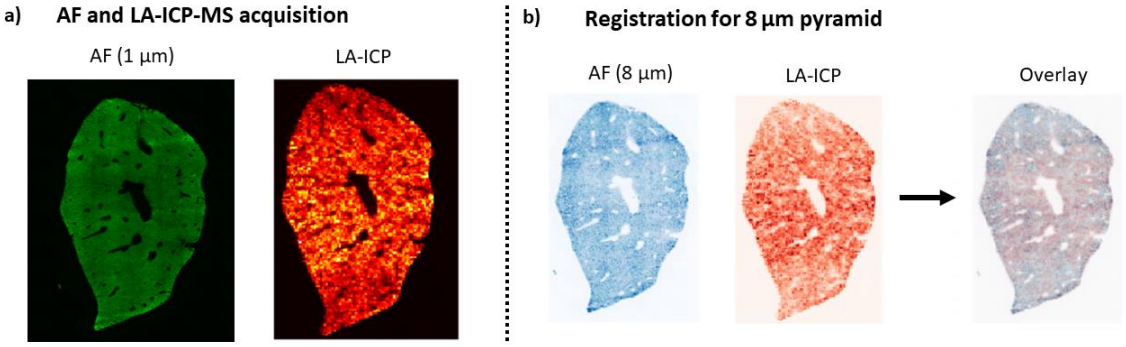

Figure 5.2. First steps in microscopy mediated registration. a) acquisition of AF and LA-ICP-MS images and b)Registration of 8 µm AF image with LA-ICP-MS.

In addition to microscopy registration approaches we believe that new image fusion methods as the one described by Van der Plas and co-workers[4] will be ideal to improve the resolution of LA-ICP-MS images and improve the quality of the information obtained from this technique, especially at resolutions lower than 50 µm. This will open new avenues to interrogate tissue sections at high resolution and obtain valuable information of suborgan regions at high resolution. The image fusion approach described by Van der Plas has been applied to MALDI-MSI, but not for LA-ICP-MS. We believe that a workflow similar to the one described in Figure 5.3. will be ideal for performing image fusion for microscopy and LA-ICP-MS. In our group, we had made advances in image registration and transformations that start building towards applying image fusion to microscopy and LA-ICP-MS.

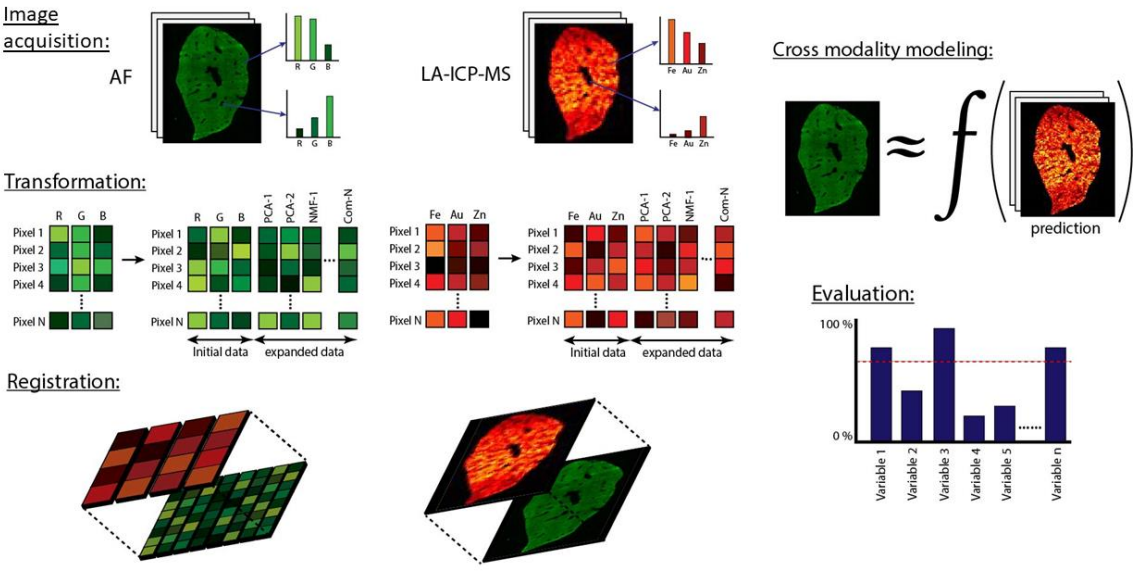

Figure 5.3. Proposed workflow for LA-ICP-MS and microscopy image fusion

5.2.2 Nanoparticle excretion

We performed several experiments to determine the excretion of nanomaterials from tissues. Previous reports from our research group had study the excretion of NPs after 12 hours, 1 or 2 days.[1,2,5] However, longer timepoints to determine how NPs are being excreted had not been performed. We developed an experiment in which we compare the excretion of three nanomaterials with different surface charge TTMA (positive charge), TEGCOOH (negative charge) and ZW (neutral) in day 1 (D1) and day 6 (D6) after injection. With each of the mice we perform a mass balance in which we assume that the total ng of Au injected is 100% and based on this the total ng of Au found in mice was calculated. The total Au in mice correspond to the sum in ng of the Au found in each of the organs studied, on D1 and D6 and the results are displayed in Figure 5.4. Our results show that there is some excretion of NPs from TTMA and ZW after D6, but TEGCOOH NPs had very similar quantities of NPs on day 1 vs day 6, indicating that the NPs are not being excreted properly in TEGCOOH mice.

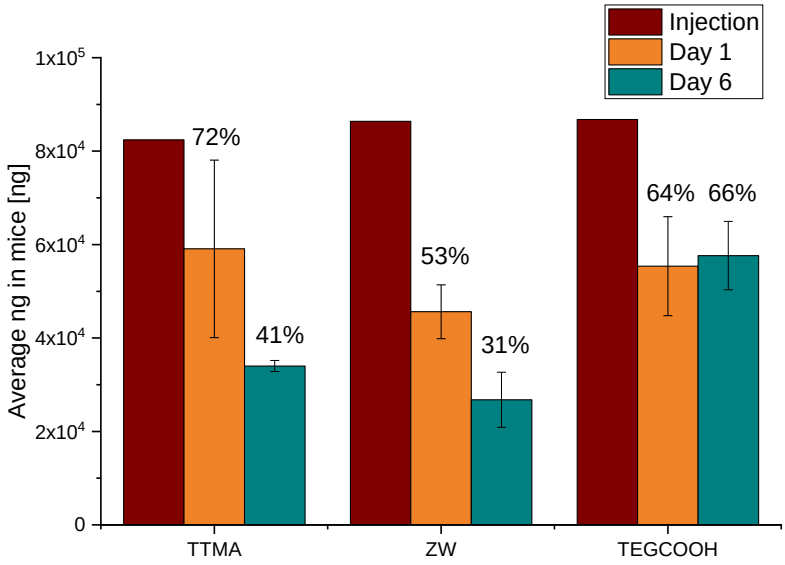

Figure 5.4. Mass balance showing average ng of Au found in mice injected with TTMA, ZW and TEGCOOH. Tissue collection was performed at day 1 and day 6. Each bar corresponds to the average of 3 mouse.

In addition to total Au in the mice, we calculated the concentration of Au in each organ, using tissue digestion in ICP-MS and the results are shown in Figure 5.5. We found the following differences in excretion of the three nanomaterials TTMA, ZW and TEGCOOH:

- Liver: Au concentration decreases in TTMA (-50%) and ZW (-28%), but in COOH the concentration remains almost the same on D6.
- Spleen: concentration increases in all NPs from D1 to D6 TTMA (+56%), ZW(+174%), COOH (+230%). This increase is considerably high in COOH.
- Kidney: concentration slightly decrease in TTMA (-10%) and increases in ZW (+40%) and COOH (+146%).
- Blood: The initial concentration of ZW in blood on D1 is considerable high, with respect of the other NPs. The concentration decreases for all NPs on D6.

The differences in the excretion patterns suggests that the TEGCOOH nanomaterials are not easily cleared from mice, as it shows nor or very small liver excretion and accumulation in Kidney and Spleen in comparison with its TTMA and ZW counterparts. To improve our understanding of the NPs excretion in the suborgan regions of the liver, we performed a series of images in LA-ICP-MS, from D1 and D6 liver tissue and the results are displayed in Figure 5.6. The scale on the images corresponds to a concentration scale, since the LA-ICP-MS experiments were performed using a calibration standard. Using our software for image reconstruction and analysis we calculated the average concentration, using all the tissue pixels and its standard deviation, to properly get an assessment of NPs distribution, results are displayed Table 5.1.

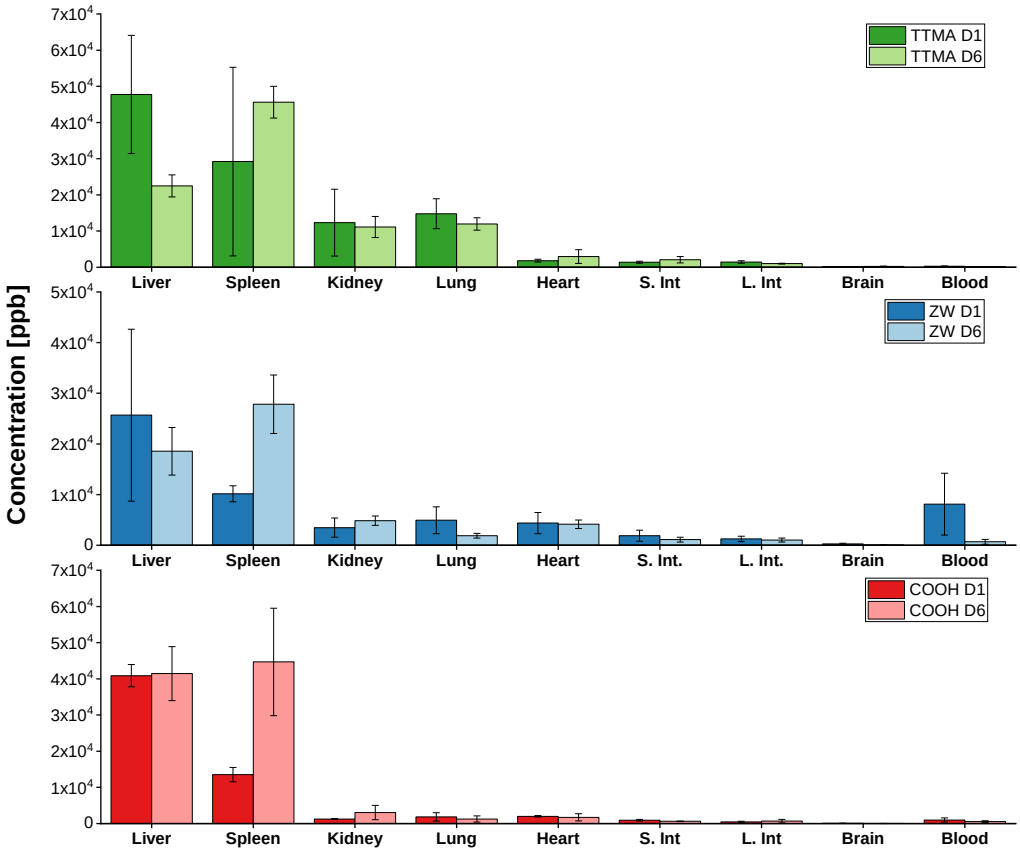

Figure 5.5. concentration of Au in each of the organs by ICP-MS in solution digestion. D1 and D6 were evaluated for each of the three nanomaterials. Each bar corresponds to experiments performed on 3 mice.

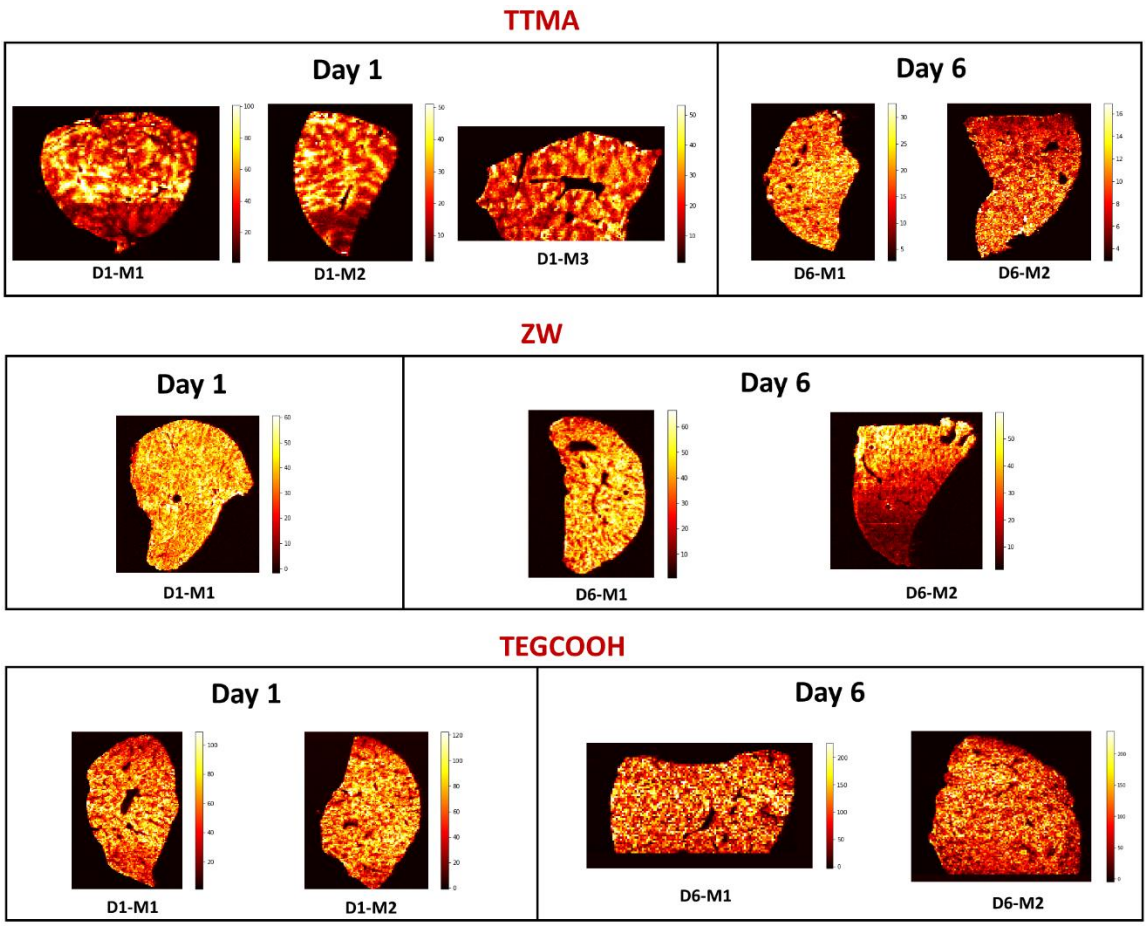

Figure 5.6. LA-ICP-MS images from tissue sections obtained from NPs injected mouse.

The table and images in Figure 5.6 and Table 5.1 clearly shows that TTMA and ZW nanoparticles show a decrease in concentration in the tissues as shown by the tissue average. On the other hand, TEGCOOH nanoparticles show an increase in liver concentration, showing an accumulation of this type of nanomaterials in the tissue sections. Finally, we evaluated the distribution of all the tissue pixels using histograms as shown in Figure 5.7, and we determined that the TEGCOOH pixels shift towards higher concentration and broadens in its distribution as the NPs accumulate in the liver. These offer us already more information about the nature of the accumulation, showing that certain parts of the tissue section accumulate more of these NPs in time. To get a better picture of the accumulation process we could analyze the distribution per

suborgan regions, which would require the implementation of techniques that can improve the resolution of the images, such as Image Fusion.

Table 5.1. Tissue average concentration in tissue sections injected with TTMA, ZW and TEGCOOH NPs on day 1 and day 6.

Tissue	NP	Day	Mouse	Tissue Avg	Tissue std
Liver	TTMA	D1	M1	43.11	23.39
Liver	TTMA	D1	M2	24.08	11.18
Liver	TTMA	D1	M3	23.97	10.59
Liver	TTMA	D6	M1	19.65	5.56
Liver	TTMA	D6	M2	8.89	2.92
Liver	ZW	D1	M1	37.59	10.45
Liver	ZW	D6	M1	40.92	12.47
Liver	ZW	D6	M2	25.02	14.18
Liver	COOH	D1	M1	57.10	21.78
Liver	COOH	D1	M2	66.76	24.91
Liver	COOH	D6	M1	101.35	53.62
Liver	COOH	D6	M2	99.75	50.58

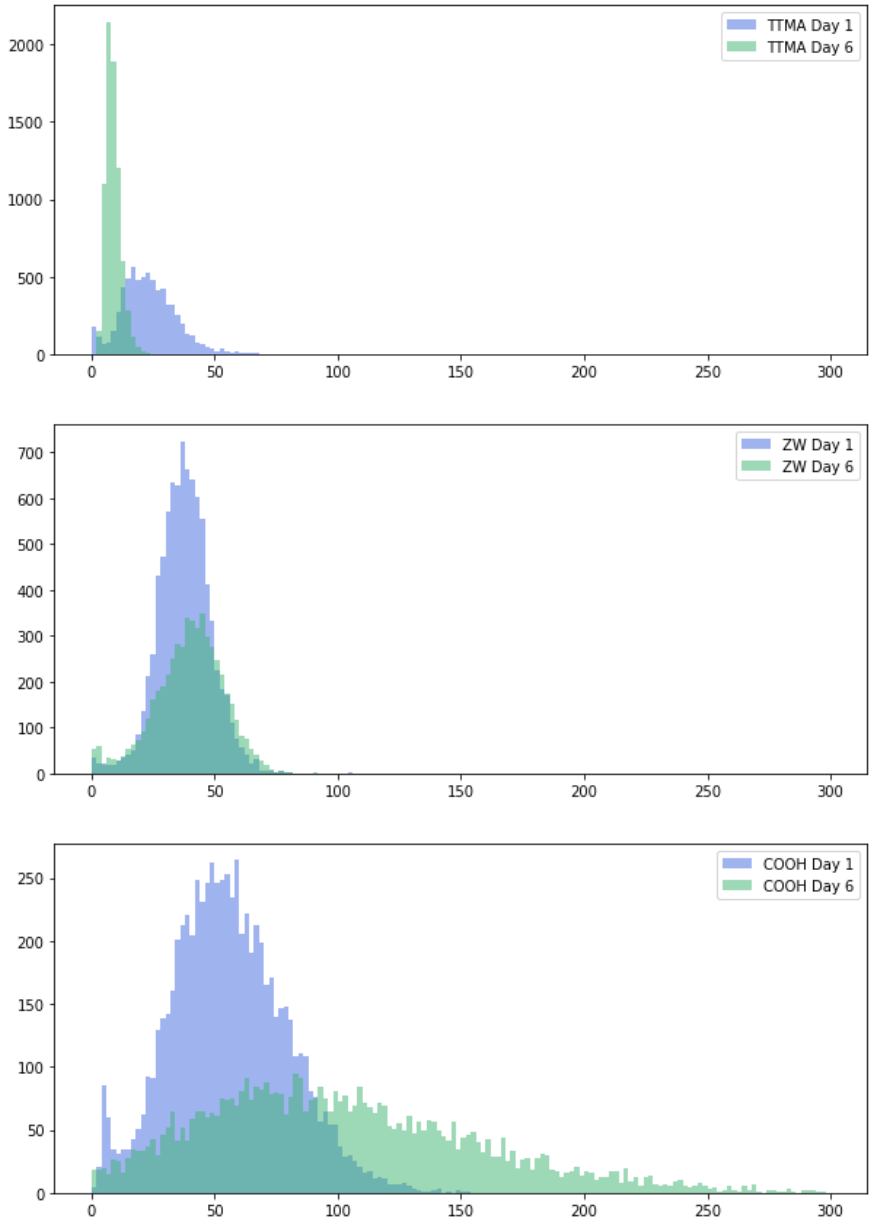

Figure 5.7. Evaluation of pixel distribution on liver tissues injected with TTMA, ZW and TEGCOOH.

5.3 References

(1) Elci, S. G.; Jiang, Y.; Yan, B.; Kim, S. T.; Saha, K.; Moyano, D. F.; Yesilbag Tonga, G.; Jackson, L. C.; Rotello, V. M.; Vachet, R. W. Surface Charge Controls the Suborgan Biodistributions of Gold Nanoparticles. *ACS Nano* **2016**, *10* (5), 5536–5542.

(2) Elci, S. G.; Yan, B.; Kim, S. T.; Saha, K.; Jiang, Y.; Klemmer, G. A.; Moyano, D. F.; Tonga, G. Y.; Rotello, V. M.; Vachet, R. W. Quantitative Imaging of 2 Nm Monolayer-Protected Gold Nanoparticle Distributions in Tissues Using Laser Ablation Inductively-Coupled Plasma Mass Spectrometry (LA-ICP-MS). *Analyst* **2016**, *141* (8), 2418–2425.

(3) Patterson, N. H.; Tuck, M.; Lewis, A.; Kaushansky, A.; Norris, J. L.; Van de Plas, R.; Caprioli, R. M. Next Generation Histology-Directed Imaging Mass Spectrometry Driven by Autofluorescence Microscopy. *Anal. Chem.* **2018**, *90* (21), 12404–12413.

(4) Van De Plas, R.; Yang, J.; Spraggins, J.; Caprioli, R. M. Image Fusion of Mass Spectrometry and Microscopy: A Multimodality Paradigm for Molecular Tissue Mapping. *Nat. Methods* **2015**, *12* (4), 366–372.

(5) Elci, S. G.; Tonga, G. Y.; Yan, B.; Kim, S. T.; Kim, C. S.; Jiang, Y.; Saha, K.; Moyano, D. F.; Marsico, A. L. M.; Rotello, V. M.; Vachet, R. W. Dual-Mode Mass Spectrometric Imaging for Determination of in Vivo Stability of Nanoparticle Monolayers. *ACS Nano.* **2017**, *11* (7), 7424–7430.

APPENDIX A

Jupyter Notebook RecSegImage-LA: Reconstruction, Segmentation of LA-ICP Imaging Data

Here, we display the content of the Jupyter notebook used for the reconstruction and segmentation of LA-ICP data. The use of this code is described in Chapter 2. The workflow consists of six steps showed in the image below, orange circles show input parameters, while gray boxes show the workflow steps. Each of the steps is documented in the Jupyter notebook showing the variable type ("integer", "string", "float", etc) and the input required in each case.

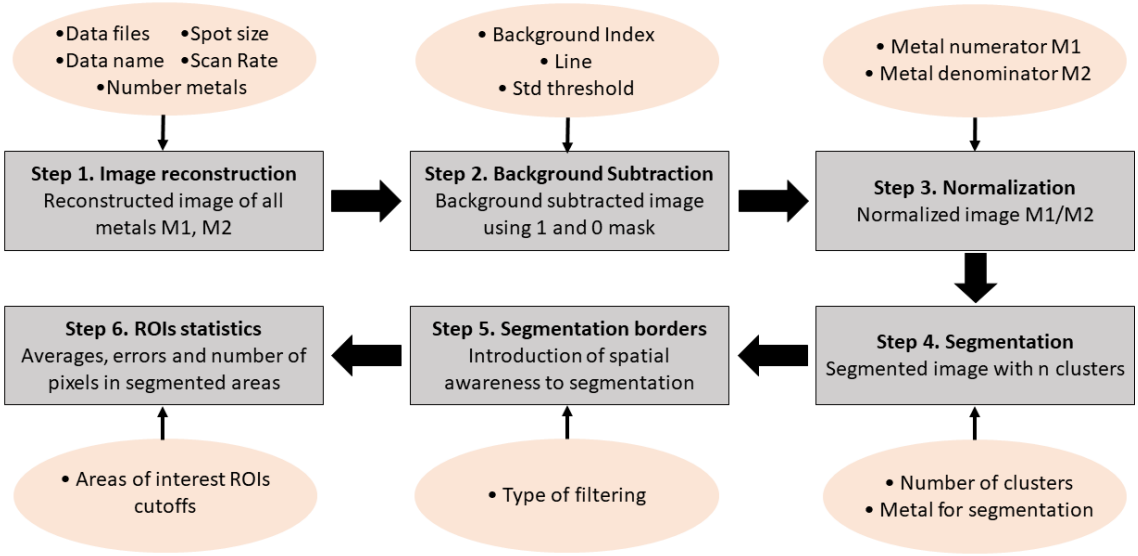


```
import sys
sys.path.append("../") # go to parent dir
from recsegimage import *

import numpy as np
import matplotlib.pyplot as plt
import glob
import re
%matplotlib inline
```

Reconstruction of images for the analyzed metals

The following lines of code perform image reconstruction of LA-ICP-MS data, save the data in the results folder and generate plots of the reconstructed images. The final images are in order of acquisition in the raw data (Metal1, Metal2, Metal3, ... , Metaln)

- **foldername** = string, name of the folder that includes the raw data files and the ipython script RecSegImage-LA.ipynb
- **data_name** = string, name given to the data (no blank spaces allowed in the name)
- **spot_size** = integer, spot size in microns of the laser used to acquire the data
- **scan_rate** = integer, scan rate of the laser in microns/second
- **nmetals** = integer, number of metals analyzed, when performing the images
- **ldiscard** = integer, number of columns on the far left side of the image to be eliminated in case there is sample carryover. Default value is 0

```
foldername = "data/"
data_name = "Example"
spot_size = 50
scan_rate = 15
nmetals = 4
ldiscard = 0

# Image reconstruction of the LA-ICP-MS raw data
final_matrices,sumdata =
image_reconstruction(foldername,ldiscard,"*.xl",nmetals,spot_size,sca
n_rate)

# Save the analysis in .csv files in the folder RegSegImage-
LA/results folder
write_data_analysis(final_matrices,ldiscard,sumdata,nmetals)

# Generate the image plots of all the analyzed metals
generate_plot_all_metals(final_matrices, nmetals)
```

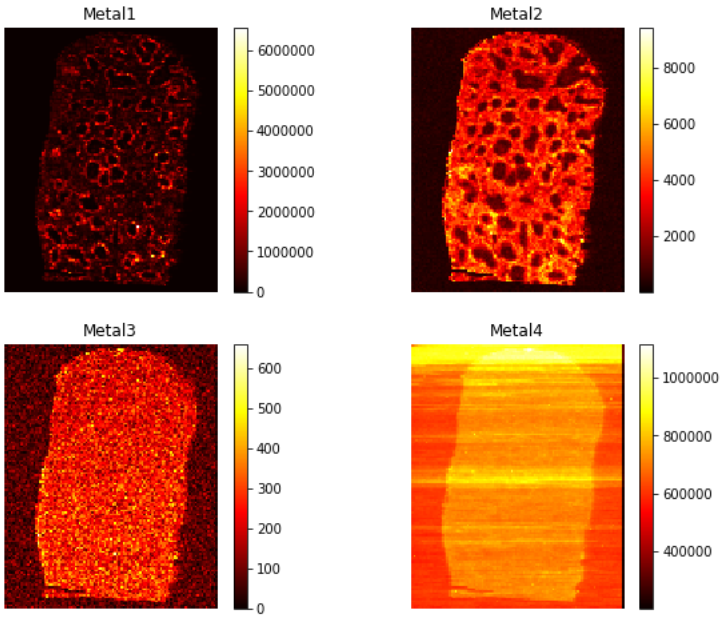

Reconstruction of the image of a single metal

Image reconstruction of one of all the analyzed metals. The metal index of the metal needs to be specified. The metal index corresponds to the order in which the metal is analyzed by the ICP-MS. For this particular example, the ICP-MS performs the readings of the metals in the following order: Bi, Fe, Zn, S. This means that the associated indexes are: Bi (Metal1, metal_index=1), Fe (Metal2, metal_index=2), Zn (Metal3, metal_index=3) and S (Metal4, metal_index=4)

- **metal_index** = integer, index of the metal that we want to plot. For example, for Metal 2 (Fe), the index is 2.

```
metal_index = 2

# Functions to generate image of one metal plot
generate_metal_plot(final_matrices,metal_index,nmetals)
```

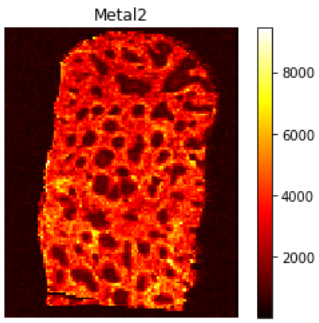

Background subtraction

Use the Zn image (or other metal that marks the tissue boundary) to differentiate tissue from background

- **background_index** = integer, index of the image used for background subtraction. In this case is the Zn image
- **line** = integer, row or column from which the standard deviation will be calculated. By default, the value is 1, which corresponds to the first row and column. The script will calculate the smallest standard deviation among the selected rows and columns
- **std_threshold** = integer, how many standard deviations will be tolerated to set the threshold of what is considered to be tissue and background

```
background_index = 3
line = 1
std_threshold = 4

background_mask =
remove_background(final_matrices,background_index,line,std_threshold)
background_plot = generate_background_plot(background_mask)
```

Normalization with background subtraction

Normalization of the image with background subtraction. Background subtraction should be done first to obtain the background mask. The normalization corresponds to a pixel/pixel division of the images, so metal_numerator/metal_denominator should be specified in the following parameters:

- **metal_numerator** = integer, index of the metal that will correspond to the metal numerator in the division operation
- **metal_denominator** = integer, index of the metal that will correspond to the metal denominator in the division operation

The normalized image with background subtraction is saved as a text file in the results folder. The name of the file is: "Normalization Background Metal_numerator / Metal_denominator"

```
metal_numerator = 1
metal_denominator = 3

normalization_with_background(final_matrices,background_mask,metal_nu
merator,metal_denominator)
```

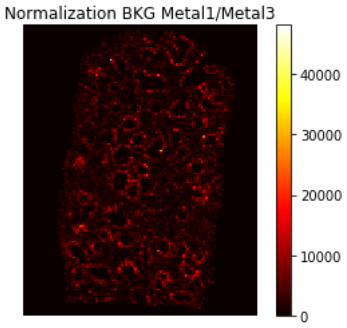

k-means segmentation

Segmentation of the images using k-means clustering. This is without spatial awareness.

- **metal_segmentation_index** = integer, index of the metal used for segmentation. In this example we use Fe and the index of Fe in the reconstructed data corresponds to 2
- **clusters** = integer, number of clusters to perform k-means segmentation. For this particular common example we had determined that the ideal number of clusters is 2

```
metal_segmentation_index = 2
segmentation_clusters = 2

label_image,segmented_image =
segmentation(final_matrices,background_mask,metal_segmentation_index,
segmentation_clusters)
```

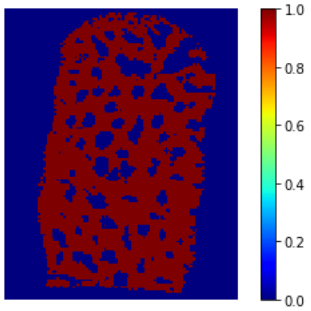

k-means multimetal segmentation with neighboring pixel evaluation

Application of neighboring pixel evaluation using average filtering. The k-means segmentation part of the code should be run first before performing neighboring pixel evaluation. The number of clusters and metal segmentation index are the ones specified in the k-means segmentation part of the code. If the user wants to change these parameters, this can be done in the k-means segmentation part of the code. No inputs are required here by the user

Multimetal segmented images correspond to the segmented images using Fe and the background mask (Zn) for segmentation. A weighted image corresponds to the image after filtering to determine the tissue boundaries.

```
weighted_pixels = neighbouring_average(label_image,background_mask)
```

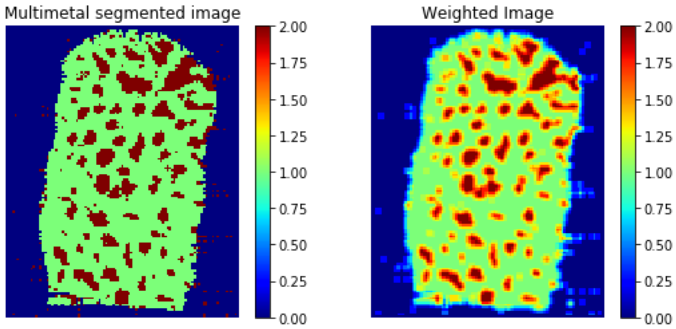

Image masks of the segmented areas

It is possible to set up to four different areas determined by segmentation and neighboring pixel evaluation. It is necessary to set up the cutoffs of the areas in relation to the weighted image (0 to 18 scale). For this particular example we set up the cutoff values for:

Area 1 = Background (values between 0 and 5)
Area 2 = Red Pulp (values between 6 and 10)
Area 3 = Marginal zone (values between 11 and 14)
Area 4 = White pulp (values between 15 and 18)

The variables shown should specify the low and high cutoff of a particular area:

- **low_A1** = integer, low cutoff of Area 1
- **high_A1** = integer, high cutoff of Area 1
- **low_A2** = integer, low cutoff of Area 2
- **high_A2** = integer, high cutoff of Area 2
- **low_A3** = integer, low cutoff of Area 3
- **high_A3** = integer, high cutoff of Area 3
- **low_A4** = integer, low cutoff of Area 4
- **high_A4** = integer, high cutoff of Area 4

```
low_A1 = 0
high_A1 = 0.59

low_A2 = 0.60
high_A2 = 1.19

low_A3 = 1.20
high_A3 = 1.49

low_A4 = 1.50
high_A4 = 2.0

area1,area2,area3,area4 =
image_masks(weighted_pixels,low_A1,high_A1,low_A2,high_A2,low_A3,high
_A3,low_A4,high_A4)
```

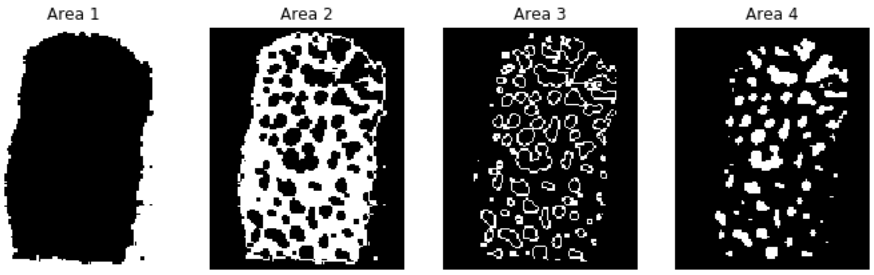

Quantitation in different segments

Quantitation of pixels in the different segments determined by the image masks. Four different areas of a tissue were determined after segmentation. The segmented areas can be use to get the number of pixels in each of the particular areas, find the average and error of any of the metals in each of the segmented areas. It is necessary to choose the metal that we desire to quantify in each of the areas as the (quantitation_index). In this particular example, we want to quantify the Bismuth (quantitation_index=1) so the index needs to be set to the Bi index (Bismuth index is 1). It is also possible to quantify the average signal of any of the other metals, for example if we want to quantify the Fe in each of the segmented areas we should set (quantitation_index=2) as the Fe corresponds to the metal with the index=2.

- **quantitation_index** = int, index of the metal that we want to quantify in each of the segments

```
quantitation_index = 2

quantitation_segments(final_matrices,area1,area2,area3,area4,quantita
tion_index)
```

```
Area 1 Quantitation:
Area 1 pixels are: 5308
Area 1 average is: 518.7432395475972
Area 1 error is: 7.172345137306754
```

```
Area 2 Quantitation:
Area 2 pixels are: 4822
Area 2 average is: 3890.3483368180314
Area 2 error is: 15.287243249381316

Area 3 Quantitation:
Area 3 pixels are: 1545
Area 3 average is: 2777.1852567092023
Area 3 error is: 23.262159826047085

Area 4 Quantitation:
Area 4 pixels are: 1509
Area 4 average is: 1337.1421460333133
Area 4 error is: 9.673310098229521
```

APPENDIX B

Source code of RecSegImage-LA: Reconstruction, Segmentation of LA-ICP Imaging Data

Here we have generated a copy of the functions used for reconstruction and segmentation of LA-ICP data, as defined in the module _functions.py of the RecSegImage-LA repository, as shown in the following github link (git@github.com:Vachet-Lab/RecSegImage-LA.git). The use of this code is described in Chapter 2. The comments for each of the functions are shown in red, the description contains a brief explanation of the function, input and outputs description with its variable type.

```
import numpy as np
import matplotlib.pyplot as plt
import glob
import re
import warnings; warnings.simplefilter('ignore')
from sklearn.cluster import KMeans

global ldiscard
ldiscard=0

def atoi(text):
    '''
        Natural Sorting of data: Functions used to organize the data in terms
of type. Import the package re. Allow the use of
        backslashes to indicate special forms without evoking the special
meaning.

        atoi function:
            input = str, text
            output = str and int, text
    '''
    return int(text) if text.isdigit() else text

def natural_keys(text):
    '''
        alist.sort(key=natural_keys) sorts in human order
        http://nedbatchelder.com/blog/200712/human_sorting.html
        (See Toothy's implementation in the comments)
    '''
    return [ atoi(c) for c in re.split('(\d+)', text) ]

def processfile(filename,ldiscard,spot_size,scan_rate):
    '''
        Function processfile used to load and read the data in a single file

        Input:
            filename = str, name of the folder where the data files are stored
            ldiscard = integer, number of columns on the far left side of the
image to be eliminated. Default value is 0
            spot_size = integer, spot size in microns of the laser used to
acquire the data
            scan_rate = integer, scan rate of the laser in microns/second
```

```
        Ouput:
            new_matrix = nd array, reduced data summed by sumdata amounts
            sumdata = int, number of data points that make one pixel (depends
on laser spot size and scan rate)
    '''
    data_matrix = np.loadtxt(filename, delimiter=",", skiprows=(2+ldiscard))
    pixel_time = spot_size/scan_rate
    data_point_time = data_matrix[6,0]-data_matrix[5,0]
    sumdata = int(round(pixel_time/data_point_time))
    nrows = data_matrix.shape[0]//sumdata
    ncols = data_matrix.shape[1]-1
    new_matrix = np.zeros((nrows+1,ncols))
    for n in range(nrows):
        new_matrix[n,:] =
np.sum(data_matrix[n*sumdata:(n+1)*sumdata,1:],axis=0)
    new_matrix[n+1,:] = np.sum(data_matrix[(n+1)*sumdata:,1:],axis=0)
    return new_matrix, sumdata

def
image_reconstruction(foldername,ldiscard,extension,ncolumns,spot_size,scan_rate
):
    '''
        Function image_reconstruction used for load files in a directory

        Input:
            foldername = str, folder in which the data files and script are
located
            ldiscard = integer, number of columns on the far left side of the
image to be eliminated. Default value is 0
            extension = str, extension of the data files
            ncolumns = int, number of columns in the reduced matrix (equal to
the number of metals)
            spot_size = integer, spot size in microns of the laser used to
acquire the data
            scan_rate = integer, scan rate of the laser in microns/second

            Output:
            final_matrices = dic, dictionary composed of np.arrays of the final
data of different analyzed metals
            sumdata = int, number of data points that make one pixel (depends
on laser spot size and scan rate)
    '''
    files = glob.glob1(foldername,extension)
    files.sort(key=natural_keys)
    nfiles = len(files)
    dic_data = {}
    for n in range(ncolumns):
        dic_data[n]=[]
    for file in files:
        processed_matrix,sumdata =
processfile(foldername+'/'+file,ldiscard,spot_size,scan_rate)
        for col in range(ncolumns):
            dic_data[col].append(processed_matrix[:,col])
    final_matrices={}
    for n in range(ncolumns):
        final_matrices[n]=np.array(dic_data[n])
    return final_matrices, sumdata

def
write_data_analysis(final_matrices,ldiscard,sumdata,nmetals,foldername='results
'):
    '''
```

```
        Function write_data_analysis use to write the processed data into
separate csv files

        Input:
            final_matrices = dic, dictionary composed of np.arrays of the final
data of different analyzed metals
            ldiscard = int, number of datapoints discarded in each of the
files, if needed
            sumdata = int, number of data points that make one pixel (depends
on laser spot size and scan rate)
            nmetals = int, number of metals analyzed, when performing the
images

        Output:
            files for each of the analyzed metals writen in .csv inside the
/results directory
    '''
    dic_of_metals = {}
    keys = range(nmetals)
    for i in keys:
        dic_of_metals[i+1] = "Metal" + str(i+1)
    for metal in final_matrices:
        filename = foldername + "/Reconstruction-%s.xl" %
(dic_of_metals[metal+1])
        np.savetxt(filename, final_matrices[metal], delimiter=',',
newline='\n')

def generate_plot_all_metals(final_matrices,nmetals):
    '''
        Function genetate_plot_all_metals to plot all the metal images in one
plot

        Input:
            final_matrices = dic, dictionary composed of np.arrays of the final
data matrices of different analyzed metals
            nmetals = int, number of metals analyzed, when performing the
images

        Output:
            matplotlib image of the analyzed metals in one image (in the
Jupyter notebook)
    '''
    dic_of_metals = {}
    keys = range(nmetals)
    for i in keys:
        dic_of_metals[i+1] = "Metal" + str(i+1)
    fig = plt.figure(figsize=[10,8])
    for n in range(1,nmetals+1):
        ax = fig.add_subplot(2,2,n)
        plt.imshow(final_matrices[n-1], interpolation='None', cmap=plt.cm.hot)
        plt.title("%s" % dic_of_metals[n])
        plt.axis('off')
        plt.colorbar()
    plt.show()


def generate_metal_plot(final_matrices,metal_index,nmetals):
    '''
        Function generate_metal_plot used to generate a plot of one metal

        Input:
```

```
            final_matrices = dic, dictionary composed of np.arrays of the final
data matrices of different analyzed metals
            metal_index = int, index of the specified metal in the dictionary
(1 to nmetals)
            nmetals = int, number of metals analyzed, when performing the
images

        Output:
            matplotlib image of a particular metal inline
    '''
    dic_of_metals = {}
    keys = range(nmetals)
    for i in keys:
        dic_of_metals[i+1] = "Metal" + str(i+1)
    fig = plt.figure(figsize=[5,4])
    ax = fig.add_subplot(1,1,1)
    plt.imshow(final_matrices[metal_index-1], interpolation='None',
cmap=plt.cm.hot)
    plt.title("%s" % dic_of_metals[metal_index])
    plt.axis('off')
    plt.colorbar()
    plt.show()

def populate_border(matrix):
    '''
        Function populate_border used to fine tune, delimitate border of the
tissue sample, based on any metal content. This function is
        concatenated with the remove_background function

        Input:
            matrix = np array, correspond to the matrix index_threshold. This
is the matrix that have the applied condition
            matrix < threshold, this matrix correspond to a boolean matrix
which have defined True and False values.

        Output:
            border = np array
    '''
    border = np.ones(matrix.shape)
    for n in range(matrix.shape[0]):
        for m in range(matrix.shape[1]):
            if matrix[n, m] == True:
                border[n, m] = 0
            elif matrix[n, m] == False:
                break
    for n in range(matrix.shape[0]):
        for m in range(matrix.shape[1]):
            if matrix[n, matrix.shape[1] - m - 1] == True:
                border[n, matrix.shape[1] - m - 1] = 0
            elif matrix[n, matrix.shape[1] - m - 1] == False:
                break
    for m in range(matrix.shape[1]):
        for n in range(matrix.shape[0]):
            if matrix[n, m] == True:
                border[n, m] = 0
            elif matrix[n, m] == False:
                break
    for m in range(matrix.shape[1]):
        for n in range(matrix.shape[0]):
            if matrix[matrix.shape[0] - n - 1, m] == True:
                border[matrix.shape[0] - n - 1, m] = 0
            elif matrix[matrix.shape[0] - n - 1, m] == False:
```

```
                break
    return border

def remove_background(final_matrices,background_index,line,std_threshold):
    '''
        Function remove_background used to calculate the average and std of the
background and set the theshold values

        Input:
            matrix = np array, data matrix with the Zn data
final_matrices[Zn_index]
            line = int, index of the line that will be used to perform the
background calculation, usually 0
            tolerance_std = int, tolerance of the std, usually is 3

        Output:
            background_mask = np array, background mask of the image data
    '''
    matrix = final_matrices[background_index-1]
    average_col = np.mean(matrix[:, line-1])
    std_col = np.std(matrix[:, line-1])
    average_row = np.mean(matrix[line-1, :])
    std_row = np.std(matrix[line-1, :])
    if std_col < std_row:
        average = average_col
        std = std_col
    else:
        average = average_row
        std = std_row
    threshold = average + std_threshold*std
    index_threshold = matrix < threshold
    background_mask = populate_border(index_threshold)
    return background_mask

def generate_background_plot(background_mask):
    '''
        Function generate_background_plot used to generate a plot of the
background mask

        Input:
            background_mask = np array, background mask of the image data

        Output:
            matplotlib inline image of the background mask
    '''
    fig = plt.figure(figsize=[5,4])
    ax = fig.add_subplot(1,1,1)
    plt.imshow(background_mask, interpolation='None', cmap=plt.cm.hot)
    plt.title('Background mask')
    plt.axis('off')
    plt.show()

def
normalization_with_background(final_matrices,background_mask,metal_numerator,me
tal_denominator,vmin=None,vmax=None,inter='None',
                                foldername='results'):
    '''
        Function normalization_with_background to divide two matrices
(metal1/metal2), saved the data and plotted it inline

        Input:
```

```
            final_matrices = dic, dictionary composed of np.arrays of the final
data matrices of different analyzed metals
            background_mask = np array, background mask of the image data
            metal_numerator = integer, index of the metal that will correspond
to the metal numerator in the division operation
            metal_denominator = integer, index of the metal that will
correspond to the metal denominator in the division operation

        Output:
            file inside the results directory with the results of the
metal_numerator/metal_denominator division
            matplotlib inline image of the metal_numerator/metal_denominator
division
    '''
    old_err_state = np.seterr(divide='raise')
    ignored_states = np.seterr(**old_err_state)
    fig = plt.figure(figsize=[5,4])
    ax = fig.add_subplot(1,1,1)
    division_background = (final_matrices[metal_numerator-
1]/final_matrices[metal_denominator-1])*background_mask
    division_background[np.isnan(division_background)] = 0
    np.savetxt(foldername+'/Normalization-Background-
Metal'+str(metal_numerator)+'-
'+'Metal'+str(metal_denominator),division_background,delimiter=',',newline='\n'
)

plt.imshow(division_background,interpolation=inter,vmin=vmin,vmax=vmax,cmap=plt
.cm.hot)
    plt.title('Normalization BKG
'+'Metal'+str(metal_numerator)+'/Metal'+str(metal_denominator))
    plt.axis('off')
    plt.colorbar()
    plt.show()

def
segmentation(final_matrices,background_mask,metal_segmentation_index,segmentati
on_clusters):
    '''
        Function segmentation for the segmentation of the images using k-means
clustering without filtering

        Input:
            final_matrices = dic, dictionary composed of np.arrays of the final
data matrices of different analyzed metals
            background_mask = np array, background mask of the image data
            metal_segmentation_index = int, index of the metal used for
segmentation.
            segmentation_clusters = int, number of clusters to perform k-means
segmentation.

        Output:
            label_image = np array, segmented image with its labels
            segmented_image = np array, segmented image with its centroids
    '''
    metal_segmentation = final_matrices[metal_segmentation_index-
1]*background_mask
    rows = metal_segmentation.shape[0]
    columns = metal_segmentation.shape[1]
    metal_segmentation_vector = metal_segmentation.reshape(rows*columns, 1)
    # specifies that kmeans will be applied with n-clusters
    kmeans = KMeans(segmentation_clusters)
    # Perform kmeans over metal_segmentation_vector
```

```
    kmeans.fit(metal_segmentation_vector)
    # Find cluster center associated with each data point
    segmented_vector =
kmeans.cluster_centers_[kmeans.predict(metal_segmentation_vector)]
    # Find labels associated with each cluster
    centroids = np.sort(np.unique(segmented_vector))
    labels = np.zeros(segmented_vector.shape)
    for index, centroid in enumerate(centroids):
        labels[segmented_vector==centroid] = index
    label_image = labels.reshape(rows, columns)
    # Reshaped of the image, plotting and comparison with raw_data
    segmented_image = segmented_vector.reshape(rows, columns)
    # Image plot of the labels
    plt.imshow(label_image, cmap='jet')
    plt.colorbar()
    plt.axis('off')
    plt.show()
    return label_image,segmented_image

def neighbouring_average(label_image,background_mask):
    '''
        Function neighbouring_average for filtering the multimetal image

        Input:
            label_image = np array, segmented image with its labels
            background_mask = np array, background mask of the image data

        Output:
            weighted_pixels = np array, filtering of label image data
    '''
    # Re-asignation of zero values
    label_image[label_image == 0] = 2
    # Differentiation of bacgkround using the background mask
    M = label_image*background_mask
    # Weighted pixel calculation
    weighted_pixels = np.zeros(M.shape)
    for n in range(1, M.shape[0]-1):
        for m in range(1, M.shape[1]-1):
            weighted_pixels[n, m]= (M[n-1,m-1] + M[n-1,m] + M[n-1,m+1] + M[n,m-
1] + M[n,m] + M[n, m+1] + M[n+1, m-1] + M[n+1, m] + M[n+1, m+1])/9
    # Image generation of the multimetal segmentation
    plt.figure(figsize=(9, 4))
    ax1=plt.subplot(1, 2, 1)
    plt.imshow(M, cmap='jet')
    plt.colorbar()
    plt.axis('off')
    plt.title('Multimetal segmented image')
    # Image generation of the weighted image
    ax1=plt.subplot(1, 2, 2)
    plt.imshow(weighted_pixels, interpolation='none', cmap='jet')
    plt.colorbar()
    plt.axis('off')
    plt.title('Weighted Image')
    plt.show()
    return weighted_pixels

def image_masks(weighted_pixels, low_A1, high_A1, low_A2, high_A2, low_A3,
high_A3, low_A4, high_A4):
    '''
        Function image_masks to obtain the masks images of the segmented areas

        Input:
```

```
            low_A1 = integer, low cutoff of Area 1
            high_A1 = integer, high cutoff of Area 1
            low_A2 = integer, low cutoff of Area 2
            high_A2 = integer, high cutoff of Area 2
            low_A3 = integer, low cutoff of Area 3
            high_A3 = integer, high cutoff of Area 3
            low_A4 = integer, low cutoff of Area 4
            high_A4 = integer, high cutoff of Area 4

        Output:
            area1 = image of image mask of area 1
            area2 = image of image mask of area 2
            area3 = image of image mask of area 3
            area4 = image of image mask of area 4
    '''
    area1 = (weighted_pixels <= high_A1)
    area2 = (weighted_pixels <= high_A2) ^ (weighted_pixels <= low_A2)
    area3 = (weighted_pixels <= high_A3) ^ (weighted_pixels <= low_A3)
    area4 = (weighted_pixels <= high_A4) ^ (weighted_pixels <= low_A4)
    # Image generation
    plt.figure(figsize=(12, 9))
    ax=plt.subplot(1, 4, 1)
    plt.imshow(area1, cmap='gray')
    plt.axis('off')
    plt.title('Area 1')
    ax=plt.subplot(1, 4, 2)
    plt.imshow(area2, interpolation='none', cmap='gray')
    plt.axis('off')
    plt.title('Area 2')
    ax=plt.subplot(1, 4, 3)
    plt.imshow(area3, interpolation='none', cmap='gray')
    plt.axis('off')
    plt.title('Area 3')
    ax=plt.subplot(1, 4, 4)
    plt.imshow(area4, interpolation='none', cmap='gray')
    plt.axis('off')
    plt.title('Area 4')
    plt.show()
    return area1, area2, area3, area4

def
quantitation_segments(final_matrices,area1,area2,area3,area4,quantitation_index
):
    '''
        Function quantitation_segments to obtain the masks images of the
segmented areas

        Input:
            final_matrices = dic, dictionary composed of np.arrays of the final
data matrices of different analyzed metals
            area1 = image of image mask of area 1
            area2 = image of image mask of area 2
            area3 = image of image mask of area 3
            area4 = image of image mask of area 4
            quantitation_index = int, index of the metal that we want to
quantify in each of the segments

        Output:
            inline results of the averages, standard error and number of pixels
of the segmented areas
    '''
    metal_quantitation = final_matrices[quantitation_index-1]
```

```
# Area 1
print ('Area 1 Quantitation:')
pixels_A1 = len(metal_quantitation[area1])
avg_A1 = np.mean(metal_quantitation[area1])
error_A1 = np.std(metal_quantitation[area1])/np.sqrt(pixels_A1)
print ('Area 1 pixels are:', pixels_A1)
print ('Area 1 average is:', avg_A1)
print ('Area 1 error is:', error_A1)
# Area 2
print (' ')
print ('Area 2 Quantitation:')
pixels_A2 = len(metal_quantitation[area2])
avg_A2 = np.mean(metal_quantitation[area2])
error_A2 = np.std(metal_quantitation[area2])/np.sqrt(pixels_A2)
print ('Area 2 pixels are:', pixels_A2)
print ('Area 2 average is:', avg_A2)
print ('Area 2 error is:', error_A2)
# Area 3
print (' ')
print ('Area 3 Quantitation:')
pixels_A3 = len(metal_quantitation[area3])
avg_A3 = np.mean(metal_quantitation[area3])
error_A3 = np.std(metal_quantitation[area3])/np.sqrt(pixels_A3)
print ('Area 3 pixels are:', pixels_A3)
print ('Area 3 average is:', avg_A3)
print ('Area 3 error is:', error_A3)
# Area 4
print (' ')
print ('Area 4 Quantitation:')
pixels_A4 = len(metal_quantitation[area4])
avg_A4 = np.mean(metal_quantitation[area4])
error_A4 = np.std(metal_quantitation[area4])/np.sqrt(pixels_A4)
print ('Area 4 pixels are:', pixels_A4)
print ('Area 4 average is:', avg_A4)
print ('Area 4 error is:', error_A4)
```

APPENDIX C

Code for LA-ICP-MS and MALDI-MS dimensionality reduction, registration, and validation

Here we present the code used for registration described in Chapter 3. Comments to the code are shown in (#). The code has the following steps, commented through the code:

- t-SNE dimensionality reduction of MALDI and LA-ICP datasets
  - Rendering of MALDI tissue slide
  - Image rotation
  - Hotspot removal
  - Rendering of MALDI images before background subtraction
  - Rendering of MALDI images after hotspot removal
  - t-SNE dimensionality reduction of each analyte in 3D embedded space
  - t-SNE dimensionality reduction for single image representation
  - Display of the reduced images in RGB colors
  - MALDI t-SNE reduction to one image
  - Image pre-processing LA-ICP
  - Hotspot removal LA-ICP
- Registration and validation of MALDI and LA-ICP images
  - Upload segments masks
  - Upload images for registration
  - Translation registration
  - Rigid registration
  - Affine registration
  - No-linear registration
  - Transformation of the masks
  - DSC calculation
  - Landmark registration
  - Annotated mask registration
  - Correlation coefficients calculation
  - Transformation of LA-ICP signals into the MALDI coordinate system
  - Correlation plot of LA and MALDI signals

t-SNE Dimensionality reduction of MALDI and LA-ICP datasets

Rendering of MALDI tissue slide

```
from pyimzml.ImzMLParser import ImzMLParser
import matplotlib.pyplot as plt
import numpy as np
```

```
# Parse the data into slide

slide = ImzMLParser('111920_Liver_TTMA_D6.imzML')

# Obtain spectrum coordinates for p1

for i, (x,y,z) in enumerate(slide.coordinates):
    slide.getspectrum(i)

# Get the ion image of the slide, import geitionimage class from the parser.
Choose the 796.554 +- 0.501 signal

from pyimzml.ImzMLParser import getionimage

peakMZ1 = 339.088
tolMZ1 = 0.286

im1 = getionimage(slide, peakMZ1, tol=tolMZ1)

plt.figure(figsize=(16, 4))
plt.imshow(im1)
plt.colorbar()
plt.show()

print ('Shape of the imzML file', im1.shape)
```

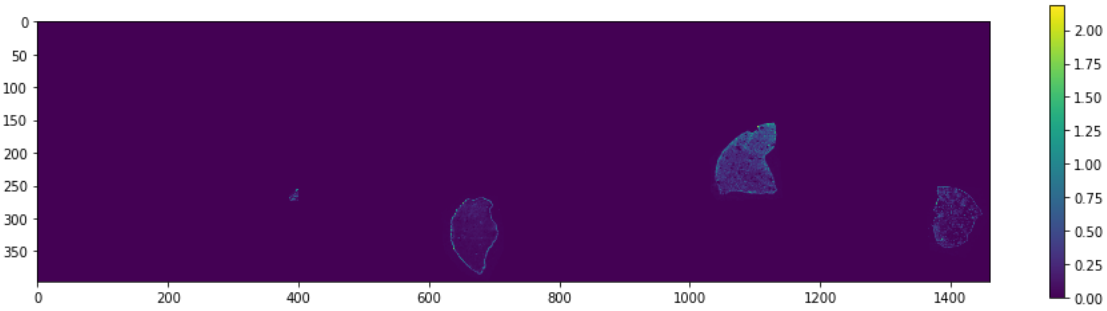


```
Shape of the imzML file (397, 1461)
```

Image Rotation

```
# Function to cut the image from the slide in X and Y

from scipy import ndimage

Y1 = 150
Y2 = 270
X1 = 1035
X2 = 1140

Degree_rotation = 180

MALDI_image_raw = getionimage(slide, peakMZ1, tol=tolMZ1)[Y1:Y2, X1:X2]
MALDI_rot = ndimage.rotate(MALDI_image_raw, Degree_rotation, reshape=True)

print ('MALDI image shape:', MALDI_image_raw.shape)

plt.figure(figsize=(12, 5))
```

```
ax=plt.subplot(1,2,1)
plt.imshow(MALDI_image_raw)
plt.colorbar()
plt.axis('off')
plt.title('Raw image')
ax=plt.subplot(1,2,2)
plt.imshow(MALDI_rot)
plt.colorbar()
plt.axis('off')
plt.title('Rotated image')
plt.show()
```

```
MALDI image shape: (120, 105)
```

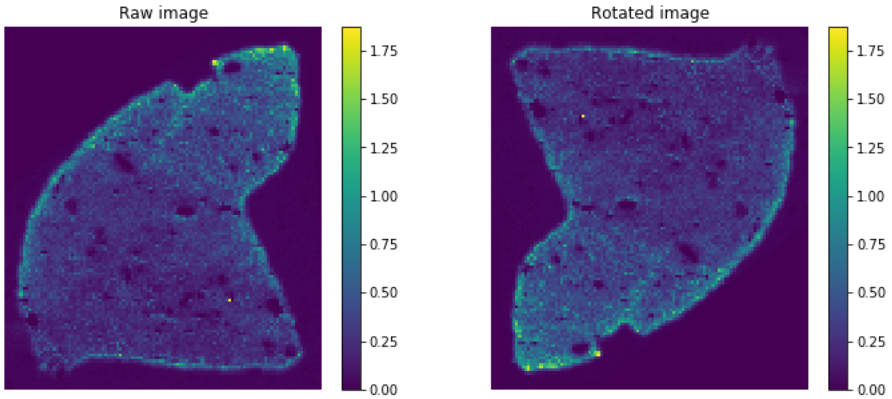

Hotspot removal

```
# We will calculate the 0.99 quantile range and assign the data points above
this value to the 0.99 value.

Quantile_99 = np.quantile(MALDI_rot, 0.99)
print('Quantile 0.99 is:', Quantile_99)

MALDI_image_hot = MALDI_rot.copy()
MALDI_image_hot[MALDI_image_hot > Quantile_99] = Quantile_99
print('Data points above 99% =', np.count_nonzero([MALDI_rot > Quantile_99]))
print('Data points below 99% =', np.count_nonzero([MALDI_rot < Quantile_99]))

# np.savetxt('D6_mz_796.csv', MALDI_image_hot)

# box and whisker plots

row_hot, col_hot = MALDI_image_hot.shape

MALDI_vector_raw = MALDI_rot.reshape(row_hot*col_hot)
MALDI_vector_hot = MALDI_image_hot.reshape(row_hot*col_hot)

plt.figure(figsize=(18, 10))
ax = plt.subplot(2, 2, 1)
plt.imshow(MALDI_rot)
plt.axis('off')
plt.colorbar()
ax = plt.subplot(2, 2, 2)
plt.boxplot(MALDI_vector_raw)
ax = plt.subplot(2, 2, 3)
```

```
plt.imshow(MALDI_image_hot)
plt.colorbar()
plt.axis('off')
ax = plt.subplot(2, 2, 4)
plt.boxplot(MALDI_vector_hot)
plt.show()
```

```
Quantile 0.99 is: 0.9698840579710164

Data points above 99% = 126

Data points below 99% = 12474
```

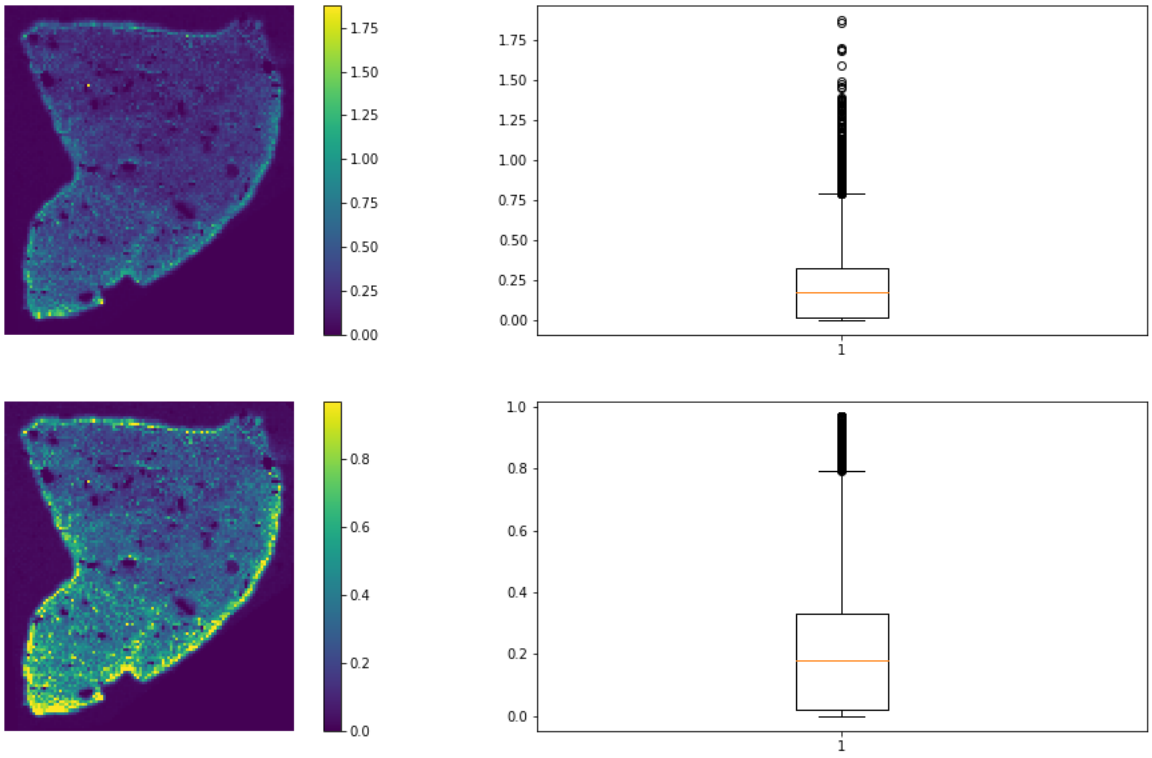

Rendering of MALDI images before background substraction

```
# Import list of the most abundance signals above 500m/z

import csv
import math

datafile = open('111920_Signals_M2.csv', 'r')
reader = csv.reader(datafile)

Ions = []
Tolerance = []
for row in reader:
    Ions.append(float(row[0]))
    Tolerance.append(float(row[1]))

images = []
```

```
for i,t in zip(Ions, Tolerance):
    image = (getionimage(slide, i, tol=t)[Y1:Y2, X1:X2])
    im = ndimage.rotate(image, Degree_rotation, reshape=True)
    images.append(im)
# Images of the selected signals

length = len(images)
rows_graph = math.ceil(length/5)

plt.figure(figsize=(18, 28))
for n,im in enumerate(images):
    ax = plt.subplot(rows_graph, 5, (n+1))
    plt.imshow(im)
    plt.axis('off')
    plt.colorbar()
    plt.title('m/z {0}'.format(Ions[n]))
plt.show()
```

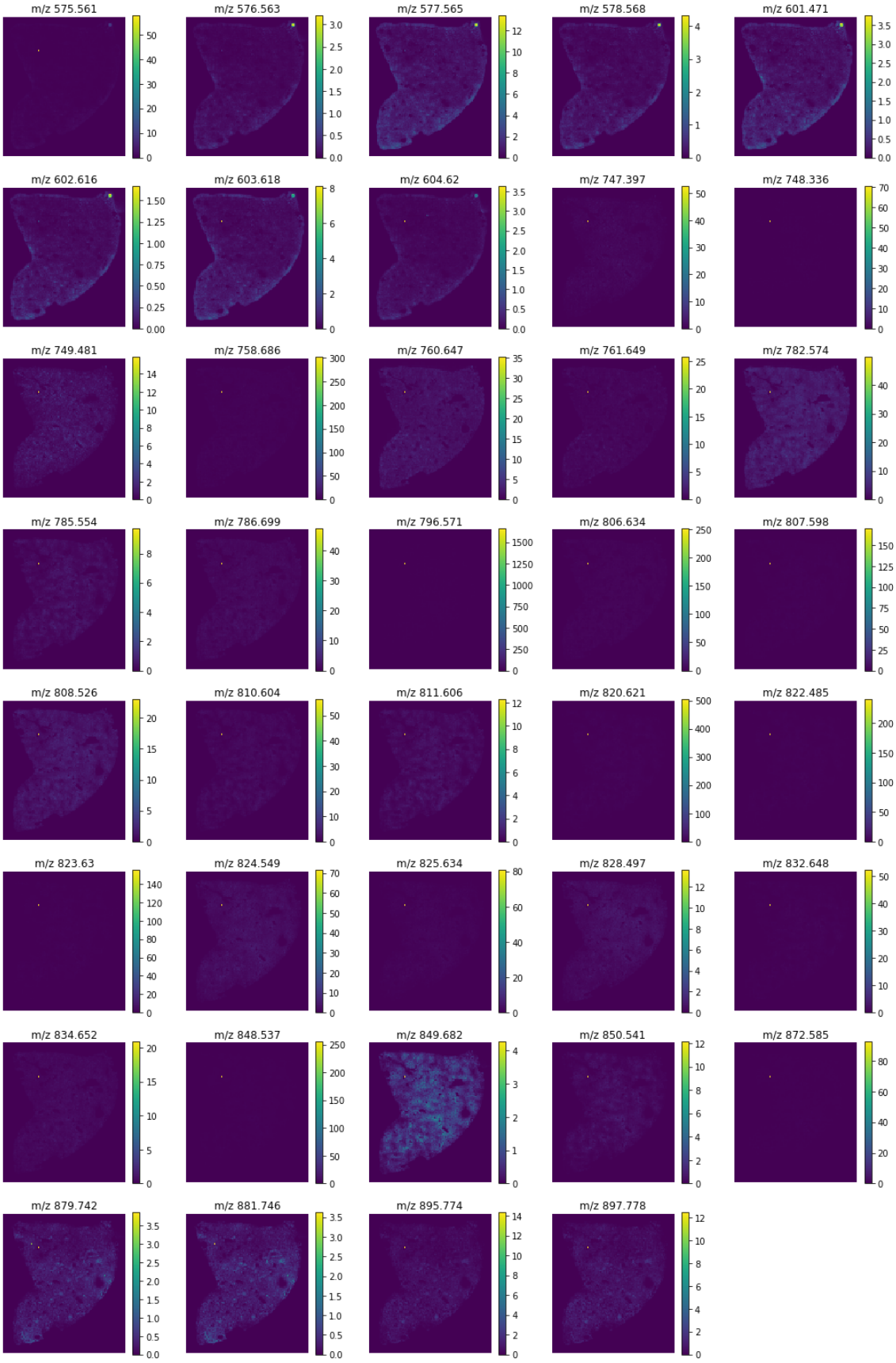
m/z 575.561
m/z 576.563
m/z 577.565
m/z 578.568
m/z 601.471
m/z 602.616
m/z 603.618
m/z 604.62
m/z 747.397
m/z 748.336
m/z 749.481
m/z 758.686
m/z 760.647
m/z 761.649
m/z 782.574
m/z 785.554
m/z 786.699
m/z 796.571
m/z 806.634
m/z 807.598
m/z 808.526
m/z 810.604
m/z 811.606
m/z 820.621
m/z 822.485
m/z 823.63
m/z 824.549
m/z 825.634
m/z 828.497
m/z 832.648
m/z 834.652
m/z 848.537
m/z 849.682
m/z 850.541
m/z 872.585
m/z 879.742
m/z 881.746
m/z 895.774
m/z 897.778

Rendering of MALDI images after hotspot removal

```
images_hotspot = images.copy()

plt.figure(figsize=(18, 28))
for n,im in enumerate(images_hotspot):
    Quantile_99 = np.quantile(im, 0.99)
    im[im > Quantile_99] = Quantile_99
    ax = plt.subplot(rows_graph, 5, (n+1))
    plt.imshow(im)
    plt.axis('off')
    plt.colorbar()
    plt.title('m/z {0}'.format(Ions[n]))
plt.show()

np.savetxt('D1_mz_796.csv', images_hotspot[17], delimiter=',')
```

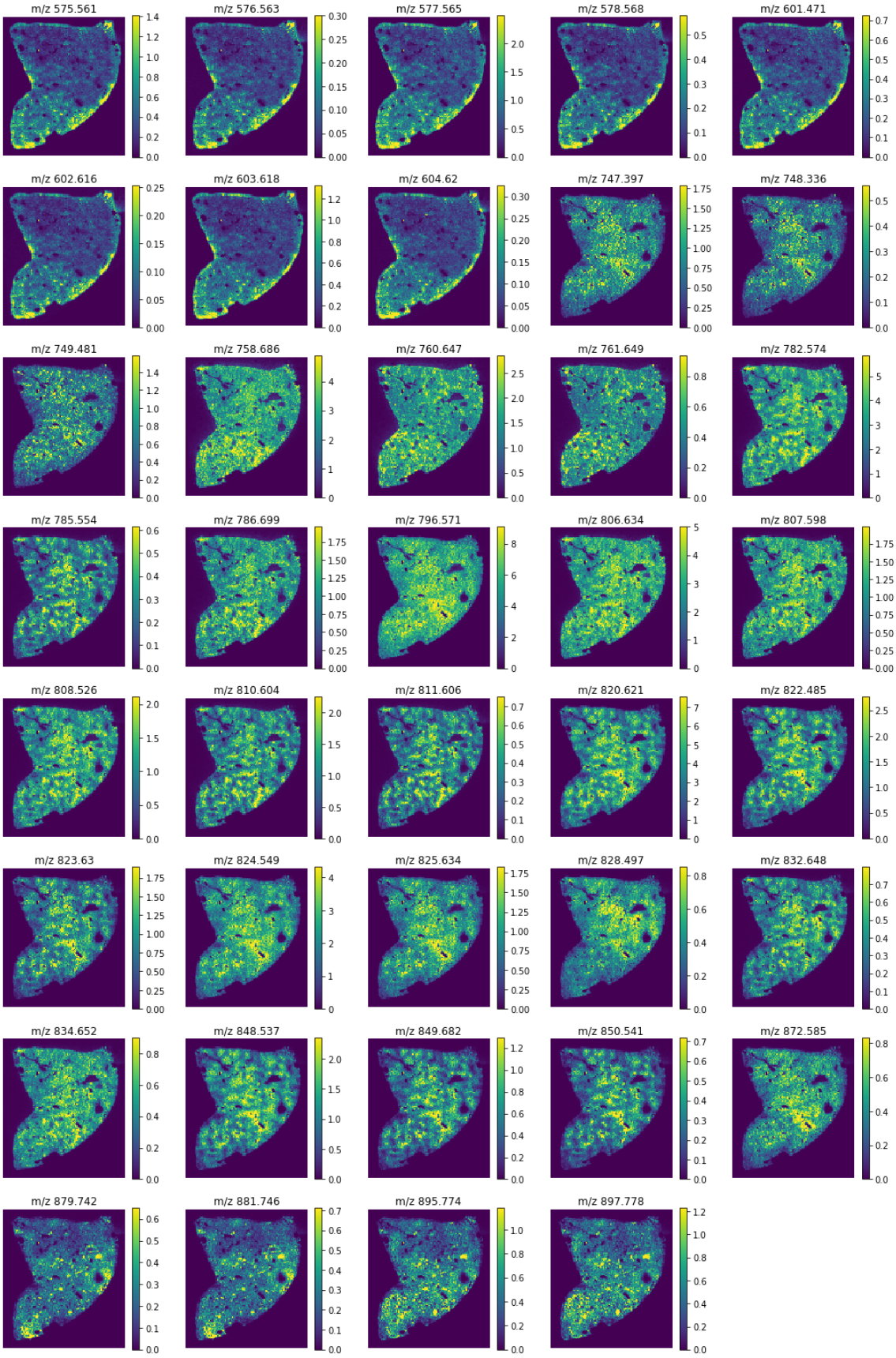
m/z 575.561
m/z 576.563
m/z 577.565
m/z 578.568
m/z 601.471
m/z 602.616
m/z 603.618
m/z 604.62
m/z 747.397
m/z 748.336
m/z 749.481
m/z 758.686
m/z 760.647
m/z 761.649
m/z 782.574
m/z 785.554
m/z 786.699
m/z 796.571
m/z 806.634
m/z 807.598
m/z 808.526
m/z 810.604
m/z 811.606
m/z 820.621
m/z 822.485
m/z 823.63
m/z 824.549
m/z 825.634
m/z 828.497
m/z 832.648
m/z 834.652
m/z 848.537
m/z 849.682
m/z 850.541
m/z 872.585
m/z 879.742
m/z 881.746
m/z 895.774
m/z 897.778

```
# Save all the coregistered data in a .npy file to open it in a new script

MALDI_M2_All = np.array(images_hotspot)

np.save('MALDI_M2_All', MALDI_M2_All)
```

t-SNE dimensionality reduction of each analyte in 3D embedded space

```
# Upload of background mask used for substract background

MALDI_BM = np.loadtxt('M2_MALDI_796_mask.csv', delimiter=',')
MALDI_BM[MALDI_BM == 255] = 1

# Generate array of vectorized images for dimensionality reduction

rows = images[0].shape[0]
columns = images[0].shape[1]

n_images = len(images)
n_pixels = len(MALDI_BM[MALDI_BM == 1])

print('Total number of pixels per image:', rows*columns)
print('Number of tissue pixels', len(MALDI_BM[MALDI_BM == 1]))
print('Number of background pixels', len(MALDI_BM[MALDI_BM == 0]))

vector_3D_raw = np.zeros((n_images, n_pixels))
vector_3D_hot = np.zeros((n_images, n_pixels))

flat_mask = MALDI_BM.reshape(rows*columns)

for n, image in enumerate(images):
    flat_raw = image.reshape(rows*columns)
    vector_3D_raw[n,:] = flat_raw[flat_mask==1]

for n, image in enumerate(images_hotspot):
    flat_hot = image.reshape(rows*columns)
    vector_3D_hot[n,:] = flat_hot[flat_mask==1]
```

```
Total number of pixels per image: 12600
Number of tissue pixels 6964
Number of background pixels 5636
```

```
from sklearn import manifold
from mpl_toolkits.mplot3d import Axes3D

# Apply tsn to the vectorized images, with and without hotspots

tsne_3D = manifold.TSNE(n_components=3, random_state=0)
vector_tsne_3D_raw = tsne_3D.fit_transform(vector_3D_raw)
vector_tsne_3D_hot = tsne_3D.fit_transform(vector_3D_hot)

print('vector images 3D without reduction:', vector_3D_raw.shape,
vector_3D_hot.shape)
print('vector images 3D tsne reduced dimensions', vector_tsne_3D_raw.shape,
vector_tsne_3D_hot.shape)

# Separation of the reduced matrix into component vectors

X_3D_raw = vector_tsne_3D_raw[:,0]
```

```
Y_3D_raw = vector_tsne_3D_raw[:,1]
Z_3D_raw = vector_tsne_3D_raw[:,2]

X_3D_hot = vector_tsne_3D_hot[:,0]
Y_3D_hot = vector_tsne_3D_hot[:,1]
Z_3D_hot = vector_tsne_3D_hot[:,2]

# Images of the embedded space classification in 3D

fig = plt.figure(figsize=(18, 8))

ax = fig.add_subplot(121, projection='3d')
ax.scatter(X_3D_raw, Y_3D_raw, Z_3D_raw, c='r', marker='o')
for i, ion in enumerate(Ions):
    ax.text(X_3D_raw[i], Y_3D_raw[i], Z_3D_raw[i], ion)
plt.title('Embedded Space Raw')

ax = fig.add_subplot(122, projection='3d')
ax.scatter(X_3D_hot, Y_3D_hot, Z_3D_hot, c='r', marker='o')
for i, ion in enumerate(Ions):
    ax.text(X_3D_hot[i], Y_3D_hot[i], Z_3D_hot[i], ion)
plt.title('Embedded Space without Hotspot')

plt.show()
```

```
vector images 3D without reduction: (39, 6964) (39, 6964)
vector images 3D tsne reduced dimensions (39, 3) (39, 3)
```

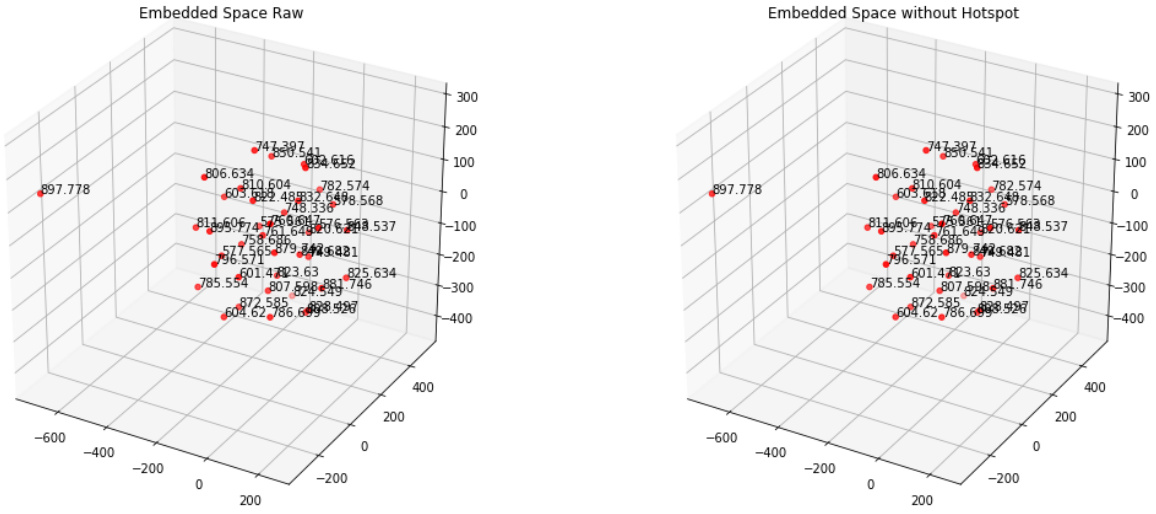

t-SNE dimensionality reduction for single image representation

```
# initial vector used for classification in the embedded space is transposed
for reduction in the other dimension

vector_seg_raw = vector_3D_raw.T
vector_seg_hot = vector_3D_hot.T

print('vector images before tsne seg:', vector_seg_raw.shape,
vector_seg_hot.shape)
```

```
# Aplication of the TSNE dimensionality reduction to 3 image channels of only
tissue pixels (no backgroung)

tsne_seg = manifold.TSNE(n_components=3, random_state=0)
vector_tsne_seg_raw_tissue = tsne_seg.fit_transform(vector_seg_raw)
vector_tsne_seg_hot_tissue = tsne_seg.fit_transform(vector_seg_hot)

print('vector images after tsne seg:', vector_tsne_seg_raw_tissue.shape,
vector_tsne_seg_hot_tissue.shape)
```

```
vector images before tsne seg: (6964, 39) (6964, 39)
vector images after tsne seg: (6964, 3) (6964, 3)
```

```
# Generation of a set of vectors that will correspond to the reduced images
plus background pixels for proper
# image reconstruction vector_tsne_seg_raw and vector_tsne_seg_hot

vector_tsne_seg_raw = np.zeros((rows*columns, 3))
vector_tsne_seg_hot = np.zeros((rows*columns, 3))

# for loop over the three reduced vectors that will introduce the background
pixels that were removed for tsne
# to introduce the 0 bacgkround pixels, the minimum value of the image should
be zero, so the minimum value should
# be substracted in the loop.

for n in range(0,3):
    vector_tsne_seg_raw[:,n][flat_mask==1]=vector_tsne_seg_raw_tissue[:,n]-
np.min(vector_tsne_seg_raw_tissue[:,n])
    vector_tsne_seg_hot[:,n][flat_mask==1]=vector_tsne_seg_hot_tissue[:,n]-
np.min(vector_tsne_seg_hot_tissue[:,n])

# Separation of the 3 image into the three components of the embedded space

X_seg_raw = vector_tsne_seg_raw[:,0]
Y_seg_raw = vector_tsne_seg_raw[:,1]
Z_seg_raw = vector_tsne_seg_raw[:,2]

X_seg_hot = vector_tsne_seg_hot[:,0]
Y_seg_hot = vector_tsne_seg_hot[:,1]
Z_seg_hot = vector_tsne_seg_hot[:,2]

# Plot of the embedded spcae for the reduced data

fig = plt.figure(figsize=(18, 8))
ax = fig.add_subplot(121, projection='3d')
ax.scatter(X_seg_raw, Y_seg_raw, Z_seg_raw, c='b', marker='o')
plt.title('Embedded Space Raw Data')
ax = fig.add_subplot(122, projection='3d')
ax.scatter(X_seg_hot, Y_seg_hot, Z_seg_hot, c='b', marker='o')
plt.title('Embedded Space Hotspot Removal Data')
plt.show()
```

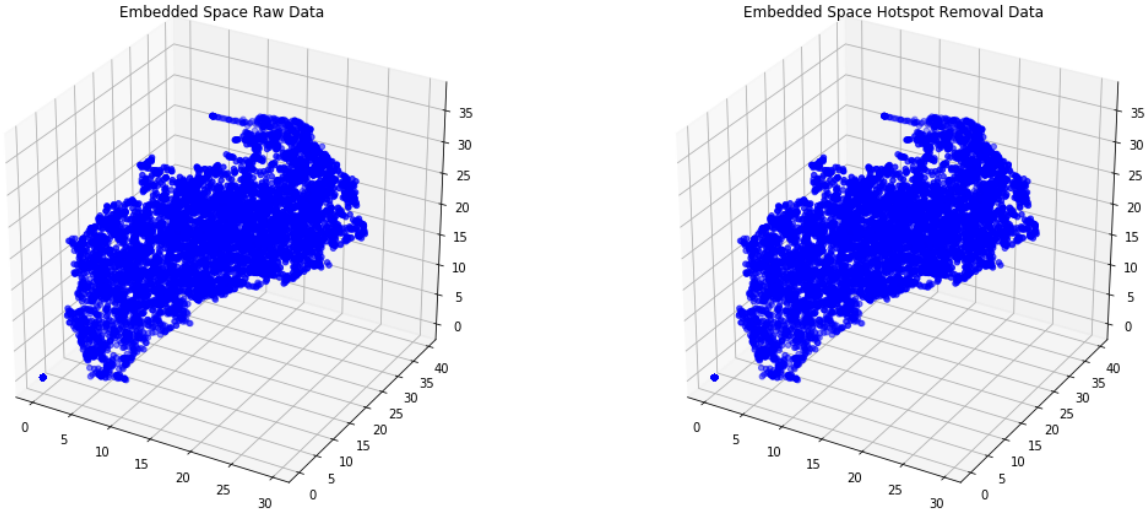


```
# Normalization of the 3 reduced images to the 0-255 scale

# Calculation of max values of the positive scale images for normalization to
the 255 scale:

X_seg_raw_max, Y_seg_raw_max, Z_seg_raw_max = np.max(X_seg_raw),
np.max(Y_seg_raw), np.max(Z_seg_raw)
X_seg_hot_max, Y_seg_hot_max, Z_seg_hot_max = np.max(X_seg_hot),
np.max(Y_seg_hot), np.max(Z_seg_hot)

print('X raw and hot max:', X_seg_raw_max, X_seg_hot_max)
print('Y raw and hot max:', Y_seg_raw_max, Y_seg_hot_max)
print('Z raw and hot max:', Z_seg_raw_max, Z_seg_hot_max)

# Conversion of values to the RGB 255 scale:

X_seg_raw_RGB = ((X_seg_raw/X_seg_raw_max)*255)
Y_seg_raw_RGB = ((Y_seg_raw/Y_seg_raw_max)*255)
Z_seg_raw_RGB = ((Z_seg_raw/Z_seg_raw_max)*255)

X_seg_hot_RGB = ((X_seg_hot/X_seg_hot_max)*255)
Y_seg_hot_RGB = ((Y_seg_hot/Y_seg_hot_max)*255)
Z_seg_hot_RGB = ((Z_seg_hot/Z_seg_hot_max)*255)

# Plot of the scattered data:

fig = plt.figure(figsize=(18, 8))
ax = fig.add_subplot(121, projection='3d')
ax.scatter(X_seg_raw_RGB, Y_seg_raw_RGB, Z_seg_raw_RGB, c='b', marker='o')
plt.title('Embedded Space Raw Data')

ax = fig.add_subplot(122, projection='3d')
ax.scatter(X_seg_hot_RGB, Y_seg_hot_RGB, Z_seg_hot_RGB, c='b', marker='o')
plt.title('Embedded Space Hotspot Removal Data')
plt.show()
X raw and hot max: 29.78743553161621 29.78743553161621
Y raw and hot max: 39.464359283447266 39.464359283447266
Z raw and hot max: 36.77463150024414 36.77463150024414
```

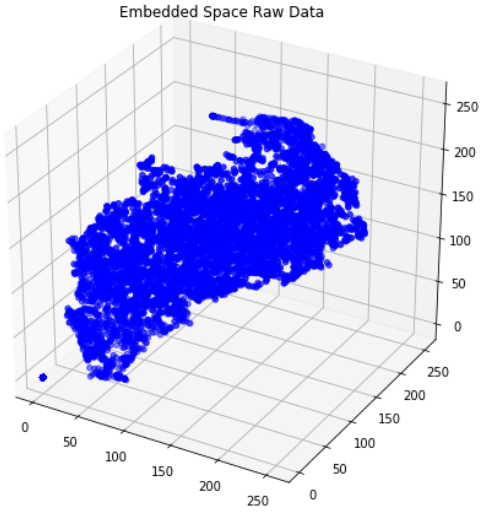

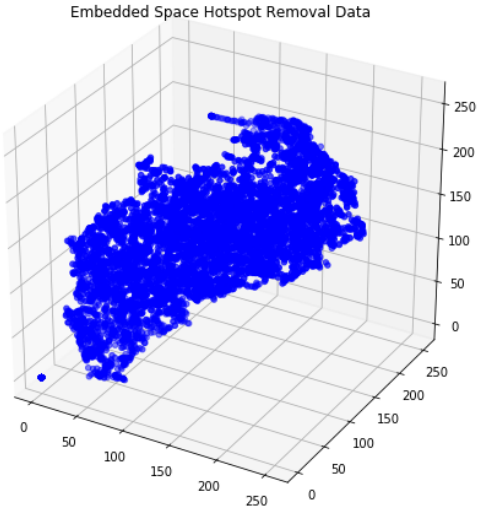


```
# Reshape of the 3 reduced vectors into 2D images

import seaborn as sns

X_seg_raw_RGB_rsp = X_seg_raw_RGB.reshape(rows, columns).astype(int)
Y_seg_raw_RGB_rsp = Y_seg_raw_RGB.reshape(rows, columns).astype(int)
Z_seg_raw_RGB_rsp = Z_seg_raw_RGB.reshape(rows, columns).astype(int)

X_seg_hot_RGB_rsp = X_seg_hot_RGB.reshape(rows, columns).astype(int)
Y_seg_hot_RGB_rsp = Y_seg_hot_RGB.reshape(rows, columns).astype(int)
Z_seg_hot_RGB_rsp = Z_seg_hot_RGB.reshape(rows, columns).astype(int)

print ('Reshaped Image Shape:', X_seg_raw_RGB_rsp.shape)

# image display in the 0-255 scale

plt.figure(figsize=(15, 10))
plt.subplot(2,3,1)
plt.imshow(X_seg_raw_RGB_rsp)
plt.colorbar()
plt.axis('off')
plt.title('Raw 1')
plt.subplot(2,3,2)
plt.imshow(Y_seg_raw_RGB_rsp)
plt.colorbar()
plt.axis('off')
plt.title('Raw 2')
plt.subplot(2,3,3)
plt.imshow(Z_seg_raw_RGB_rsp)
plt.colorbar()
plt.axis('off')
plt.title('Raw 3')
plt.subplot(2,3,4)
plt.imshow(X_seg_hot_RGB_rsp)
plt.colorbar()
plt.axis('off')
plt.title('Hot 1')
plt.subplot(2,3,5)
plt.imshow(Y_seg_hot_RGB_rsp)
plt.colorbar()
plt.axis('off')
```

```
plt.title('Hot 2')
plt.subplot(2,3,6)
plt.imshow(Z_seg_hot_RGB_rsp)
plt.colorbar()
plt.axis('off')
plt.title('Hot 3')
plt.show()
```

```
Reshaped Image Shape: (120, 105)
```

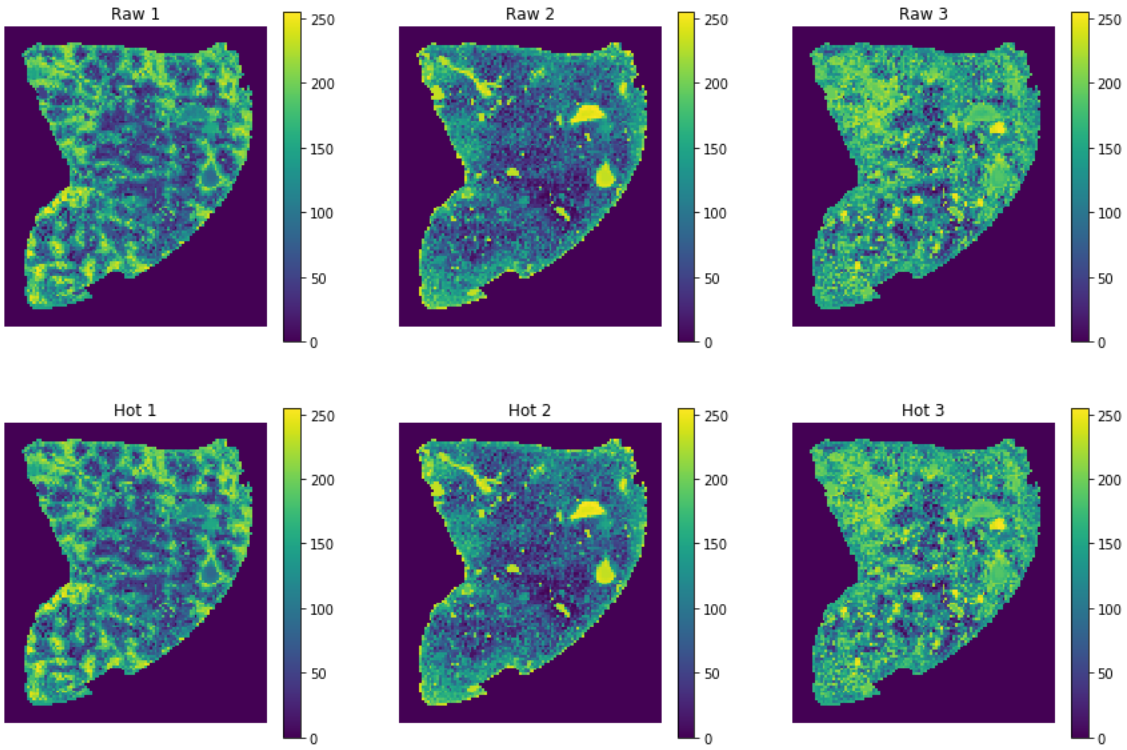

Display of the reduced images in RGB colors

```
# Display of the reduced images in the RGB colors

plt.figure(figsize=(15, 10))
plt.subplot(2,3,1)
cmap1 = sns.dark_palette("Red", as_cmap=True)
sns.heatmap(X_seg_raw_RGB_rsp, square=True, cmap=cmap1, xticklabels=False,
yticklabels=False)
plt.title('Raw 1')
plt.subplot(2,3,2)
cmap2 = sns.dark_palette("Green", as_cmap=True)
sns.heatmap(Y_seg_raw_RGB_rsp, square=True, cmap=cmap2, xticklabels=False,
yticklabels=False)
plt.title('Raw 3')
plt.subplot(2,3,3)
cmap3 = sns.dark_palette("Blue", as_cmap=True)
sns.heatmap(Z_seg_raw_RGB_rsp, square=True, cmap=cmap3, xticklabels=False,
yticklabels=False)
plt.title('Raw 4')
```

```
plt.subplot(2,3,4)
cmap1 = sns.dark_palette("Red", as_cmap=True)
sns.heatmap(X_seg_hot_RGB_rsp, square=True, cmap=cmap1, xticklabels=False,
yticklabels=False)
plt.title('Raw 1 BS')
plt.subplot(2,3,5)
cmap2 = sns.dark_palette("Green", as_cmap=True)
sns.heatmap(Y_seg_hot_RGB_rsp, square=True, cmap=cmap2, xticklabels=False,
yticklabels=False)
plt.title('Raw 2 BS')
plt.subplot(2,3,6)
cmap3 = sns.dark_palette("Blue", as_cmap=True)
sns.heatmap(Z_seg_hot_RGB_rsp, square=True, cmap=cmap3, xticklabels=False,
yticklabels=False)
plt.title('Raw 3 BS')
plt.show()
```

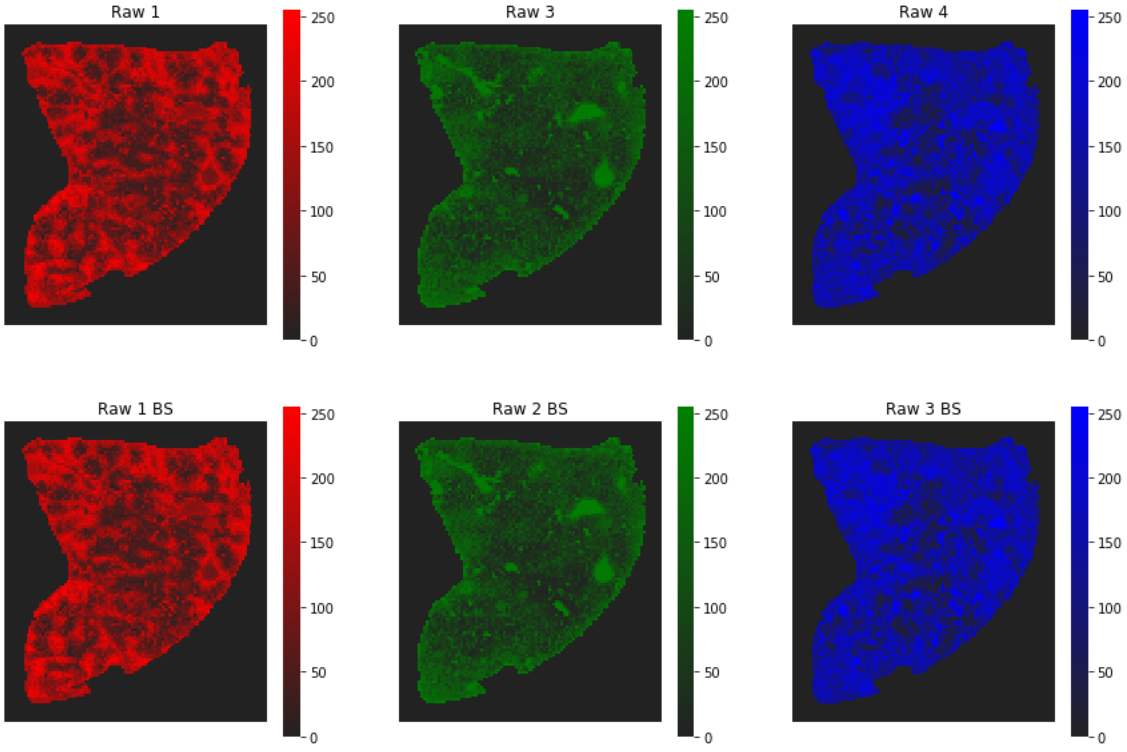


```
'''
    Merge of the RGB images into a color image using the merge approach in
cv2. The colors are different, due to
    all the possible color combinations:

        RGB_merged_1 merging of the images using cv2.merge and using R=X,
G=Y, B=Z
        RGB_merged_2 merging of the images using cv2.merge and using R=Z,
G=X, B=Y
'''

import cv2

RGB_merged_raw_1 = cv2.merge((X_seg_raw_RGB_rsp, Y_seg_raw_RGB_rsp,
Z_seg_raw_RGB_rsp))
```

```
RGB_merged_raw_2 = cv2.merge((Z_seg_raw_RGB_rsp, X_seg_raw_RGB_rsp,
Y_seg_raw_RGB_rsp))

RGB_merged_hot_1 = cv2.merge((X_seg_hot_RGB_rsp, Y_seg_hot_RGB_rsp,
Z_seg_raw_RGB_rsp))
RGB_merged_hot_2 = cv2.merge((Z_seg_hot_RGB_rsp, X_seg_hot_RGB_rsp,
Y_seg_raw_RGB_rsp))

print ('Shape of the merged image ', RGB_merged_raw_1.shape)

plt.figure(figsize=(18, 6))
plt.subplot(1,4,1)
plt.imshow(RGB_merged_raw_1)
plt.axis('off')
plt.subplot(1,4,2)
plt.imshow(RGB_merged_raw_2)
plt.axis('off')
plt.subplot(1,4,3)
plt.imshow(RGB_merged_hot_1)
plt.axis('off')
plt.subplot(1,4,4)
plt.imshow(RGB_merged_hot_2)
plt.axis('off')
plt.show()
```

```
Shape of the merged image  (120, 105, 3)
```

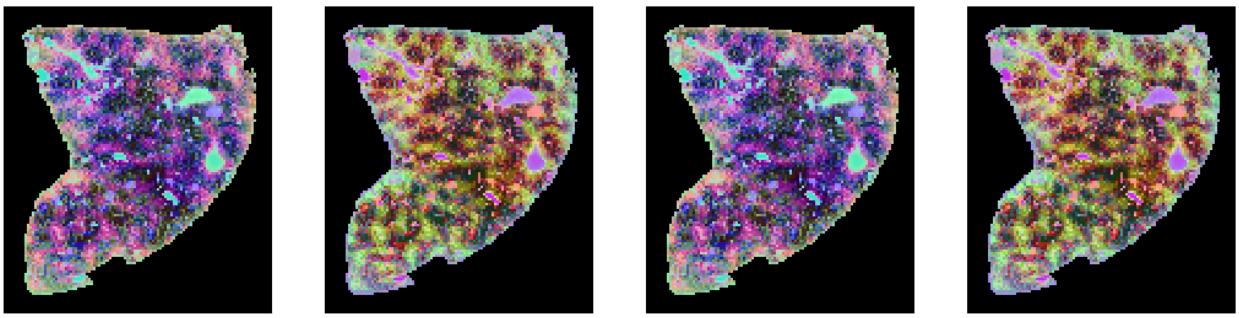

MALDI t-SNE reduction to one image

```
# Copy the input vector containing the tissue only data for segmentation

vector_R1_raw_tissue = vector_seg_raw.copy()
vector_R1_hot_tissue = vector_seg_hot.copy()

print('vector images before tsne seg:', vector_R1_raw_tissue.shape,
vector_R1_hot_tissue.shape)

# Aplication of the TSNE dimensionality reduction to 1 channels

tsne_R1 = manifold.TSNE(n_components=1, random_state=0)
vector_tsne_R1_raw_tissue = tsne_R1.fit_transform(vector_R1_raw_tissue)
vector_tsne_R1_hot_tissue = tsne_R1.fit_transform(vector_R1_hot_tissue)

print('vector images after tsne seg:', vector_tsne_R1_raw_tissue.shape)
```

```
vector images before tsne seg: (6964, 39) (6964, 39)
vector images after tsne seg: (6964, 1)
```

```
# Generation of a set of vectors that will correspond to the reduced images
plus background pixels for proper
# image reconstruction vector_tsne_seg_raw and vector_tsne_seg_hot

vector_tsne_R1_raw = np.zeros((rows*columns, 1))
vector_tsne_R1_hot = np.zeros((rows*columns, 1))

print('Image vector for the whole image', vector_tsne_R1_raw.shape)

# to introduce the 0 bacgkround pixels, the minimum value of the image should
be zero, so the minimum value should
# be substracted.

vector_tsne_R1_raw[flat_mask==1] = vector_tsne_R1_raw_tissue -
np.min(vector_tsne_R1_raw_tissue)
vector_tsne_R1_hot[flat_mask==1] = vector_tsne_R1_hot_tissue -
np.min(vector_tsne_R1_hot_tissue)

vector_R1_raw_norm = (vector_tsne_R1_raw/np.max(vector_tsne_R1_raw))*100
vector_R1_hot_norm = (vector_tsne_R1_hot/np.max(vector_tsne_R1_hot))*100

vector_R1_raw_rsp = vector_R1_raw_norm.reshape(rows, columns)
vector_R1_hot_rsp = vector_R1_hot_norm.reshape(rows, columns)

plt.figure(figsize=(15, 6))
plt.subplot(1,2,1)
plt.imshow(vector_R1_raw_rsp)
plt.colorbar()
plt.axis('off')
plt.title('R1 raw')
plt.subplot(1,2,2)
plt.imshow(vector_R1_hot_rsp)
plt.colorbar()
plt.axis('off')
plt.title('R1 hot')
plt.show()
```

```
Image vector for the whole image (12600, 1)
```

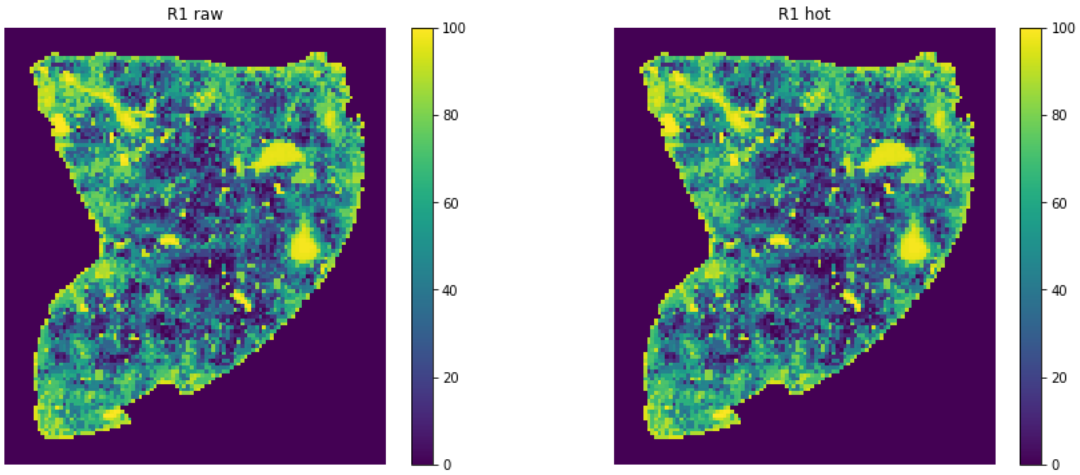


```
# save the t-sne images as .csv files and .npy images to use in the
registration script

np.savetxt('M2_MALDI_tSNE.csv', vector_R1_raw_rsp, delimiter=',')
```

Image pre-processing LA-ICP

```
# import LA-ICP data from text images

LA_1_raw = np.loadtxt('M2_LA_1.xl', delimiter=',')
LA_2_raw = np.loadtxt('M2_LA_2.xl', delimiter=',')
LA_3_raw = np.loadtxt('M2_LA_3.xl', delimiter=',')

plt.figure(figsize=(18, 6))
ax=plt.subplot(1, 3, 1)
plt.imshow(LA_1_raw)
plt.colorbar()
plt.axis('off')
plt.title('LA Fe')
ax=plt.subplot(1, 3, 2)
plt.imshow(LA_2_raw)
plt.colorbar()
plt.axis('off')
plt.title('LA Au')
ax=plt.subplot(1, 3, 3)
plt.imshow(LA_3_raw)
plt.colorbar()
plt.axis('off')
plt.title('LA Zn')
plt.show()
```

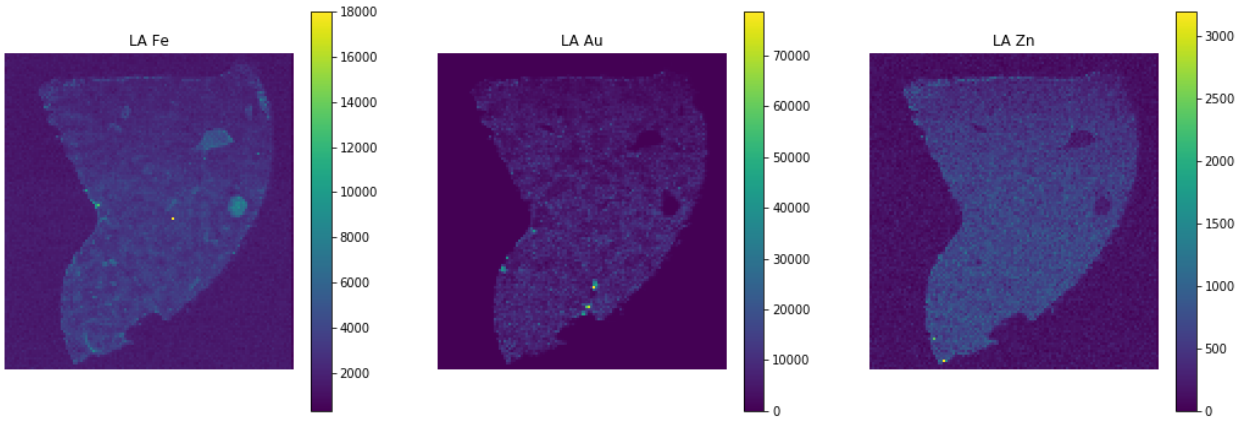

Hotspot removal LA-ICP

```
# We will calculate the 0.99 quantile range and assign the data points above
this value to the 0.99 value.

Q_LA_1 = np.quantile(LA_1_raw, 0.99)
Q_LA_2 = np.quantile(LA_2_raw, 0.99)
Q_LA_3 = np.quantile(LA_3_raw, 0.99)

print('Quantile of LA images is:', Q_LA_1, Q_LA_2, Q_LA_3)

LA_1_hot = LA_1_raw.copy()
LA_2_hot = LA_2_raw.copy()
LA_3_hot = LA_3_raw.copy()
```

```
LA_1_hot[LA_1_raw > Q_LA_1] = Q_LA_1
LA_2_hot[LA_2_raw > Q_LA_2] = Q_LA_2
LA_3_hot[LA_3_raw > Q_LA_3] = Q_LA_3

# box and whisker plots

row_LA, col_LA = LA_1_raw.shape

print ('LA image shape:', LA_1_raw.shape)

vector_LA_1_raw = LA_1_raw.reshape(row_LA*col_LA)
vector_LA_2_raw = LA_2_raw.reshape(row_LA*col_LA)
vector_LA_3_raw = LA_3_raw.reshape(row_LA*col_LA)

vector_LA_1_hot = LA_1_hot.reshape(row_LA*col_LA)
vector_LA_2_hot = LA_2_hot.reshape(row_LA*col_LA)
vector_LA_3_hot = LA_3_hot.reshape(row_LA*col_LA)

plt.figure(figsize=(18, 15))
ax = plt.subplot(3, 3, 1)
plt.imshow(LA_1_raw)
plt.colorbar()
plt.axis('off')
plt.title('LA 1 raw')
ax = plt.subplot(3, 3, 2)
plt.imshow(LA_1_hot)
plt.colorbar()
plt.axis('off')
plt.title('LA 1 hot')
ax = plt.subplot(3, 3, 3)
plt.boxplot([vector_LA_1_raw, vector_LA_1_hot])
plt.title('LA 1 boxplot')
ax = plt.subplot(3, 3, 4)
plt.imshow(LA_2_raw)
plt.colorbar()
plt.axis('off')
plt.title('LA 2 raw')
ax = plt.subplot(3, 3, 5)
plt.imshow(LA_2_hot)
plt.colorbar()
plt.axis('off')
plt.title('LA 2 hot')
ax = plt.subplot(3, 3, 6)
plt.boxplot([vector_LA_2_raw, vector_LA_2_hot])
plt.title('LA 2 boxplot')
ax = plt.subplot(3, 3, 7)
plt.imshow(LA_3_raw)
plt.colorbar()
plt.axis('off')
plt.title('LA 3 raw')
ax = plt.subplot(3, 3, 8)
plt.imshow(LA_3_hot)
plt.colorbar()
plt.axis('off')
plt.title('LA 3 hot')
ax = plt.subplot(3, 3, 9)
plt.boxplot([vector_LA_3_raw, vector_LA_3_hot])
plt.title('LA boxplot')
plt.show()
Quantile of LA images is: 5015.872981954924 14492.288902966888 940.002934010539
LA image shape: (129, 118)
```

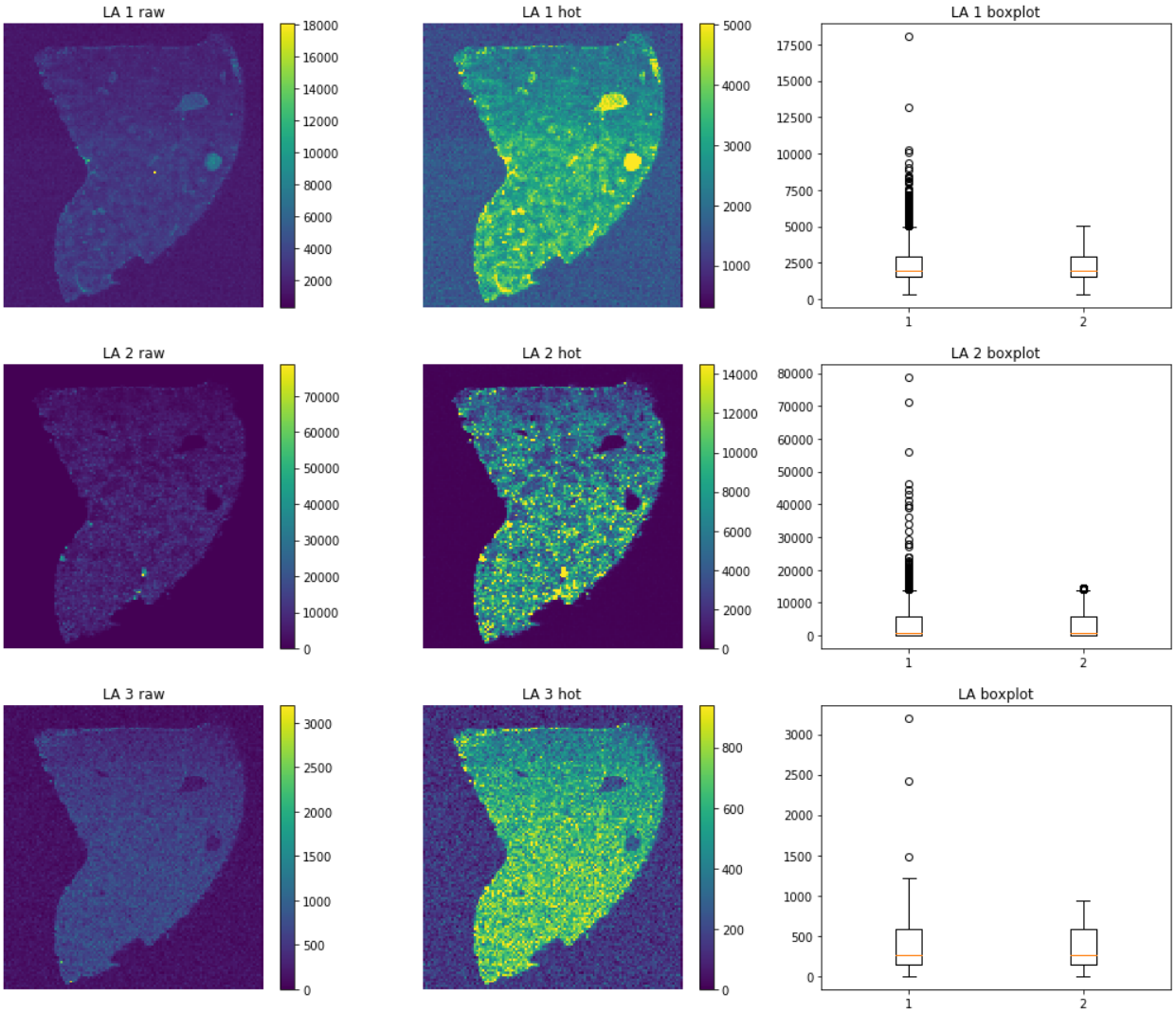


```
# Vectorize the images from the images to a matrix vector_images_seg with
dimensions(n_pixels_seg, n_signals_seg)

n_pixels_LA = row_LA*col_LA
n_signals_LA = 3

vector_images_LA = np.zeros((n_pixels_LA, n_signals_LA))

vector_images_LA[:,0] = vector_LA_1_hot
vector_images_LA[:,1] = vector_LA_2_hot
vector_images_LA[:,2] = vector_LA_3_hot

print('vector images shape:', vector_images_LA.shape)

# Aplication of the TSNE dimensionality reduction to 1 channel

tsne_LA = manifold.TSNE(n_components=1, random_state=0)
reduction_tsne_LA = tsne_LA.fit_transform(vector_images_LA)

print('LA tsne reduction:', reduction_tsne_LA.shape)
```

```
vector images shape: (15222, 3)
LA tsne reduction: (15222, 1)
```

```
# Image the TSNE one channel reduction to LA

LA_tsne_reshaped = reduction_tsne_LA.reshape(row_LA, col_LA)
LA_tsne_reshaped = LA_tsne_reshaped.astype(int)

plt.imshow(LA_tsne_reshaped)
plt.colorbar()
plt.axis('off')
plt.title('LA image segmentation')
plt.show()
```

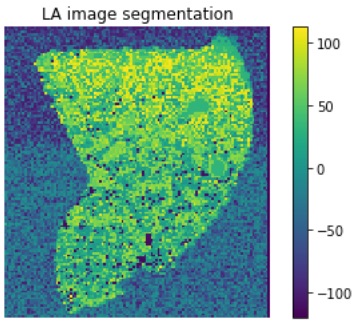


```
# save the LA-ICP Fe image as .csv files and .npy images to use in the
registration script

np.savetxt('M2_LA_hot_1.csv', LA_1_hot, delimiter=',')
np.savetxt('M2_LA_hot_2.csv', LA_2_hot, delimiter=',')
np.savetxt('M2_LA_hot_3.csv', LA_3_hot, delimiter=',')
```

Registration and validation of MALDI and LA-ICP images

```
import SimpleITK as sitk
import numpy as np
import matplotlib.pyplot as plt
import PIL
# import images from the pre-processing script for MALDI t-SNE and LA-ICP -
image crop

from numpy import loadtxt

LA_background_mask = np.loadtxt('M2_LA_Background_Mask.csv', delimiter=',')
LA_background_mask[LA_background_mask == 255] = 1

LA_raw = loadtxt('M2_LA_hot_1.csv', delimiter=',')
LA_BS = LA_raw*LA_background_mask
LA_crop = LA_BS[0:129, 5:118]

MALDI_raw = loadtxt('M2_MALDI_tSNE.csv', delimiter=',')

print('LA raw:',LA_raw.shape,'LA crop:',LA_crop.shape,'MALDI
raw:',MALDI_raw.shape)

plt.figure(figsize=(18, 10))
ax=plt.subplot(1, 4, 1)
plt.imshow(LA_raw, cmap='Reds')
```

```
plt.axis('off')
plt.title('LA raw Fe')
ax=plt.subplot(1, 4, 2)
plt.imshow(LA_BS, cmap='Reds')
plt.axis('off')
plt.title('LA BS Fe')
ax=plt.subplot(1, 4, 3)
plt.imshow(LA_crop, cmap='Reds')
plt.axis('off')
plt.title('LA cropped Fe')
ax=plt.subplot(1, 4, 4)
plt.imshow(MALDI_raw, cmap='Blues')
plt.axis('off')
plt.title('MALDI t-SNE')
plt.show()

#np.savetxt('M2_LA_reg_input.csv', LA_crop, delimiter=',')
#np.savetxt('M2_MALDI_reg_input.csv', MALDI_raw, delimiter=',')
```

```
LA raw: (129, 118) LA crop: (129, 113) MALDI raw: (120, 105)
```

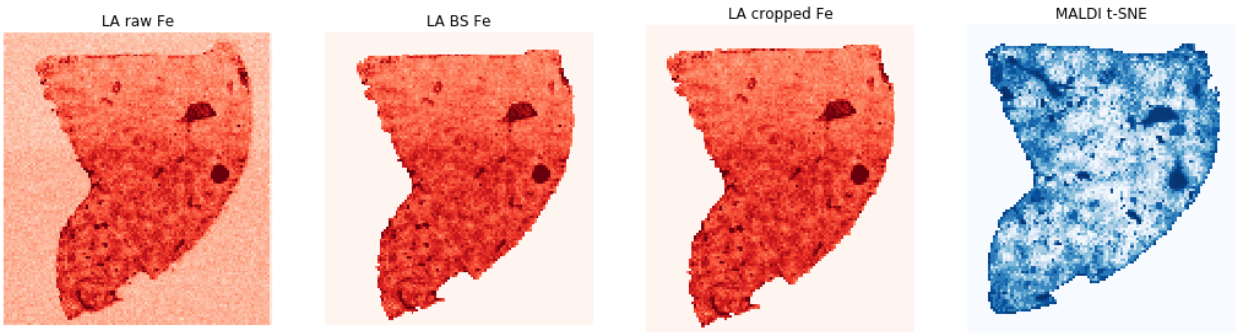

Upload segment masks

```
# Segment masks obtained in imagej

LA_mask = np.loadtxt('M2_LA_reg_mask.csv', delimiter=',')[0:129, 5:118]
LA_mask[LA_mask == 255] = 1

MALDI_mask = np.loadtxt('M2_MALDI_reg_mask.csv', delimiter=',')
MALDI_mask[MALDI_mask == 255] = 1

LA_norm = LA_crop/np.amax(LA_crop)
MALDI_norm = MALDI_raw/np.amax(MALDI_raw)

plt.figure(figsize=(18, 9))
ax=plt.subplot(1,4,1)
plt.imshow(MALDI_norm, cmap='Blues')
plt.axis('off')
plt.title('MALDI image')
ax=plt.subplot(1,4,2)
plt.imshow(MALDI_norm, cmap='Blues', alpha=0.8)
plt.axis('off')
plt.imshow(MALDI_mask, cmap='Greys', alpha=0.6)
plt.axis('off')
plt.title('MALDI overlay')
ax=plt.subplot(1,4,3)
```

```
plt.imshow(LA_norm, cmap='Reds')
plt.axis('off')
plt.title('LA image')
ax=plt.subplot(1,4,4)
plt.imshow(LA_norm, cmap='Reds', alpha=0.8)
plt.axis('off')
plt.imshow(LA_mask, cmap='Greys', alpha=0.6)
plt.axis('off')
plt.title('LA overlay')
plt.show()
```

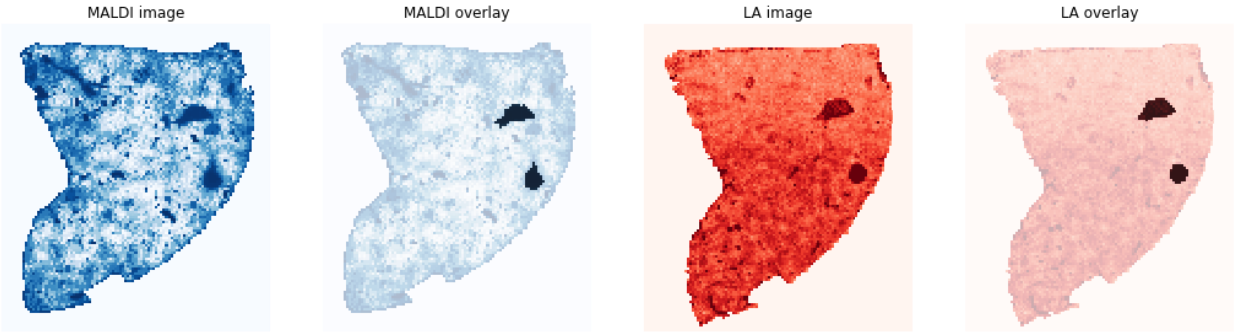

Upload images for registration

```
# Uploading Fixed and Moving images in simpleelastix

FixedImage = sitk.GetImageFromArray(MALDI_raw)
MovingImage = sitk.GetImageFromArray(LA_crop)

print ('Fixed image type:', type(FixedImage), 'Input image shape:',
np.shape(FixedImage))
print ('Moving image type:', type(MovingImage), 'Input image shape:',
np.shape(MovingImage))
```

```
Fixed image type: <class 'SimpleITK.SimpleITK.Image'> Input image shape: (12600,)
Moving image type: <class 'SimpleITK.SimpleITK.Image'> Input image shape: (14577,)
```

Translation registration

```
# Set the fixed and moving images, the parameter map and execute the
calculation with translation

parameterMap_1 = sitk.GetDefaultParameterMap('translation')

elastixImageFilter = sitk.ElastixImageFilter()
elastixImageFilter.SetFixedImage(FixedImage)
elastixImageFilter.SetMovingImage(MovingImage)
elastixImageFilter.SetParameterMap(parameterMap_1)
elastixImageFilter.Execute()

# Obtain result image and transform parameter map

ResultImage_1 = elastixImageFilter.GetResultImage()
transformParameterMap_1 = elastixImageFilter.GetTransformParameterMap()
```

```
# Convert SITK images to np arrays for visualization of the result and input
images in Matplotlib

ResultArray_1 = sitk.GetArrayFromImage(ResultImage_1)

FixedArray = sitk.GetArrayFromImage(FixedImage)
MovingArray = sitk.GetArrayFromImage(MovingImage)

# Normalization of the images for proper overlap

FixedArrayNorm = FixedArray/np.amax(FixedArray)
MovingArrayNorm = MovingArray/np.amax(MovingArray)
ResultArrayNorm_1 = ResultArray_1/np.amax(ResultArray_1)

# Rendering of the translation optimization

plt.figure(figsize=(18,8))
ax = plt.subplot(1, 5, 1)
plt.imshow(FixedArray, cmap='Blues')
plt.axis('off')
plt.title('Fixed Image')
ax = plt.subplot(1, 5, 2)
plt.imshow(MovingArray, cmap='Reds')
plt.axis('off')
plt.title('Moving Image')
ax = plt.subplot(1, 5, 3)
plt.imshow(ResultArray_1, cmap='Reds')
plt.axis('off')
plt.title('Result Image')
ax = plt.subplot(1, 5, 4)
plt.imshow(FixedArrayNorm, cmap='Blues', alpha=0.8)
plt.axis('off')
plt.imshow(MovingArrayNorm, cmap='Reds', alpha=0.4)
plt.axis('off')
plt.title('Before optimization')
ax = plt.subplot(1, 5, 5)
plt.imshow(FixedArrayNorm, cmap='Blues', alpha=0.8)
plt.axis('off')
plt.imshow(ResultArrayNorm_1, cmap='Reds', alpha=0.4)
plt.axis('off')
plt.title ('After optimization')
plt.show()
```

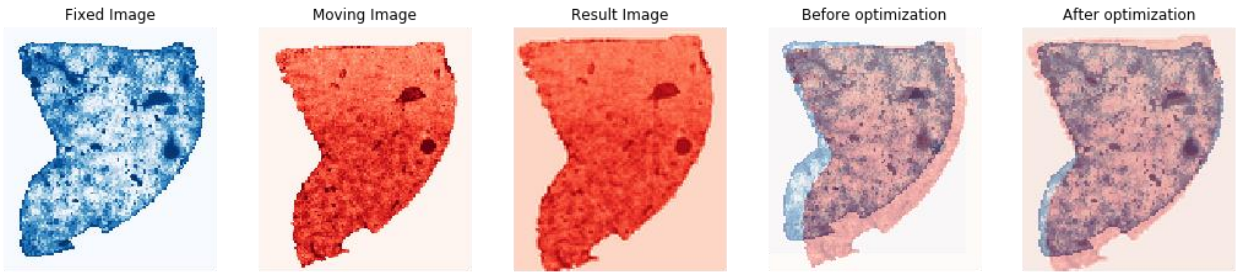

Rigid registration

```
# Set the fixed and moving images, the parameter map and execute the
calculation with rigid
```

```
parameterMap_2 = sitk.GetDefaultParameterMap('rigid')
parameterMap_2['MaximumNumberOfIterations'] = ['2000']

elastixImageFilter = sitk.ElastixImageFilter()
elastixImageFilter.SetFixedImage(FixedImage)
elastixImageFilter.SetMovingImage(MovingImage)
elastixImageFilter.SetParameterMap(parameterMap_2)
elastixImageFilter.Execute()

# Obtain result image and transform parameter map

ResultImage_2 = elastixImageFilter.GetResultImage()
transformParameterMap_2 = elastixImageFilter.GetTransformParameterMap()
# Convert SITK image to np arrays for visualization of the input images in
Matplotlib

ResultArray_2 = sitk.GetArrayFromImage(ResultImage_2)

# Normalization of the images for proper overlap

ResultArrayNorm_2 = ResultArray_2/np.amax(ResultArray_2)

# Rendering of the translation optimization

plt.figure(figsize=(18,8))
ax = plt.subplot(1, 5, 1)
plt.imshow(FixedArray, cmap='Blues')
plt.axis('off')
plt.title('Fixed Image')
ax = plt.subplot(1, 5, 2)
plt.imshow(MovingArray, cmap='Reds')
plt.axis('off')
plt.title('Moving Image')
ax = plt.subplot(1, 5, 3)
plt.imshow(ResultArray_2, cmap='Reds')
plt.axis('off')
plt.title('Result Image')
ax = plt.subplot(1, 5, 4)
plt.imshow(FixedArrayNorm, cmap='Blues', alpha=0.8)
plt.axis('off')
plt.imshow(MovingArrayNorm, cmap='Reds', alpha=0.4)
plt.axis('off')
plt.title('Before optimization')
ax = plt.subplot(1, 5, 5)
plt.imshow(FixedArrayNorm, cmap='Blues', alpha=0.8)
plt.axis('off')
plt.imshow(ResultArrayNorm_2, cmap='Reds', alpha=0.4)
plt.axis('off')
plt.title ('After optimization')
plt.show()
```

Affine registration

```
# Set the fixed and moving images, the parameter map and execute the
calculation with affine

parameterMap_3 = sitk.GetDefaultParameterMap('affine')
parameterMap_3['MaximumNumberOfIterations'] = ['4000']

elastixImageFilter = sitk.ElastixImageFilter()
elastixImageFilter.SetFixedImage(FixedImage)
elastixImageFilter.SetMovingImage(MovingImage)
elastixImageFilter.SetParameterMap(parameterMap_3)
elastixImageFilter.Execute()

# Obtain result image and transform parameter map

ResultImage_3 = elastixImageFilter.GetResultImage()
transformParameterMap_3 = elastixImageFilter.GetTransformParameterMap()
# Convert SITK image to np arrays for visualization of the input images in
Matplotlib

ResultArray_3 = sitk.GetArrayFromImage(ResultImage_3)

# Normalization of the images for proper overlap

ResultArrayNorm_3 = ResultArray_3/np.amax(ResultArray_3)

# Rendering of the translation optimization

plt.figure(figsize=(18,8))
ax = plt.subplot(1, 5, 1)
plt.imshow(FixedArray, cmap='Blues')
plt.axis('off')
plt.title('Fixed Image')
ax = plt.subplot(1, 5, 2)
plt.imshow(MovingArray, cmap='Reds')
plt.axis('off')
plt.title('Moving Image')
ax = plt.subplot(1, 5, 3)
plt.imshow(ResultArray_3, cmap='Reds')
plt.axis('off')
plt.title('Result Image')
ax = plt.subplot(1, 5, 4)
plt.imshow(FixedArrayNorm, cmap='Blues', alpha=0.8)
plt.axis('off')
plt.imshow(MovingArrayNorm, cmap='Reds', alpha=0.4)
plt.axis('off')
plt.title('Before optimization')
ax = plt.subplot(1, 5, 5)
plt.imshow(FixedArrayNorm, cmap='Blues', alpha=0.8)
plt.axis('off')
plt.imshow(ResultArrayNorm_3, cmap='Reds', alpha=0.4)
plt.axis('off')
plt.title ('After optimization')
plt.show()
```

Non-linear registration

```
elastixImageFilter = sitk.ElastixImageFilter()
elastixImageFilter.SetFixedImage(FixedImage)
elastixImageFilter.SetMovingImage(MovingImage)

parameterMapVector = sitk.VectorOfParameterMap()

parameterMapAffine = sitk.GetDefaultParameterMap('affine')
parameterMapAffine['MaximumNumberOfIterations'] = ['4000']

parameterMapBspline = sitk.GetDefaultParameterMap("bspline")
parameterMapBspline['MaximumNumberOfIterations'] = ['8000']
parameterMapBspline['Metric'] = ['NormalizedMutualInformation']
parameterMapBspline['FinalGridSpacingInPhysicalUnits'] = ['50.00000']

parameterMapVector.append(parameterMapAffine)
parameterMapVector.append(parameterMapBspline)
elastixImageFilter.SetParameterMap(parameterMapVector)
elastixImageFilter.Execute()

# Obtain result image and transform parameter map

ResultImage_4 = elastixImageFilter.GetResultImage()
transformParameterMap_4 = elastixImageFilter.GetTransformParameterMap()
#Convert SITK image to np arrays for visualization of the input images in
Matplotlib

ResultArray_4 = sitk.GetArrayFromImage(ResultImage_4)

# Normalization of the images for proper overlap

ResultArrayNorm_4 = ResultArray_4/np.amax(ResultArray_4)

# Rendering of the translation optimization

plt.figure(figsize=(18,8))
ax = plt.subplot(1, 5, 1)
plt.imshow(FixedArray, cmap='Blues')
plt.axis('off')
plt.title('Fixed Image')
ax = plt.subplot(1, 5, 2)
plt.imshow(MovingArray, cmap='Reds')
plt.axis('off')
plt.title('Moving Image')
ax = plt.subplot(1, 5, 3)
plt.imshow(ResultArray_4, cmap='Reds')
plt.axis('off')
```

```
plt.title('Result Image')
ax = plt.subplot(1, 5, 4)
plt.imshow(FixedArrayNorm, cmap='Blues', alpha=0.8)
plt.axis('off')
plt.imshow(MovingArrayNorm, cmap='Reds', alpha=0.4)
plt.axis('off')
plt.title('Before optimization')
ax = plt.subplot(1, 5, 5)
plt.imshow(FixedArrayNorm, cmap='Blues', alpha=0.8)
plt.axis('off')
plt.imshow(ResultArrayNorm_4, cmap='Reds', alpha=0.4)
plt.axis('off')
plt.title ('After optimization')
plt.show()
```

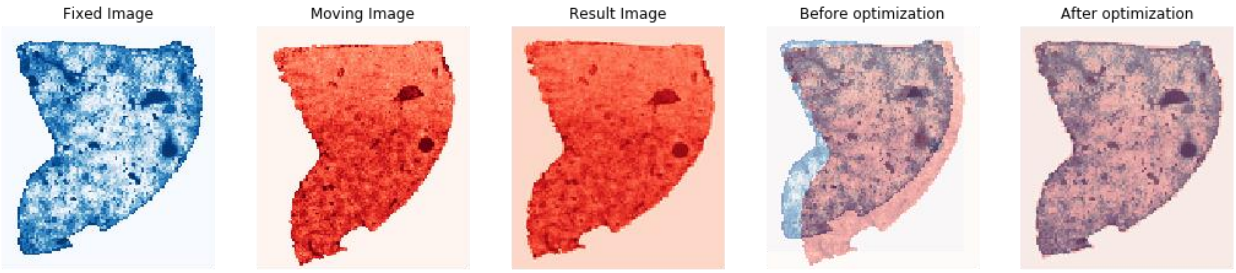

Transformation of the masks

```
# Transformation of the manual mask using the appropiate ParameterMap

transformixImageFilter = sitk.TransformixImageFilter()
transformixImageFilter.SetTransformParameterMap(transformParameterMap_4)

transformixImageFilter.SetMovingImage(sitk.GetImageFromArray(LA_mask))
transformixImageFilter.Execute()
LA_trans_mask =
sitk.GetArrayFromImage(transformixImageFilter.GetResultImage())

print('LA mask shape:', LA_mask.shape)
print('Transformed mask shape', LA_trans_mask.shape)

# Background_transformed is the transformed image

from sklearn.cluster import KMeans

rows_transformed = LA_trans_mask.shape[0]
columns_transformed = LA_trans_mask.shape[1]

transformed_vector =
LA_trans_mask.reshape(rows_transformed*columns_transformed, 1)
kmeans_background = KMeans(2)
kmeans_background.fit(transformed_vector)
transformed_segmented =
kmeans_background.cluster_centers_[kmeans_background.predict(transformed_vect
or)]

transformed_labels = kmeans_background.labels_
```

```
transformed_reshaped = transformed_segmented.reshape(rows_transformed,
columns_transformed)
centroids = np.sort(np.unique(transformed_segmented))
labels = np.zeros(transformed_segmented.shape)
for index, centroid in enumerate(centroids):
    labels[transformed_segmented==centroid] = index
LA_trans_final = labels.reshape(rows_transformed, columns_transformed)

plt.figure(figsize=(18,5))
ax = plt.subplot(1, 4, 1)
plt.imshow(LA_mask, cmap='gray')
plt.colorbar()
plt.axis('off')
plt.title('LA mask')
ax = plt.subplot(1, 4, 2)
plt.imshow(LA_trans_mask, cmap='gray')
plt.colorbar()
plt.axis('off')
plt.title('Transformed LA Mask')
ax = plt.subplot(1, 4, 3)
plt.imshow(LA_trans_final, cmap='gray')
plt.colorbar()
plt.axis('off')
plt.title('Transformed LA kmeans')
ax = plt.subplot(1, 4, 4)
plt.imshow(MALDI_mask, cmap='gray')
plt.colorbar()
plt.axis('off')
plt.title('MALDI mask')
plt.show()
```

```
LA mask shape: (129, 113)
Transformed mask shape (120, 105)
```

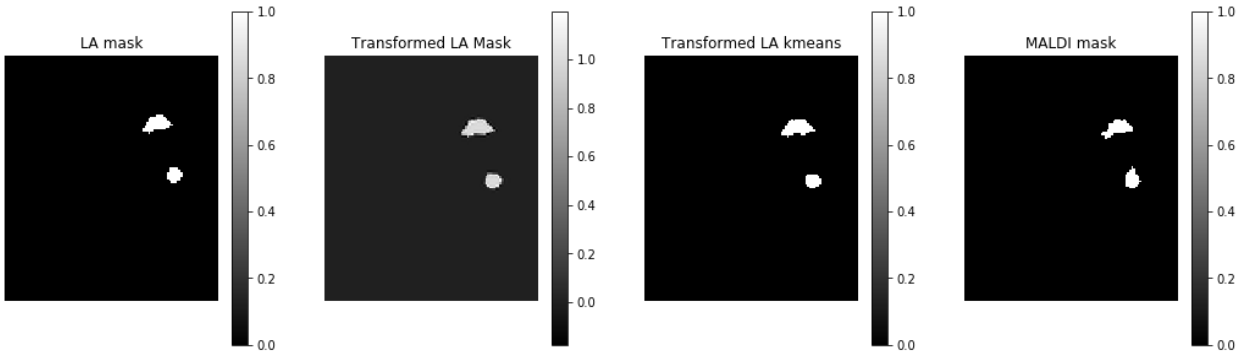

DSC calculation

```
## MALDI scaled will be changed to find out which are the true positives and
the true negatives

MALDI_overlay_scale = np.zeros(MALDI_mask.shape)
MALDI_overlay_scale[MALDI_mask==1] =2

Combined_masks = MALDI_overlay_scale + LA_trans_final

plt.figure(figsize=(10,7))
plt.imshow(Combined_masks, cmap='jet')
```

```
plt.title('Combined mask')
plt.colorbar()
plt.axis('off')
plt.show()
```

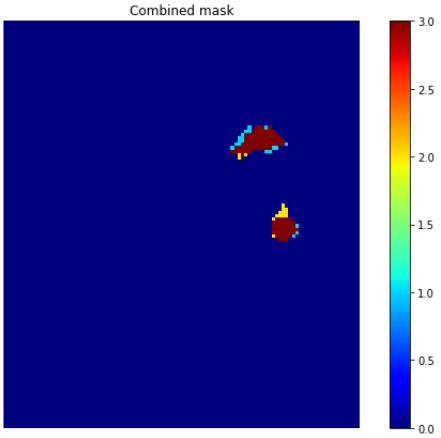


```
Pixel_1 = Combined_masks[Combined_masks == 1]
Pixel_2 = Combined_masks[Combined_masks == 2]
Pixel_3 = Combined_masks[Combined_masks == 3]

DSC = (2*len(Pixel_3))/((2*len(Pixel_3))+len(Pixel_2)+len(Pixel_1))

print('Pixel 1 - LA Only pixels (FN) =', len(Pixel_1))
print('Pixel 2 - MALDI Only pixels (FP) =', len(Pixel_2))
print('Pixel 3 - Overlapping pixels =', len(Pixel_3))
print('DSC value', DSC)
```

```
Pixel 1 - LA Only pixels (FN) = 20
Pixel 2 - MALDI Only pixels (FP) = 15
Pixel 3 - Overlapping pixels = 117
DSC value 0.8698884758364313
```

```
import seaborn as sns
import matplotlib.colors

norm = matplotlib.colors.Normalize(0,3)
colors = [[norm(0), "#000000"], [norm(1), "#7CFC00"], [norm(2), "#FF00FF"],
[norm(3), "#FFFFFF"]]
cmap1 = matplotlib.colors.LinearSegmentedColormap.from_list("", colors)

plt.figure(figsize=(10,10))
sns.heatmap(Combined_masks, square=True, cmap=cmap1, cbar=False,
xticklabels=False, yticklabels=False)
```

```
<matplotlib.axes._subplots.AxesSubplot at 0x7fd7c5efafd0>
```

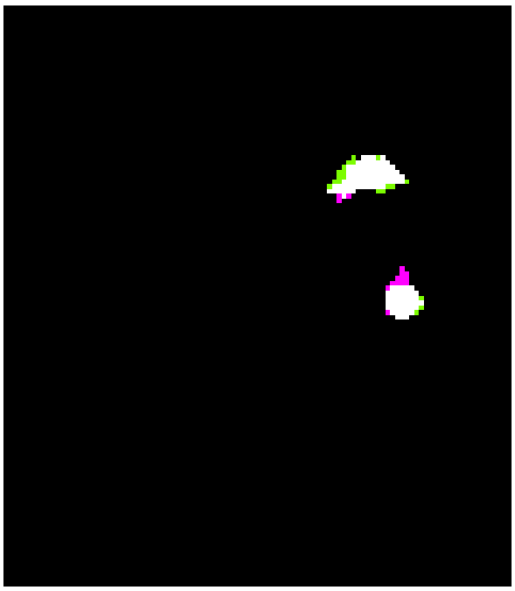

Landmark registration

```
# Annotated data points were obtained in imagej

Annotated_LA = np.zeros(MovingArray.shape)

Annotated_LA[70,32] = 1
Annotated_LA[66,89] = 2
Annotated_LA[32,77] = 3
Annotated_LA[35,87] = 4
Annotated_LA[108,60] = 5
Annotated_LA[120,20] = 6
Annotated_LA[82,23] = 7
Annotated_LA[64,32] = 8
Annotated_LA[11,14] = 9
Annotated_LA[22,95] = 10

Annotated_MALDI = np.zeros(FixedArray.shape)

Annotated_MALDI[63,25] = 1
Annotated_MALDI[64,82] = 2
Annotated_MALDI[32,73] = 3
Annotated_MALDI[35,81] = 4
Annotated_MALDI[100,48] = 5
Annotated_MALDI[107,8] = 6
Annotated_MALDI[72,15] = 7
Annotated_MALDI[55,25] = 8
Annotated_MALDI[8,11] = 9
Annotated_MALDI[23,90] = 10

from matplotlib import cm
from matplotlib.colors import ListedColormap, LinearSegmentedColormap

cmap1 = ListedColormap(['white', 'darkblue', 'dodgerblue', 'forestgreen',
'lime', 'yellow', 'orange', 'red',
                        'darkviolet', 'deeppink', 'lightpink'])
```

```
cmap2 = ListedColormap(['black', 'darkblue', 'dodgerblue', 'forestgreen',
'lime', 'yellow', 'orange', 'red',
                        'darkviolet', 'deeppink', 'lightpink'])

plt.figure(figsize=(18,20))
ax = plt.subplot(2, 2, 1)
plt.imshow(Annotated_LA, cmap=cmap2)
plt.axis('off')
ax = plt.subplot(2, 2, 2)
plt.imshow(MovingArrayNorm, cmap='gray_r', alpha=0.7)
plt.axis('off')
plt.imshow(Annotated_LA, cmap=cmap1, alpha=0.8)
plt.axis('off')
ax = plt.subplot(2, 2, 3)
plt.imshow(Annotated_MALDI, cmap=cmap2)
plt.axis('off')
ax = plt.subplot(2, 2, 4)
plt.imshow(FixedArrayNorm, cmap='gray_r', alpha=0.7)
plt.axis('off')
plt.imshow(Annotated_MALDI, cmap=cmap1, alpha=0.8)
plt.axis('off')
plt.show()
```

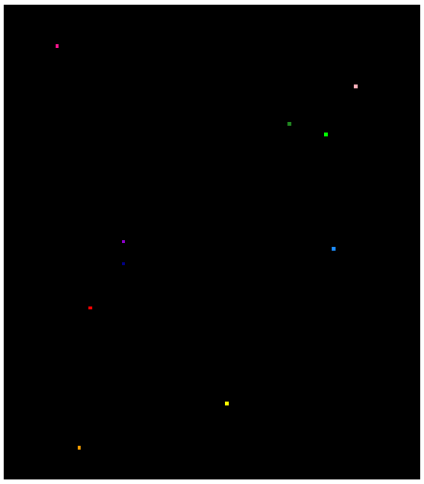

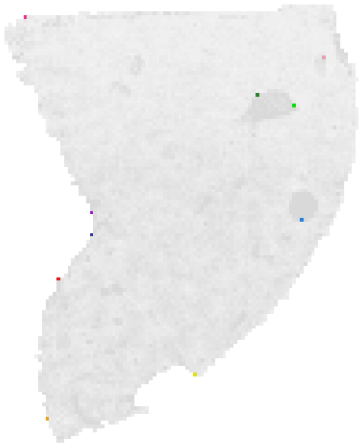

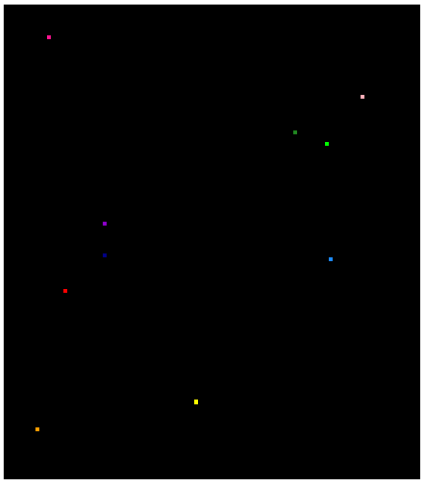

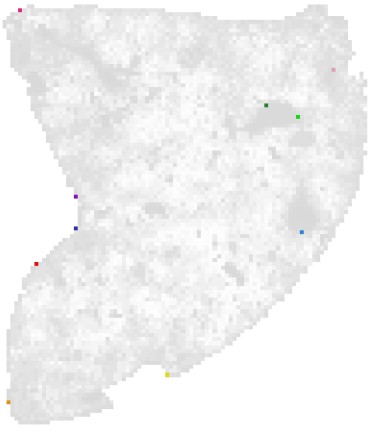

Annotated mask registration

```
# LA ablation annotated mask (Moving image) should be transformed

transformixImageFilter = sitk.TransformixImageFilter()
transformixImageFilter.SetTransformParameterMap(transformParameterMap_4)

transformixImageFilter.SetMovingImage(sitk.GetImageFromArray(Annotated_LA))
transformixImageFilter.Execute()
Transformed_annotated_LA =
sitk.GetArrayFromImage(transformixImageFilter.GetResultImage())

print('Initial annotation shape:', Annotated_LA.shape)
print('Transformed annotated shape', Transformed_annotated_LA.shape)

plt.figure(figsize=(18,7))
ax = plt.subplot(1, 3, 1)
plt.imshow(Annotated_LA, cmap=cmap2)
plt.axis('off')
ax = plt.subplot(1, 3, 2)
plt.imshow(Transformed_annotated_LA, cmap='jet')
plt.axis('off')
ax = plt.subplot(1, 3, 3)
plt.imshow(ResultArray_4, cmap='gray_r', alpha=0.8)
plt.axis('off')
plt.imshow(Annotated_MALDI, cmap=cmap1, alpha=0.7)
plt.axis('off')
plt.show()
```

```
Initial annotation shape: (129, 113)
Transformed annotated shape (120, 105)
```

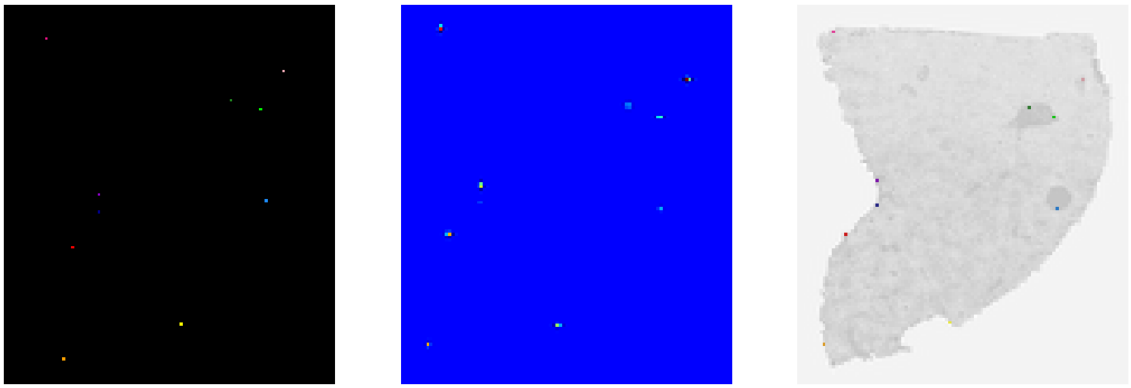

Annotated binary mask transformation

```
# Conversion of the annotated mask to a binary

Annotated_LA_bin = np.zeros(Annotated_LA.shape)
Annotated_LA_bin[Annotated_LA > 0] = 1

# LA ablation annotated mask (Moving image) should be transformed

transformixImageFilter = sitk.TransformixImageFilter()
transformixImageFilter.SetTransformParameterMap(transformParameterMap_4)
```

```
transformixImageFilter.SetMovingImage(sitk.GetImageFromArray(Annotated_LA_bin
))
transformixImageFilter.Execute()
Transformed_annotated_LA_bin =
sitk.GetArrayFromImage(transformixImageFilter.GetResultImage())

print('Initial annotation shape:', Annotated_LA_bin.shape)
print('Transformed annotated shape', Transformed_annotated_LA_bin.shape)

plt.figure(figsize=(18,9))
ax = plt.subplot(1, 2, 1)
plt.imshow(Annotated_LA_bin, cmap='gray')
plt.axis('off')
plt.colorbar()
ax = plt.subplot(1, 2, 2)
plt.imshow(Transformed_annotated_LA_bin, cmap='gray')
plt.axis('off')
plt.colorbar()
plt.show()
```

```
Initial annotation shape: (129, 113)
Transformed annotated shape (120, 105)
```

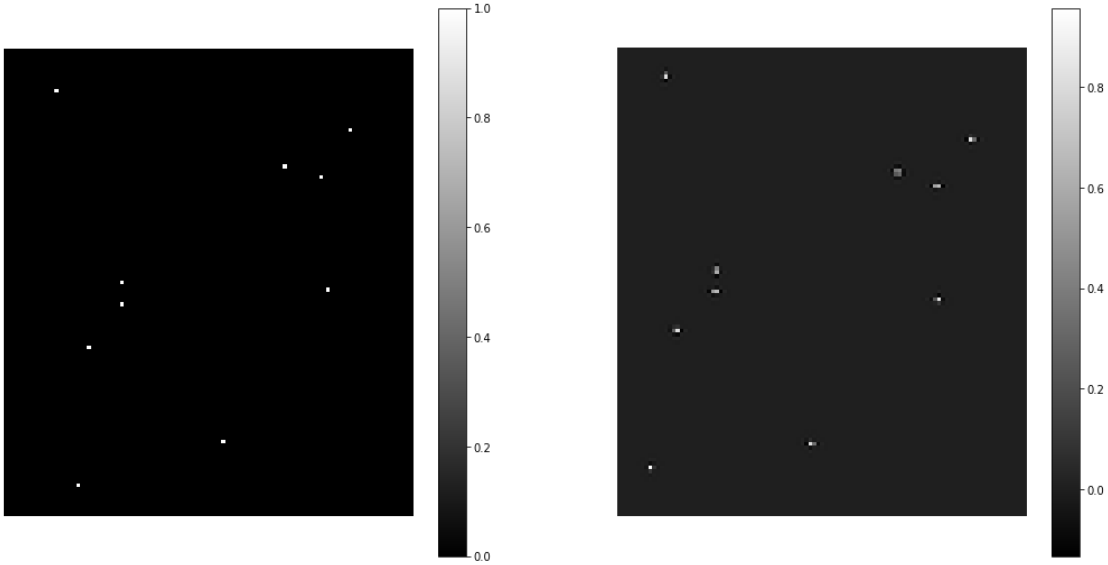


```
Annotated_MALDI_bin = np.zeros(Annotated_MALDI.shape)
Annotated_MALDI_bin[Annotated_MALDI > 0] = 1

plt.figure(figsize=(18,10))
ax = plt.subplot(1, 3, 1)
plt.imshow(Annotated_MALDI_bin, cmap='gray')
plt.axis('off')
ax = plt.subplot(1, 3, 2)
plt.imshow(Transformed_annotated_LA_bin, cmap='gray')
plt.axis('off')
ax = plt.subplot(1, 3, 3)
plt.imshow(Annotated_MALDI_bin, cmap='gray', alpha=1)
plt.axis('off')
plt.imshow(Transformed_annotated_LA_bin, cmap='gray', alpha=0.7)
plt.axis('off')
plt.title ('overlay')
```

```
Text(0.5, 1.0, 'overlay')
```


```
import seaborn as sns
import matplotlib.colors

#norm = matplotlib.colors.Normalize(0,3)
#colors = [[norm(0), "#000000"], [norm(1), "#7CFC00"], [norm(2), "#FF00FF"],
[norm(3), "#FFFFFF"]]
#cmap1 = matplotlib.colors.LinearSegmentedColormap.from_list("", colors)

vmin = 0
vmax = 1

cmap1 = sns.dark_palette("Green", as_cmap=True)
cmap2 = sns.dark_palette("Magenta", as_cmap=True)

plt.figure(figsize=(18, 20))
plt.subplot(2, 2, 1)
sns.heatmap(Annotated_MALDI_bin, square=True, cmap=cmap1, xticklabels=False,
yticklabels=False, cbar=False)
plt.subplot(2, 2, 2)
sns.heatmap(Transformed_annotated_LA_bin, square=True, cmap=cmap2,
xticklabels=False, yticklabels=False, vmin=0,
            vmax=1, cbar=False)
plt.subplot(2, 2, 3)
sns.heatmap(Annotated_MALDI_bin, square=True, cmap=cmap1, xticklabels=False,
yticklabels=False, cbar=False)
sns.heatmap(Transformed_annotated_LA_bin, square=True, cmap=cmap2,
xticklabels=False, yticklabels=False,
            cbar=False, vmin=0, vmax=1, alpha=0.3)
plt.subplot(2, 2, 4)
sns.heatmap(Annotated_LA_bin, square=True, cmap=cmap2, xticklabels=False,
yticklabels=False, cbar=False)

plt.show()
```

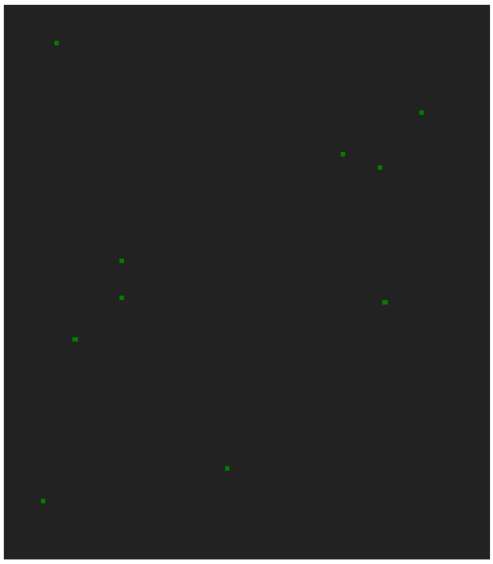
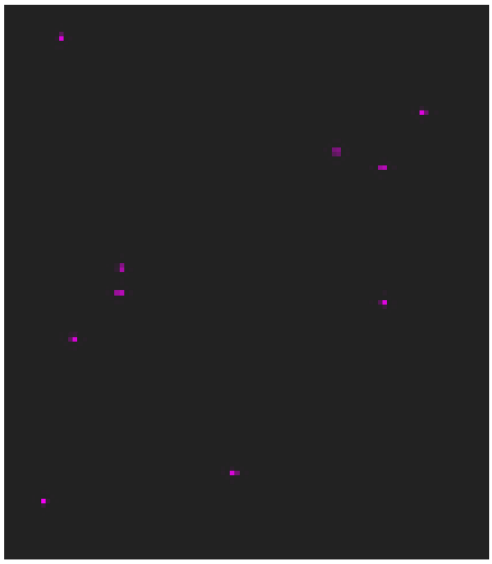

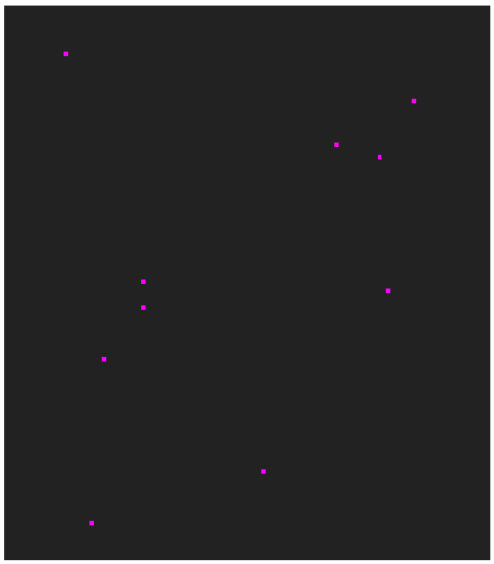

```
np.savetxt('M2_LDM_LA_pixels', Annotated_LA_bin, delimiter=',')
np.savetxt('M2_LDM_LA_transformed_pixels', Transformed_annotated_LA_bin,
delimiter=',')
np.savetxt('M2_LDM_MALDI_pixels', Annotated_MALDI_bin, delimiter=',')
```

Correlation coefficient calculations

```
# Import the MALDI data and apply the same transformations as the t-sne
image:

from pyimzml.ImzMLParser import ImzMLParser
from pyimzml.ImzMLParser import getionimage
from scipy import ndimage
```

```
# Parse the data into slide

slide = ImzMLParser('111920_Liver_TTMA_D6.imzML')

# Specify where the slide will be cut to get the images

Y1 = 150
Y2 = 270
X1 = 1035
X2 = 1140

Degree_rotation = 180

# Import list of the most abundance signals above 500m/z

import csv
import math

datafile = open('111920_Signals_M2.csv', 'r')
reader = csv.reader(datafile)

Ions = []
Tolerance = []
for row in reader:
    Ions.append(float(row[0]))
    Tolerance.append(float(row[1]))

images = []

# Extract the signals in MALDI

for i,t in zip(Ions, Tolerance):
    image = (getionimage(slide, i, tol=t)[Y1:Y2, X1:X2])
    im = ndimage.rotate(image, Degree_rotation, reshape=True)
    Quantile_99 = np.quantile(im, 0.99)
    im[im > Quantile_99] = Quantile_99
    images.append(im)

print('MALDI images shape:', images[0].shape)

# Images of the selected signals

length = len(images)
rows_graph = math.ceil(length/5)

plt.figure(figsize=(18, 28))
for n,im in enumerate(images):
    ax = plt.subplot(rows_graph, 5, (n+1))
    plt.imshow(im)
    plt.axis('off')
    plt.colorbar()
    plt.title('m/z {0}'.format(Ions[n]))
plt.show()
```

```
MALDI images shape: (120, 105)
```

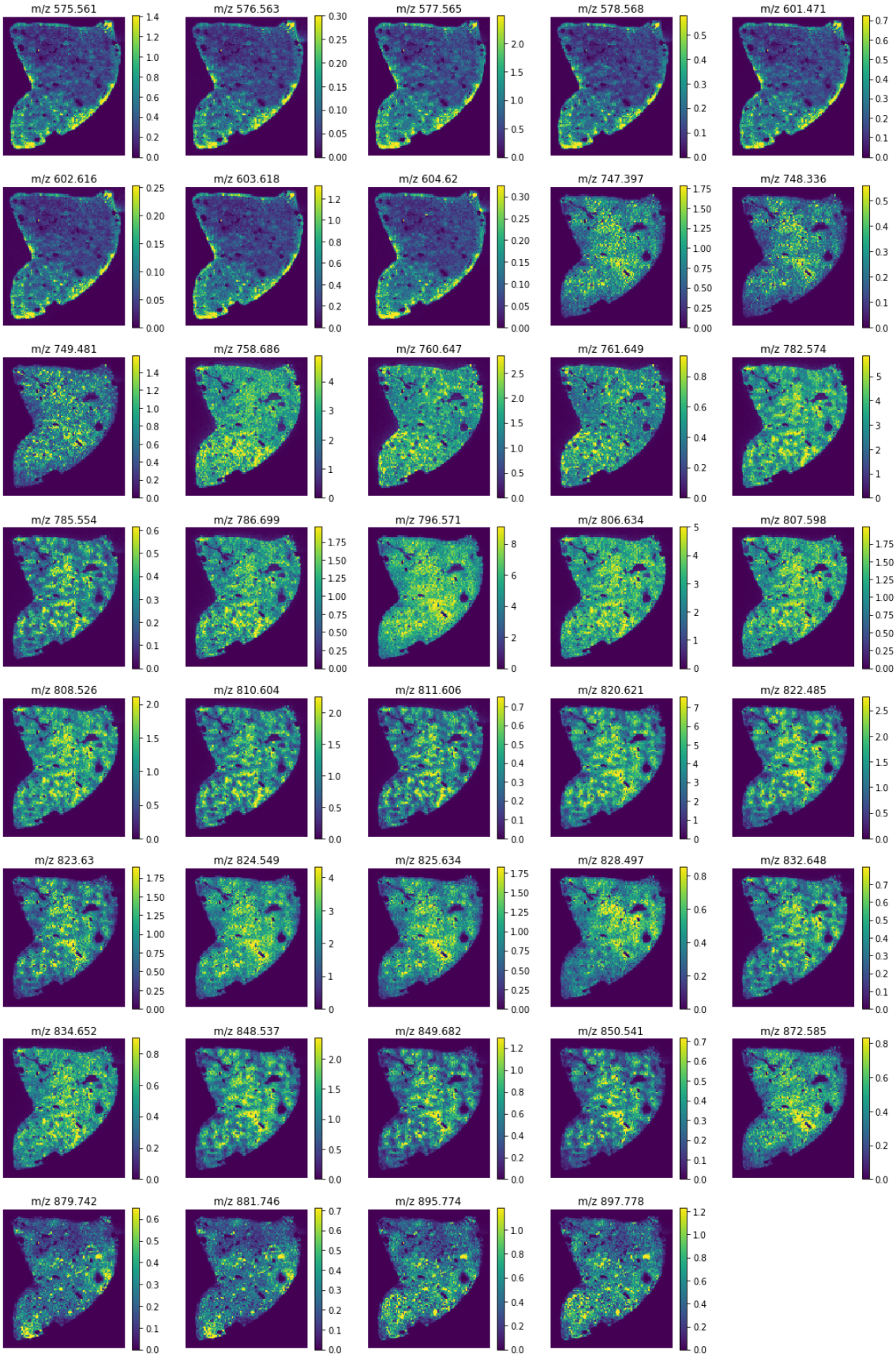
m/z 575.561
m/z 576.563
m/z 577.565
m/z 578.568
m/z 601.471
m/z 602.616
m/z 603.618
m/z 604.62
m/z 747.397
m/z 748.336
m/z 749.481
m/z 758.686
m/z 760.647
m/z 761.649
m/z 782.574
m/z 785.554
m/z 786.699
m/z 796.571
m/z 806.634
m/z 807.598
m/z 808.526
m/z 810.604
m/z 811.606
m/z 820.621
m/z 822.485
m/z 823.63
m/z 824.549
m/z 825.634
m/z 828.497
m/z 832.648
m/z 834.652
m/z 848.537
m/z 849.682
m/z 850.541
m/z 872.585
m/z 879.742
m/z 881.746
m/z 895.774
m/z 897.778

Transformation of LA-ICP signals into the MALDI coordinate system

```
# Transformation of the LA-ICP images

Fe = loadtxt('M2_LA_hot_1.csv', delimiter=',')[0:129, 5:118]
Au = loadtxt('M2_LA_hot_2.csv', delimiter=',')[0:129, 5:118]
Zn = loadtxt('M2_LA_hot_3.csv', delimiter=',')[0:129, 5:118]

MALDI_BM = np.loadtxt('M2_MALDI_796_mask.csv', delimiter=',')
MALDI_BM[MALDI_BM == 255] = 1

transformixImageFilter = sitk.TransformixImageFilter()
transformixImageFilter.SetTransformParameterMap(transformParameterMap_4)

transformixImageFilter.SetMovingImage(sitk.GetImageFromArray(Fe))
transformixImageFilter.Execute()
Fe_trans = sitk.GetArrayFromImage(transformixImageFilter.GetResultImage())

transformixImageFilter.SetMovingImage(sitk.GetImageFromArray(Au))
transformixImageFilter.Execute()
Au_trans = sitk.GetArrayFromImage(transformixImageFilter.GetResultImage())

transformixImageFilter.SetMovingImage(sitk.GetImageFromArray(Zn))
transformixImageFilter.Execute()
Zn_trans = sitk.GetArrayFromImage(transformixImageFilter.GetResultImage())

Fe_trans_BS = Fe_trans*MALDI_BM
Au_trans_BS = Au_trans*MALDI_BM
Zn_trans_BS = Zn_trans*MALDI_BM

print('Transform LA shape:', Fe_trans.shape)

plt.figure(figsize=(18, 10))
ax=plt.subplot(1, 6, 1)
plt.imshow(Fe_trans, cmap='gray')
plt.axis('off')
plt.title('Fe transformed')
ax=plt.subplot(1, 6, 2)
plt.imshow(Au_trans, cmap='gray')
plt.axis('off')
plt.title('Au transformed')
ax=plt.subplot(1, 6, 3)
plt.imshow(Zn_trans, cmap='gray')
plt.axis('off')
plt.title('Zn transformed')
ax=plt.subplot(1, 6, 4)
plt.imshow(Fe_trans_BS, cmap='gray')
plt.axis('off')
plt.title('Fe transformed BS')
ax=plt.subplot(1, 6, 5)
plt.imshow(Au_trans_BS, cmap='gray')
plt.axis('off')
plt.title('Au transformed BS')
ax=plt.subplot(1, 6, 6)
plt.imshow(Zn_trans_BS, cmap='gray')
plt.axis('off')
plt.title('Zn transformed BS')
plt.show()
Transform LA shape: (120, 105)
```

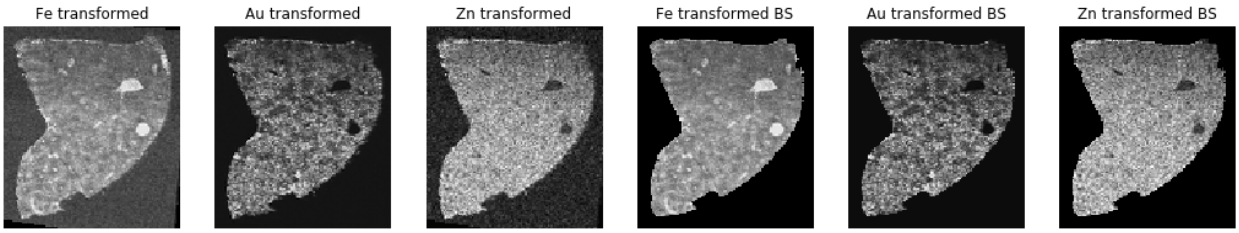

Calculation of correlation coefficients

```
# Calculation of the correlation values, rows and columns values need to be
calculated. Background mask needs to
# be imported and cut to have the same dimensions as the MALDI input images.

import scipy.stats

MALDI_rows = images[0].shape[0]
MALDI_columns = images[0].shape[1]

images_all = [Fe_trans_BS, Au_trans_BS, Zn_trans_BS] + images
Ions_all = ['Fe', 'Au', 'Zn'] + Ions

corr_matrix = np.zeros((len(images_all), len(images_all)))

for index1,im1 in enumerate(images_all):
    im1_vector = im1[MALDI_BM==1]
    for index2,im2 in enumerate(images_all):
        im2_vector = im2[MALDI_BM==1]
        corr, p = scipy.stats.pearsonr(im1_vector, im2_vector)
        corr_matrix[index1, index2] = corr
```

Correlation plot of LA and MALDI signals

```
# To change scale of the plot change vmin and vmax

import matplotlib as mpl

fig = plt.figure(figsize=(18, 15))

ax1 = plt.gca()

cmap = plt.get_cmap('RdBu_r')

ax1.imshow(corr_matrix, cmap=cmap, origin='upper', vmin=-1, vmax=1)

ax1.set_xticks(range(len(Ions_all)))
ax1.set_xticklabels(Ions_all, rotation=90)
ax1.tick_params(top=True, bottom=False, labeltop=True, labelbottom=False,
labelsize=16)
ax1.set_aspect('equal')

ax1.set_yticks(range(len(Ions_all)))
ax1.set_yticklabels(Ions_all)

norm = mpl.colors.Normalize(vmin=-1,vmax=1)
```

```
norm =
mpl.colors.Normalize(vmin=np.amin(corr_matrix),vmax=np.amax(corr_matrix))
sm = plt.cm.ScalarMappable(cmap=cmap, norm=norm)
sm.set_array([])
plt.colorbar(sm, pad=0.01, aspect=30)

plt.show()
```

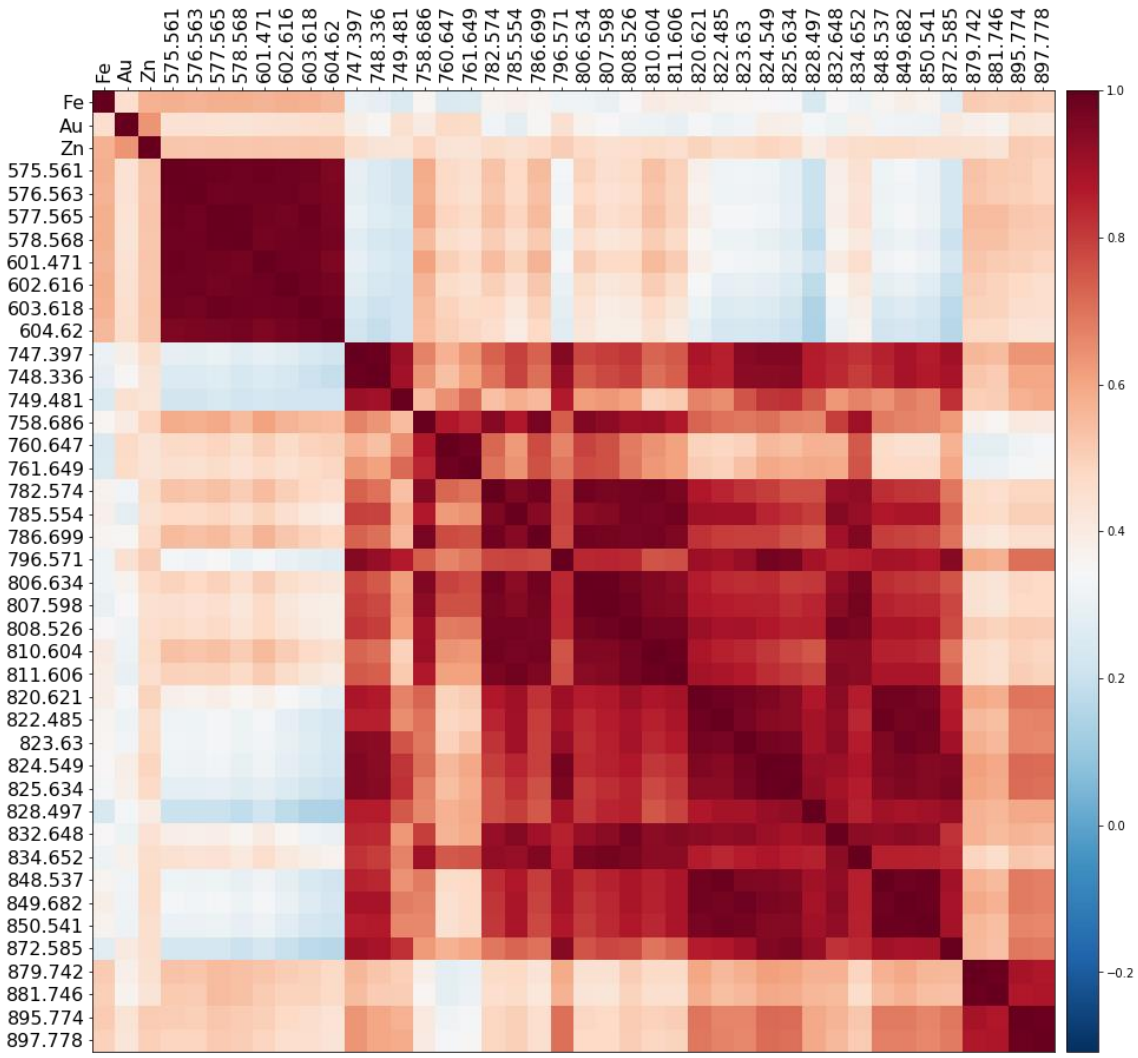

BIBLIOGRAPHY

Abdelmoula, W. M.; Balluff, B.; Englert, S.; Dijkstra, J.; Reinders, M. J. T.; Walch, A.; McDonnell, L. A.; Lelieveldt, B. P. F. Data-Driven Identification of Prognostic Tumor Subpopulations Using Spatially Mapped t-SNE of Mass Spectrometry Imaging Data. *Proc. Natl. Acad. Sci. U. S. A.* **2016**, *113* (43), 12244–12249.

Abdelmoula, W. M.; Škrášková, K.; Balluff, B.; Carreira, R. J.; Tolner, E. A.; Lelieveldt, B. P. F.; van der Maaten, L.; Morreau, H.; van den Maagdenberg, A. M. J. M.; Heeren, R. M. A.; McDonnell, L. A.; Dijkstra, J. Automatic Generic Registration of Mass Spectrometry Imaging Data to Histology Using Nonlinear Stochastic Embedding. *Anal. Chem.* **2014**, *86* (18), 9204–9211.

Alexandrov, T. PyimzML. https://github.com/alexandrovteam/pyimzML 2021.

Alexandrov, T.; Becker, M.; Deininger, S.-O.; Ernst, G.; Wehder, L.; Grasmair, M.; von Eggeling, F.; Thiele, H.; Maass, P. Spatial Segmentation of Imaging Mass Spectrometry Data with Edge-Preserving Image Denoising and Clustering. *J. Proteome Res.* **2010**, *9* (12), 6535–6546.

Alexandrov, T.; Kobarg, J. H. Efficient Spatial Segmentation of Large Imaging Mass Spectrometry Datasets with Spatially Aware Clustering. *Bioinformatics.* **2011**, *27* (13), i230–i238.

Alphandéry, E. Iron Oxide Nanoparticles for Therapeutic Applications. *Drug Discov. Today* **2020**, *25* (1), 141–149.

Anselmo, A. C.; Gokarn, Y.; Mitragotri, S. Non-Invasive Delivery Strategies for Biologics. *Nat. Rev. Drug Discov.* **2018**, *18* (1), 19–40.

Austin, C.; Fryer, F.; Lear, J.; Bishop, D.; Hare, D.; Rawling, T.; Kirkup, L.; McDonagh, A.; Doble, P. Factors Affecting Internal Standard Selection for Quantitative Elemental Bio-Imaging of Soft Tissues by LA-ICP-MS. *J. Anal. At. Spectrom.* **2011**, *26* (7), 1494–1501.

Becker, J. S.; Matusch, A.; Wu, B. Bioimaging Mass Spectrometry of Trace Elements - Recent Advance and Applications of LA-ICP-MS: A Review. *Anal. Chim. Acta* **2014**, *835*, 1–18.

Becker, J. S.; Salber, D. New Mass Spectrometric Tools in Brain Research. *TrAC - Trends Anal. Chem.* **2010**, *29* (9), 966–979.

Becker, J. S.; Zoriy, M.; Matusch, A.; Wu, B.; Salber, D.; Palm, C.; Becker, S. Bioimaging of Metals by Laser Ablation Inductively Coupled Plasma Mass Spectrometry LA-ICP-MS. *Mass Spectrom. Rev.* **2010**, *29* (1), 156–175.

Bemis, K. D.; Harry, A.; Eberlin, L. S.; Ferreira, C. R.; van de Ven, S. M.; Mallick, P.; Stolowitz, M.; Vitek, O. Probabilistic Segmentation of Mass Spectrometry (MS) Images Helps Select Important Ions and Characterize Confidence in the Resulting Segments. *Mol. Cell. Proteomics.* **2016**, *15* (5), 1761–1772.

Blanco, E.; Shen, H.; Ferrari, M. Principles of Nanoparticle Design for Overcoming Biological Barriers to Drug Delivery. *Nat. Biotechnol.* **2015**, *33* (9), 941–951.

Boaru, S. G.; Merle, U.; Uerlings, R.; Zimmermann, A.; Flechtenmacher, C.; Willheim, C.; Eder, E.; Ferenci, P.; Stremmel, W.; Weiskirchen, R. Laser Ablation Inductively Coupled Plasma Mass Spectrometry Imaging of Metals in Experimental and Clinical Wilson's Disease. *J. Cell. Mol. Med.* **2015**, *19* (4), 806–814.

Bocklitz, T. W.; Crecelius, A. C.; Matthäus, C.; Tarcea, N.; Von Eggeling, F.; Schmitt, M.; Schubert, U. S.; Popp, J. Deeper Understanding of Biological Tissue: Quantitative Correlation of MALDI-TOF and Raman Imaging. *Anal. Chem.* **2013**, *85* (22), 10829–10834.

Böhme, S.; Stärk, H. J.; Kühnel, D.; Reemtsma, T. Exploring LA-ICP-MS as a Quantitative Imaging Technique to Study Nanoparticle Uptake in Daphnia Magna and Zebrafish (Danio Rerio) Embryos. *Anal. Bioanal. Chem.* **2015**, *407* (18), 5477–5485.

Brust, M.; Walker, M.; Bethell, D.; Schiffrin, D. J.; Whyman, R. Synthesis of Thiol-Derivatised Gold Nanoparticles in a Two-Phase Liquid–Liquid System. *J. Chem. Soc., Chem. Commun.* **1994**, *7* (7), 801–802.

Buchberger, A. R.; DeLaney, K.; Johnson, J.; Li, L. Mass Spectrometry Imaging: A Review of Emerging Advancements and Future Insights. *Anal. Chem.* **2018**, *90* (1), 240–265.

Büchner, T.; Drescher, D.; Traub, H.; Schrade, P.; Bachmann, S.; Jakubowski, N.; Kneipp, J. Relating Surface-Enhanced Raman Scattering Signals of Cells to Gold Nanoparticle Aggregation as Determined by LA-ICP-MS Micromapping. *Anal. Bioanal. Chem.* **2014**, *406* (27), 7003–7014.

Cao-Milán, R.; He, L. D.; Shorkey, S.; Tonga, G. Y.; Wang, L.-S.; Zhang, X.; Uddin, I.; Das, R.; Sulak, M.; Rotello, V. M. Modulating the Catalytic Activity of Enzyme-like Nanoparticles through Their Surface Functionalization. *Mol. Syst. Des. Eng.* **2017**, *2* (5), 624–628.

Caprioli, R. M.; Farmer, T. B.; Gile, J. Molecular Imaging of Biological Samples: Localization of Peptides and Proteins Using MALDI-TOF MS. *Anal. Chem.* **1997**, *69* (23), 4751–4760.

Cassat, J. E.; Moore, J. L.; Wilson, K. J.; Stark, Z.; Prentice, B. M.; Van de Plas, R.; Perry, W. J.; Zhang, Y.; Virostko, J.; Colvin, D. C.; Rose, K. L.; Judd, A. M.; Reyzer, M. L.; Spraggins, J. M.; Grunenwald, C. M.; Gore, J. C.; Caprioli, R. M.; Skaar, E. P. Integrated Molecular Imaging Reveals Tissue Heterogeneity Driving Host-Pathogen Interactions. *Sci. Transl. Med.* **2018**, *10* (432), eaan6361.

Castellanos-García, L. J.; Gokhan Elci, S.; Vachet, R. W. Reconstruction, Analysis, and Segmentation of LA-ICP-MS Imaging Data Using Python for the Identification of Sub-Organ Regions in Tissues. *Analyst* **2020**, *145* (10), 3705–3712.

Chaurand, P.; Cornett, D. S.; Angel, P. M.; Caprioli, R. M. From Whole-Body Sections down to Cellular Level, Multiscale Imaging of Phospholipids by MALDI Mass Spectrometry. *Mol. Cell. Proteomics.* **2011**, *10* (2), S1–S11.

Chompoosor, A.; Han, G.; Rotello, V. M. Charge Dependence of Ligand Release and Monolayer Stability of Gold Nanoparticles by Biogenic Thiols. *Bioconjug. Chem.* **2008**, *19* (7), 1342–1345.

Chumbley, C. W.; Reyzer, M. L.; Allen, J. L.; Marriner, G. A.; Via, L. E.; Barry, C. E.; Caprioli, R. M. Absolute Quantitative MALDI Imaging Mass Spectrometry: A Case of Rifampicin in Liver Tissues. *Anal. Chem.* **2016**, *88* (4), 2392–2398.

Cornett, D. S.; Reyzer, M. L.; Chaurand, P.; Caprioli, R. M. MALDI Imaging Mass Spectrometry: Molecular Snapshots of Biochemical Systems. *Nat. Methods.* **2007**, *4* (10), 828–833.

Cruz-Alonso, M.; Fernandez, B.; Navarro, A.; Junceda, S.; Astudillo, A.; Pereiro, R. Laser Ablation ICP-MS for Simultaneous Quantitative Imaging of Iron and Ferroportin in Hippocampus of Human Brain Tissues with Alzheimer's Disease. *Talanta.* **2019**, *197*, 413–421.

Diamond, A.; Abad, S.; Mench, C.; Rojas, S.; Gispert, J. D.; Martı, R. Biodistribution of Nanoparticles . In Vivo Studies Based on 18 F Radionuclide Emission. **2011**, No. 7, 5552–5559.

Doble, P. A.; de Vega, R. G.; Bishop, D. P.; Hare, D. J.; Clases, D. Laser Ablation–Inductively Coupled Plasma–Mass Spectrometry Imaging in Biology. *Chem. Rev.* **2021**, acs.chemrev.0c01219.

Dreaden, E. C.; Alkilany, A. M.; Huang, X.; Murphy, C. J.; El-Sayed, M. a. The Golden Age: Gold Nanoparticles for Biomedicine. *Chem. Soc. Rev.* **2012**, *41* (7), 2740.

Dreisewerd, K. Recent Methodological Advances in MALDI Mass Spectrometry. *Anal. Bioanal. Chem.* **2014**, *406* (9–10), 2261–2278.

Drescher, D.; Giesen, C.; Traub, H.; Panne, U.; Kneipp, J.; Jakubowski, N. Quantitative Imaging of Gold and Silver Nanoparticles in Single Eukaryotic Cells by Laser Ablation ICP-MS. *Anal. Chem.* **2012**, *84* (22), 9684–9688.

Dukhinova, M. S.; Prilepskii, A. Y.; Vinogradov, V. V.; Shtil, A. A. Metal Oxide Nanoparticles in Therapeutic Regulation of Macrophage Functions. *Nanomaterials* **2019**, *9* (11), 1–20.

Egger, A. E.; Theiner, S.; Kornauth, C.; Heffeter, P.; Berger, W.; Keppler, B. K.; Hartinger, C. G. Quantitative Bioimaging by LA-ICP-MS: A Methodological Study on the Distribution of Pt and Ru in Viscera Originating from Cisplatin- and KP1339-Treated Mice. *Metallomics* **2014**, *6* (9), 1616–1625.

Elci, S. G.; Tonga, G. Y.; Yan, B.; Kim, S. T.; Kim, C. S.; Jiang, Y.; Saha, K.; Moyano, D. F.; Marsico, A. L. M.; Rotello, V. M.; Vachet, R. W. Dual-Mode Mass Spectrometric Imaging for Determination of in Vivo Stability of Nanoparticle Monolayers. *ACS Nano.* **2017**, *11* (7), 7424–7430.

Elci, S. G.; Yan, B.; Kim, S. T.; Saha, K.; Jiang, Y.; Klemmer, G. A.; Moyano, D. F.; Tonga, G. Y.; Rotello, V. M.; Vachet, R. W. Quantitative Imaging of 2 Nm Monolayer-Protected Gold Nanoparticle Distributions in Tissues Using Laser Ablation Inductively-Coupled Plasma Mass Spectrometry (LA-ICP-MS). *Analyst* **2016**, *141* (8), 2418–2425.

Elci, S. G.; Jiang, Y.; Yan, B.; Kim, S. T.; Saha, K.; Moyano, D. F.; Yesilbag Tonga, G.; Jackson, L. C.; Rotello, V. M.; Vachet, R. W. Surface Charge Controls the Suborgan Biodistributions of Gold Nanoparticles. *ACS Nano* **2016**, *10* (5), 5536–5542.

Ellis, S. R.; Paine, M. R. L.; Eijkel, G. B.; Pauling, J. K.; Husen, P.; Jervelund, M. W.; Hermansson, M.; Ejsing, C. S.; Heeren, R. M. A. Automated, Parallel Mass Spectrometry Imaging and Structural Identification of Lipids. *Nat. Methods.* **2018**, *15* (7), 515–518.

Fay, D.; Palmer, A. D.; Vitaly, K.; Alexandrov, T. pyimzML Github repository. https://github.com/alexandrovteam/pyimzML (accessed 2020-01-11).

Fonville, J. M.; Carter, C. L.; Pizarro, L.; Steven, R. T.; Palmer, A. D.; Griffiths, R. L.; Lalor, P. F.; Lindon, J. C.; Nicholson, J. K.; Holmes, E.; Bunch, J. Hyperspectral Visualization of Mass Spectrometry Imaging Data. *Anal. Chem.* **2013**, *85* (3), 1415–1423.

García, K. P.; Zarschler, K.; Barbaro, L.; Barreto, J. A.; O'Malley, W.; Spiccia, L.; Stephan, H.; Graham, B. Zwitterionic-Coated "Stealth" Nanoparticles for Biomedical Applications: Recent Advances in Countering Biomolecular Corona Formation and Uptake by the Mononuclear Phagocyte System. *Small* **2014**, *10* (13), 2516–2529.

Gardner, W.; Cutts, S. M.; Phillips, D. R.; Pigram, P. J. Understanding Mass Spectrometry Images: Complexity to Clarity with Machine Learning. *Biopolymers.* **2021**, *112* (4), e23400.

Gaumet, J. J.; Strouse, G. F. Electrospray Mass Spectrometry of Semiconductor Nanoclusters: Comparative Analysis of Positive and Negative Ion Mode. *J. Am. Soc. Mass Spectrom.* **2000**, *11* (4), 338–344.

Gemperline, E.; Keller, C.; Jayaraman, D.; Maeda, J.; Sussman, M. R.; Ané, J.-M.; Li, L. Examination of Endogenous Peptides in Medicago Truncatula Using Mass Spectrometry Imaging. *J. Proteome Res.* **2016**, *15* (12), 4403–4411.

Gessel, M. M.; Norris, J. L.; Caprioli, R. M. MALDI Imaging Mass Spectrometry: Spatial Molecular Analysis to Enable a New Age of Discovery. *J. Proteomics* **2014**, *107*, 71–82.

González de Vega, R.; Fernández Sanchez, M. L.; Eiro, N.; Vizoso, F. J.; Sperling, M.; Karst, U.; Sanz Medel, A. Multimodal Laser Ablation/Desorption Imaging Analysis of Zn and MMP-11 in Breast Tissues. *Anal. Bioanal. Chem.* **2018**, *410* (3), 913–922.

Grodzinski, P.; Kircher, M.; Goldberg, M.; Gabizon, A. Integrating Nanotechnology into Cancer Care. *ACS Nano* **2019**, *13* (7), 7370–7376.

Groseclose, M. R.; Castellino, S. A Mimetic Tissue Model for the Quantification of Drug Distributions by MALDI Imaging Mass Spectrometry. *Anal. Chem.* **2013**, *85* (21), 10099–10106.

Han, G.; Ghosh, P.; Rotello, V. M. Functionalized Gold Nanoparticles for Drug Delivery. *Nanomedicine* **2007**, *2*, 113–123.

Han, X.; Xu, K.; Taratula, O.; Farsad, K. Applications of Nanoparticles in Biomedical Imaging. *Nanoscale* **2019**, *11* (3), 799–819.

Hardie, J.; Jiang, Y.; Tetrault, E. R.; Ghazi, P. C.; Tonga, G. Y.; Farkas, M. E.; Rotello, V. M. Simultaneous Cytosolic Delivery of a Chemotherapeutic and SiRNA Using Nanoparticle-Stabilized Nanocapsules. *Nanotechnology.* **2016**, *27* (37), 374001.

Hare, D.; Burger, F.; Austin, C.; Fryer, F.; Grimm, R.; Reedy, B.; Scolyer, R. A.; Thompson, J. F.; Doble, P. Elemental Bio-Imaging of Melanoma in Lymph Node Biopsies. *Analyst* **2009**, *134* (3), 450–453.

Harkness, K. M.; Cliffel, D. E.; McLean, J. A. Characterization of Thiolate-Protected Gold Nanoparticles by Mass Spectrometry. *Analyst* **2010**, *135* (5), 868–874.

Heeren, R. M. A. Getting the Picture: The Coming of Age of Imaging MS. *Int. J. Mass Spectrom.* **2015**, *377* (1), 672–680.

Heuer-Jungemann, A.; Feliu, N.; Bakaimi, I.; Hamaly, M.; Alkilany, A.; Chakraborty, I.; Masood, A.; Casula, M. F.; Kostopoulou, A.; Oh, E.; Susumu, K.; Stewart, M. H.; Medintz, I. L.; Stratakis, E.; Parak, W. J.; Kanaras, A. G. The Role of Ligands in the Chemical Synthesis and Applications of Inorganic Nanoparticles. *Chem. Rev.* **2019**, *119* (8), 4819–4880.

Ho, Y.-N.; Shu, L.-J.; Yang, Y.-L. Imaging Mass Spectrometry for Metabolites: Technical Progress, Multimodal Imaging, and Biological Interactions. *Wiley Interdiscip. Rev. Syst. Biol. Med.* **2017**, *9* (5), e1387.

Holzlechner, M.; Bonta, M.; Lohninger, H.; Limbeck, A.; Marchetti-Deschmann, M. Multisensor Imaging—From Sample Preparation to Integrated Multimodal Interpretation of LA-ICPMS and MALDI MS Imaging Data. *Anal. Chem.* **2018**, *90* (15), 8831–8837.

Huber, K.; Khamehgir-Silz, P.; Schramm, T.; Gorshkov, V.; Spengler, B.; Römpp, A. Approaching Cellular Resolution and Reliable Identification in Mass Spectrometry Imaging of Tryptic Peptides. *Anal. Bioanal. Chem.* **2018**, *410* (23), 5825–5837.

Hunter, J. D. Matplotlib: A 2D Graphics Environment. *Comput. Sci. Eng.* **2007**, *9* (3), 90–95.

Iakab, S. A.; Ràfols, P.; Correig-Blanchar, X.; García-Altares, M. Perspective on Multimodal Imaging Techniques Coupling Mass Spectrometry and Vibrational Spectroscopy: Picturing the Best of Both Worlds. *Anal. Chem.* **2021**, *93* (16), 6301–6310.

Jiang, Y.; Hardie, J.; Liu, Y.; Ray, M.; Luo, X.; Das, R.; Landis, R. F.; Farkas, M. E.; Rotello, V. M. Nanocapsule-Mediated Cytosolic SiRNA Delivery for Anti-Inflammatory Treatment. *J. Control. Release.* **2018**, *283*, 235–240.

Jiang, Y.; Huo, S.; Mizuhara, T.; Das, R.; Lee, Y. W.; Hou, S.; Moyano, D. F.; Duncan, B.; Liang, X. J.; Rotello, V. M. The Interplay of Size and Surface Functionality on the Cellular Uptake of Sub-10 Nm Gold Nanoparticles. *ACS Nano* **2015**, *9* (10), 9986–9993.

Jiang, Y.; Tang, R.; Duncan, B.; Jiang, Z.; Yan, B.; Mout, R.; Rotello, V. M. Direct Cytosolic Delivery of SiRNA Using Nanoparticle-Stabilized Nanocapsules. *Angew. Chemie Int. Ed.* **2014**, *54* (2), 506–510.

Johnson, J.; Sharick, J. T.; Skala, M. C.; Li, L. Sample Preparation Strategies for High-Throughput Mass Spectrometry Imaging of Primary Tumor Organoids. *J. Mass Spectrom.* **2020**, *55* (4), e4452.

Jones, E. A.; Deininger, S. O.; Hogendoorn, P. C. W.; Deelder, A. M.; McDonnell, L. A. Imaging Mass Spectrometry Statistical Analysis. *J. Proteomics* **2012**, *75* (16), 4962–4989.

Jones, M. A.; Cho, S. H.; Patterson, N. H.; Van de Plas, R.; Spraggins, J. M.; Boothby, M. R.; Caprioli, R. M. Discovering New Lipidomic Features Using Cell Type Specific Fluorophore Expression to Provide Spatial and Biological Specificity in a Multimodal Workflow with MALDI Imaging Mass Spectrometry. *Anal. Chem.* **2020**, *92* (10), 7079–7086.

Kaur, D.; Kaur, Y. Various Image Segmentation Techniques: A Review. *Int. J. Comput. Sci. Mob. Comput.* **2014**, *3* (5), 809–814.

Kaya, I.; Sämfors, S.; Levin, M.; Borén, J.; Fletcher, J. S. Multimodal MALDI Imaging Mass Spectrometry Reveals Spatially Correlated Lipid and Protein Changes in Mouse Heart with Acute Myocardial Infarction. *J. Am. Soc. Mass Spectrom.* **2020**, *31* (10), 2133–2142.

Kevadiya, B. D.; Ottemann, B.; Mukadam, I. Z.; Castellanos, L.; Sikora, K.; Hilaire, J. R.; Machhi, J.; Herskovitz, J.; Soni, D.; Hasan, M.; Anandakumar, S.; Garrison, J.; Mcmillan, J.; Edagwa, B.; Mosley, R. L.; Vachet, R. W.; Gendelman, H. E. Rod-Shape Theranostic Nanoparticles Facilitate Antiretroviral Drug Biodistribution and Activity in Human Immunodeficiency Virus Susceptible Cells and Tissues. *Theranostics* **2020**, *10* (2), 630–656.

Khovidhunkit, W.; Kim, M. S.; Memon, R. A.; Shigenaga, J. K.; Moser, A. H.; Feingold, K. R.; Grunfeld, C. Effects of Infection and Inflammation on Lipid and Lipoprotein Metabolism: Mechanisms and Consequences to the Host. *J. Lipid Res.* **2004**, *45* (7), 1169–1196.

Kim, C.; Tonga, G. Y.; Yan, B.; Kim, C. S.; Kim, S. T.; Park, M.-H.; Zhu, Z.; Duncan, B.; Creran, B.; Rotello, V. M. Regulating Exocytosis of Nanoparticles via Host–Guest Chemistry. *Org. Biomol. Chem.* **2015**, *13* (8), 2474–2479.

Kim, S. T.; Saha, K.; Kim, C.; Rotello, V. M. The Role of Surface Functionality in Determining Nanoparticle Cytotoxicity. *Acc. Chem. Res.* **2013**, *46* (3), 681–691.

Kim, Y. P.; Shon, H. K.; Shin, S. K.; Lee, T. G. Probing Nanoparticles and Nanoparticle-Conjugated Biomolecules Using Time-of-Flight Secondary Ion Mass Spectrometry. *Mass Spectrom. Rev.* **2015**, *34* (2), 237–247.

Klein, S.; Staring, M. Elastix 4.9.0 - Manual. **2018**, 60.

Klein, S.; Staring, M.; Murphy, K.; Viergever, M. A.; Pluim, J. P. W. Elastix: A Toolbox for Intensity-Based Medical Image Registration. *IEEE Trans. Med. Imaging.* **2010**, *29* (1), 196–205.

Kleinridders, A.; Ferris, H. A.; Reyzer, M. L.; Rath, M.; Soto, M.; Manier, M. L.; Spraggins, J.; Yang, Z.; Stanton, R. C.; Caprioli, R. M.; Kahn, C. R. Regional Differences in Brain Glucose Metabolism Determined by Imaging Mass Spectrometry. *Mol. Metab.* **2018**, *12*, 113–121.

Kodinariya, T. M.; Makwana, P. R. Review on Determining Number of Cluster in K-Means Clustering. *Int. J. Adv. Res. Comput. Sci. Manag. Stud.* **2013**, *1* (6), 90–95.

Lee, J. H.; Cho, H. Y.; Choi, H. K.; Lee, J. Y.; Choi, J. W. Application of Gold Nanoparticle to Plasmonic Biosensors. *Int. J. Mol. Sci.* **2018**, *19* (7).

Lee, Y. W.; Mout, R.; Luther, D. C.; Liu, Y.; Castellanos-García, L.; Burnside, A. S.; Ray, M.; Tonga, G. Y.; Hardie, J.; Nagaraj, H.; Das, R.; Phillips, E. L.; Tay, T.; Vachet, R. W.; Rotello, V. M. In Vivo Editing of Macrophages through Systemic Delivery of CRISPR-Cas9-Ribonucleoprotein-Nanoparticle Nanoassemblies. *Adv. Ther.* **2019**, *2* (10), 1–7.

Li, T.; Shi, S.; Goel, S.; Shen, X.; Xie, X.; Chen, Z.; Zhang, H.; Li, S.; Qin, X.; Yang, H.; Wu, C.; Liu, Y. Recent Advancements in Mesoporous Silica Nanoparticles towards Therapeutic Applications for Cancer. *Acta Biomater.* **2019**, *89*, 1–13.

Lim, E. K.; Kim, T.; Paik, S.; Haam, S.; Huh, Y. M.; Lee, K. Nanomaterials for Theranostics: Recent Advances and Future Challenges. *Chem. Rev.* **2015**, *115* (1), 327–394.

Lin, P.; Lin, S.; Wang, P. C.; Sridhar, R. Techniques for Physicochemical Characterization of Nanomaterials. *Biotechnol. Adv.* **2014**, *32* (4), 711–726.

Liu, Q.; Sun, Y.; Yang, T.; Feng, W.; Li, C.; Li, F. Sub-10 Nm Hexagonal Lanthanide-Doped NaLuF 4 Upconversion Nanocrystals for Sensitive Bioimaging in Vivo. **2011**, 17122–17125.

Liu, X. Y.; Wang, J. Q.; Ashby, C. R.; Zeng, L.; Fan, Y. F.; Chen, Z. S. Gold Nanoparticles: Synthesis, Physiochemical Properties and Therapeutic Applications in Cancer. *Drug Discov. Today* **2021**, *26* (5), 1284–1292.

Llombart, V.; Trejo, S. A.; Bronsoms, S.; Morancho, A.; Feifei, M.; Faura, J.; García-Berrocoso, T.; Simats, A.; Rosell, A.; Canals, F.; Hernández-Guillamón, M.; Montaner, J. Profiling and Identification of New Proteins Involved in Brain Ischemia Using MALDI-Imaging-Mass-Spectrometry. *J. Proteomics.* **2017**, *152*, 243–253.

Lohninger, H.; Ofner, J. Multisensor Hyperspectral Imaging as a Versatile Tool for Image-Based Chemical Structure Determination. *Spectrosc. Eur.* **2014**, *26* (5), 6–10.

López-Fernández, H.; Pessôa, G. D. S.; Arruda, M. A. Z.; Capelo-Martínez, J. L.; Fdez-Riverola, F.; Glez-Peña, D.; Reboiro-Jato, M. LA - IMageS : A Software for Elemental Distribution Bioimaging Using LA – ICP – MS Data. *J. Cheminform.* **2016**, *8* (1), 65.

Lowekamp, B.; Marstal, K.; Blezek, D.; Chen, D.; Yaniv, Z.; King, B. SimpleElastix. *GitHub*. 2020.

Masyuko, R.; Lanni, E. J.; Sweedler, J. V; Bohn, P. W. Correlated Imaging – a Grand Challenge in Chemical Analysis. *Analyst* **2013**, *138* (7), 1924–1939.

Matusch, A.; Depboylu, C.; Palm, C.; Wu, B.; Höglinger, G. U.; Schäfer, M. K. H.; Becker, J. S. Cerebral Bioimaging of Cu, Fe, Zn, and Mn in the MPTP Mouse Model of Parkinson's Disease Using Laser Ablation Inductively Coupled Plasma Mass Spectrometry (LA-ICP-MS). *J. Am. Soc. Mass Spectrom.* **2010**, *21* (1), 161–171.

McCombie, G.; Staab, D.; Stoeckli, M.; Knochenmuss, R. Spatial and Spectral Correlations in MALDI Mass Spectrometry Images by Clustering and Multivariate Analysis. *Anal. Chem.* **2005**, *77* (19), 6118–6124.

Mccormick, M.; Liu, X.; Jomier, J.; Marion, C.; Ibanez, L. ITK: Enabling Reproducible Research and Open Science. *Front. Neuroinform.* **2014**, *8* (FEB), 1–11.

Mebius, R. E.; Kraal, G. Structure and Function of the Spleen. *Nat. Rev. Immunol.* **2005**, *5* (8), 606–616.

Mitchell, M. J.; Billingsley, M. M.; Haley, R. M.; Wechsler, M. E.; Peppas, N. A.; Langer, R. Engineering Precision Nanoparticles for Drug Delivery. *Nat. Rev. Drug Discov.* **2021**, *20* (2), 101–124.

Modena, M. M.; Rühle, B.; Burg, T. P.; Wuttke, S. Nanoparticle Characterization: What to Measure? *Adv. Mater.* **2019**, *31* (32), 1–26.

Mout, R.; Ray, M.; Lee, Y.; Tay, T.; Sasaki, K.; Rotello, V. M. Direct Cytosolic Delivery of CRISPR/Cas9- Ribonucleoprotein for Efficient Gene Editing. *ACS Nano* **2017**.

Neumann, E. K.; Comi, T. J.; Spegazzini, N.; Mitchell, J. W.; Rubakhin, S. S.; Gillette, M. U.; Bhargava, R.; Sweedler, J. V. Multimodal Chemical Analysis of the Brain by High Mass Resolution Mass Spectrometry and Infrared Spectroscopic Imaging. *Anal. Chem.* **2018**, *90* (19), 11572–11580.

Neumann, E. K.; Djambazova, K. V.; Caprioli, R. M.; Spraggins, J. M. Multimodal Imaging Mass Spectrometry: Next Generation Molecular Mapping in Biology and Medicine. *J. Am. Soc. Mass Spectrom.* **2020**, *31* (12), 2401–2415.

Nicolardi, S.; Van Der Burgt, Y. E. M.; Codée, J. D. C.; Wuhrer, M.; Hokke, C. H.; Chiodo, F. Structural Characterization of Biofunctionalized Gold Nanoparticles by Ultrahigh-Resolution Mass Spectrometry. *ACS Nano* **2017**, *11* (8), 8257–8264.

Niehoff, A.-C.; Schulz, J.; Soltwisch, J.; Meyer, S.; Kettling, H.; Sperling, M.; Jeibmann, A.; Dreisewerd, K.; Francesconi, K. A.; Schwerdtle, T.; Karst, U. Imaging by Elemental and Molecular Mass Spectrometry Reveals the Uptake of an Arsenolipid in the Brain of Drosophila Melanogaster. *Anal. Chem.* **2016**, *88* (10), 5258–5263.

Nikitina, A.; Huang, D.; Li, L.; Peterman, N.; Cleavenger, S. E.; Fernández, F. M.; Kemp, M. L. A Co-Registration Pipeline for Multimodal MALDI and Confocal Imaging Analysis of Stem Cell Colonies. *J. Am. Soc. Mass Spectrom.* **2020**, *31* (4), 986–989.

Norris, J. L.; Caprioli, R. M. Analysis of Tissue Specimens by Matrix-Assisted Laser Desorption/Ionization Imaging Mass Spectrometry in Biological and Clinical Research. *Chem. Rev.* **2013**, *113* (4), 2309–2342.

Oros-Peusquens, A. M.; Matusch, A.; Becker, J. S.; Shah, N. J. Automatic Segmentation of Tissue Sections Using the Multielement Information Provided by LA-ICP-MS Imaging and k-Means Cluster Analysis. *Int. J. Mass Spectrom.* **2011**, *307*, 245–252.

Osterholt, T.; Salber, D.; Matusch, A.; Becker, J. S.; Palm, C. IMAGENA : Image Generation and Analysis – An Interactive Software Tool Handling LA-ICP-MS Data. *Int. J. Mass Spectrom.* **2011**, *307* (1–3), 232–239.

Ottemann, B. M.; Helmink, A. J.; Zhang, W.; Mukadam, I.; Woldstad, C.; Hilaire, J. R.; Liu, Y.; Mcmillan, J. M.; Edagwa, B. J.; Mosley, R. L.; Garrison, J. C.; Kevadiya, B. D.; Gendelman, H. E. Bioimaging Predictors of Rilpivirine Biodistribution and Antiretroviral Activities. *Biomaterials* **2018**, *185*, 174–193.

Ovchinnikova, K.; Stuart, L.; Rakhlin, A.; Nikolenko, S.; Alexandrov, T. ColocML: Machine Learning Quantifies Co-Localization between Mass Spectrometry Images. *Bioinformatics* **2020**, *36* (10), 3215–3224.

Parameswaran, N.; Patial, S. Tumor Necrosis Factor-α Signaling in Macrophages Narayanan. *Crit Rev Eukaryot Gene Expr.* **2010**, *20* (2), 87–103.

Parchur, A. K.; Sharma, G.; Jagtap, J. M.; Gogineni, V. R.; Laviolette, P. S.; Flister, M. J.; White, S. B.; Joshi, A. Vascular Interventional Radiology-Guided Photothermal Therapy of Colorectal Cancer Liver Metastasis with Theranostic Gold Nanorods. *ACS Nano* **2018**, *12* (7), 6597–6611.

Paton, C.; Hellstrom, J.; Paul, B.; Woodhead, J.; Hergt, J. Iolite: Freeware for the Visualisation and Processing of Mass Spectrometric Data. *J. Anal. At. Spectrom.* **2011**, *26* (12), 2508–2518.

Patterson, N. H.; Tuck, M.; Lewis, A.; Kaushansky, A.; Norris, J. L.; Van de Plas, R.; Caprioli, R. M. Next Generation Histology-Directed Imaging Mass Spectrometry Driven by Autofluorescence Microscopy. *Anal. Chem.* **2018**, *90* (21), 12404–12413.

Patterson, N. H.; Yang, E.; Kranjec, E.; Chaurand, P. Co-Registration and Analysis of Multiple Imaging Mass Spectrometry Datasets Targeting Different Analytes. *Bioinformatics.* **2019**, *35* (7), 1261–1262.

Paul, B.; Hare, D. J.; Bishop, D. P.; Paton, C.; Nguyen, V. T.; Cole, N.; Niedwiecki, M. M.; Andreozzi, E.; Vais, A.; Billings, J. L.; Bray, L.; Bush, A.; McColl, G.; Roberts, B. R.; Adlard, P. A.; Finkelstein, D. I.; Hellstrom, J.; Hergt, J. M.; Woodhead, J. D.; Doble, P. A. Visualising Mouse Neuroanatomy and Function by Metal Distribution Using Laser Ablation-Inductively Coupled Plasma-Mass Spectrometry Imaging. *Chem. Sci.* **2015**, *6* (10), 5383–5393.

Pedregosa, F.; Varoquaux, G.; Gramfort, A.; Michael, V.; Thirion, B.; Grisel, O.; Blondel, M.; Prettenhofer, P.; Weiss, R.; Dubourg, V.; Vanderplas, J.; Passos, A.; Cournapeau, D.; Brucher, M.; Perrot, M.; Duchesnay, E. Scikit-Learn: Machine Learning in Python. *J. Mach. Learn. Res.* **2011**, *12*, 2825–2830.

Peng, H. S.; Chiu, D. T. Soft Fluorescent Nanomaterials for Biological and Biomedical Imaging. *Chem. Soc. Rev.* **2015**, *44* (14), 4699–4722.

Perry, W. J.; Spraggins, J. M.; Sheldon, J. R.; Grunenwald, C. M.; Heinrichs, D. E.; Cassat, J. E.; Skaar, E. P.; Caprioli, R. M. Staphylococcus Aureus Exhibits Heterogeneous Siderophore Production within the Vertebrate Host. *Proc. Natl. Acad. Sci.* **2019**, *116* (44), 21980–21982.

Petrus, J. A.; Chew, D. M.; Leybourne, M. I.; Kamber, B. S. A New Approach to LA-ICP-MS Using the Flexible Map Interrogation Tool Monocle. *Chem. Geol.* **2017**, *463*, 76–93.

Porta Siegel, T.; Hamm, G.; Bunch, J.; Cappell, J.; Fletcher, J. S.; Schwamborn, K. Mass Spectrometry Imaging and Integration with Other Imaging Modalities for Greater Molecular Understanding of Biological Tissues. *Mol. Imaging Biol.* **2018**, *20* (6), 888–901.

Pozebon, D.; Scheffler, G. L.; Dressler, V. L. Recent Applications of Laser Ablation Inductively Coupled Plasma Mass Spectrometry (LA-ICP-MS) for Biological Sample Analysis: A Follow-up Review. *J. Anal. At. Spectrom.* **2017**, *32* (5), 890–919.

Probst, C. E.; Zrazhevskiy, P.; Bagalkot, V.; Gao, X. Quantum Dots as a Platform for Nanoparticle Drug Delivery Vehicle Design. *Adv. Drug Deliv. Rev.* **2013**, *65* (5), 703–718.

Qing, Z.; Bai, A.; Xing, S.; Zou, Z.; He, X.; Wang, K.; Yang, R. Progress in Biosensor Based on DNA-Templated Copper Nanoparticles. *Biosens. Bioelectron.* **2019**, *137* (April), 96–109.

Rao, C. N. R.; Vivekchand, S. R. C.; Biswas, K.; Govindaraj, A. Synthesis of Inorganic Nanomaterials. *J. Chem. Soc. Dalt. Trans.* **2006**, No. 34, 3728–3749.

Robison, G.; Zakharova, T.; Fu, S.; Jiang, W.; Fulper, R.; Barrea, R.; Marcus, M. A.; Zheng, W.; Pushkar, Y. X-Ray Fluorescence Imaging: A New Tool for Studying Manganese Neurotoxicity. *PLoS one.* **2012**, *7* (11), e48899.

Rohlfing, T. Image Similarity and Tissue Overlaps as Surrogates for Image Registration Accuracy: Widely Used but Unreliable. *IEEE Trans. Med. Imaging.* **2012**, *31* (2), 153–163.

Ryan, D. J.; Spraggins, J. M.; Caprioli, R. M. Protein Identification Strategies in MALDI Imaging Mass Spectrometry: A Brief Review. *Curr. Opin. Chem. Biol.* **2019**, *48*, 64–72.

Sabine Becker, J. Imaging of Metals in Biological Tissue by Laser Ablation Inductively Coupled Plasma Mass Spectrometry (LA-ICP-MS): State of the Art and Future Developments. *J. Mass Spectrom.* **2013**, *48* (2), 255–268.

Scaletti, F.; Hardie, J.; Lee, Y. W.; Luther, D. C.; Ray, M.; Rotello, V. M. Protein Delivery into Cells Using Inorganic Nanoparticle-Protein Supramolecular Assemblies. *Chem. Soc. Rev.* **2018**, *47* (10), 3421–3432.

Scheffer, A.; Engelhard, C.; Sperling, M.; Buscher, W. ICP-MS as a New Tool for the Determination of Gold Nanoparticles in Bioanalytical Applications. *Anal. Bioanal. Chem.* **2008**, *390* (1), 249–252.

Schindelin, J.; Arganda-Carreras, I.; Frise, E.; Kaynig, V.; Longair, M.; Pietzsch, T.; Preibisch, S.; Rueden, C.; Saalfeld, S.; Schmid, B.; Tinevez, J. Y.; White, D. J.; Hartenstein, V.; Eliceiri, K.; Tomancak, P.; Cardona, A. Fiji: An Open-Source Platform for Biological-Image Analysis. *Nat. Methods.* **2012**, *9* (7), 676–682.

Sforna, M. C.; Lugli, F. MapIT! A Simple and User-Friendly MATLAB Script to Elaborate Elemental Distribution Images from LA-ICP-MS Data. *J. Anal. At. Spectrom.* **2017**, *32* (5), 1035–1043.

Sikora, K. N.; Hardie, J. M.; Castellanos-García, L. J.; Liu, Y.; Reinhardt, B. M.; Farkas, M. E.; Rotello, V. M.; Vachet, R. W. Dual Mass Spectrometric Tissue Imaging of Nanocarrier Distributions and Their Biochemical Effects. *Anal. Chem.* **2020**, *92* (2), 2011–2018.

Smets, T.; Waelkens, E.; De Moor, B. Prioritization of m/ z-Values in Mass Spectrometry Imaging Profiles Obtained Using Uniform Manifold Approximation and Projection for Dimensionality Reduction. *Anal. Chem.* **2020**, *92* (7), 5240–5248.

Sussulini, A.; Becker, J. S.; Becker, J. S. Laser Ablation ICP-MS: Application in Biomedical Research. *Mass Spectrom. Rev.* **2017**, *36* (1), 47–57.

Suzuki, T.; Sakata, S.; Makino, Y.; Obayashi, H.; Ohara, S.; Hattori, K.; Hirata, T. IQuant2: Software for Rapid and Quantitative Imaging Using Laser Ablation-ICP Mass Spectrometry. *Mass Spectrom.* **2018**, *7* (1), A0065.

Swales, J. G.; Hamm, G.; Clench, M. R.; Goodwin, R. J. A. Mass Spectrometry Imaging and Its Application in Pharmaceutical Research and Development: A Concise Review. *Int. J. Mass Spectrom.* **2019**, *437*, 99–112.

Tang, R.; Kim, C. S.; Solfiell, D. J.; Rana, S.; Mout, R.; Velázquez-Delgado, E. M.; Chompoosor, A.; Jeong, Y.; Yan, B.; Zhu, Z. J.; Kim, C.; Hardy, J. A.; Rotello, V. M. Direct Delivery of Functional Proteins and Enzymes to the Cytosol Using Nanoparticle-Stabilized Nanocapsules. *ACS Nano* **2013**, *7* (8), 6667–6673.

Tededyne CETAC Technologies. HDIP LA-ICP-MS Image Processing Software http://www.teledynecetac.com/products/laser-ablation/hdip-imaging-software.

Theiner, S.; Kornauth, C.; Varbanov, H. P.; Galanski, M.; Van Schoonhoven, S.; Heffeter, P.; Berger, W.; Egger, A. E.; Keppler, B. K. Tumor Microenvironment in Focus: LA-ICP-MS Bioimaging of a Preclinical Tumor Model upon Treatment with Platinum(IV)-Based Anticancer Agents. *Metallomics.* **2015**, *7* (8), 1256–1264.

Tian, X.; Xie, B.; Zou, Z.; Jiao, Y.; Lin, L. E.; Chen, C. L.; Hsu, C. C.; Peng, J.; Yang, Z. Multimodal Imaging of Amyloid Plaques: Fusion of the Single-Probe Mass Spectrometry Image and Fluorescence Microscopy Image. *Anal. Chem.* **2019**, *91* (20), 12882–12889.

Tobias, F.; Hummon, A. B. Considerations for MALDI-Based Quantitative Mass Spectrometry Imaging Studies. *J. Proteome Res.* **2020**, *19* (9), 3620–3630.

Tonga, G. Y.; Jeong, Y.; Duncan, B.; Mizuhara, T.; Mout, R.; Das, R.; Kim, S. T.; Yeh, Y. C.; Yan, B.; Hou, S.; Rotello, V. M. Supramolecular Regulation of Bioorthogonal Catalysis in Cells Using Nanoparticle-Embedded Transition Metal Catalysts. *Nat. Chem.* **2015**, *7* (7), 597–603.

Tonga, G. Y.; Moyano, D. F.; Kim, C. S.; Rotello, V. M. Inorganic Nanoparticles for Therapeutic Delivery: Trials, Tribulations and Promise. *Curr. Opin. Colloid Interface Sci.* **2014**, *19* (2), 49–55.

Touboul, D.; Laprévote, O.; Brunelle, A. Micrometric Molecular Histology of Lipids by Mass Spectrometry Imaging. *Curr. Opin. Chem. Biol.* **2011**, *15* (5), 725–732.

Uerlings, R.; Matusch, A.; Weiskirchen, R. Reconstruction of Laser Ablation Inductively Coupled Plasma Mass Spectrometry (LA-ICP-MS) Spatial Distribution Images in Microsoft Excel 2007. *Int. J. Mass Spectrom.* **2016**, *395*, 27–35.

Virtanen, P.; Gommers, R.; Oliphant, T. E.; Haberland, M.; Reddy, T.; Cournapeau, D.; Burovski, E.; Peterson, P.; Weckesser, W.; Bright, J.; Walt, S. J. Van Der; Brett, M.; Wilson, J.; Millman, K. J.; Mayorov, N.; Nelson, A. R. J.; Jones, E.; Kern, R.; Larson, E.; Carey, C. J.; Polat, I.; Feng, Y.; Moore, E. W.; VanderPlas, J.; Laxalde, D.; Perktold, J.; Cimrman, R.; Henriksen, I.; Quintero, E. A.; Harris, C. R.; Archibald, A. M.; Ribeiro, A. H.; Pedregosa, F.; Mulbregt, P. van. SciPy 1.0: Fundamental Algorithms for Scientific Computing in Python. *Nat. Methods.* **2020**, *17* (3), 261–272.

Wallace, M.; Morris, C.; O'Grada, C. M.; Ryan, M.; Dillon, E. T.; Coleman, E.; Gibney, E. R.; Gibney, M. J.; Roche, H. M.; Brennan, L. Relationship between the Lipidome, Inflammatory Markers and Insulin Resistance. *Mol. Biosyst.* **2014**, *10* (6), 1586–1595.

Van Der Walt, S.; Colbert, S. C.; Varoquaux, G. The NumPy Array: A Structure for Efficient Numerical Computation. *Comput. Sci. Eng.* **2011**, *13* (2), 22–30.

Wang, Y.; Huang, L. A Window onto SiRNA Delivery. *Nat. Biotechnol.* **2013**, *31* (7), 611–612.

Wang, Y.; Feng, L.; Wang, S. Conjugated Polymer Nanoparticles for Imaging, Cell Activity Regulation, and Therapy. *Adv. Funct. Mater.* **2019**, *29* (5), 1–20.

Wu, Y.; Ali, M. R. K.; Chen, K.; Fang, N.; El-Sayed, M. A. Gold Nanoparticles in Biological Optical Imaging. *Nano Today* **2019**, *24*, 120–140.

Wu, Z.; Yang, S.; Wu, W. Shape Control of Inorganic Nanoparticles from Solution. *Nanoscale* **2016**, *8* (3), 1237–1259.

Yan, B.; Zhu, Z.-J.; Miranda, O. R.; Chompoosor, A.; Rotello, V. M.; Vachet, R. W. Laser Desorption/Ionization Mass Spectrometry Analysis of Monolayer-Protected Gold Nanoparticles. *Anal. Bioanal. Chem.* **2010**, *396* (3), 1025–1035.

Yang, L.; Seah, M. P.; Gilmore, I. S.; Morris, R. J. H.; Dowsett, M. G.; Boarino, L.; Sparnacci, K.; Laus, M. Depth Profiling and Melting of Nanoparticles in Secondary Ion Mass Spectrometry (SIMS). *J. Phys. Chem. C* **2013**, *117* (31), 16042–16052.

Zenobi, R.; Knochenmuss, R. Ion Formation in MALDI Mass Spectrometry. *Mass Spectrom. Rev.* **1998**, *17* (337), 337–366.

Zhang, K.; Gao, Y. J.; Yang, P. P.; Qi, G. Bin; Zhang, J. P.; Wang, L.; Wang, H. Self-Assembled Fluorescent Organic Nanomaterials for Biomedical Imaging. *Adv. Healthc. Mater.* **2018**, *7* (20), 1–16.

Zhang, Y.; Liu, X. Machine Learning Techniques for Mass Spectrometry Imaging Data Analysis and Applications. *Bioanalysis* **2018**, *10*, 519–522.

Zhang, Y.; Fang, F.; Li, L.; Zhang, J. Self-Assembled Organic Nanomaterials for Drug Delivery, Bioimaging, and Cancer Therapy. *ACS Biomater. Sci. Eng.* **2020**, *6* (9), 4816–4833.

Jupyter. https://jupyter.org/ 2014.